Prace Transactions

INSTYTUTU LOTNICTWA of the INSTITUTE of AVIATION

200

SILNIKI TURBINOWE I RAKIETOWE — **TURBINE AND ROCKET ENGINES**
AEROELASTYCZNOŚĆ I AERODYNAMIKA — **AEROELASTICITY AND AERODYNAMICS**
PROBLEMY SPALANIA I ZANIECZYSZCZEŃ — **COMBUSTION AND POLLUTION ISSUES**
OPTYMALIZACJA KOMPOZYTÓW — **COMPOSITES OPTIMISATION**
NIEZAWODNOŚĆ I WYTRZYMAŁOŚĆ — **RELIABILITY AND STRENGTH**
HAŁAS I DOKŁADNOŚĆ W OBRABIARKACH — **NOISE AND ACCURACY IN MACHINERY**
ELIMINACJA DRGAŃ — **VIBRATION ELIMINATION**

2009

Over 80 years in the service of Polish Science

Prace Transactions

INSTYTUTU LOTNICTWA

of the INSTITUTE of AVIATION

200

2009

Over 80 years in the service of Polish Science

SILNIKI TURBINOWE I RAKIETOWE	***TURBINE AND ROCKET ENGINES***
AEROELASTYCZNOŚĆ I AERODYNAMIKA	***AEROELASTICITY AND AERODYNAMICS***
PROBLEMY SPALANIA I ZANIECZYSZCZEŃ	***COMBUSTION AND POLLUTION ISSUES***
OPTYMALIZACJA KOMPOZYTÓW	***COMPOSITES OPTIMISATION***
NIEZAWODNOŚĆ I WYTRZYMAŁOŚĆ	***RELIABILITY AND STRENGTH***
HAŁAS I DOKŁADNOŚĆ W OBRABIARKACH	***NOISE AND ACCURACY IN MACHINERY***
ELIMINACJA DRGAŃ	***VIBRATION ELIMINATION***

IL

ISSN 0509-6669

TRANSACTIONS OF THE INSTITUTE OF AVIATION

Scientific Quarterly
5/2009 (200)

CONTENTS

Edition is sponsored by Ministry of Science and Higher Education

PRACE INSTYTUTU LOTNICTWA

KWARTALNIK NAUKOWY
5/2009 (200)

ТРУДЫ ИНСТИТУТА АВИАЦИИ

НАУЧНОЙ ЖУРНАЛ (КВАРТАЛНИК)
5/2009 (200)

Publisher: Institute of Aviation Scientific Publications
Al. Krakowska 110/114 02-256 Warsaw, Poland
phone: (4822) 846 00 11 ext. 442, fax: (4822) 846 44 32
Edition, revision and computer layout: Michal Bakowski,
Agata Chrzanowska MA, Tadeusz Korsak MSc, ME
Printers: ALKOR, 05-070 Sulejowek, Krucza 4

AN INVESTIGATION OF NONLINEAR AEROELASTICITY IN AIRCRAFT WINGS

Arthur Faflik-Brooks
Institute of Aviation, Engineering Design Center

Abstract

The investigation involved exploring the properties of the nonlinear spring models for aircraft wings. The theory which leads to the set of differential equations govering the motion of the aircraft wing was then described. A previous student had already made a program called wforce.f. The Runge-Kutta-Fehlberg method used in this program was described and the program was validated using examples made in past references. These were found to correspond to the results for the program. Finally an investigation was made into the effect of changing the cubic spring on the amplitude of motion of the wing after a perturbation. A harder cubic spring was found to reduce the amplitude of the limit cycle in which the wing oscillated.

1. INTRODUCTION

The response of the wing to a perturbation when in flight is critical. A perturbation caused by a gust, birdstrike or other loading could result in undesirable divergent oscillations, potentially leading to stall, higher stresses in the wing, a loss in performance of the aircraft or a combination of the three. The wing's aeroelastic behaviour, or the "interaction of inertia, structural and aerodynamic force", therefore ranks highly in importance when designing and analysing its performance.

The velocity at which the aircraft flies is restricted by its flutter velocity. At this velocity any perturbation will result in an oscillation with the same amplitude and no convergence. Any velocity above the flutter velocity will result in divergent oscillations, and any velocity below will result in convergence. Hence the aircraft must stay below the flutter velocity.

Normal elastic behaviour yields an elastic force, which is a linear function of the elastic displacement. Aeroelastic behaviour in wings, however, can be strongly nonlinear, with the gradient of a force-displacement curve dependent on the displacement. The nonlinearities arise both from aerodynamic and structural effects. The aerodynamic nonlinearities result from compressed flow causing shock waves with destabilise the pitching motion of the aerofoil. The structural nonlinearities arise from the nonlinear behaviour of hinges, linkages and systems in the wing as well as from the behaviour of thin wings in torsion and from wings undergoing buckling. In this project the structural nonlinearities were investigated.

The elastic linear and nonlinear properties of the wing are distributed – the displacement at a given point corresponding to a unit displacement at a certain degree of freedom is dependent on the position of the point. The distributed model can, however, be translated to a concentrated point model via mode shape functions, which will be described in more detail later in the report.

If the shape functions are known then the system can be idealised as a mass-spring-damper system and described in terms of n equations of motion, corresponding to n degrees of freedom.

These can then be rewritten to give a vector **X** and the derivative of **X** given by **f(X)**, and the system integrated for a desired time using various integration methods such as Houbolt's finite difference method, or the Runge-Kutta-Fehlberg method, as used in this project.

The purpose of this project was to continue on the work of an earlier student, E. Baldassin, and confirm the functioning of his program *wforce*, written in the FORTRAN-77 language (reference 7), and investigate the behaviour of the equations for different constants of a *cubic* elastic term in the equations of motion.

2. THE CUBIC SPRING

The model of a wing as a purely-linear spring in rotation becomes inaccurate when nonlinearities arise due to leakages and fatigue of joints and hinges, the behaviour of thin wings in torsion, buckling of the wing, attachments to the wing such as the engine or missile pylons under fatigue and other factors. There are other models for nonlinear elastic springs. The following diagram shows a hysteresis nonlinearity, with linear behaviour exhibited up until a certain point, when the linear elastic constant suddenly changes. When the displacement is changing in the opposite direction, the change may occur at another point, such as in the diagram below:

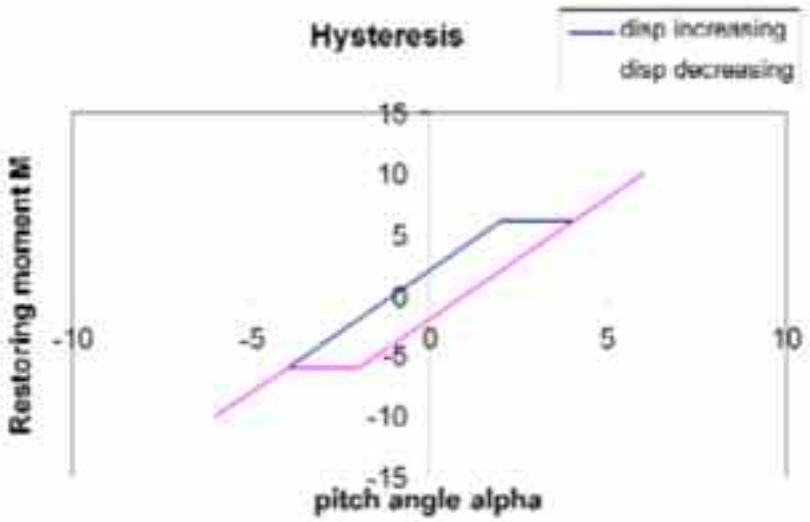

Fig. 1. Example of hysteresis nonlinearity

Ductile materials present in systems in the wing, such as hinge mechanisms, may lead to hardening hysteresis behaviour under cyclic loading. Below is a graph of store yaw amplitude against force moment for the F-111 fighter.

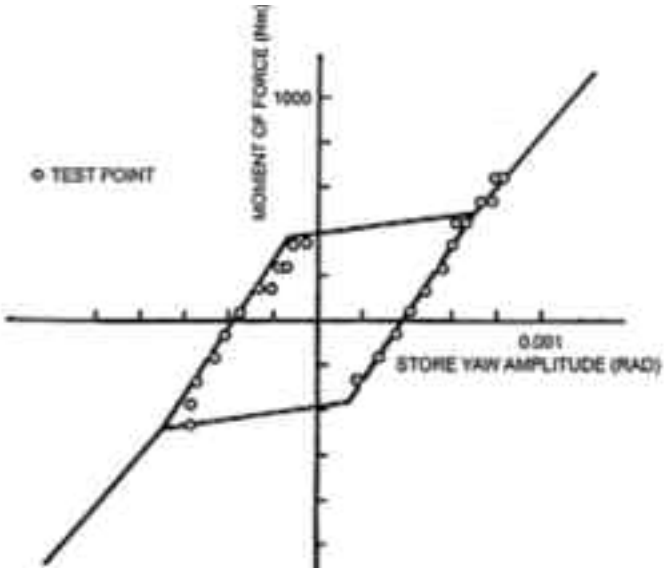

Fig. 2. Store yaw amplitude vs. force moment for the F-111 aircraft

The bilinear spring is another model which consists of three regions along the displacement axis: At first, from the negative displacement, the spring has a certain elastic constant. In the second region, the system adopts another elastic constant, before returning to the first, as shown in the diagram below:

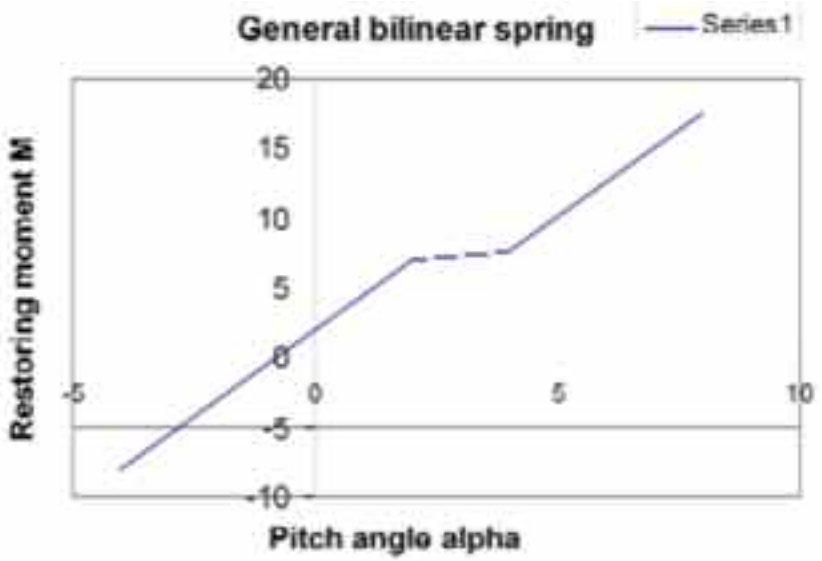

Fig. 3. General bilinear spring

In this project the investigation was concentrated on cubic spring behaviour with no hysteresis. The elastic term in the equations of motion includes a function of the displacement vector, in this case the angle of attack, raised to a power of 3. In this way the "spring" can be modelled either to soften or harden with increasing angle of attack. The equation for the elastic force is then as shown in equation (1) below:

$$F = \beta_0 + \beta_1\alpha + \beta_2\alpha^2 + \beta_3\alpha^3 \tag{1}$$

Should the wing buckle, the wing will adopt the elastic characteristics of a softening spring with stiffness decreasing as the angle of rotation increases, as shown in the diagram below:

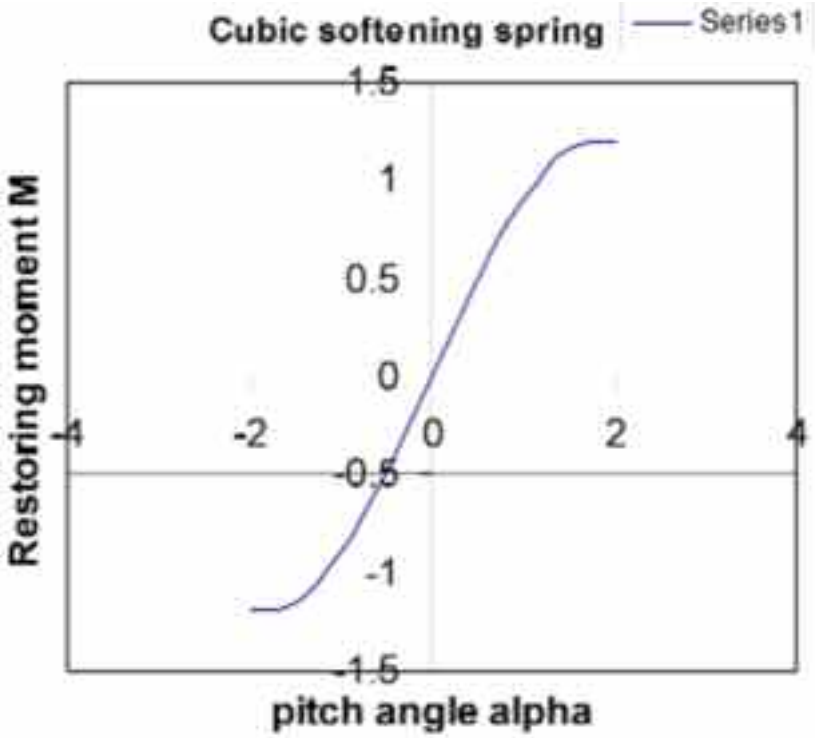

Fig. 4. Cubic softening spring

Hardening of the wing at higher angles of attack can have beneficial effects on the wing response to perturbations, enabling the wing to return to a lower angle of attack and the oscillations to occur between limit cycles instead of diverging at velocities above the flutter velocity for the wing with just a linear term. This can be a useful property for an aircraft travelling at high speed.

A thin wing undergoing torsion will most likely adopt the behaviour of a cubic spring, adopting greater stiffness as the torsion angle increases. This is shown in the diagram (figure 5) below:

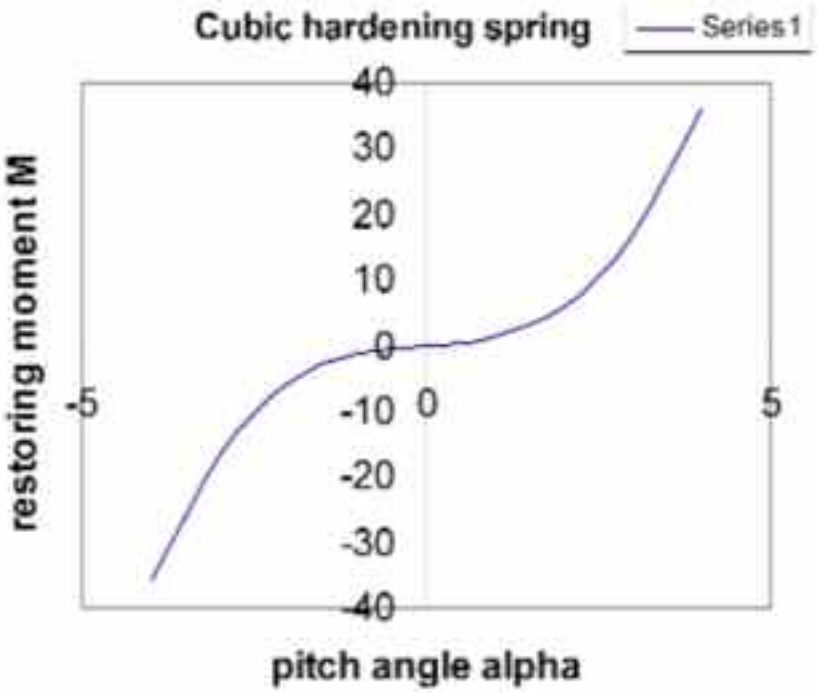

Fig. 5. Cubic hardening spring

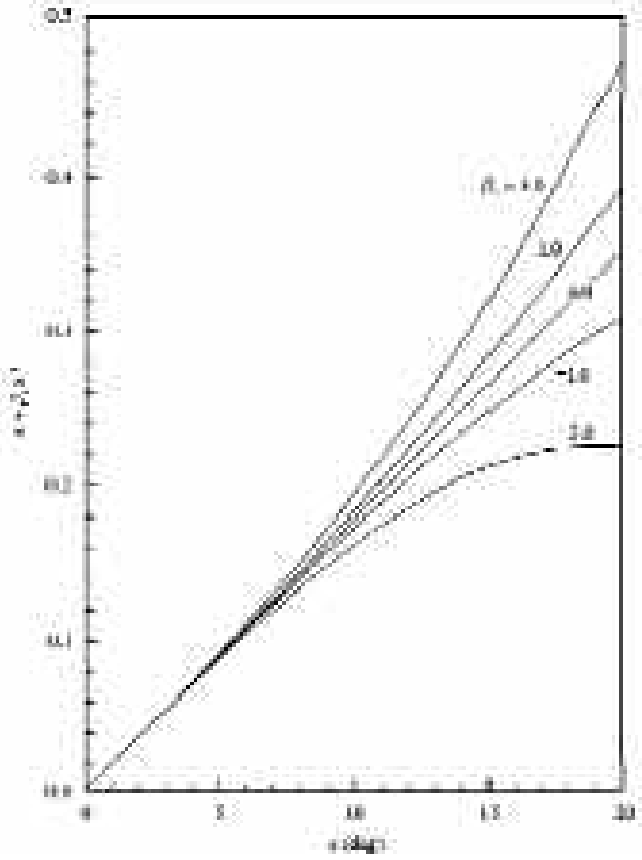

Fig. 6. Cubic spray with various cube parameters

The differences in characteristics of elastic systems with differing cubic spring coefficients is shown in the figure 6 on previous page.

The graph shows the effect of hardening springs on the restoring moment, which is shown on the vertical axis. A hardening spring will produce a higher restoring moment than a simple linear spring, while a softening spring will reduce the restoring moment.

3. THEORY

In this section general analytic theory used for the project is discussed. Extensive use was made of reference [1] in this section.

3.1 Equations of motion

In this section the mathematical derivation leading up to the formulation of the differential equations for use in the program wforce.f is discussed. The program is listed in reference 7.

3.1.2 Use of shape functions

The diagram on the top of the next page shows the wing with its co-ordinate system:

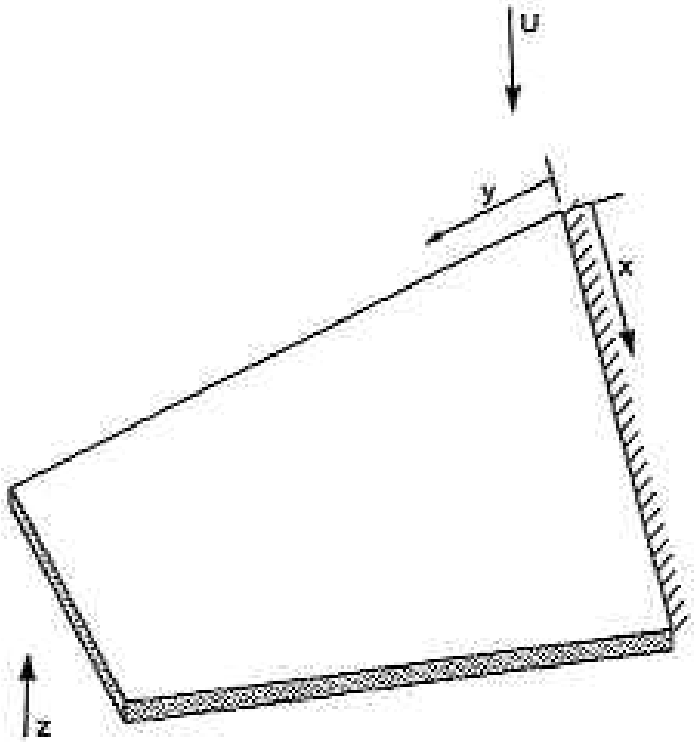

Fig. 7. Wing coordinate system

The following analysis uses theory taken from reference [1], pages 221 to 226:

The displacement *z* at a position *(x, y)* for a mode *i* point displacement *q* can be described through the following equation:

$$z_i(x,y,t) = \varphi_i(x,y)q_i(t) \tag{2}$$

where $\varphi_i(x,y)$ is the *shape function* for the mode *i.*

The total displacement is then given by the sum of the displacements for the individual modes, given by:

$$z(x,y,t) = \sum_{i=1}^{n} \varphi_i(x,y)q_i(t) \tag{3}$$

The equations of motion can be expressed in terms of the generalised displacement vector **q** as

$$[M]\{\ddot{q}\}+[C]\{\dot{q}\}+[K]\{q\}=\{F\} \tag{4}$$

where M is the mass matrix, C the damping matrix, K the stiffness matrix and F the load vector.

For systems with nonlinear elastic terms the matrix [K] is replaced by the matrix [Q]. The individual matrices M, C, K and/or Q for a 2 degree-of-freedom system are described as follows…

$$[M]=\begin{bmatrix} M_1 & 0 \\ 0 & M_2 \end{bmatrix} \quad [C]=\begin{bmatrix} C_1 & 0 \\ 0 & C_2 \end{bmatrix} \quad [K]=\begin{bmatrix} K_1 & 0 \\ 0 & K_2 \end{bmatrix}$$

...with Q taking the same form as K. Strictly speaking there should be a coupling damping term C_{12} and C_{21} but these are stated in reference [1] page 222 to be insignificant.
A mass term M_i will hold the same kinetic energy for the point model moving with velocity $\dot{q}_i$ as the sum of all infinitesimal parts of with mass per unit area m and area dA moving with velocity $\varphi_i\dot{q}_i$, and belonging to the region A. Hence

$$M_i=\int_A m\varphi_i^2 dA \tag{5}$$

Similarly the damping term C_i signifies a generalised damper which, at velocity $\dot{q}_i$, dissipates energy at the same rate as the sum of infinitesimal dampers which exert the local viscous pressure per unit velocity p_{di} on an area dA running counterphase to the local displacement velocity $\varphi_i\dot{q}_i$. The local damping force is then $p_{di}\varphi_i\dot{q}_i dA$ and the energy dissipation rate, or power, of the damper is the force multiplied by the local velocity. Hence the generalised damping term is given by:

$$C_i=\int_A p_{di}\varphi_i^2 dA \tag{6}$$

The generalised elastic term K_i or Q_i absorbs the same potential energy when displaced by an amount q_i as the sum of infinitesimal components along the wing absorbing potential energy when displaced by an amount $\varphi_i q_i$. With the wing idealised as a beam of flexural stiffness EI and length s with x being a displacement in the same direction as s, this leads to the equation for the generalised elastic term being written as:

$$K_i=\int_s EI\left\{\frac{d^2\varphi_i}{dx^2}\right\}dx \tag{7}$$

Finally the generalised force is the force which, when displaced by a *virtual displacement* δq_i does the same amount of *virtual* work as the local pressure $p(x,y,t)$ does at a local displacement $\varphi_i\delta q_i$. Hence the generalised force is given as:

$$F_i=\int_A p(x,y,t)\varphi_i dA \tag{8}$$

In terms of the motion of the wing, the displacements to be considered are the vertical "plunge" displacement and the rotational displacement: the angle of attack of the wing with respect to the airflow. The various dimensions of the wing that will be used throughout the theoretical analysis are described as in the diagram on the next page.

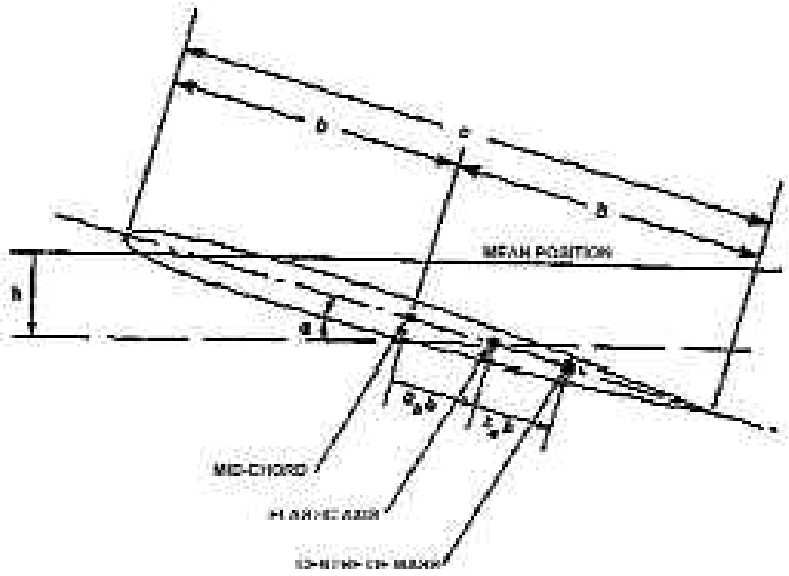

Fig. 8. Wing cross-section dimensions

The wing is idealised as a flat wing. Two degrees of freedom are considered: rotational (pitch) and vertical (plunge) motion.

3.1.2 The wing

The inertial force per unit span for the wing in plunge has components of both $\ddot{h}$ and $\ddot{\alpha}$, as the pitch motion has a vertical component. The vertical acceleration component due to the pitch is then $r\ddot{\alpha}$. Taking *r* as the distance from the elastic axis, positive towards the leading edge, the inertial force per unit span for vertical motion is given by

$$\int_h \left(\ddot{h} + r\ddot{\alpha}\right) dm$$

$\ddot{h}$ and $\ddot{\alpha}$ are both constant over the wing, and so the inertial term for motion in plunge can be written as $m\ddot{h} + S\ddot{\alpha}$ where

$m = \int_h dm$ and $S = \int_h r\,dm$, the first static moment of area.

In rotation, the inertial moment is measured in the second degree-of-freedom equation. For each infinitesimal component this is given by the inertial force multiplied by the distance from the elastic centre. Hence the inertial moment in rotation is given by

$$\int_h r\left(\ddot{h} + r\ddot{\alpha}\right) dm = I_\alpha \ddot{\alpha} + S\ddot{h}$$

Where I_α is the moment of inertia of the wing about the elastic axis.

In damping, for the plunge motion the damping coefficient can be written as C_h and for the rotational motion it can be written as C_α.

$\bar{G}(h)$ is the elastic term in plunge and $\bar{M}(\alpha)$ the elastic term is pitch. In this project $\bar{M}(\alpha)$ takes on a nonlinear for, given by the equation

$$\bar{M}(\alpha) = \beta_0 + \beta_1\alpha - \beta_2\alpha^2 + \beta_3\alpha^3 \tag{9}$$

Finally, $p(t)$ and $r(t)$ are the applied vertical force and rotational moment respectively. The equations of motion can now be written as:

$$m\ddot{h} + S\ddot{\alpha} + C_l\dot{h} + \bar{G}(h) = p(t) \tag{10}$$

$$S\ddot{h} + I_\alpha\ddot{\alpha} + C_\alpha\dot{\alpha} + \bar{M}(\alpha) = r(t) \tag{11}$$

$p(t)$ and $r(t)$ are composed of the lift and pitching moment as well as any extra external forces applied through hinges and any other sources.

The system of equations was then written in nondimensional form. In order to achieve this several new variables were introduced as follows:

ω_ξ and ω_α, the natural frequencies of the plunge and pitch "spring systems" respectively were defined as:

$\omega_\xi = \sqrt{\frac{K_\xi}{m}}$ and $\omega_\alpha = \sqrt{\frac{K_\alpha}{I_\alpha}}$

with K_ξ and K_α being the plunge and pitch linear spring constants respectively.

$r_\alpha = \sqrt{\frac{I_\alpha}{mb^2}}$ giving the radius of gyration about the elastic axis

$\mu = \frac{m}{\pi\rho b}$ giving the air-wing density ratio

$x_\alpha = \frac{S}{mb}$

With the substitutions made, the equations can then be simplified as in ref [1] to

$$\xi'' + x_\alpha\alpha'' + 2\zeta_\xi\frac{\varpi}{U^*}\xi' + \left(\frac{\varpi}{U^*}\right)^2 G(\xi) = -\frac{1}{\pi\mu}C_l(\tau) + \frac{P(\tau)b}{mU^2}, \tag{12}$$

$$\frac{x_\alpha}{r_\alpha^2}\xi'' + \alpha'' + 2\frac{\zeta_\alpha}{U^*}\alpha' + \frac{1}{U^{*2}}M(\alpha) = \frac{2}{\pi\mu r_\alpha^2}C_M(\tau) + \frac{Q(\tau)}{mU^2r_\alpha^2} \tag{13}$$

where $G(\xi) = \bar{G}(h)/K_\xi$ and $M(\alpha) = \bar{M}(\alpha)/K_\alpha$ and where $\dot{\alpha}, \dot{\xi}, \ddot{\alpha}, \ddot{\xi}$, the derivatives in normal time, are replaced by $\alpha', \xi', \alpha'', \xi''$, the derivatives in nondimensional time.

The velocity, angular velocity and time were also converted to give non-dimensional variables, given by:

$U^* = \frac{U}{b\omega_\alpha}$, $\varpi = \frac{\omega_\xi}{\omega_\alpha}$ and $\tau = \frac{Ut}{b}$

P and Q are respectively the externally-applied forces and moments, while the lift and moment coefficients C_L and C_M were given by Fung [5] as:

$$\begin{aligned} C_L(\tau) &= \pi(\xi'' - a_h\alpha'' + \alpha') + 2\pi\left\{\alpha(0) + \xi'(0) + \left[\frac{1}{2} - a_h\right]\alpha'(0)\right\}\varphi(\tau) \\ &+ 2\pi\int_0^\tau \varphi(\tau-\sigma)\left[\alpha'(\sigma) + \xi''(\sigma) + \left(\frac{1}{2} - a_h\right)\alpha''(\sigma)\right]d\sigma \end{aligned} \tag{14}$$

and

$$C_M(\tau)=\pi\left(\frac{1}{2}+a_h\right)\left\{\alpha(0)+\xi'(0)+\left[\frac{1}{2}-a_h\right]\alpha'(0)\right\}\varphi(\tau)$$
$$+\pi\left(\frac{1}{2}+a_h\right)\int_0^\tau\varphi(\tau-\sigma)\left\{\alpha'(\sigma)+\xi''(\sigma)+\left(\frac{1}{2}-a_h\right)\alpha''(\sigma)\right\}d\sigma$$
$$+\frac{\pi}{2}a_h(\xi''-a_h\alpha'')-\left(\frac{1}{2}-a_h\right)\frac{\pi}{2}\alpha'-\frac{\pi}{16}\alpha'' \tag{15}$$

where $\varphi(\tau)$ is the Wagner function given by:

$$\varphi(\tau)=1-\psi_1e^{-\varepsilon_1\tau}-\psi_2e^{-\varepsilon_2\tau} \tag{16}$$

where $\psi_1=0.165$, $\psi_2=0.335$, $\varepsilon_1=0.0455$ and $\varepsilon_2=0.3$.

The integral terms in the above equations for C_m and C_L are difficult to integrate numerically. Lee [6] introduced four new variables w_1 to w_4, defined below:

$$w_1=\int_0^\tau e^{-\varepsilon_1(\tau-\sigma)}\alpha(\sigma)d\sigma$$
$$w_2=\int_0^\tau e^{-\varepsilon_2(\tau-\sigma)}\alpha(\sigma)d\sigma$$
$$w_3=\int_0^\tau e^{-\varepsilon_1(\tau-\sigma)}\xi(\sigma)d\sigma$$
$$w_4=\int_0^\tau e^{-\varepsilon_2(\tau-\sigma)}\xi(\sigma)d\sigma \tag{17}$$

Equations (12) and (13) can now be written in general form as (from reference [1]):

$$c_0\xi''+c_1\alpha''+c_2\xi'+c_3\alpha'+c_4\xi+c_5\alpha+c_6w_1+c_7w_2+c_8w_3+c_9w_4$$
$$+\left(\frac{\varpi}{U^*}\right)^2G(\xi)=f(\tau) \tag{18}$$

$$d_0\xi''+d_1\alpha''+d_2\alpha'+d_3\alpha+d_4\xi'+d_5\xi+d_6w_1+d_7w_2+d_8w_3+d_9w_4$$
$$+\left(\frac{1}{U^*}\right)^2M(\alpha)=g(\tau) \tag{19}$$

The constants c_1 to c_9, along with d_1 through to d_9 are shown in appendix A.
If $P = Q = 0$, the equations for $f(\tau)$ and $g(\tau)$ are as below:

$$f(\tau)=\frac{2}{\mu}\left(\left(\frac{1}{2}-a_h\right)\alpha(0)+\xi(0)\right)\left(\psi_1\varepsilon_1e^{-\varepsilon_1\tau}+\psi_2\varepsilon_2e^{-\varepsilon_2\tau}\right) \tag{20}$$

and

$$g(\tau)=-\frac{(1+2a_h)f(\tau)}{2r_\alpha^2} \tag{21}$$

A vector $\mathbf{X}=\{x_1, x_2 \ldots x_8\}^T$ is then introduced, such that

$$x_1=\alpha,\ x_2=\alpha',\ x_3=\xi,\ x_4=\xi',\ x_5=w_1,\ x_6=w_2,\ x_7=w_3,\ x_8=w_4,$$

Equations (18) and (19) can then be expressed as a differential of the vector **X**:

$$\dot{X} = f(X) \tag{22}$$

The differential of the term w_1 above is given as $w_1' = \alpha - \varepsilon_1 w_1$, and the derivatives of w_2, w_3 and w_4 can be similarly derived.

Treating equations (18) and (19) as a pair of simultaneous equations, the individual differential terms then are given by

$$x_1' = x_2,\ x_2' = (c_0 H - d_0 P)/(d_0 c_1 - c_0 d_1),\ x_3' = x_4,\ x_4' = (-c_1 H + d_1 P)/(d_0 c_1 - c_0 d_1),$$
$$x_5' = x_1 - \varepsilon_1 x_5,\ x_6' = x_1 - \varepsilon_2 x_6,\ x_7' = x_3 - \varepsilon_1 x_7,\ x_8' = x_3 - \varepsilon_2 x_8 \tag{23}$$

where

$$P = c_0 x_2 + c_1 x_2 + c_4 x_3 + c_5 x_1 + c_6 x_5 + c_7 x_6 + c_8 x_7 + c_9 x_8 + \left(\frac{\varpi}{U^*}\right)^2 G(x_1) - f(\tau) \tag{24}$$

$$H = d_1 x_2 + d_2 x_1 + d_3 x_4 + d_5 x_3 + d_6 x_5 + d_7 x_6 + d_8 x_7 + d_9 x_8 + \left(\frac{1}{U^*}\right)^2 M(x_1) - g(\tau) \tag{25}$$

3.2 Bifurcation analysis

The definition of a bifurcation is a change in the characteristics of a graph of a parameter of a nonlinear system against one of its vectors. Bifurcations come in many forms. The Hopf bifurcation occurs when the vector state changes from convergence to a single point to a limit cycle oscillation. A period-doubling bifurcation occurs when a vector oscillating in a certain number of limit cycles changes to existing in twice that number of limit cycles. The period-tripling bifurcation is analogous to the period-doubling bifurcation but with the number of limit cycles tripling. This is also the case for greater number period-multiplying bifurcations.

The hopf bifurcation points can be found for a linear system of differential equations where $\dot{X} = f(X)$ as follows:

Let $\mathbf{X_E}$ be a fixed point in the system. When the vector of **X** is $\mathbf{X_E}$ then $\dot{X} = 0$ and the only way for the vector to change is if a perturbation is applied. Let this perturbation be written as $\mathbf{y}(\boldsymbol{\tau})$. Then $\mathbf{y}(\boldsymbol{\tau})$ can be expressed as:

$$y(\tau) = X(\tau) - X_E \tag{27}$$

The rate of growth/decay of this perturbation can then be given by the following equation:

$$\dot{y} = \frac{d}{d\tau}(X - X_E) = \dot{X} = f(X) = f(X_E + y) \tag{28}$$

The term $\mathbf{f}(\mathbf{X_E} + \mathbf{y})$ can be expanded about $\mathbf{X_E}$ using the Taylor series to the first order:

$$f(X_E + y) = f(X_E) + \left.\frac{\partial F}{\partial X}\right|_{X_E} y + O(y^2) \tag{29}$$

Since $\mathbf{f}(\mathbf{X_E})=0$ since at this point $\dot{X} = 0$, $\dot{y}$ is given by

$$\dot{y} = \left.\frac{\partial f(X)}{\partial X}\right|_{X_E} y = Jy \tag{30}$$

where **J** is the Jacobian matrix of $\mathbf{f}(\mathbf{X})$.

If every eigenvalue of **J** is non-zero and has a negative real part, then the system is stable. If, however, *one* eigenvalue has a positive real part, then the system will grow exponentially.

3.3 Integrating schemes

3.3.1 Runge-Kutta method

The differential equation for the state space system is written below:

$$\frac{d\dot{X}}{dt} = f\left(\vec{X}, t\right)$$

In order to evaluate this computationally a **Fehlberg Method** of order 4 was used. More detail on this can be found in reference [4].

3.3.2 Fehlberg Method of Order 4

This method is a variation on the *Runge-Kutta method* of order 4. With the initial conditions $\mathbf{X_0}$ known at time t=0, the Fehlberg method is used to find the value of **X** at time t+dt, where dt is a small increment. The function f is evaluated in this interval for five points in time, the values at those points being denoted by fk_1 through to fk_5, and five hypothetical values of X based on the f-value for the previous point, as shown below:

$$fk_1 = f(x,t)$$

$$fk_2 = f\left(x+\frac{\Delta t}{4} fk_1, t+\frac{\Delta t}{4}\right)$$

$$fk_3 = f\left(x+\frac{3\Delta t}{32} fk_1 + \frac{9\Delta t}{32} fk_2, t+\frac{3\Delta t}{8}\right)$$

$$fk_4 = f\left(x+\frac{1932\Delta t}{2197} fk_1 - \frac{7200\Delta t}{2197} fk_2 + \frac{7296\Delta t}{2197} fk_3, t+\frac{12\Delta t}{13}\right)$$

$$fk_5 = f\left(x+\frac{439\Delta t}{216} fk_1 - 8\Delta t fk_2 + \frac{3680\Delta t}{513} fk_3 - \frac{845\Delta t}{4104} fk_4, t+\Delta t\right) \tag{31}$$

The value of **X** at time t = t+dt can now be found as follows:

$$X(t+\Delta t) = X(t) + \Delta t\left(\frac{25}{216} fk_1 - \frac{1408}{2565} fk_3 + \frac{2197}{4104} fk_4 - \frac{1}{5} fk_5\right) \tag{32}$$

The Runge-Kutta-Fehlberg method is accurate to the order of Δt^5. This compares well with other methods used, such as Houbolt's finite difference scheme, as described in reference [7], which is accurate only to order Δt^4, although it is less efficient than Houbolt's method, which was used by Lee et al to calculate the reference graphs in the results section. The time step used as quoted in Lee[1] was quoted as being sufficiently small when having a value of 1/256. In this investigation a time-step of 0.001 was used, making it even more accurate.

4. VERIFICATION OF PROGRAM

The program wforce was verified using a series of tests to see whether it corresponded with the results given in reference [1].

4.1 Vector-time diagrams

The first test consisted of running the program with an initial condition of x_1 = 1° with x_2 through to x_8 set to zero, and with the parameters set as in the table below:

Tab. 1.

μ	x_α	a_h	r_α	ϖ	c_α	ζ_ξ	U^*/U^*_ξ	β_1 (1/rad)	β_3 (1/rad)
100	0.25	-0.5	0.5	0.2	0	0	0.8	1	3

The iterations were run for 200 seconds. The output from the program wforce was given for α against t and for ξ against t and compared to the results given in reference [2], figures 10 and 11. Note that the results for reference [2] were calculated using Houbolt's finite difference method instead of a Runge-Kutta-Fehlberg method, as in the program wforce.

Below is the graph of α versus t from the program:

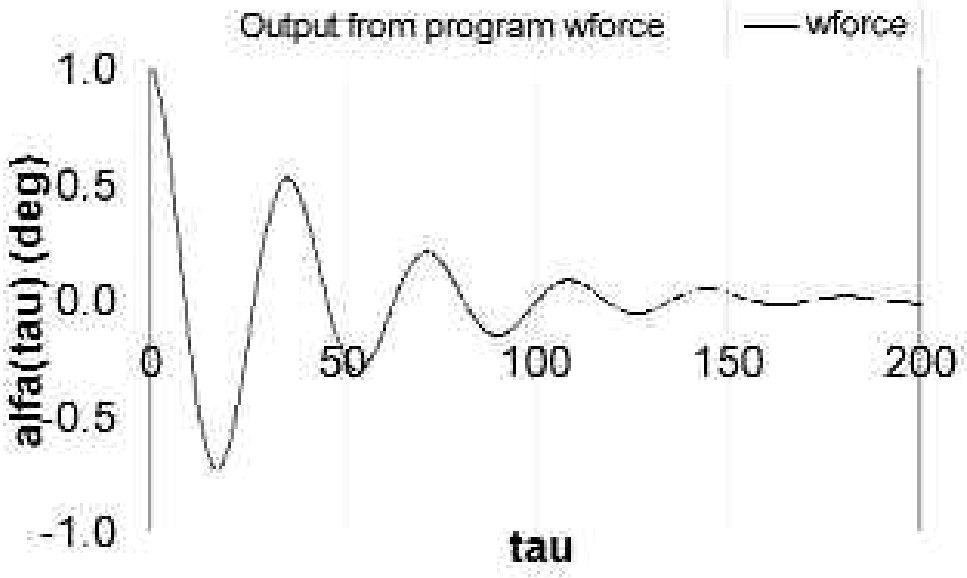

Fig. 9. Output from wForce F program

The amplitude decreases with time and converges to zero, as would be predicted for a system below the linear flutter velocity.

The comparison output from reference [2] is shown below.

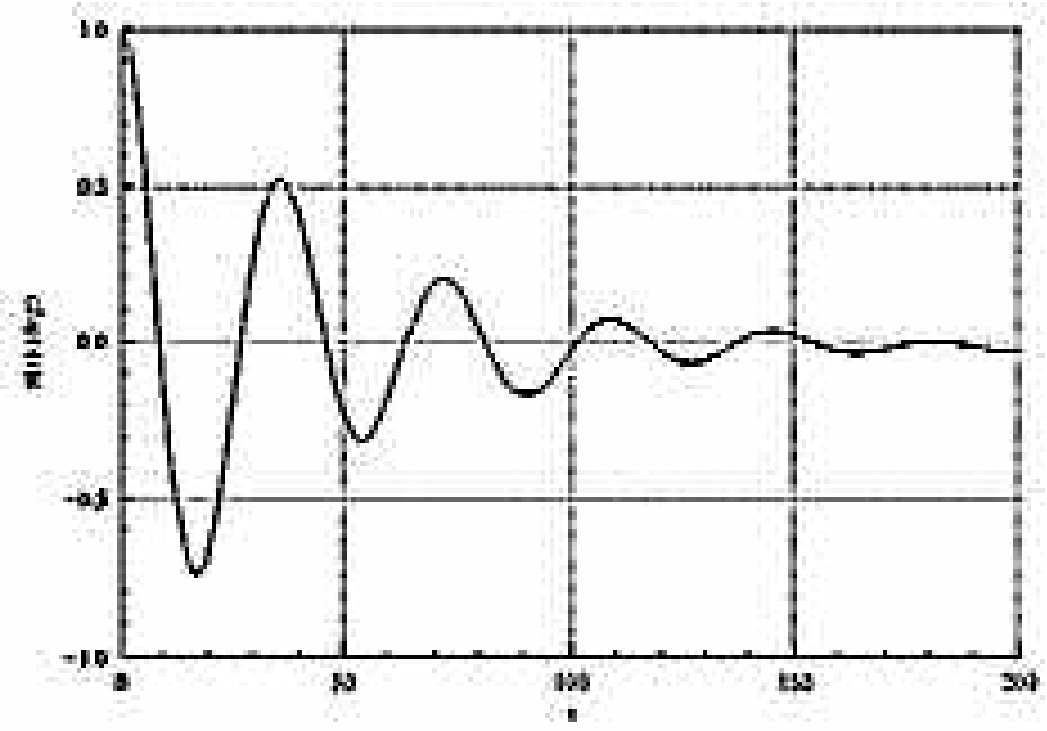

Fig. 10. Output from ref 3 corresponding to wforce.F output

The two graphs are seen to correspond very well, with the period, amplitude and phase being the same in both figures for the same moments in time.

Below is the graph of ξ versus t from the program:

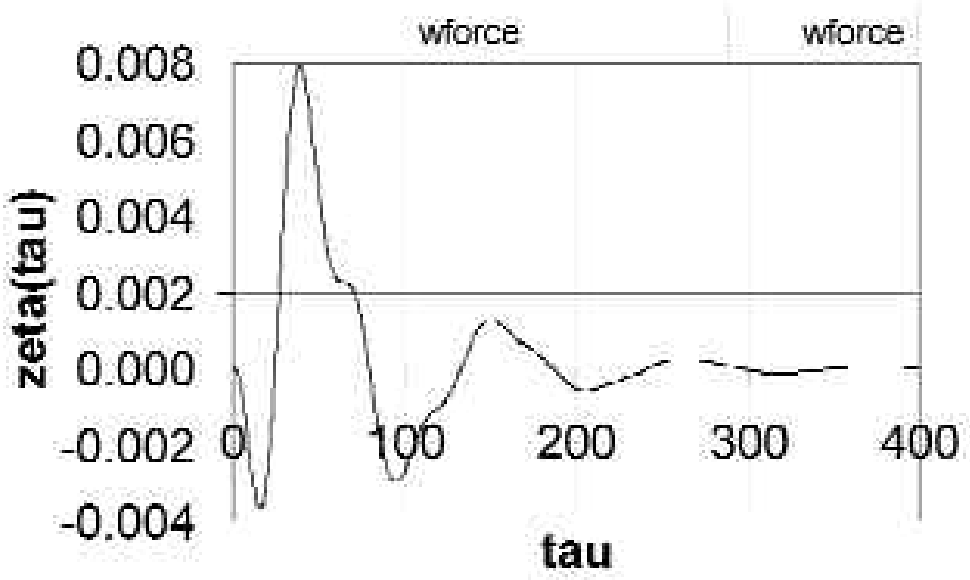

Fig. 11. ξ versus t from the wforce.F program

This compares to figure 11 in reference [2], as shown above.

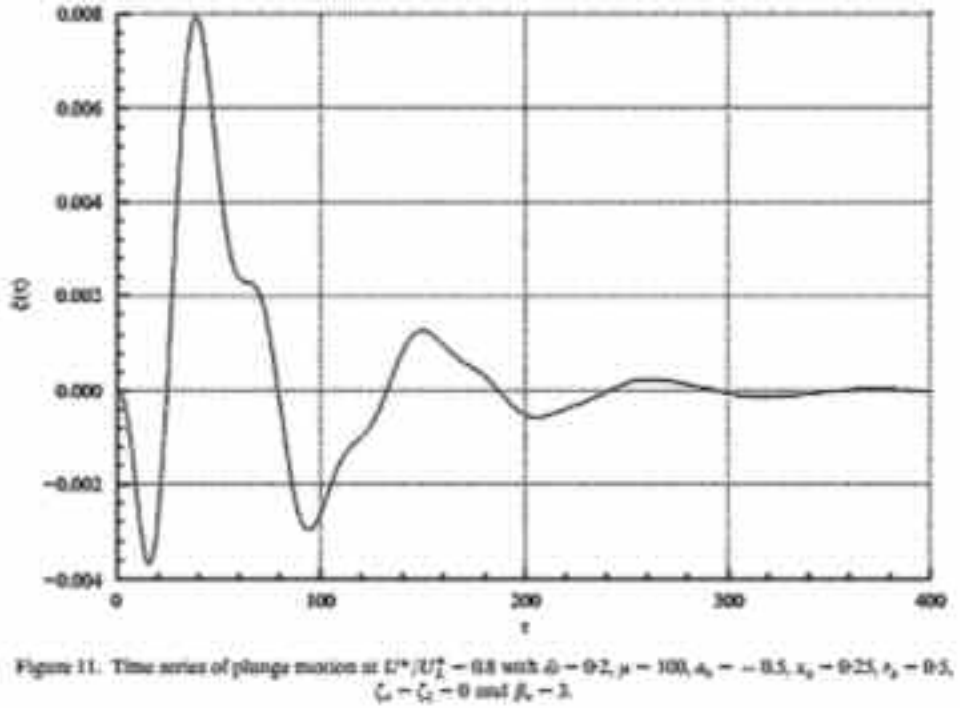

Figure 11. Time series of plunge motion at $U^*/U_L^* = 0.8$ with $\bar{a} = 0.2$, $\mu = 100$, $a_h = -0.5$, $x_\theta = 0.25$, $r_\theta = 0.5$, $\zeta_h = \zeta_\alpha = 0$ and $\beta_c = 3$.

Fig. 12. Graph from reference 2 with parameters coresponding to Fig. 11

The results are seen to compare almost exactly. Initially there are large oscillations of plunge, with the amplitude initially increasing, but then levelling out due to the velocity being well below the linear flutter velocity and due to the cubic spring factor.

4.2 Bifurcation diagrams

A bifurcation diagram was produced showing the behaviour of α against U^*/U^*_L (where U^*_L is the linear flutter velocity for a system with the relevant parameters, a cubic spring constant of zero and a linear spring constant of 1). This diagram proceeded from U^*/U^*_L = 0.1 to U^*/U^*_L = 1.0, with initial conditions of $\alpha(0)$ = 7. The parameters used are shown in the table on the next page.

Tab. 2.

μ	x_θ	a_h	r_θ	ϖ	ζ_θ	ζ_h	β_1 (1/rad)	β_3 (1/rad)
100	0.25	-0.5	0.5	0.2	0	0	0.1	40

The integration was carried out for 400 seconds at each value of U^*/U^*_L, with intervals of U^*/U^*_L = 0.01. The initial conditions for the next value of U^*/U^*_L were taken as the final **X**-vector at 400 seconds for the preceding U^*/U^*_L. The diagram then is as follows on the top of the next page.

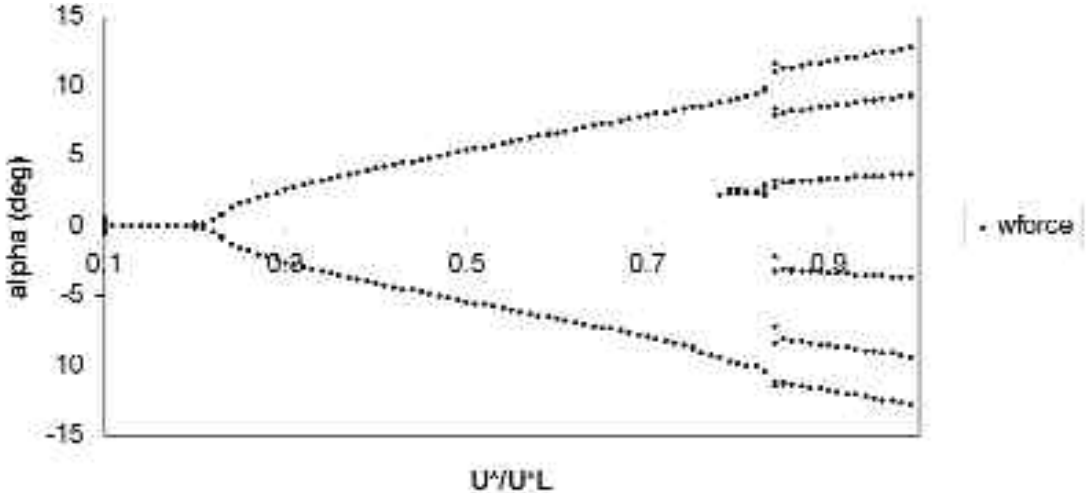

Fig. 13. α vs. U^*/U^*_L for parameters in table 2

It is seen that a Hopf bifurcation occurs at U^*/U^*_L, followed by a single limit cycle, with a "period-tripling" cycle occurring at U^*/U^*_L = 0.83. The limit cycle amplitudes then diverge towards higher values of α. It is noted that the oscillations in this region are above 10°. This has two implications: Since the stalling angle for most aerofoils lies between 10° and 15°, it would not be desired for the aircraft to fly at any higher value of U^*/U^*_L. Secondly, since in the equations of motion small angles of attack are assumed for the purposes of finding the C_L with a linear lift-curve slope, these equations would become increasingly inaccurate with α becoming large.
The graph compares to figure 3 in reference [3], as shown below:

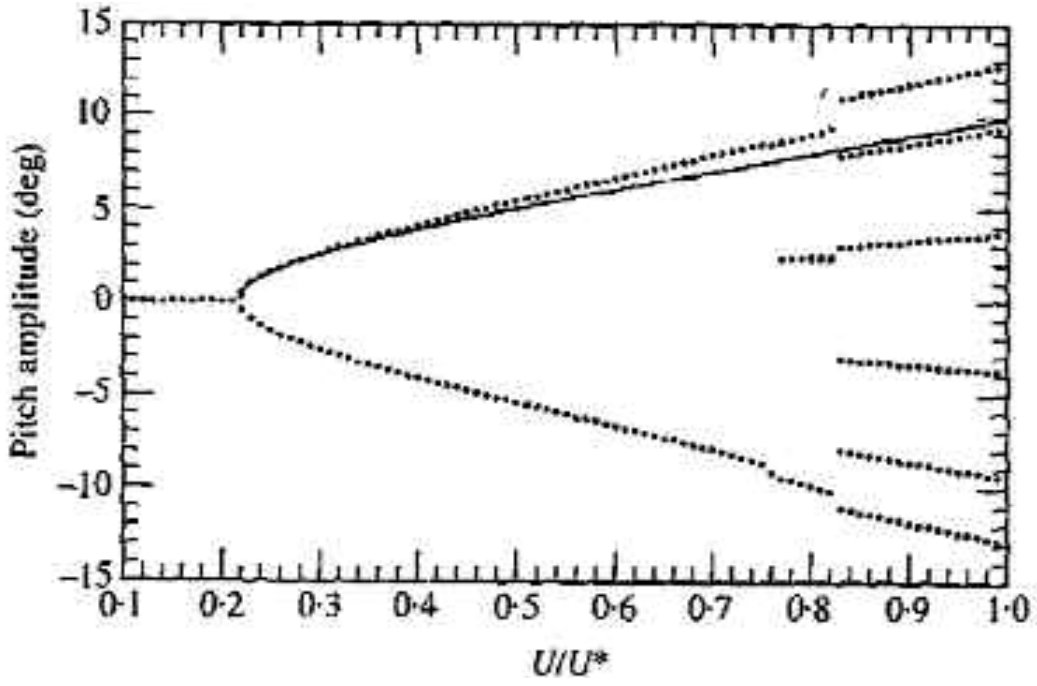

Fig. 14. Graph in reference 3 using parameters from Fig. 13

The solid line shows the analytical results predicted using a describing function, as described on page 180 of reference [3].

Next another bifurcation diagram was produced to compare results between the program and with reference [3] for different parameters and a harder spring, with a lower elastic term. This proceeded at values of U^*/U^*_L from U/U^*_L = 0.1 to U^*/U^*_L = 0.6, with intervals of U^*/U^*_L = 0.002. The time step was 0.001, with the integration period being 1200 between U^*/U^*_L = 0.14 and U^*/U^*_L = 0.18, 1600 between U^*/U^*_L = 0.27 and U^*/U^*_L = 0.31, 2400 between U^*/U^*_L = 0.44 and U^*/U^*_L = 0.52, and 200 seconds elsewhere. The integration period was extended in the regions specified because it was earlier found that key changes in the limit cycle patterns took place in those regions, and hence a longer settling time might be expected. The input was $\alpha(0) = 3°$. The parameters for the calculation were as follows:

Tab. 3

μ	x_α	a_h	r_α	ϖ	ζ_α	ζ_ξ	β_1 (1/rad)	β_3 (1/rad)
200	0.25	-0.5	0.5	0.2	0	0	0.01	50

The bifurcation diagram as created from data calculated by the program is shown below:

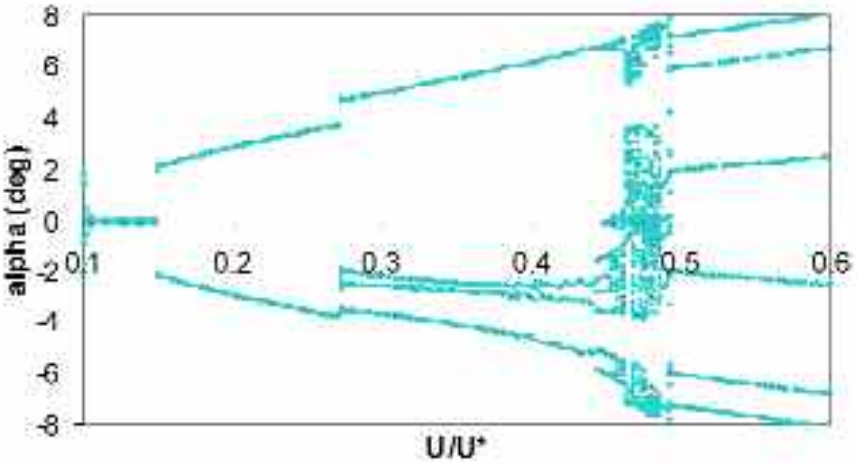

Fig. 15. α vs. U/U* for parameters in table 2

The comparison diagram from reference [3] for the same input parameters is shown below:

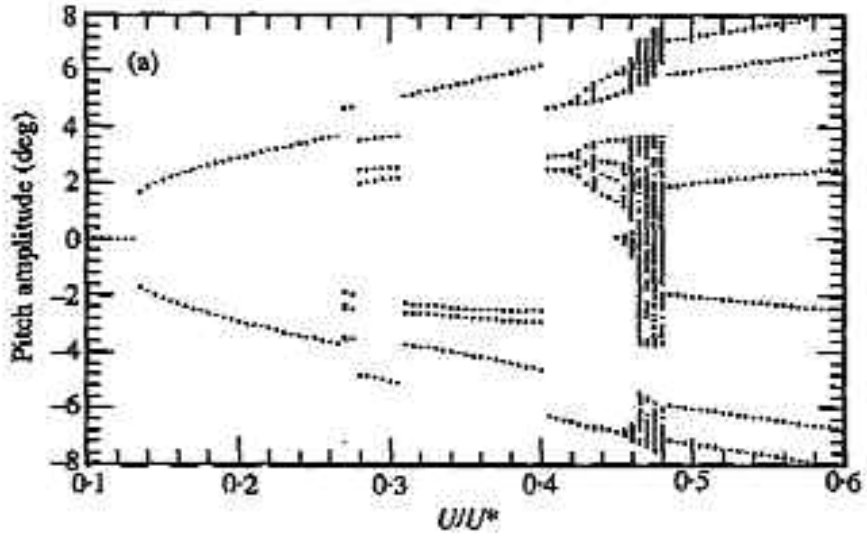

Fig. 16. Graph from reference 3 for parameters used in Fig. 15

Both diagrams show a Hopf bifurcation at U^*/U^*_L (denoted U/U^* in the reference) = 0.13. A period-doubling bifurcation also takes place at U^*/U^*_L = 0.27. At U^*/U^*_L = 0.425 more period-doubling bifurcations take place at each limit cycle, with further period-doubling bifurcations taking place at U^*/U^*_L = 0.438. Where there are scattered points in the diagram, chaos is present. Localised chaos within the existing limit cycles is seen to take place at U^*/U^*_L = 0.47, with the chaotic region spreading to cover the majority of the pitch amplitude at U^*/U^*_L = 0.81. The Lyapunov exponent can be used to check for the chaotic behaviour of a system. If the Lyapunov exponent is negative or zero, the system is non-chaotic. However, if the exponent is positive, then chaotic behaviour is present. Price et al in reference [3] computed the Lyapunov exponents along the diagram. They found that for various velocities on the diagram the exponent was negative or zero. However, for U^*/U^*_L = 0.47, the exponent was 0.01, indicating chaos.

There are some differences between the two diagrams. These can be ascribed to the different methods of integration used and, more importantly, to different attractors being followed. After the final time iteration for each value of U^*/U^*_L, the values of x_1 through to x_8 are taken to be the initial conditions for the new value of U^*/U^*_L.

The paths between U^*/U^*_L = 0.3 and U^*/U^*_L = 0.5 follow the limit cycles only because the initial conditions for each value of U^*/U^*_L dictate that these should be followed. Were one or more of the eight initial conditions x_1 through to x_8 changed to be the negative of the original one, the limit cycle might change to be centred on another attractor. The table of initial conditions at U^*/U^*_L = 0.305 is shown below:

Tab. 4.

x(1)	*x*(2)	*x*(3)	*x*(4)
-0.02416	0.00492	0.09652	0.01007
x(5)	*x*(6)	*x*(7)	*x*(8)
-0.74867	-0.11479	-0.07438	0.20067

From x_1 to x_4, each initial condition was changed and the program run for the same time just at U^*/U^*_L = 0.305. The results of x_1 against x_2 (or α against $\dot{\alpha}$) for each case were recorded and a 2D state-space diagram produced for those conditions. First the diagram with all initial conditions as normal was produced, and this is shown below:

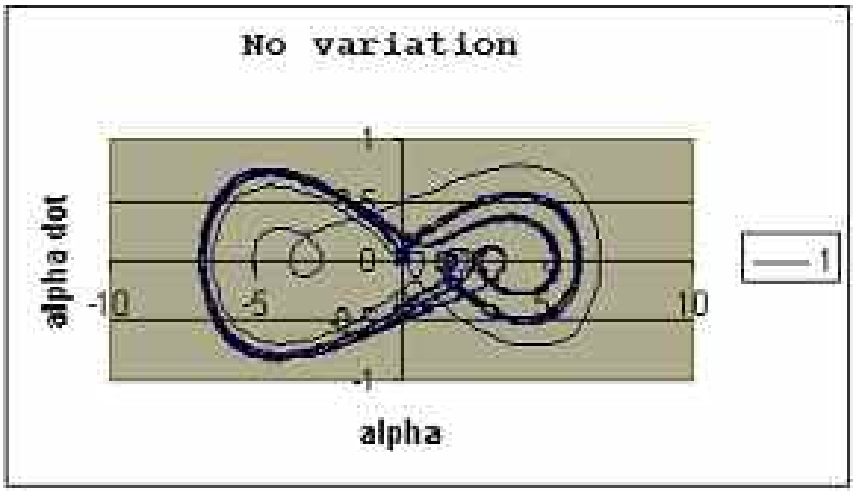

Fig. 17. 2D state-space diagram with initial conditions as in table 4

This shows limit cycles in addition to the high-amplitude limit cycles present just to the right of α=0°. Next, the value of x_1 was changed to the negative of its original. This resulted in the following state space diagram:

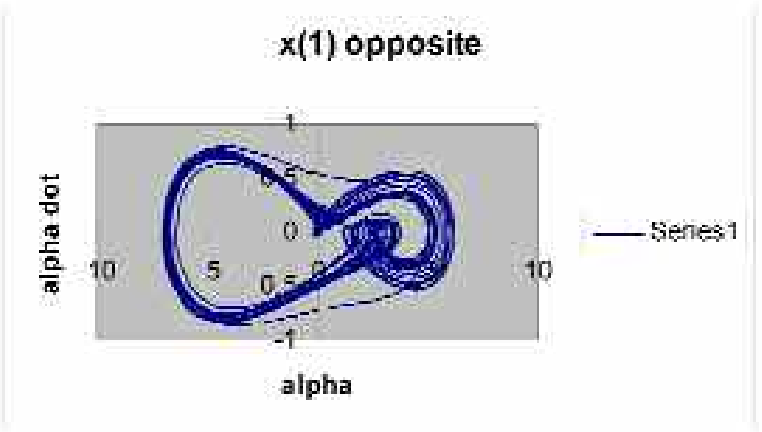

Fig. 18. State-space diagram with sign-change of x(1) in table 4

As can be seen the outer limit cycle on the right loses some stability and the points diverge. Next, the value of x_2 was changed to its negative, in addition to x_1 already being the negative of its original, shown on the next page.

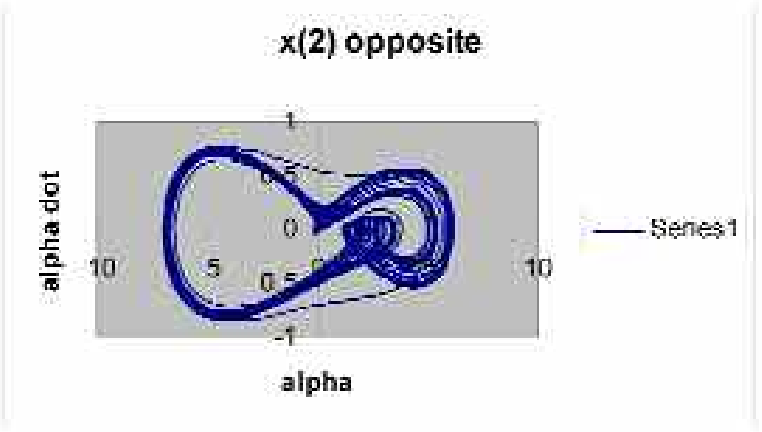

Fig. 19. State-space diagram with sign-change of x(2) in table 4

The right-side limit cycle becomes slightly less stable than before, however the limit cycles are still centred around the same points. With x_3 changed as well, the shape of the diagram became completely different, as shown below:

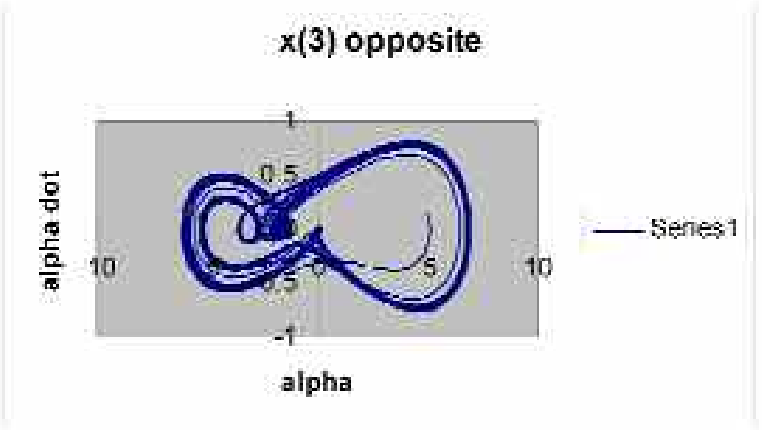

Fig. 20. State-space diagram with sign-change of x(3) in table 4

The limit cycle has switched sides, with the smaller limit cycles now moving to the left of α = 0°. The different initial conditions meant that the trajectory was able to converge to a different path. Finally, with x_1, x_2, x_3 and x_4 all the negative of their original values, this resulted in the diagram on the next page.

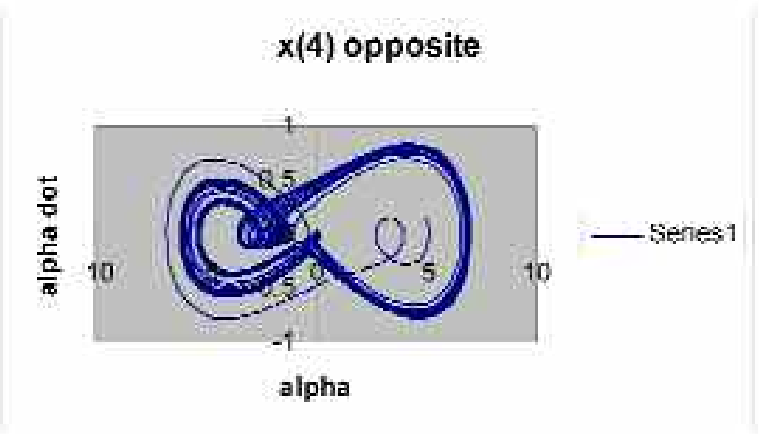

Fig. 21. State-space diagram with sign-change of x(4) in table 4

This shows slightly-less condensed paths indicating less stability and attraction to the main limit cycle paths.

With x_1, x_2 and x_3 changed as above, another series was produced between U^*/U^*_L 0.305 and U^*/U^*_L = 0.5. This is shown in purple in the diagram below:

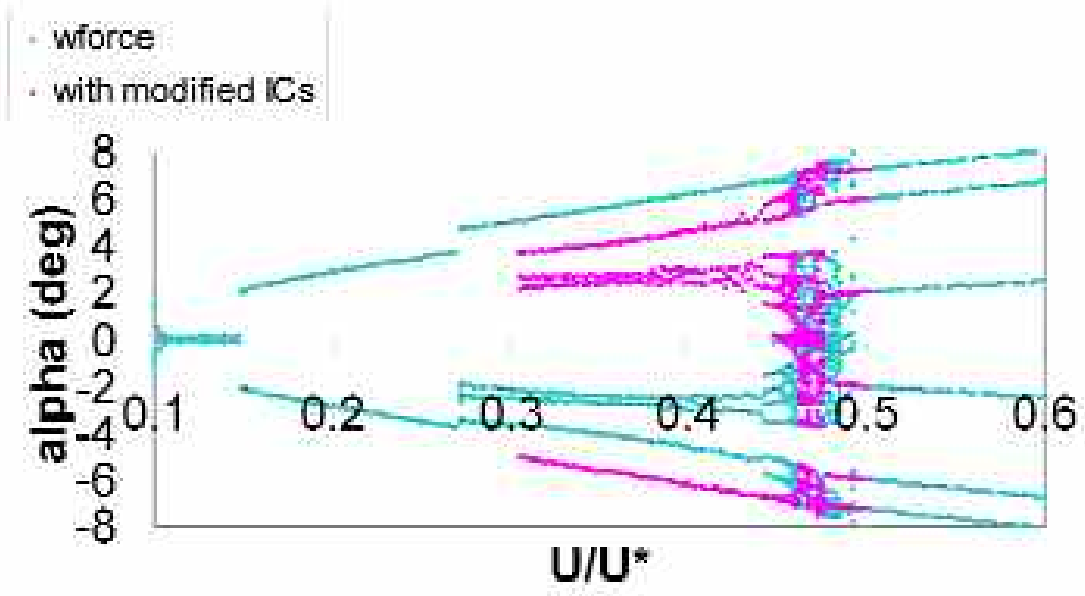

Fig. 22. α vs. U/U^* diagram with sign change of x_1 to x_3 in table 3

The results for the modified initial conditions at U/U^* = 0.3 are seen to correspond to the reference bifurcation diagram in figure 16.

4.3 Poincare map

The Poincare map can be used to check for chaotic behaviour by looking at the distribution of points on an $\alpha - \dot{\alpha}$ diagram. Poincare maps can be produced by various methods and produce differing outputs depending on what criteria were used to produce them. In this case data was recorded at the points where ξ reached a maximum or a minimum as a function of time, at U^*/U^*_L = 0.47, with the initial conditions α=3° and x_2 through to x_8 = 0, and the parameters as for figures 15 through to 22. On the top of the next page is the Poincare map for the parameters (figure 23).

The Poincare map shows scattered points which have are non-periodic and chaotic in the regions where the limit cycles used to exist. For periodic behaviour the points in each part of the diagram would have coincided with each other as with each period repetition the alpha and alpha dot would have had the same value.

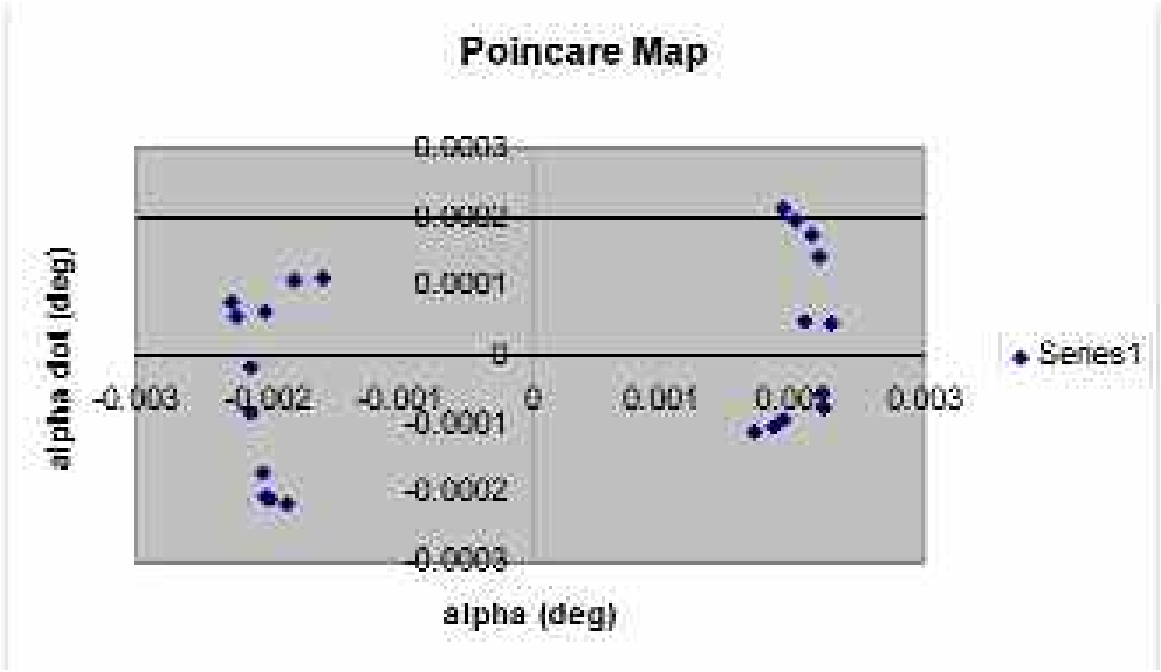

Fig. 23. Poincare map with parameters as for Figs. 5 to 22

5. OTHER RESULTS

For just a linear spring present, the system is linear and has decaying oscillations right up until $U^*/U^*_L = 1.0$, after which the oscillations become divergent.

For a linear spring, the system converges to α=0° from $U^*/U^*_L = 0$ to $U^*/U^*_L = 1$. At $U^*/U^*_L = 1$, the system changes to diverging towards infinity. This means that, if the integration period was long enough, the value of α would go towards infinity.

Another type of bifurcation diagram was made for the final investigation. The behaviour of α against β_3 was investigated for β_3 decreasing from 100, at intervals of 0.5, for the general parameter values as in the table below:

Tab. 5.

μ	x_α	a_h	r_α	ϖ	ς_α	ζ_ξ
200	0.25	-0.5	0.5	0.2	0	0

The bifurcation diagrams were made with β_3 decreasing and not increasing because it was soon discovered that as the value became smaller, the limit cycles grew larger in amplitude. It is best to start at the smallest value so that the values do not converge to zero and so that behaviour can be seen at larger amplitudes. For all cases the input conditions were $\alpha(0) = 3°$, with all the other variables set to 0.

For a linear spring constant of $\beta_1 = 0.01$ and at $U^*/U^*_L = 0.2$, the bifurcation diagram was made with the varying parameter being β_3. The diagram is shown on top of the next page (figure 24).

There are no bifurcations present in the diagram, instead the limit cycles merely diverge as the value of β_3 tends to 10. At around $\beta_3 = 30$, the gradient of the curve becomes significant. It would therefore be preferable to have a β_3 value larger than 30 which would make the limit cycle smaller. The initial perturbation was $\alpha(0)$=3°. It was seen that increasing $\alpha(0)$ merely had the effect of making the limit cycles bigger in a proportionate manner, with the shape staying constant. The diagram was originally investigated for values of β_3 down to $\beta_3 = 0$. It was found, however, that at these low values of β_3 the oscillations increased in the same manner as before, with

the steepness of the curve rapidly increasing and the limit cycles growing unreasonably-large to be displayed on the diagram.

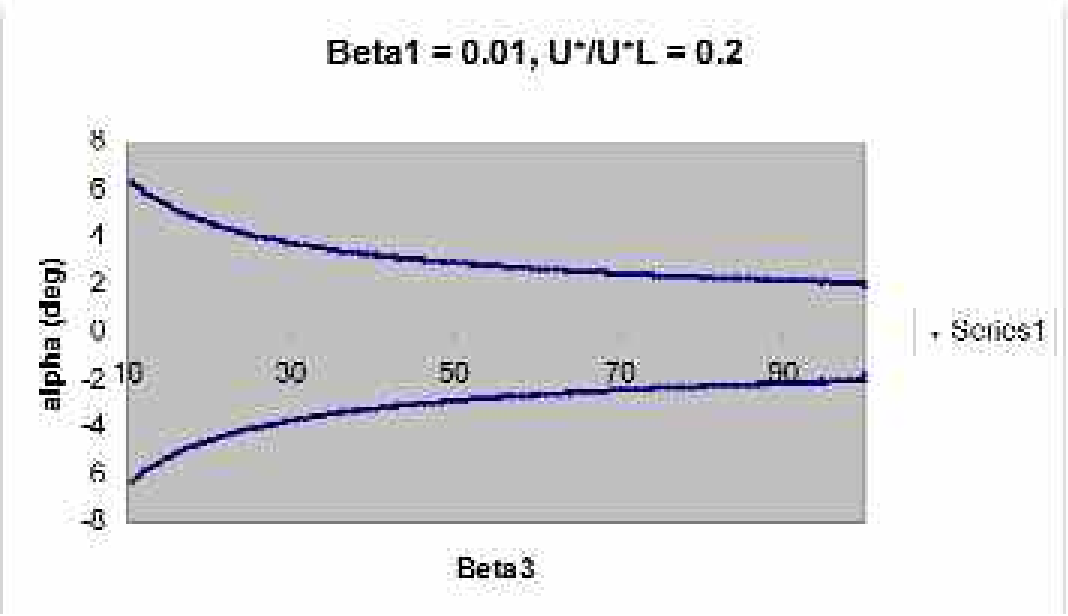

Fig. 24. variation of α vs. β_3 for β_1=0,01 and U^*/U^*_L = 0.2

Next, the system was investigated for β_1 = 1 and U^*/U^*_L = 1. This is significant as this is the flutter velocity for the linear spring constant chosen. The diagram was made for values of β_1 from 100 down to –50, and the results are shown in the graph below:

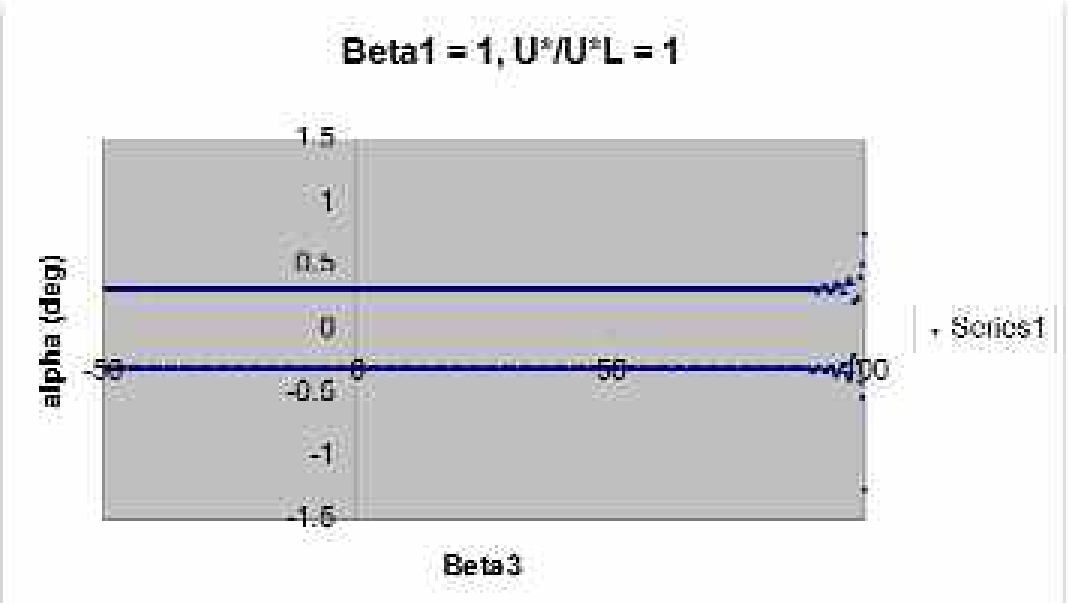

Fig. 25. variation of α vs. β_3 for β_1=1 and U^*/U^*_L = 1.0

The oscillations are seen to rapidly die down from their initial perturbation to a settled value of around α = +/-0.31°, and then stay fixed in a straight line. Having a large cubic coefficient is hence seen to have no effect on the oscillations, hence making them *independent* of it. Closer analysis of the numerical results shows the reduction in oscillation amplitude at a given cubic term near 100 to be small, with the bulk of the reduction taking place due to the cubic term decreasing. This means that were the cubic term to stay constant, one should not expect such a damped oscillation, or indeed any damping, as might initially seem from the diagram above.

Finally the behaviour was investigated at β_1 = 0.01 and U^*/U^*_L = 1. The diagram is shown on the next page.

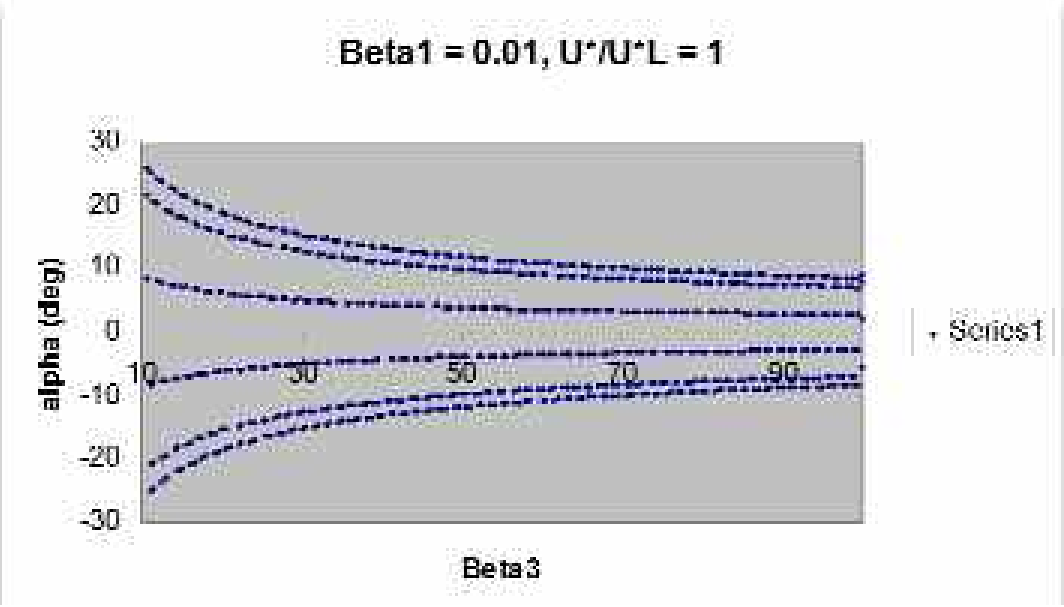

Fig. 26. variation of α vs. β_3 for β_1=0,01 and U^*/U^*_L = 1

It is seen that there are three limit cycles present with amplitudes increasing to α=15° at β_3 = 30. An aircraft in flight with these parameters would be dangerous to fly in, as any perturbation will result in the angle of attack going dangerously high, decreasing the amount of control that the pilot has on the aircraft and bringing the angle of attack too close to the stalling angle for the aerofoil.

6. CONCLUSION

Nonlinear behaviour of the type covered in this project is commonplace in aircraft wings. It can not only affect the velocity at which flutter occurs but also the motion resulting from perturbations to it. The presence of limit cycle oscillations in a nonlinear system has the potential, if not corrected, to cause fatigue of the wing through repeated loading and unloading of the wing if not corrected. Added to this a loss in aerodynamic performance is to be expected through the deviation from optimal angle of attack for flight, leading to an increase in drag, lift and hence possibly other aircraft modes of oscillation such as the phugoid motion. The correction of a perturbation in a limit cycle may lead to greater work for the pilot and, if the period of oscillation is of the same magnitude as the pilot's reaction time, to potential reinforcement of the oscillation amplitude through the pilot applying force at the wrong time in the period. Ideally the period of oscillation should be long enough for the pilot to be able to judge when to apply the correcting force on the stick.

In a linear system it is the linear flutter velocity that is the most important value. For the nonlinear system the critical point to consider is the Hopf bifurcation point. It is at this point that the system ceases to converge to a fixed point and instead oscillates in a limit cycle between two extreme values. This Hopf bifurcation point is found for linear systems using the Jacobian matrix of the derivative equation as described in section 3.2.

It is also important to know the effects of having different cubic spring coefficients on the behaviour of the system. These were investigated in this project through making a bifurcation diagram, with the finding being that at higher values of β_3 the amplitude of the limit cycle oscillations is lower. The Hopf bifurcation points for bifurcation diagrams of α against U^*/U^*_L would, of course, have to be found as well. If these have a lower value of U^*/U^*L for a higher value of β_3 then the overriding requirement for safety and controllability at higher values of U^*/U^*_L would mean that it would be preferable for the wing to have less hardening properties.

The program was tested against references [2] and [3] and the results were found to correspond. The bifurcation diagram in this report in figure 15 was even found to be more accurate

than the corresponding figure for the reference because the limit cycle boundaries followed the same path instead of switching paths, as they did in figure 16.

As has been discussed, nonlinearities arise not only from the hardening of the wing in torsion but also from linkages, hinges, flaps and other systems in the wing. This was not taken into account in the analysis here. The nonlinearities which these systems possess tend to be bilinear or hysteresis nonlinearities. In order for this to be taken into account extra lines would have to be written in the wforce program to incorporate extra terms into the elastic term depending on the value of α, using IF statements to input different equations for restoring moments for different values of α.

Another improvement on the program would be to make use of a more efficient routine than the Runge-Kutta-Fehlberg method. Houbolt's finite difference scheme is described on page 239 of reference [1] and could be made use of.

The results produced have been for cases with zero structural damping. With damping present, the oscillations would decrease quicker and the limit cycles would be of a lower amplitude due to some of the energy being absorbed by the dampers. The dampers may also exert some influence over the Hopf bifurcation velocity in a α vs U^*/U^*_L bifurcation diagram.

Overall the results, as well as confirming the validity of the program wforce, provide a good insight into the response of the system to perturbations, and are useful in determining the properties of the limit cycle oscillations and the properties of the aircraft in flight. They lay a good basis for expanding the study in the future.

7. REFERENCES

[1] **Lee BHK, Price SJ and Wong YS.:** *Nonlinear aeroelastic analysis of airfoils: bifurcation and chaos*; Progress in Aerospace Sciences 35 (1999) p205-334

[2] **Lee BHK, Jiang LY and Wong YS.:** *Flutter of an airfoil with a cubic nonlinear restoring force*, AIAA paper 98-1725, 39th AIAA/ASME/ASCE/AHS/ASC Structures, Structural Dynamics and Materials Conference, 20-23 April, Long Beach, CA, 1998.

[3] **Price SJ, Alighanbari H and Lee BHK.:** *The aeroelastic response of a two-dimensional airfoil with bilinear and cubic structural nonlinearities*. Journal of Fluids and Structures 1995; volume 9, pages 175-193.

[4] **Cheney W, Kincaid D.:** Numerical Mathematics and Computing 4th edition. Brooks/Cole 1999 Fung YC. *An introduction to the theory of aeroelasticity*. New York: Dover 1993.

[5] **Lee BHK, Gong L, Wong YS.:** *Analysis and computation of nonlinear dynamic response of a two degree-of-freedom system and its application in aeroelasticity*. Jourrnal of Fluids and Stuctures 1997; Volume 11, pages 225-246

[6] **Houbolt JC.:** *A recurrence matrix solution for the dynamic response of elastic aircraft*. J Aeronaut Sci 1950; Volyume 17: pages 540-550

[7] **Baldassin E.:** program wforce.F, written by E. Baldassin, Imperial College London

Glossary of symbols used

$f(X)$ - function which gives derivative in time of X
Mi - Generalised mass term for the i degree of freedom
Ci - Generalised damping term for the i degree of freedom
Ki - Generalised elastic term for the i degree of freedom
Fi - Generalised force term for the i degree of freedom
βi - Coefficient of αi in nonlinear elastic pitch term.
M - Nonlinear elastic restoring moment term.
μ - aerofoil/mass ratio (m/πρb2)
zi - Displacement perpendicular to xy plane for mode i
φi - Mode shape function for mode i

qi - Point displacement for degree of freedom i
EI - Flexural stiffness of wing
h - plunge distance
α - angle of attack
ξ - Nondimensional plunge distance (h/b)
m - mass per unit span of wing
S - First moment of area per unit span of wing about elastic axis
r_α - Radius of gyration about elastic axis
ω - angular velocity (subscript dictates mode)
U^* - Nondimensional velocity (U/b$\omega\alpha$)
τ - Nondimensional time (tU/b)
ϖ - Nondimensional angular velocity ($\omega\xi/\omega\alpha$)
CL - Lift coefficient
CM - Pitching moment coefficient
a_h - nondimensional distance from aerofoil midchord to elastic axis
$\varphi(\tau)$ - Wagner function at time τ
b - aerofoil semi-chord
c - aerofoil chord

Appendix A

Given

$$\xi'' + x_\alpha \alpha'' + 2\zeta_\xi \frac{\varpi}{U^*}\xi' + \left(\frac{\varpi}{U^*}\right)^2 G(\xi) = -\frac{1}{\pi\mu} C_L(\tau) + \frac{P(\tau)b}{mU^2},$$

and

$$\frac{x_\alpha}{r_\alpha^2}\xi'' + \alpha'' + 2\frac{\zeta_\alpha}{U^*}\alpha' + \frac{1}{U^{*2}} M(\alpha) = \frac{2}{\pi\mu r_\alpha^2} C_M(\tau) + \frac{Q(\tau)}{mU^2 r_\alpha^2}$$

with

$$C_L(\tau) = \pi\left(\xi'' - a_h\alpha'' + \alpha'\right) + 2\pi\left\{\alpha(0) + \xi'(0) + \left[\frac{1}{2} - a_h\right]\alpha'(0)\right\}\varphi(\tau)$$

$$+2\pi\int_0^\tau \varphi(\tau - 0)\left[\alpha'(\sigma) + \xi''(\sigma) + \left(\frac{1}{2} - a_h\right)\alpha''(\sigma)\right]d\sigma$$

and

$$C_M(\tau) = \pi\left(\frac{1}{2} + a_h\right)\left\{\alpha(0) + \xi'(0) + \left[\frac{1}{2} - a_h\right]\alpha'(0)\right\}\varphi(\tau)$$

$$+\pi\left(\frac{1}{2} + a_h\right)\int_0^\tau \varphi(\tau - \sigma)\left\{\alpha'(\sigma) + \xi''(\sigma) + \left(\frac{1}{2} - a_h\right)\alpha''(\sigma)\right\}d\sigma$$

$$+\frac{\pi}{2}a_h\left(\xi'' - a_h\alpha''\right) - \left(\frac{1}{2} - a_h\right)\frac{\pi}{2}\alpha' - \frac{\pi}{16}\alpha''$$

the equations can be simplified by substituting the equations in for C_L and C_M and rearranging. The equations then simplify to:

$$c_0\xi'' + c_1\alpha'' + c_2\xi' + c_3\alpha' + c_4\xi + c_5\alpha + c_6 w_1 + c_7 w_2 + c_8 w_3 + c_9 w_4 + \left(\frac{\varpi}{U^*}\right)^2 G(\xi) = f(\tau)$$

and

$$d_0\xi'' + d_1\alpha'' + d_2\alpha' + d_3\alpha + d_4\xi' + d_5\xi + d_6 w_1 + d_7 w_2 + d_8 w_3 + d_9 w_4 + \left(\frac{1}{U^*}\right)^2 M(\alpha) = g(\tau)$$

where

$$c_0 = 1 + \frac{1}{\mu},\quad c_1 = x_\alpha - \frac{a_h}{\mu},\quad c_2 = 2\zeta_\xi \frac{\bar{\omega}}{U^*} + \frac{2}{\mu}(1 - \psi_1 - \psi_2),\quad c_3 = \frac{1 + 2\left(\frac{1}{2} - a_h\right)(1 - \psi_1 - \psi_2)}{\mu},$$

$$c_4 = \frac{2}{\mu}(\psi_1\varepsilon_1 + \psi_2\varepsilon_2),\quad c_5 = \frac{2}{\mu}\left[(1 - \psi_1 - \psi_2) + \left(\frac{1}{2} - a_h\right)(\psi_1\varepsilon_1 + \psi_2\varepsilon_2)\right],\quad c_6 = \frac{2}{\mu}\psi_1\varepsilon_1\left[1 - \left(\frac{1}{2} - a_h\right)\varepsilon_1\right],$$

$$c_7 = \frac{2}{\mu}\psi_2\varepsilon_2\left[1 - \left(\frac{1}{2} - a_h\right)\varepsilon_2\right],\quad c_8 = -\frac{2}{\mu}\psi_1\varepsilon_1^2,\quad c_9 = -\frac{2}{\mu}\psi_2\varepsilon_2^2,$$

$$d_0 = \frac{x_\alpha}{r_\alpha^2} - \frac{a_h}{\mu r_\alpha^2},\quad d_1 = 1 + \frac{1 + 8a_h^2}{8\mu r_\alpha^2},\quad d_2 = 2\frac{\zeta}{U^*} + \frac{1 - 2a_h}{2\mu r_\alpha^2} - \frac{(1 + 2a_h)(1 - 2a_h)(1 - \psi_1 - \psi_2)}{2\mu r_\alpha^2},$$

$$d_3 = \frac{(1 - 2a_h)(1 - \psi_1 - \psi_2)}{\mu r_\alpha^2} - \frac{(1 + 2a_h)(1 - 2a_h)(\psi_1\varepsilon_1 + \psi_2\varepsilon_2)}{2\mu r_\alpha^2},\quad d_4 = \frac{(1 - 2a_h)(1 - \psi_1 - \psi_2)}{\mu r_\alpha^2},$$

$$d_5 = -\frac{(1 + 2a_h)(\psi_1\varepsilon_1 + \psi_2\varepsilon_2)}{\mu r_\alpha^2},\quad d_6 = \frac{(1 + 2a_h)\psi_1\varepsilon_1\left[1 - \left(\frac{1}{2} - a_h\right)\varepsilon_1\right]}{\mu r_\alpha^2},$$

$$d_7 = \frac{(1 + 2a_h)\psi_2\varepsilon_2\left[1 - \left(\frac{1}{2} - a_h\right)\varepsilon_2\right]}{\mu r_\alpha^2},\quad d_8 = \frac{(1 + 2a_h)\psi_1\varepsilon_1^2}{\mu r_\alpha^2},\quad d_9 = \frac{(1 + 2a_h)\psi_2\varepsilon_2^2}{\mu r_\alpha^2}$$

Appendix B

Program used for nonlinear aeroelastic calculations, author E. Baldassin, Imperial College London.

Input is given in the file force.inp. The entries are given in the following form:

$\alpha(0)$ (degrees)

$\alpha'(0)$(degrees)

$\xi(0)$

$\xi'(0)$

μ

x_α

a_h

r_α

$\bar{\omega}$

ζ_ξ

ζ_α

U^*/U^*_L

β_1

β_3

β_ξ (cubic term for plunge elasticity, usually zero)

dτ

τ_{fin}

iprint

$d(U^*/U^*_L)$

$(U^*/U^*\mathrm{L})_{fin}$

where τ_{fin} is the integration (nondimensional) time, $d\tau$ is the time step, iprint prints the result every i iterations, $d(U^*/U^*_L)$ is the increment in U^*/U^*_L in bifurcation diagrams, and $(U^*/U^*\mathrm{L})_{fin}$ is the final value of U^*/U^*_L for the diagram. Below is the code for the program:

```
      PROGRAM omega

c     Forced oscillation: simulation example in aeroelasticity for a
c                   2 dof, fig.10 pag.241 and fig.12 pag.243

c     Dichiariazione variabili

      IMPLICIT none

      INTEGER*2 i, iconta, iprint, j,n
      PARAMETER(n=65)
      REAL*8 x(8), xk0(8), xk1(8), xk2(8), xk3(8), xmargin
      REAL*8 x1max,x1min, x1amp,x3max, x3min, x3amp, x1old, x2old
      REAL*8 w, omgforce(n), xzero(8), PI, dUx, Uxfin, xmaxprev


      REAL*8 mu, xa, ah, ra, omg, dampz,dampa, Ux, betaa, betaz
      COMMON/airfpar/mu, xa, ah, ra, omg, dampz, dampa, Ux, betaa, betaz

      REAL*8 psi1, psi2, eps1, eps2, betaa1
      COMMON/costant/ psi1, psi2, eps1, eps2, betaa1
      REAL*8 ft0, g0, FF
      COMMON/forze0/ ft0, g0, FF

      REAL*8 time, tfin, dt, time0, time1, time2, time4, time3

      REAL*8 alfa3, beta30, beta31, beta32, beta40, beta42, beta43
      REAL*8 ck0, ck2, ck3, timeset, UxL, a, xdiff
      REAL*8 fk0(8), fk1(8), fk2(8), fk3(8), fk4(8)

      REAL*8 c(10), d(10)
      COMMON/coeff/ c, d

      PI = 3.14159265359
c     inizializzazione

      FF= .03d0

      omgforce(1)= .4d0

      DO 5 i=2,n
        omgforce(i)= omgforce(i-1)+.015d0
 5    CONTINUE


      do 10 i=1,8
        x(i)=0.d0
        xzero(i)=0.d0
10    continue



      time=0.d0
      iconta=0


      psi1=0.165d0
```

```
      psi2=0.335d0
      eps1=0.0455d0
      eps2=0.3d0

c     lettura dati: condizioni iniziali e parametri del profilo

      OPEN(10, file='force.inp', status='old')

c     condizioni iniziali

      do 20 i=1,4
        READ(10,*) x(i)
        xzero(i) = x(i)
20    continue

            do i=1,2
            x(i) = x(i)*PI/180.d0
      enddo
c     parametri del profilo

      READ(10,*) mu, xa, ah, ra, omg, dampz, dampa, Ux
      READ(10,*) betaa1, betaa, betaz

c     parametri del procedimento numerico

      READ(10,*) dt, timeset, iprint
      READ(10,*) dUx, Uxfin, UxL

      Ux = UxL*Ux
      dUx = UxL*dUx
      Uxfin = UxL*Uxfin

      CLOSE(10, STATUS='KEEP')

      tfin = timeset
c     calcolo della forzante dipendente dalle condizioni iniziali

      ft0= 2.d0*((.5d0-ah)*x(1)+x(3))/mu
      g0= -(1.d0+2.d0*ah)/(2.d0*ra**2)


c     OPEN(30, file='timeF', status='unknown')
c     WRITE(30,*) time
c     OPEN(31, file='alfaF', status='unknown')
c     WRITE(31,*) time, (x(1)*180.d0/PI)
      OPEN(32, file='alfadotF', status='unknown')
c     WRITE(32,*) time, (x(2)*180.d0/PI)
c     OPEN(33, file='zetaF', status='unknown')
c     WRITE(33,*) time, (x(3)*180.d0/PI)
c     OPEN(34, file='zetadotF', status='unknown')
c     WRITE(34,*) time, (x(4)*180.d0/PI)

      OPEN(35, file='bifurcationF', status='unknown')
c     OPEN(36, file='fig10omega.out',status='unknown')
c     OPEN(37, file='fig10x3.out', status='unknown')

      OPEN(38,file='outextra', status='unknown')
      OPEN(39,file='magnitudelist', status='unknown')
```

```
c    calcolo dei coefficienti delle equazioni

     CALL subcoeff(c,d)

c    coeficienti per RK-5
     alfa3= 12.d0/13.d0
     beta30= 1932.d0/2197.d0
     beta31= -7200.d0/2197.d0
     beta32= 7296.d0/2197.d0
     beta40= 439.d0/216.d0
     beta42= 3680.d0/513.d0
     beta43= -845.d0/4104.d0
     ck0= 25.d0/216.d0
     ck2= 1408.d0/2565.d0
     ck3= 2197.d0/4104.d0

c    cicle on driving frequency


c    DO 100 j=1,n
 24  time=0.d0

     xmaxprev = 0.d0
     xmargin = 0.d0

     x1old = 0.d0
     x2old = 0.d0


c    Runge Kutta integration: RK-5

 25  iconta= iconta+1

     time0= time
     time1= time +.25d0*dt
     time2= time +.375d0*dt
     time3= time + alfa3*dt
     time4= time + dt

     time= time4

c    RK-5 calcola la funzione su 5 punti all'interno dell'intervallo dt

c    primo punto

     CALL subRK5(time0, x, fk0,w)

     DO 30 i=1,8
       xk0(i)= x(i)+dt*fk0(i)/4.d0
 30  CONTINUE

c    secondo punto

     CALL subRK5(time1, xk0, fk1,w)

     DO 40 i=1,8
       xk1(i)= x(i)+dt*(.09375d0*fk0(i)+.28125d0*fk1(i))
 40  CONTINUE

c    terzo punto
```

```
      CALL subRK5(time2, xk1, fk2,w)

      DO 50 i=1,8
        xk2(i)= x(i)+dt*(beta30*fk0(i)+beta31*fk1(i)+beta32*fk2(i))
50    CONTINUE

c     quarto punto

      CALL subRK5(time3, xk2, fk3,w)

      DO 60 i=1,8
        xk3(i)= x(i)+dt*(beta40*fk0(i)-8.d0*fk1(i)+beta42*fk2(i)+
     ?        +beta43*fk3(i))
60    CONTINUE

c     quinto punto

      CALL subRK5(time4, xk3, fk4,w)

c     funzione al tempo t+dt

      DO 70 i=1,8
        x(i)= x(i)+dt*(ck0*fk0(i)+ck2*fk2(i)+ck3*fk3(i)-0.2d0*fk4(i))
70    CONTINUE


      IF(time.GT.(tfin/2.d0)) THEN
       IF((x(2)*x2old).LT.(0.d0)) THEN
        x1max = x1old + ((x(1)-x1old)*x2old/(x(2)-x2old))
              WRITE(35,*) (Ux/UxL), (x1max*180.d0/PI)
       ENDIF
              xdiff = ABS(x1max - xmaxprev)
       xmaxprev = x1max
              IF(xdiff.GT.xmargin) THEN
        xmargin = xdiff
       ENDIF
      ENDIF



      IF(mod(iconta,iprint).EQ.0) THEN


c     WRITE(30,*) time,x(1)

c     WRITE(31,*) time, (x(1)*180.d0/PI)

      WRITE(32,*) (x(1)*180.0/PI), (x(2)*180.d0/PI)

c     WRITE(33,*) time, (x(3)*180.d0/PI)

c     WRITE(34,*) time, (x(4)*180.d0/PI)

      ENDIF

c     ciclo sul tempo

      x1old = x(1)
      x2old = x(2)
```

```
      IF(time.LT.tfin) GO TO 25

      WRITE(38,*) (Ux/UxL), x(1), x(2), x(3), x(4), x(5), x(6), x(7),
     ?         x(8)
      WRITE(39,*) (Ux/UxL), xmargin

      Ux = Ux + dUx

      a = Ux/UxL

      IF((a.GT.(0.14d0)).and.(a.LT.(0.18d0)))THEN
            tfin = timeset*6.d0
      ELSEIF((a.GT.(0.27d0)).and.(a.LT.(0.31d0))) THEN
            tfin = timeset*8.d0
      ELSEIF((a.GT.(0.44d0)).and.(a.LT.(0.52d0))) THEN
            tfin = timeset*12.d0
      ELSE
            tfin = timeset
      ENDIF

c     DO i=1,8
c      x(i) = xzero(i)
c     ENDDO
      PRINT *, a, tfin


      IF(Ux.LT.(Uxfin)) GO TO 24

c     x1amp= (x1max-x1min)/2

c     x3amp= (x3max-x3min)/2

c     WRITE(35,*) x1amp
c     WRITE(36,*) w
c     WRITE(37,*) x3amp


c 100  continue

c     DO i=1,8
c      WRITE(38,*) xzero(i)
c     ENDDO

c     CLOSE(30)
c     CLOSE(31)
      CLOSE(32)
c     CLOSE(33)
c    CLOSE(34)


      CLOSE(35)
c     CLOSE(36)
c     CLOSE(37)

      CLOSE(38)

      CLOSE(39)

      STOP
```

```
      END


      SUBROUTINE subcoeff(c,d)
c     calcolo dei coefficienti per le equazioni del moto per qualunque
c     tipo di non linearita'

      IMPLICIT none

      REAL*8 mu, xa, ah, ra, omg, dampz, dampa, Ux, betaa, betaz
      COMMON/airfpar/mu, xa, ah, ra, omg, dampz, dampa, ux, betaa, betaz

      REAL*8 c(10), d(10)


      REAL*8 psi1, psi2, eps1, eps2, betaa1
      COMMON/costant/ psi1, psi2, eps1, eps2, betaa1

      REAL*8 a, u, p1p2, pe12, pe1, pe2, r, ap, am

c     termini ricorrenti

      a= .5d0-ah
      u= 2.d0/mu
      p1p2= 1.d0-psi1-psi2
      pe1= psi1*eps1
      pe2= psi2*eps2
      pe12= pe1+pe2
      r= 1.d0/(mu*ra**2)
      ap= 1.d0+2.d0*ah
      am= 1.d0-2.d0*ah

c     calcolo dei coefficienti ci

      c(1)= 1.d0+1.d0/mu
      c(2)= xa-ah/mu
      c(3)= (2.d0*dampz*omg/Ux)+u*p1p2
      c(4)= (1.d0+2.d0*a*p1p2)/mu
      c(5)= u*pe12
      c(6)= u*(p1p2+a*pe12)
      c(7)= u*pe1*(1.d0-a*eps1)
      c(8)= u*pe2*(1.d0-a*eps2)
      c(9)= -u*pe1*eps1
      c(10)= -u*pe2*eps2

c     calcolo coefficienti di

      d(1)= -ah*r+xa/ra**2
      d(2)=1.d0+r*(1.d0+8.d0*ah**2)/8.d0
      d(3)= (2.d0*dampa/Ux)+am*r*.5d0-.5d0*r*ap*am*p1p2
      d(4)= -r*ap*p1p2-.5d0*r*ap*am*pe12
      d(5)= -r*ap*p1p2
      d(6)= -ap*pe12*r
      d(7)= -r*ap*pe1*(1.d0-a*eps1)
      d(8)= -r*ap*pe2*(1.d0-a*eps2)
      d(9)= r*ap*pe1*eps1
      d(10)= r*ap*pe2*eps2

      RETURN

      END

      SUBROUTINE subRK5(time,x,fk,w)
```

```
c   integrazione numerica di Runge Kutta 5 (non linearita' di tipo cubico)

    IMPLICIT none
    REAL*8 c(10), d(10)
    COMMON/coeff/ c, d

    REAL*8 Gx3, Mx1, P, H, w, FF

    REAL*8 omg, Ux, betaa, betaz
    REAL*8 mu, xa, ah, ra, dampz, dampa
    COMMON/airfpar/mu, xa, ah, ra, omg, dampz, dampa, Ux, betaa, betaz

    REAL*8 ft, ft0, gt, g0, Pt, Qt
    COMMON/forze0/ ft0, g0, FF
    REAL*8 psi1, psi2, eps1, eps2, betaa1
    COMMON/costant/ psi1, psi2, eps1, eps2, betaa1

    REAL*8 x(8), time, fk(8)


c   tipo di non linearita': cubica

    Gx3= x(3)+betaz*x(3)**3
    Mx1= betaa1*x(1)+betaa*x(1)**3

c   calcolo delle forzanti



    Pt= 0.d0
    Qt= 0.d0

    ft= ft0*(psi1*eps1*EXP(-eps1*time)+ psi2*eps2*EXP(-eps2*time))+ Pt
    gt= g0*ft + Qt - Pt*g0

c   coefficienti P e H

    P= c(3)*x(4)+c(4)*x(2)+c(5)*x(3)+c(6)*x(1)+c(7)*x(5)+c(8)*x(6)+
   ? +c(9)*x(7)+c(10)*x(8)+Gx3*(omg/Ux)**2 - ft

    H= d(3)*x(2)+d(4)*x(1)+d(5)*x(4)+d(6)*x(3)+d(7)*x(5)+d(8)*x(6)+
   ? +d(9)*x(7)+d(10)*x(8)+Mx1*(1/Ux)**2 - gt

c   equazioni del sistema

    fk(1)= x(2)
    fk(2)= (c(1)*H-d(1)*P)/(d(1)*c(2)-c(1)*d(2))
    fk(3)= x(4)
    fk(4)= (-c(2)*H+d(2)*P)/(d(1)*c(2)-c(1)*d(2))
    fk(5)= x(1)-eps1*x(5)
    fk(6)= x(1)-eps2*x(6)
    fk(7)= x(3)-eps1*x(7)
    fk(8)= x(3)-eps2*x(8)

    RETURN

    END
```

Arthur Faflik-Brooks

BADANIA NIELINIOWEJ AEORELASTYCZNOŚCI SKRZYDEŁ PŁATOWCÓW.

Streszczenie

Praca dotyczy badania właściwości nieliniowych modeli sprężystych opisujących ruch skrzydeł płatowców. Modele ruchu skrzydeł stworzone zostały w oparciu o równania różniczkowe, do rozwiązania których wykorzystano metodę Runge-Kutta-Fehlberg'a. Walidacja wykonana w oparciu o przykłady zawarte w literaturze wykazała poprawność przyjętych modeli.

Ostatni etap pracy dotyczy badania wpływu zmiany parametrów modelu sprężyny trzeciego stopnia na amplitudę ruchu skrzydła po perturbacji. Badania wykazały korelację między twardszą sprężyną i mniejszą amplitudą cyklu granicznego drgającego skrzydła.

COLD AIR FLOW CHARACTERISTICS OF A LOW NO_X AXIAL SWIRL BURNER

Sławomir J. Golec, PhD. Eng.
General Electric Company Polska

Abstract

Recent technological changes in the Polish power industry have created opportunities for reducing NO_x, CO, SO_2 emissions, but - at the same time - created another operation problem: sulphur corrosion and erosion of boilers' water-walls as well decreasing of the boiler's efficiency. This has been the motivation for performing a detailed study of the air flow in low-NO_x burners. A measuring stand was built inside a real medium power OP-230 boiler equipped with a low-NO_x burner to measure the velocity field at the burner's outlet and to prepare experimental characteristics of the burner. To extend the description, a numerical model of the burner was constructed and numerical calculations were executed by means of the Fluent program. Numerically calculated velocity profiles were compared with the results of measurements. The obtained results have been helpful in formulating recommendations to improve burner geometry.

Keywords: *combustion, pulverised coal burner, NO_x, SO_2, environmental pollution, sulphur corrosion, LNASB*

1. Introduction

There have been many technological changes in the Polish power industry in the recent years, but coal remains a dominating source of energy and its position will certainly not be shaken in the next several years. It results both from economic reasons and from the imperative of energetic security of the country. The cost of electricity obtained from coal is half that of electricity produced from natural gas. According to a DOE report [1], natural gas fuel costs are expected to rise whereas those of coal will decline. Moreover, the question of permanent and undisturbed access to energy sources is becoming more and more important nowadays. The persistent instability in the former Soviet Union countries and in the Middle East shows that excessive reliance on foreign oil is a costly proposition - in political, military and economic terms. Fortunately, Poland has plentiful domestic resources of coal to generate electricity - and new technologies allow to meet the growing demand for electricity more efficiently. However, coal combustion is inseparably associated with environmental pollution. The major pollutants produced in the combustion process are unburned and partially burned hydrocarbons, carbon monoxide, sulphur oxides, nitrogen oxides, and particulate matter in various forms. All these compounds affect the environment and human health in many ways, the most important of which are:

- potential increase of sickness and mortality of the population,
- altered properties of the atmosphere and precipitation,
- worsened conditions of vegetation,
- soiling and deterioration of materials.

Because of the large number of uncontrolled variables, it is not easy to explicitly measure the effect of pollution on human health. However it is well known that carbon-based particles may contain adsorbed carcinogens. It is also observed that pollutants can aggravate pre-existing respiratory ailments. The occurrence of acute and chronic bronchitis can be correlated with SO2 and particulate matter. Altered properties of the atmosphere affecting local areas include: reducing visibility, increasing fog formation and precipitation, altering temperature and wind distributions, reducing solar radiation. On a larger scale, greenhouse gases may alter global climates.

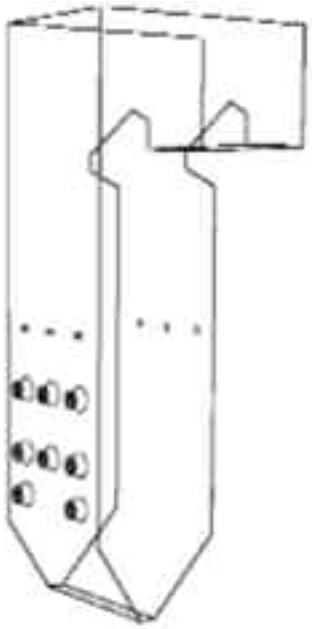

Figure 1. Burners and OFA nozzles' configuration in the OP-230 boiler

Lakes and susceptible soils are affected by acid rain produced from SO_x and NO_x emissions. Vegetation is harmed by the action of phytotoxicants SO_2, peroxyacetyl nitrate (PAN), C_2H_2 and others. Particulate matter, especially that containing sulphur, corrodes paint, masonry and electrical contacts, while ozone severely deteriorates rubber. The huge volume of combusted coal and environmental pollution caused by flue gases have resulted in a growing interest in the improvement of the coal combustion technology. In order to reduce the pollution, Poland, like other industrialized countries, has adopted stringent emission standards and implemented emission control. In the early nineties the power industry made a great organizational and financial effort to reduce the emission of nitric oxides and carbon monoxide. It was achieved in various forms, depending on the individual energy producer. Air gradation has been applied in certain installations, whereas others employed low-emission burners with air redistribution. These two types of rebuilding required only a slight modernization of air ducts and met the environmental standards close enough. Moreover, these solutions are relatively cheap.

Like many other power plants, the Heat and Power Plant „Wybrzeże" in Gdańsk took it upon themselves to modernize most of their boilers. A general overhaul of the boilers was performed in 1994.

In the case of the OP-230 boiler, with tight screening of the burning chamber with natural circulation (boiler No. 10), the modernization mainly consisted in replacing swirl-type burners with low-emission units manufactured by Babcock Energy Ltd. and in admitting additional volume of air to the combustion chamber via OFA nozzles located in front of and behind the water wall. A sketch of the side view of the boiler with eight burners and six small OFA nozzles is shown in Fig. 1. The boiler is equipped with a three-stage steam superheater, a water heater, and two rotating air heaters. It is supplied by four mills, three of them in continuous operation and the fourth kept in reserve. Each mill feeds two burners, so the fuel is injected by six burners. The burners are located on the boiler's front wall at a distance of 2.5 m from each other.

After the modernization, the boiler was in operation for 27 thousand hours, when its rear water wall was damaged in the spring of 1998 [4]. A tube was torn apart at the level of 14 m - the top row of burners. Thickness measurements of the tube walls in the vicinity of the damaged part made after the failure, revealed a reduction in thickness from 5 mm, which was the nominal value, down to a minimum thickness of 1.4 mm. The thickness defect was recorded along half-perimeter from the furnace side, 'from fin to fin', the minimum thickness being located at the top of the tube.

Chemical analyses confirmed unmistakably the correct ferrite-and-bainite structure of the tube's steel, and its low degradation level, recorded both from the side of the furnace gas and that of the furnace lining. An increased concentration of sulphur was observed in the deposits taken from tubes along with increased contents of oxygen, potassium, magnesium and calcium, which testified to a high concentration of sulphides. High contents of sulphur in the layer and uniform material decrement in the tubes testified to sulphide corrosion of the boiler's rear water wall.

Measurements of the pipe's thickness have shown that the rate of corrosion in this boiler was equal to 0.7 mm ÷ 1 mm per year, while it had been 10 times lower before the modernization.

It thus came out that the new installation significantly reduced NO_x emission, but at the same time caused serious damage to the boiler, and remained a threat to its faultless exploitation. A detailed study of combustion process in the new low-emission burner became necessary also for technological reasons.

2. Burner characteristics

The geometry of the low-NO_x emission swirl burner manufactured by Babcock Energy (Fig. 2) is more complex than that of a standard swirl burner. The air flowing into the combustion chamber is divided into core, primary, secondary and tertiary. The secondary air of the standard low-NOx burners is divided into secondary and tertiary air. In this way an additional possibility of combustion process control is achieved, through diversification of the air fluxes at the outlet. The angles of vanes mounted in the second and third air channels are different and adjustable, providing opportunities for changing the length of the swirl jet. Series of measurements were carried out to prepare the experimental characteristics of the burner and determine the velocity field at the outlet [5].

Figure 2. A Babcock Energy burner during measurements of the velocity components

in the OP-230 boiler No. 10, Heat and Power Plant in Gdańsk

Table 1. Measurement conditions for the Babcock Energy burner [4]

	Volume flow m³/hr	Temperature °C
Core air	2800	22
Primary air	7500	45
Secondary air	17000	22

During the experiment the coal mill was merely ventilated and no coal was flowing through the burner, while in the normal operation of the boiler pulverized coal is mixed with primary air. The measuring probe was mounted on a system of movable guiding rails located co-axially with the burner (Figs 2 and 3). Because of a high level of dust in the chamber, a strengthened Dantec fibre-split thermo-anemometer probe was used. The probe made it possible to measure the axial and the tangential velocity components, as well as their fluctuations. The measurements were realized in cross-sections 0, I, II, III (Fig. 3). Cross-section 0 was situated at a distance of l cm from the burner's outlet, cross-section I -20 cm, cross-section II - 66 cm, and cross-section III - 91 cm from the outlet of the burner. The output of primary and secondary air was measured independently and recorded in the control room of the power unit. Moreover, it was possible to control the swirl of secondary air using a special swirler situated in the secondary air space inside the burner. Approximate conditions of burner work are given in Tab. 1. Properties of the swirl flow can be correctly described by the swirl number, according to the following formula:

$$S = \frac{2}{d} \cdot \frac{G_\theta}{G_x} \tag{1}$$

where d is the stream diameter, G_θ is the tangential momentum component and G_x is the axial momentum component, both given by the following formulas:

$$G_\theta = \int_0^\infty (\rho UW + \rho u'w') r^2 dr \tag{2}$$

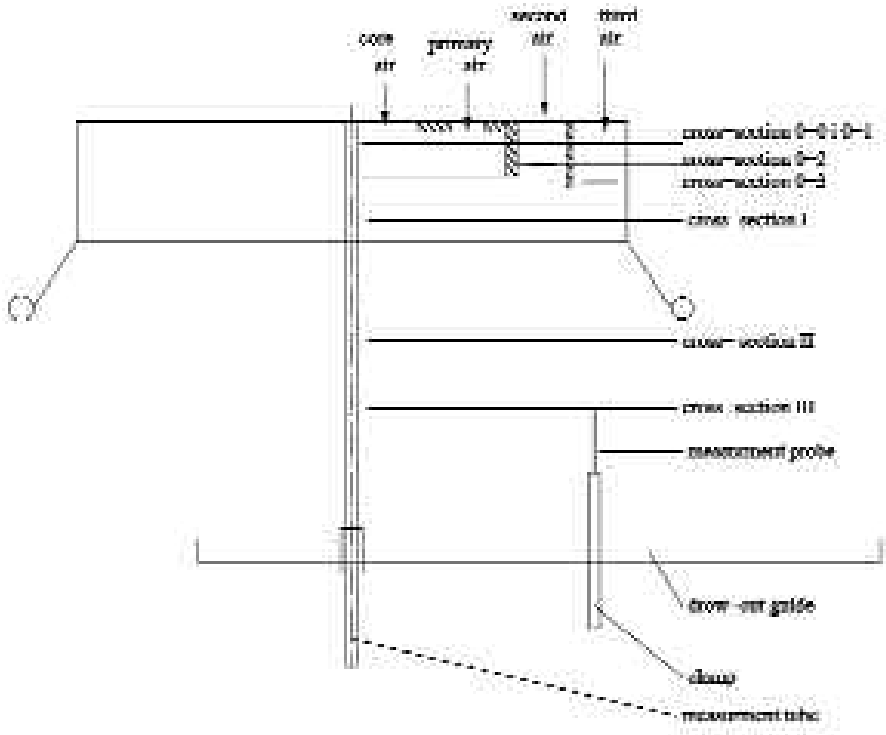

Figure 3. Measurement cross-sections at the outlet of the Babcock Energy burner

$$G_x = G_0 = \int_0^x \left(\rho U^2 + \rho u'^2 + (p - p_\infty) \right) r \, dr \tag{3}$$

where U and W are the axial and circumferential components of the air stream, while u' and w' are fluctuations of axial and circumferential components of velocity, respectively, ρ is density, p and p_∞ stand for the actual value of pressure and the value of pressure at infinity.

In the case of incompressible flow, disregarding the influence of fluctuations of velocities u' and w' simplifies the formula considerably:

$$S = \frac{2}{d} \cdot \frac{\int_0^\infty UWr^2 dr}{\int_0^\infty U^2 r dr} \tag{4}$$

On the basis of the measurements, a square-mean approximation of the swirl number was computed in relation to the swirl vane used and diaphragm settings. Their influence on the averaged S is relatively low, and the swirl number curve as a function of diaphragm setting and the swirl vane varies within the range of 0.47÷0.69.

Figure 4. Geometry of the numerical model of the burner and the profile of velocity magnitude [m/s] at a distance of 20 cm from the outlet

Table 2. Air boundary conditions for the numerical calculations of the Babcock Energy burner

	Mass flow [kg/s]	Temperature K
Core air	0.75	293
Primary air	1.7	318
Secondary air	1.2	293
Tertiary air	3.45	293

3. Measurements versus numeric

As mentioned above, the experimental characteristics of the burner were developed in several cross-sections only. To extend the description of the burner to the whole of the combustion chamber, a numerical model of the burner was constructed (Fig. 4, 5 and 8) with a part of the combustion chamber of the size 4m × 4m × 6m. The geometry of the burner was simplified. It was assumed that some of the blades were plane, while in practice they were half-rounded, and the

thickness of most of the burner walls and blades was assumed to equal zero. However, the inner walls and blades were included, as shown in Fig. 9. Because of the complicated geometry, different types of cells were used. A majority of the burner cells was of the tetrahedral type whereas the combustion chamber consisted of hexahedral cells. For most of the numerical tests the number of cells did not exceed 1000 000. All computations concerning the flow of air through the burner were carried out by means of Fluent [6]. The numerical air boundary conditions were based on the measurements and are presented in the Tab. 2. The numerical calculations were executed using a k-ε turbulence model of very good convergence, and the RNG k-ε model, which yielded a solution with the residuum exceeding 10^{-3}. Selected results of these calculations are shown in Figs 4-9. Fig. 4 shows a view of the burner in the horizontal plane, along with the velocity profile at a distance of 20 cm from the burner outlet. Looking from the left, the inlets of core and primary air are visible. One can also see covered inlets of secondary and tertiary air. The velocity profile in the plane marked in the picture is not symmetric with respect to the burner axis. This asymmetry is insignificant and results from the burner's construction.

Fig. 5 shows, in an axonometric projection, velocity magnitude contours in the vertical plane along the burner's axis. The edges of the inner walls and burner blades are also marked, along with a fragment of the modelled combustion chamber. The tangential velocity component, in the intersection along the burner axis in the vertical plane and the completely modelled combustion chamber, are presented in Fig. 6.

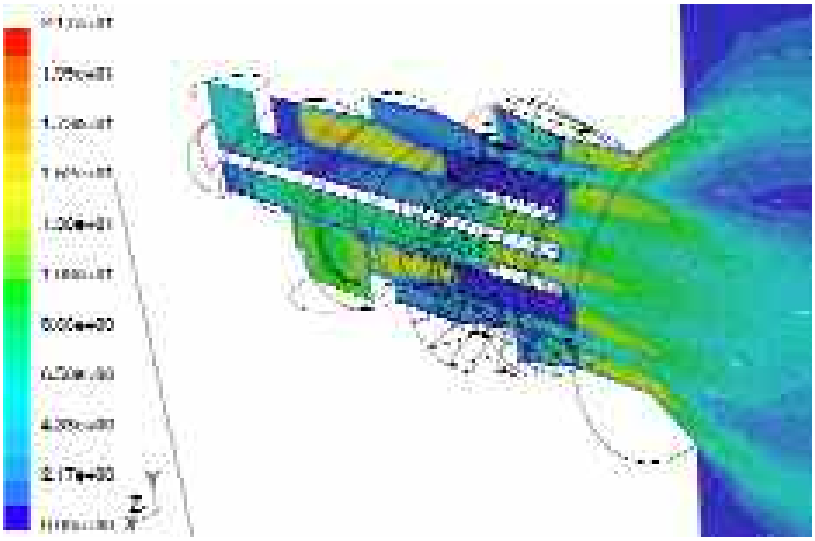

Figure 5. The velocity magnitude [m/s] in the cross-section along the burner axis

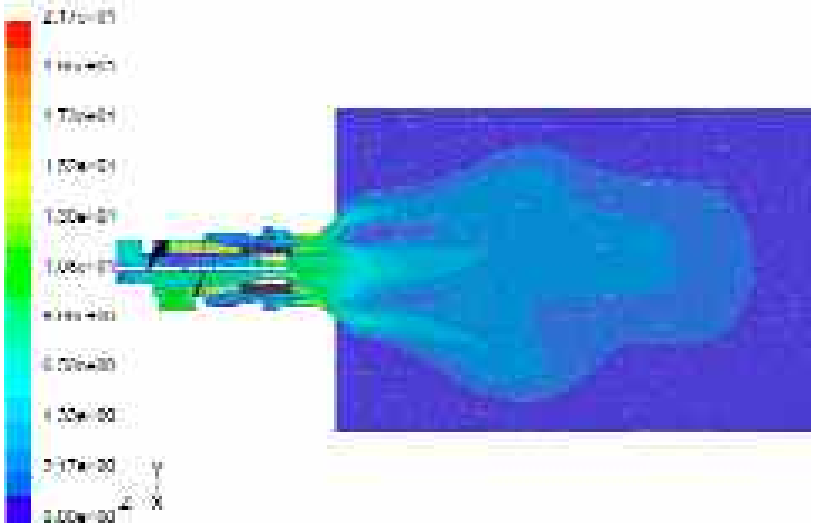

Figure 6. The velocity magnitude [m/s] in the cross-section along the burner axis - - chamber view

Velocity modulus contours at the outlet of the burner are shown in Fig. 7. One can see the influence of four separating blades and tertiary air blades on velocity. An asymmetry of the burner's work can be observed as well.

Fig. 8 shows the streamlines. Inner blades of the burner and selected fragments of walls separating particular streams of air are also shown in the figure. One can easily observe the configuration of streamlines inside the burner and inside the combustion chamber. It is noteworthy that the air blown into the numerically modelled chamber has the form of a slightly expanding stream. Velocity profiles, calculated numerically, are compared with the results of measurements in Fig. 9. The figure consists of eight plots, arranged in two columns and four rows. The first and second columns show the axial and circumferential components of the velocity vector, respectively. The rows correspond to cross-sections 0, I, II and III. In each plot, the „X" axis represents radius *r* [m] (measured from the axis of the burner), while the „Y" axis represents a component of the velocity vector [m/s]. The solid line corresponds to numerically computed values, while the dots mark the measurements data.

The least compatibility between the measurements and the calculations is observed for core air, particularly in cross-section I, for the axial component (see Fig. 9).

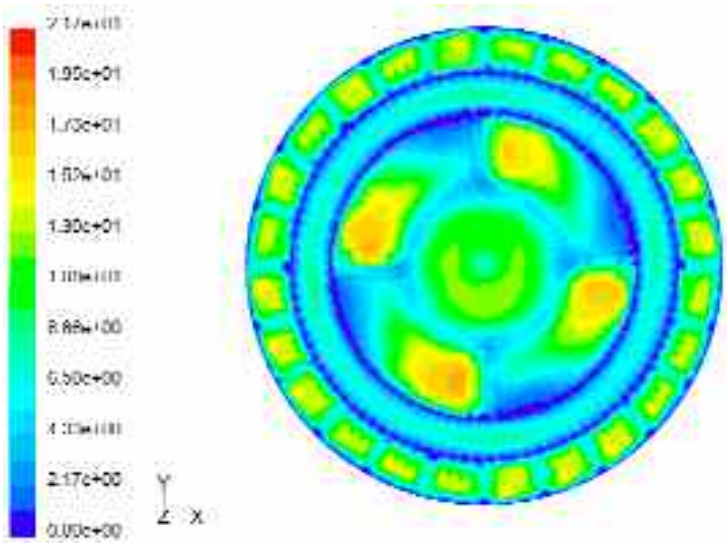

Figure 7. Velocity modulus in the crosswise direction (with respect to the axis of the burner) at the burner outlet

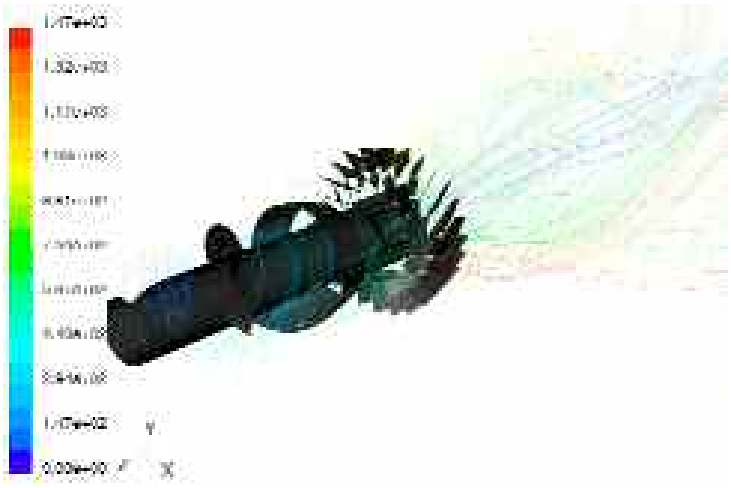

Figure 8. Streamlines with marked internal blades and the wall separating primary and secondary air; the beginning fragment of the wall separating the second from the third air flow is marked

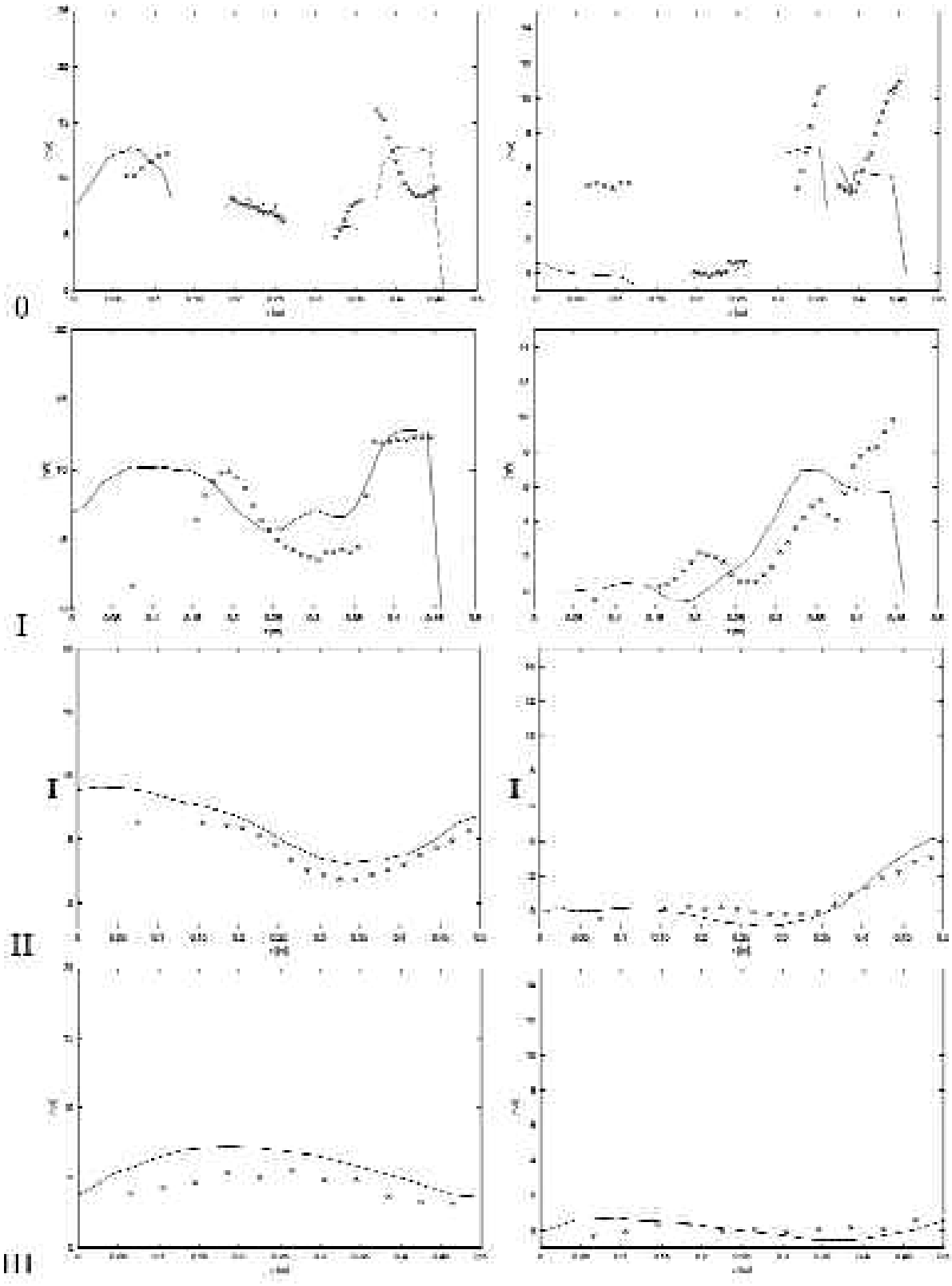

Figure 9. Velocity component cross-sections 0, I, II, III. The first and second columns present the axial and radial components, respectively. Measurement data are marked with dots, numerical results - with lines

This discrepancy may be due to the presence of the leading pipe along the burner axis. The pipe was neglected in the numerical model used for the calculations.

Further from the burner outlet (cross-sections II and III) the consistency between the calculated and measured profiles of the axial and circumferential components is better.

There is qualitatively good consistency of calculations and measurements for primary air, particularly in cross-section 0. In other cross-sections, the numerical solution is similar to most of the measurements of velocity vector components. The least consistency is observed in cross-section I. It may result from the different shapes of primary air blades (separators).

There is qualitatively good agreement for secondary air in cross-section 0, while further from the burner outlet, i.e. in cross-section I, one can observe excessive values of the axial component of the velocity vector (Fig. 9). However, the difference is insignificant.

In cross-section II, there is good consistency of the axial and tangential components of the velocity vector. These discrepancies were undoubtedly caused by the simplification of the burner geometry.

Other inconsistencies could have resulted from inaccuracies of measurement. While the real flow was three-dimensional, the probes used in the measurements were appropriate for 2D flows, which increased the measurement error. One should also bear in mind the differences in the temperature of core and primary air, and between primary (45°C) and secondary air (22°C), which were assumed equal.

4. Conclusions

Measurements and numerical calculations presented above allow the basic characteristics of the low-NO_x burner to be defined. First of them is a relatively low swirl number. The swirl is very weak at the core and primary air areas and increases in secondary and tertiary air areas. Thus, it can be concluded that primary air transports coal powder deep into the combustion chamber. This type of combustion may lead to corrosion and erosion of a boiler's rear water wail, which took place at the Wybrzeże Heat and Power Plant. This non-uniformity can be reduced by means of an additional screw blade.

Acknowledgements and additional Information

The majority of calculations were made at the Academic Computer Center TASK Gdańsk during creating of author's PhD thesis [2].

This paper is a part of paper [3] which is based on the author's PhD thesis.

References

[1] http://www.eia.doe.gov/oiaf/aeo/electricity.html

[2] Golec S: *Numerical Modelling Low NO_x Axial Swirl Burners Operation Based on Babcock Energy Burner in the OP-230 Boiler in the Gdańsk Energy and Thermal Power Plant,* PhD thesis, 2004 (in Polish)

[3] Kardaś D. and Golec S: *Flow characteristics of a low NO_x emmision burner.* 2004

[4] Kardaś D, Michalski M and Janczewski J: *2000 5th European Conf. on Industrial Furnances and Boilers,* Espinho-Porto

[5] Wierciński Z. Kardaś D. Topolski J. and Kaiser M.: *Air Characteristics of a Babcock Burner in Power Plant in Gdańsk,* IFFM Report no. 263/98 (in Polish), 1998

[6] *Fluent User's Guide, Release 6.0, Fluent Incorporated,* 2003

S. Golec

CHARAKTERYSTYKI PRZEPŁYWU ZIMNEGO POWIETRZA DLA NISKOEMISYJNEGO OSIOWEGO PALNIKA WIROWEGO (LNASB)

Streszczenie

Obecne zmiany technologiczne w polskich elektrowniach i electrociepłowniach stworzyły szanse do redukcji emisji NO_x, CO oraz SO_2 ale jednocześnie przyczyniły sie do powstania nowych problemów eksploatacyjnych takich jak np.: korozji siarkowej i erozji płaszczy kotłów jak i również obniżenia sprawności pracy kotłów. Powyższe problemy były motywacją do dogłębnej analizy przepływu powietrza w niskoemisyjnych palnikach wirowych. Stanowisko pomiarowe przeznaczone do wyznaczania pola prędkości u wylotu z palnika oraz charakterystyk pomiarowych palnika było stworzone w rzeczywistym kotle OP-230 wyposażonym w niskoemisyjny palnik. Do poszerzenia opisu zbudowano numeryczny model palnika, a obliczenia numeryczne były wykonane za pomocą pakietu oprogramowania o nazwie Fluent. Rezultaty tych obliczeń numerycznych były porównane z pomiarami. Otrzymanane wyniki były pomocne w tworzeniu wytycznych modernizacji palnika.

NUMERICAL INVESTIGATION OF FLOW IN UAV SINUSOIDAL COMPRESSOR STAGE

Bartosz BOGUCKI, MSc
Institute of Aviation, Warsaw, Poland
Engineering Design Center

Summary

Centrifugal compressors, which have lost their application in the military crew airplanes, are often implemented to small-dimension unmanned aircraft engines. Their one-stage high-pressure ratio, low-complexity construction and relatively small dimensions and weight consolidated their position in modern constructions. Continuous development of these compressors has attracted increased attention to the flow field in smaller and fast-rotating blade passages. Supersonic phenomena, mixing losses and unsteadiness of the flow in the impeller are expected to be studied with more details.

The work presented in this report was performed at the Ecole Nationale Supérieure d'Ingénieurs of Constructions Aéronautiques (ENSICA) in Toulouse within an UAV engine development program led by Department of Fluid Mechanics, ENSICA and JPX Company, France.

The purpose of this study was to investigate numerically several design solutions implemented to mixed-flow compressor stage of the 100kN turbojet engine named T100.

1. INTRODUCTION

At the beginning of conception work on the T100 engine, an 18-blades sinusoidal (mixed-flow) compressor with 9 splitters was designed (Figure 1). The main objective in placing additional blades in flow passage of the machine was to adapt as much as possible the geometry to supersonic flow expected at the inlet. Hence, from 18 full–length blades, half of them were cut at some distance from the blade leading edges to enlarge inlet throat, and as result avoid choke problems in this region. However, during experiments it occurred that the inlet conditions are subsonic and that the front section of the impeller does not have to be designed so restrict. Thus, as a method to reach higher stage efficiency it was proposed to replace the splitters by full–length blades. In the impeller without splitter more uniform flow in the blade passage, and consequently higher efficiency were expected. As the result of the two concepts, a necessity of their comparison took place.

Next improvement introduced to the compressor's design was reducing tip clearance to minimum. It was possible due to new material applied on the shroud surface, which allowed to match the blade tips up with the shroud surface by wearing down used material from the internal shroud surface (abradable process). Therefore, need of numerical trade-off study of the tip clearances effect on performance occurred.

The last analysis was dedicated to choke effect occurring in the non–splittered compressor.

Since this phenomenon has crucial significance for the impeller performance and operating range, critical back static pressure and respective mass flow rate within compressor had to be known.

The NUMECA software was used for this project. The package is highly sophisticated tool dedicated for design, analysis and optimization of turbomachinery. NUMECA provides many useful features regarded to mesh generation (IGG/AutoGrid), solving (FINE/Turbo) and post-processing (CFView) of turbomachine CFD models.

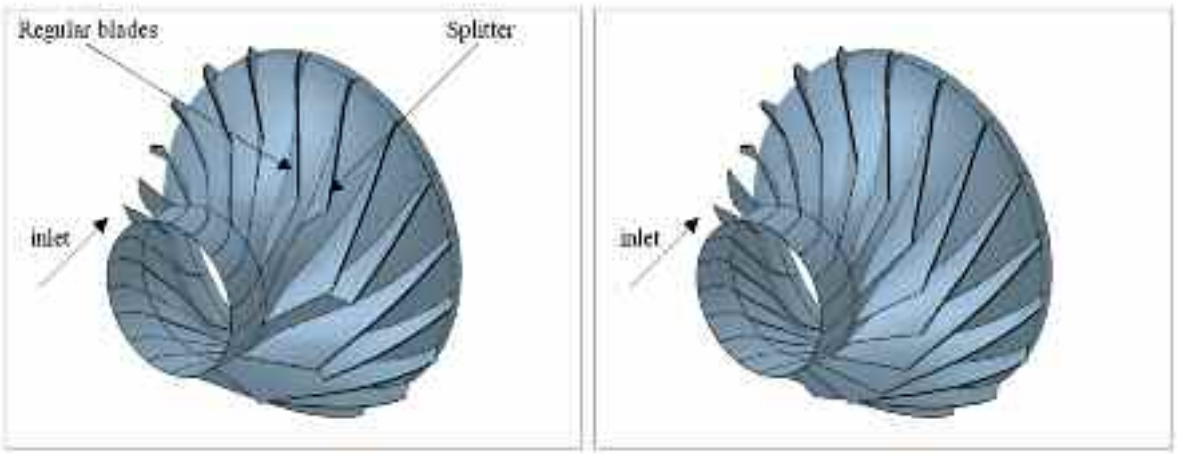

Fig. 1. Mixed-flow compressor stage with splitter (left) and without splitter (right)

2. THEORETICAL ASPECTS

To enable comparison of the two analyzed compressor designs, it is worth to define few important operating parameters that characterize turbomachines.

2.1 Efficiency

For all turbomachines efficiency is defined as ratio of work inputs into ideal and actual compressors, which have equal pressure rise [2]:

$$\eta = \frac{L_{is\,ideal}}{L_{actual}} \tag{1}$$

In adiabatic processes work input is equal to the rise in stagnation enthalpy:

$$L = h_{02} - h_{01} \tag{2}$$

Then, the efficiency is defined as:

$$\eta_{is\,comp} = \frac{h_{02is\,comp} - h_{01}}{h_{02} - h_{01}} \tag{3}$$

After introducing uncomplicated thermodynamics expressions for the enthalpy we receive simple expression for the isentropic efficiency [2]:

$$\eta_{is\,comp} = \frac{\left(p_{02}/p_{01}\right)^{(\gamma-1)/\gamma} - 1}{\left(T_{02}/T_{01} - 1\right)} \tag{4}$$

However, definition of the isentropic efficiency has one major disadvantage, i.e. it gets lower as the overall pressure ratio increases. It can be avoided by using another expression for efficiency in adiabatic compressors, called polytrophic efficiency. It removes the mentioned penalty so that compressors of the same aerodynamic quality, but significantly different pressure ratio, would have the same polytropic efficiency [2]:

$$\eta_{poly} = \frac{\gamma - 1}{\gamma} \frac{\ln(p_{02}/p_{01})}{\ln(T_{02}/T_{01})} \tag{5}$$

2.2 Slip effect

Since the compressor stage consists of rotating components we can distinguish two frames of reference: the absolute frame where velocity is related with stationary coordinate system and the relative frame is moving at the local blade speed. In these two frames we can consider relative and absolute velocities which throughout this report are denoted by *W* and *C*, respectively. The velocity triangles can be built using the vector relation: relative velocity + blade speed = absolute velocity [1]. Velocity triangles at the inlet and the outlet of the impeller are shown in Figure 2. Relative flow angle is denoted by β and absolute flow angle by α and they express inclination of the relevant velocity vectors from axial direction. Moreover, each velocity vector is usually decomposed onto components parallel to principal axes of compressor: meridional and tangential.

The designers of centrifugal impellers are interested in the real flow direction relative to the blades because in the impeller–exit area the flow direction does not follow blade geometry and deviates significantly. In general, the mean flow angle β_2 is lower then the blade angle β_{2b}. The difference between the two is called a slip angle, β_2, and the effect itself is usually called a slip effect in impeller. Due to the slip effect the pressure ratio is often lower than theoretically predicted [3].

2.3 Non-dimensional parameters

Non–dimensional design parameters allow describing the overall performance of the machine so that assessment and comparison between compressors with different dimensions and flow parameters can be easily made. The first and the most obvious dimensionless parameter is static or total pressure ratio which expresses ability of the compressor to rise the pressure in the impeller [8]:

$$\pi = \frac{p_{02}}{p_{01}} \tag{6}$$

The nominator in the given formula is the stagnation pressure at outlet of the impeller and denominator is the stagnation pressure at inlet. The choice of either static or stagnation pressure depends on the designer. Second non–dimensional parameter, which for isentropic process can be derived directly from pressure ratio, is temperature ratio [8]:

$$\tau = \frac{T_{02}}{T_{01}} \tag{7}$$

Non-dimensional mass flow is the next crucial parameter deciding about compressor performance. It is expressed as [2]:

$$\Theta = \frac{\dot{m}\sqrt{T_{01}}}{p_{01}} \tag{8}$$

Then, mass flow corrected to standard conditions expresses as [2]:

$$\Theta_{corr} = \Theta \sqrt{\frac{T_{01}}{T_{ref}}} \frac{p_{ref}}{p_{ref}} \tag{9}$$

where p_{ref}=101300 Pa and T_{ref}=288K is a reference standard atmospheric pressure at zero sea level.

2.4 Choke Flow in Compressor

Choke flow, also recalled as 'critical flow', is a special effect in compressor when due to sonic conditions in passage higher flow velocity cannot be reached. In gas flow through orifice there is a specific downstream/upstream pressure ratio for which the gas velocity reaches sonic conditions. At this point no information can be transmitted upstream through the nozzle and any further increase of the backpressure produces no increase of the mass flow and the flow becomes choked. However, mass flow can still increase due to rise of upstream pressure. As the inlet air pressure builds up, the density of the fluid also increases and since the mass flow is also a function of density, the mass flow rate increases linearly with inlet pressure [7].

The best experimental approach to create a 'choke map' for compressor is decreasing back static pressure to critical value and measuring corresponding mass flow and pressure ratio. Obtained function of pressure ratio in terms of mass flow rate is the compressor path to choke. In numerical simulation sonic conditions are achieved similarly, by lowering backpressure from value of 110% of the nominal static pressure to a point where choke is reached.

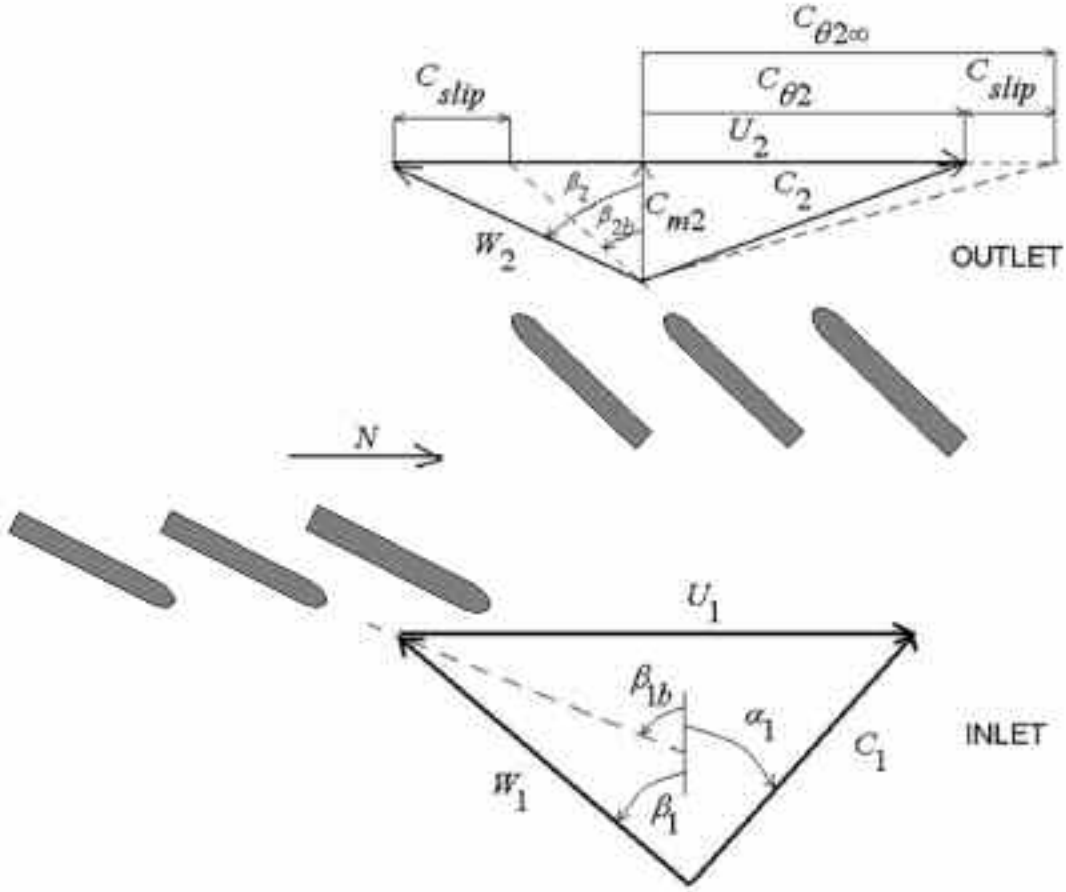

Figure 2. Velocity triangles at inlet and outlets of compressor stage

3. NUMERICAL MODELLING

Computational mesh was generated by means of the IGG/AutoGrid software. In the following turbomachinery studies the overall number of grid points ranges between 330,000 for the non-splittered compressor passage up to 950,000 for the splittered compressor passage (Figures 3 and 4). Special attention was paid to the high gradient regions like leading– and trailing–edges and to the first cell width along all solid boundaries of the profile (Figures 5 and 6).

To assess influence of turbulence model used in calculations, appropriate trade-off study for one test-case (non–splittered centrifugal compressor stage with no tip clearance) was performed. Pressure and temperature ratios and efficiencies computed during this examination are

compared in Table 1. It can be clearly seen, that the specified values for Baldwin–Lomax model differs from that for mutually similar Spalart–Allmaras and k-ε models. Having in mind that the one-equation Spalart–Allmaras turbulence model connects low numerical expenses with relatively good accuracy, this particular model was chose for all the computations. Values of y+ vary between 15 and 60, which is fully acceptable range for the Spalart-Allmaras turbulence model.

Table 1. Comparison of results for three different turbulence models

Turbulence Model	Pressure Ratio	Temperature Ratio	Isentropic Efficiency
Baldwin-Lomax	4.535	1.556	0.971
Spalart-Allmaras	4.464	1.572	0.931
Standard k-ε	4.483	1.566	0.945

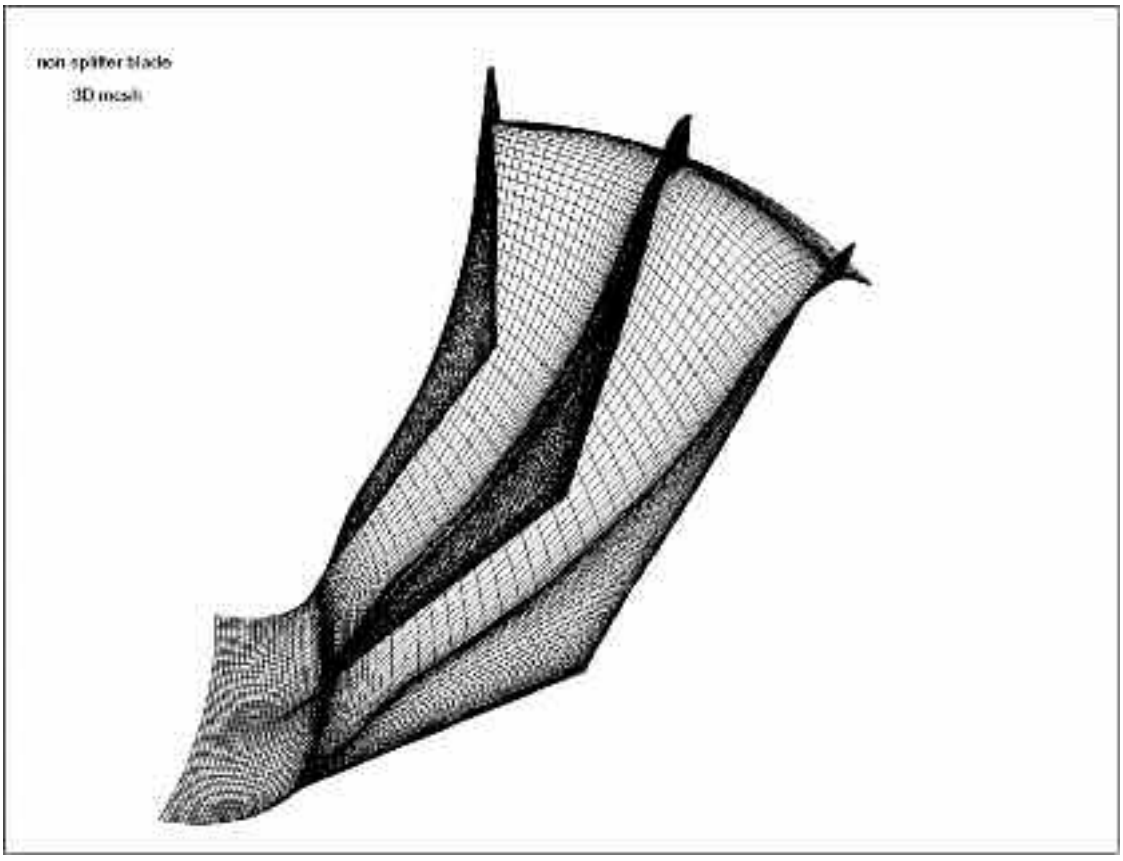

Figure 3. 3D mesh for non-splittered compressor passage

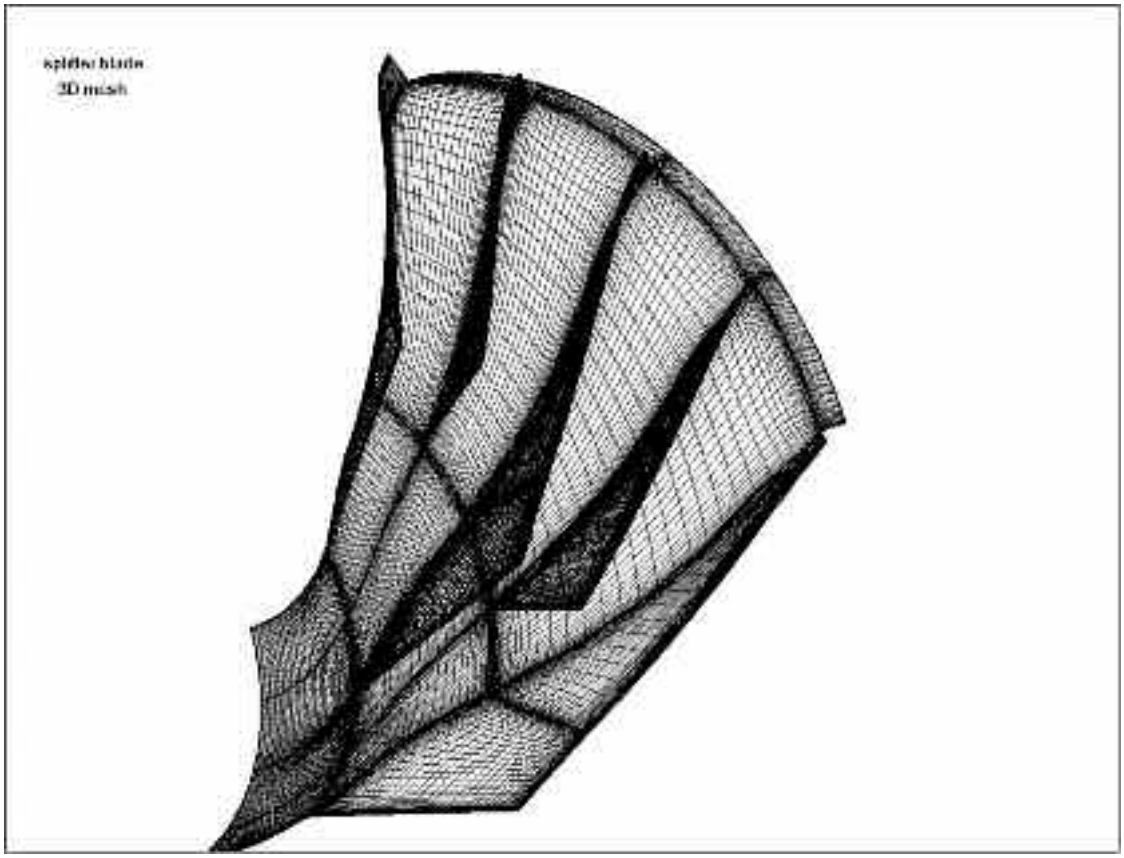

Figure 4. 3D mesh for splittered compressor passage

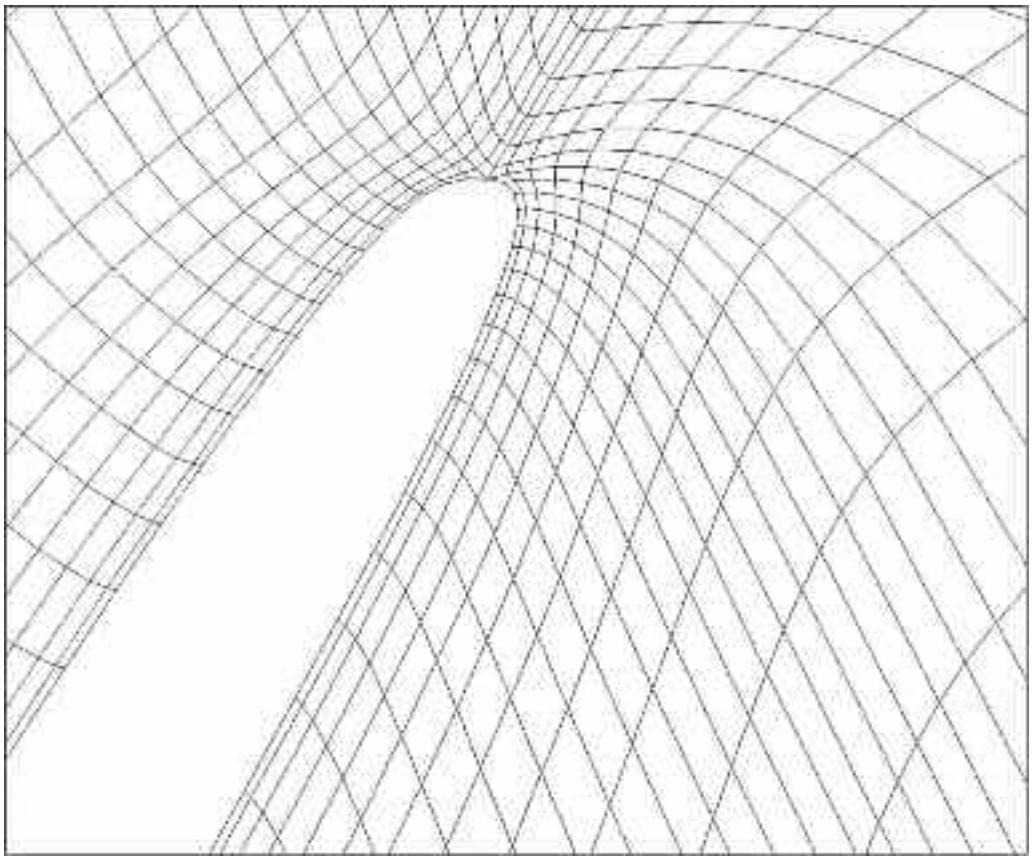

Figure 5. Clustering near the blade trailing edge

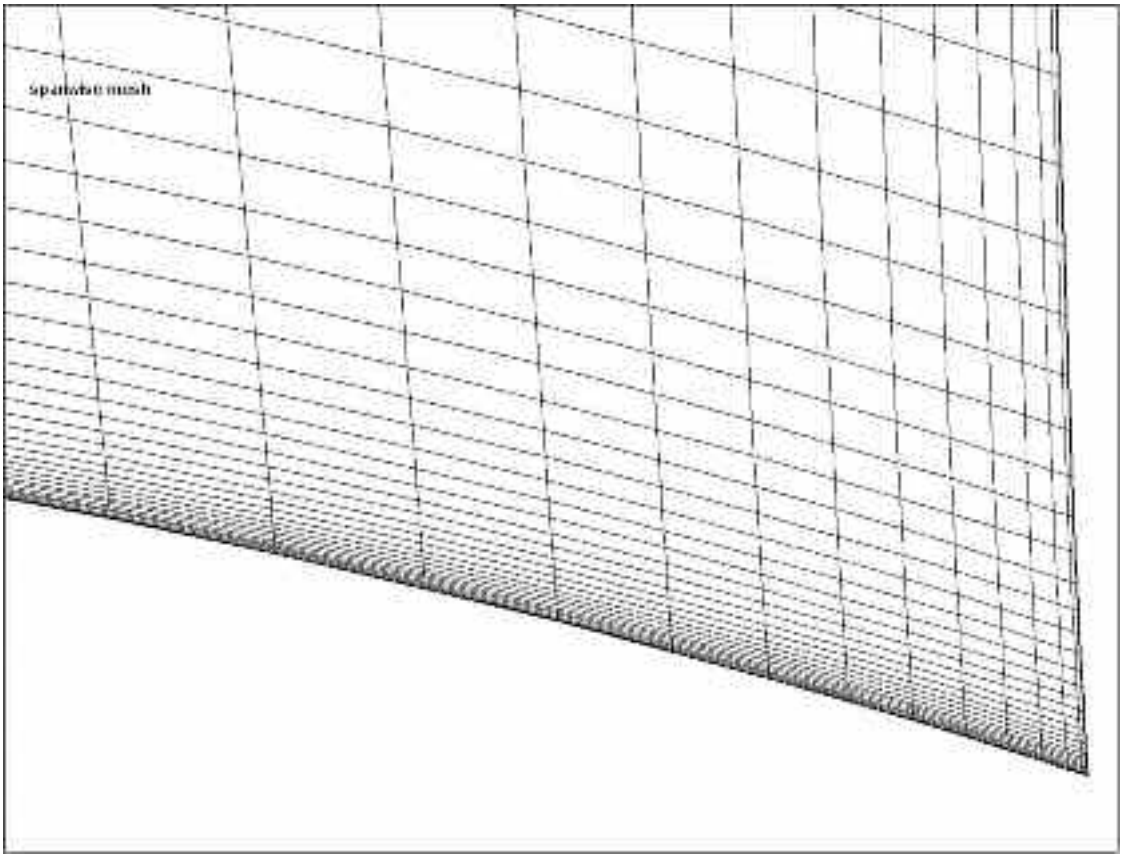

Figure 6. Near wall mesh resolution

In order to model actual conditions occurred during lab test of the compressor, a total atmospheric pressure, temperature and flow angle at the inlet were imposed. At the outlet a static pressure with radial equilibrium law was imposed. Summary of boundary conditions applied to the models is shown in Table 2.

Table 2. Boundary conditions for sinusoidal compressor stage study

Case study	Inlet	Outlet
Splittered compressor stage	$p_{t1} = 101300Pa$ $T_{t1} = 288K$	$p_2 = 180kPa$
Non–splittered compressor	$p_{t1} = 101300Pa$ $T_{t1} = 288K$	$p_2 = 180kPa$
Choke flow effect	$p_{t1} = 101300Pa$ $T_{t1} = 288K$	$p_2 = 125 \div 195kPa$
Tip clearance effect	$p_{t1} = 101300Pa$ $T_{t1} = 288K$	$p_2 = 180kPa$

5. COMPARISON STUDY RESULTS

In Table 3 the most important quantities describing flow state at the inlet and outlet are presented. The first noticeable difference in flow parameters between the cases is the mass flow

rate, which in the splittered compressor is lower by 0.2kg/s. The reason of the worse performance of the splittered compressor is a noticeable swirl generated at the splitter blade leading edge (Figure 7), which proceeds mainly to the right-hand side part of the compressor. Therefore, the right-hand side channel is less loaded and it transports only 42% of the overall mass flow. Figures 8 and 9 show clear difference in the flow pattern between these two sides of the compressor. On meridional planes, located in the middle of each channel, an absolute dimensionless velocity, C_m/U_2, for the splitter-blade configuration is plotted. Figure 10 shows flow field plotted at the cross section plane located downstream the splitter blade leading edge, and in case of non-splittered solution, in the corresponding distance from the inlet. The wake generated at the splitter blade is clearly seen as it occupies around 30% of the right-hand side flow duct of the splittered blade impeller.

Less uniform and stable flow for splittered version of the compressor leads to lower total pressure ratio achieved at the exit of the splittered impeller. Moreover, this situation is accompanied by worse isentropic efficiency, which dropped from 0.839 for the non-splittered impeller to 0.817 for the splittered compressor. Slight distinctions can be noticed in relative and absolute outlet Mach numbers which in the non–splittered compressor are bigger due to less perturbation and mixing losses. More surprising differences can be observed in the flow angles values. For impeller without splitter blade absolute and relative flow angles are 9 and 1.6 degrees greater, in respective order. It implies changes in rotor-diffuser interaction, and hence difference in the flow angles should be taken into account during designing of succeeding diffuser.

Table 3. Global flow parameters for splittered and non–splittered compressor stage

Flow parameter	Splittered impeller	Non-splittered impeller
p_{t1} [kPa]	101300	101300
T_{t1} [K]	288	288
p_2 [kPa]	185737	185675
p_{t2} [kPa]	374679	382660
T_2 [K]	367.6	364.2
T_{t2} [K]	448	446.8
M_2	1.046	1.064
β_2 [deg]	-32.2	-30.6
α_2 [deg]	45.4	54.7
$\Delta\beta_2$ [deg]	23.8	25.4
$\dot{m}$ [kg/s]	1.68	1.88
Θ_{rev}	$2.814e^{-4}$	$3.149e^{-4}$
$\pi = p_{t2}/p_{t1}$	3.7	3.78
$\tau = T_{t2}/T_{t1}$	1.555	1.551
η_{isen}	0.817	0.839
η_{poly}	0.847	0.866

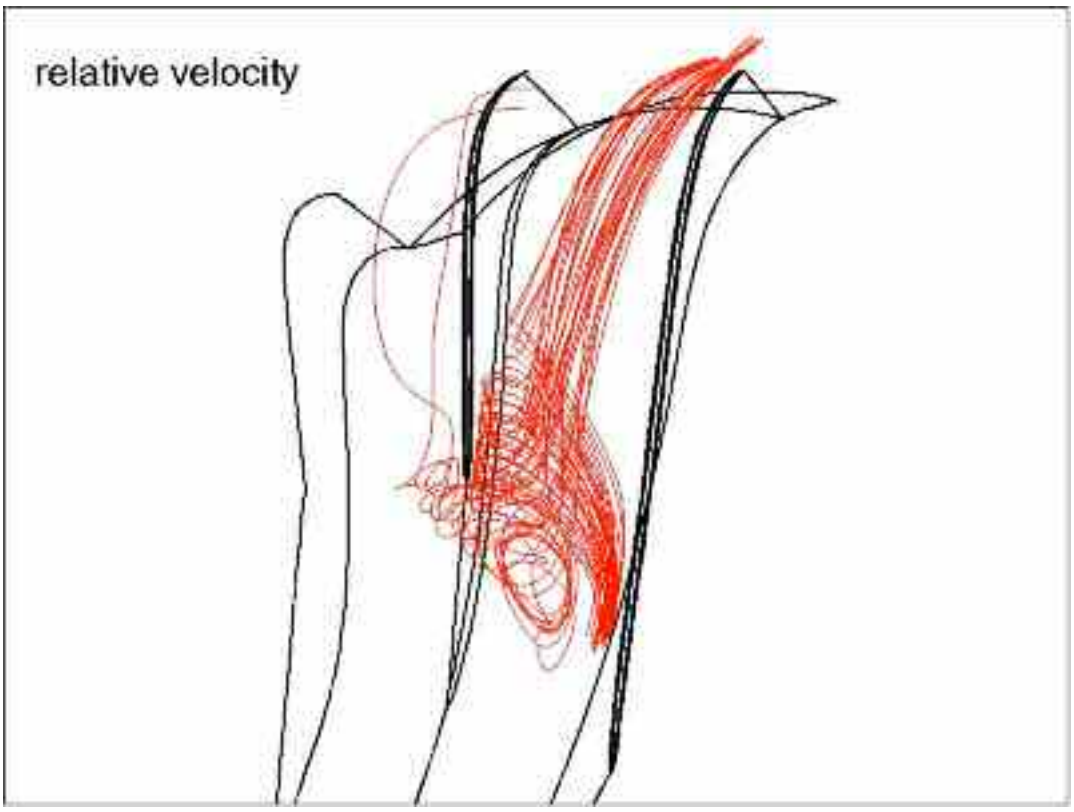

Figure 7. Swirl at the splittered compressor inlet

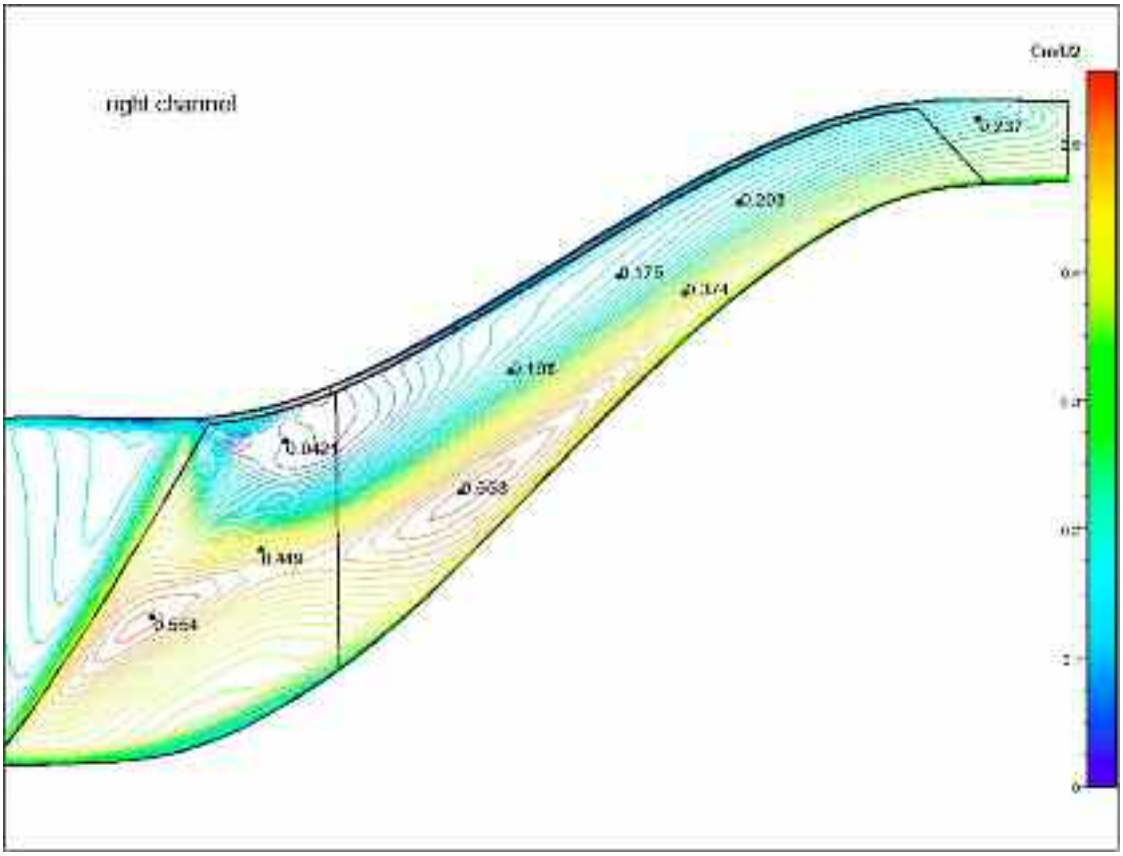

Figure 8. Flow pattern in the right-hand side channel of the splitter-blade impeller

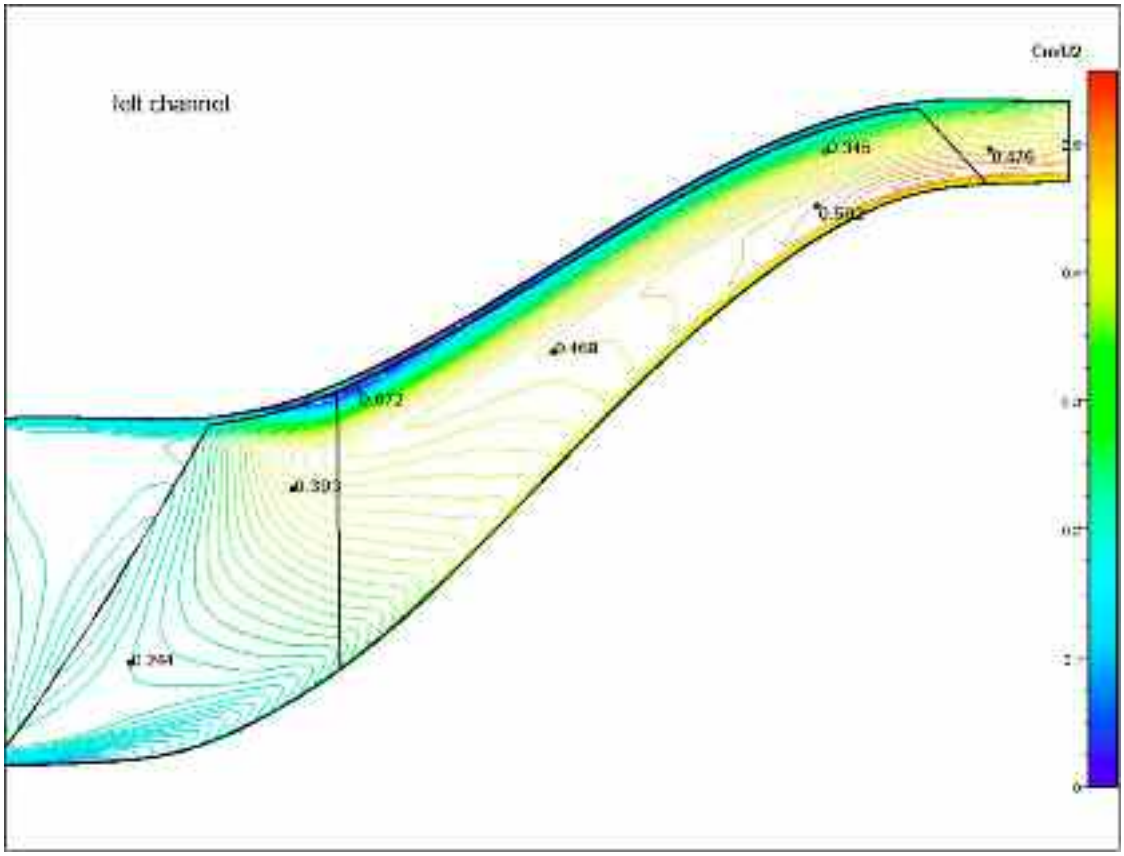

Figure 9. Flow pattern in the left-hand side channel of the splitter-blade impeller

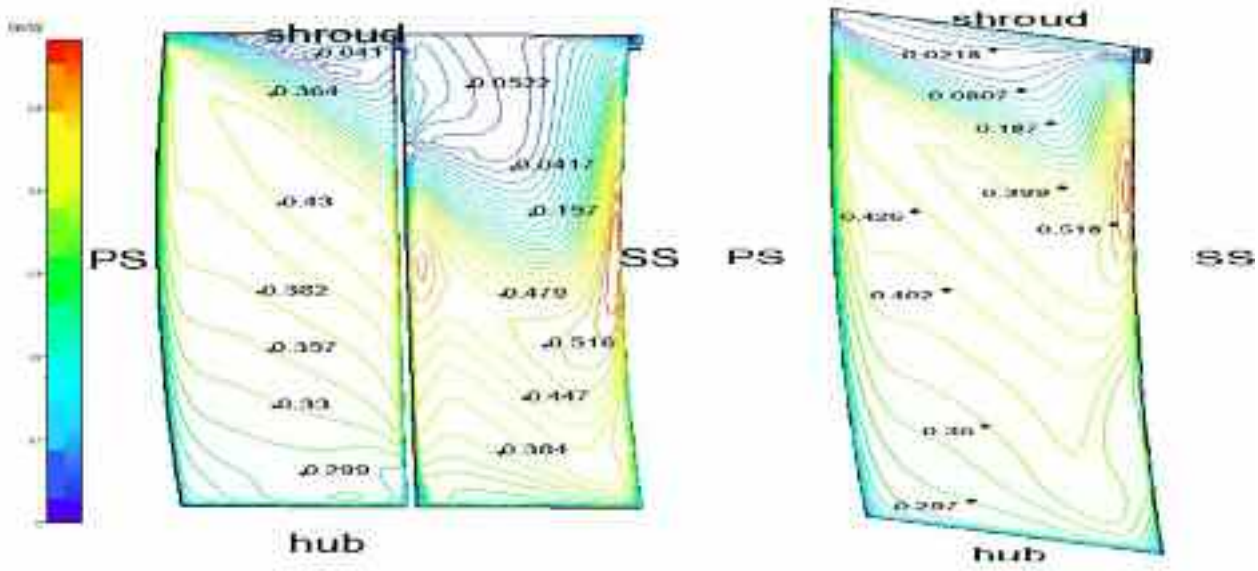

Figure 10. Flow pattern in cross-section of the impeller for splittered (left) and non-splittered (right) compressor stage. PS – pressure side; SS – suction side

6. TIP CLEARANCE EFFECT FOR NON-SPLITTERED COMPRESSOR

The numerical tests of the tip gap influence were done for the previously investigated non–splitter blade mixed-flow compressor stage with 18 blades and basic tip clearance of 0.6 mm.

The seven different values of the clearance gaps were examined. They were ranging between 0.0 and 1.0 millimetre (0.0, 0.1, 0.2, 0.4, 0.6, 0.8 and 1.0 mm). Regarding design conventions, the values were expressed in percents of blade height at outlet and were contained within 0 to over 15% of blade height.

Figure 11 reveals stagnation pressure contours at the impeller outlet for different clearances. The profile is plotted from shroud to hub. Significant decrement of the pressure magnitude from 450kPa to 390.2kPa with tip clearance rising is observed. Moreover, peak of the pressure value is shifting from the shroud towards to the centre of the channel. Slope of the pressure contour becomes steeper with higher negative gradient in hub direction. This clearly proves that flow path is affected not just near the shroud, as might be expected, but right across the passage.

Figure 12 illustrates pressure ratio change due to tip clearance rise. Again, evident linear drop in pressure ratio value from 4.1 to 3.67 can be noticed.

Figure 13 reveals values of isentropic efficiency. For tip clearance rising from 0.0 to 1.0 mm (0–15% of blade height) isentropic efficiency drops by over 7. The tendency of the function clearance–efficiency is almost linear, what agrees with literature. Moreover, the efficiency decrease rate confirms general rule, which states, that one point of stage efficiency is lost for an increment of passage clearance which is equal to 3% of the passage height at impeller discharge [4].

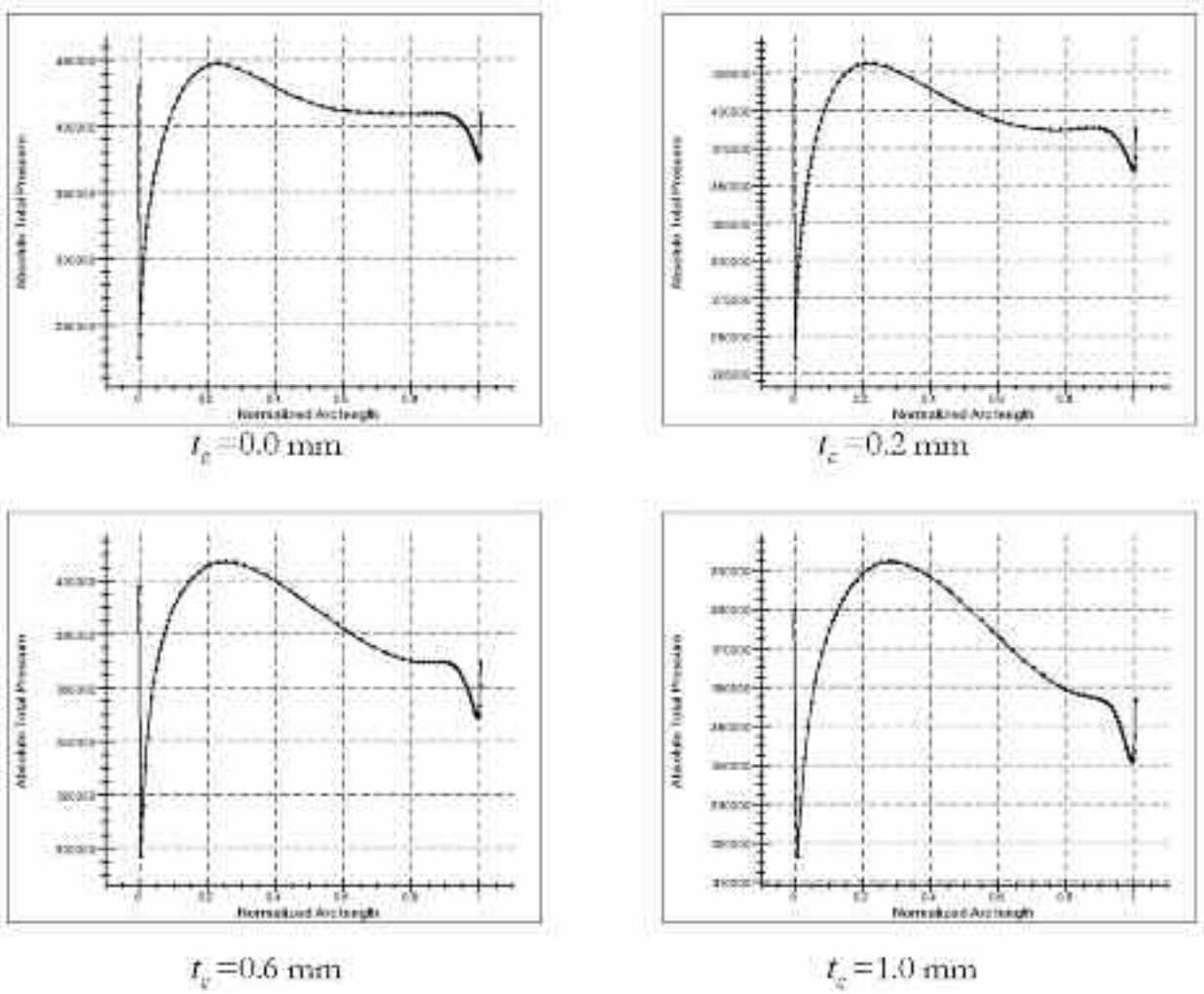

Figure 11. Total pressure profile at the impeller outlet for different tip clearances t_c

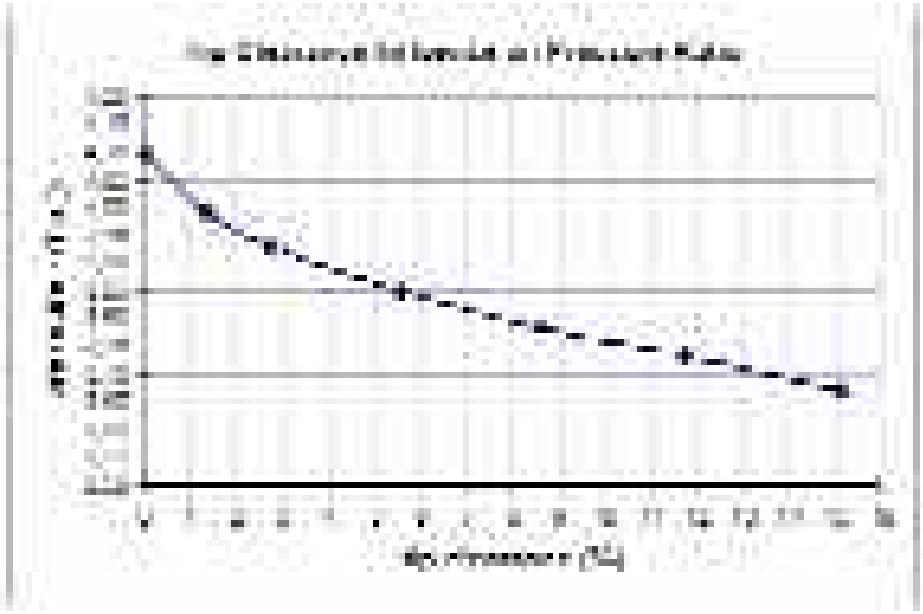

Figure 12. Pressure ratio for different tip clearance in non-splittered compressor

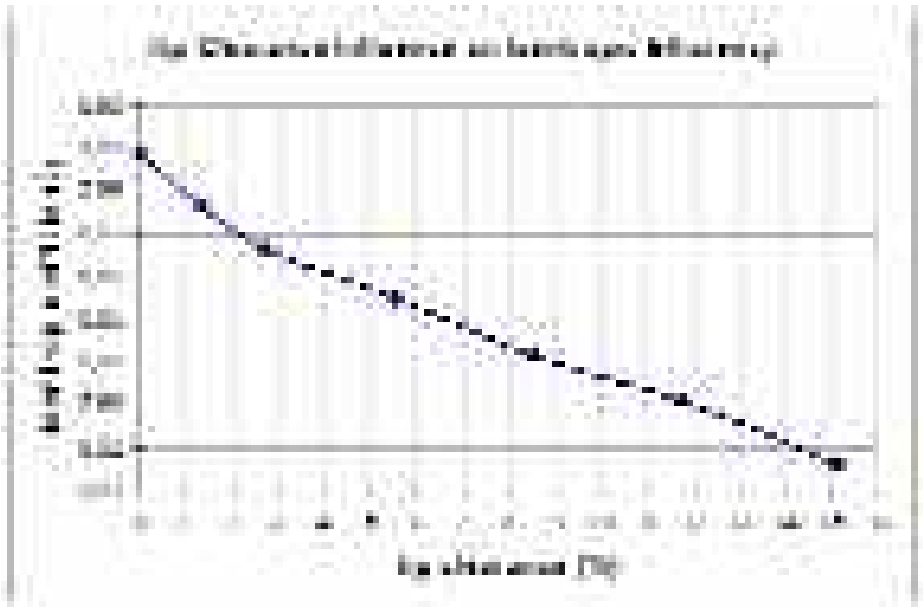

Figure 13. Influence of tip clearance on isentropic efficiency

7. COMPRESSOR MAP TO CHOKE

The model was the non–splitter centrifugal compressor stage with tip clearance 0.6mm and maximum pressure ratio of 3.85:1 and mass flow rate 1.88kg/s for 45000RPM.

In Figure 14 corrected mass flow rate and total pressure ratio are plotted versus downstream static pressure. At the beginning of decrease of the static pressure, the mass flow rate raises with high gradient. With further drop of backpressure the slope of the mass flow rate becomes less steep. Finally, in the range of 150 down to 125kPa, the rise of the flow rate is insignificant, reaching magnitude of 2.26kg/s. At the same time, pressure ratio drops with almost linear function, from 3.88:1 to 3.6:1. For the lowest, critical outlet static pressure of 125kPa, a supersonic flow occupies significant part of the blade channel. The outlet of the impeller is completely blocked by supersonic flow (Figure 15). Complete compressor choke map is presented in Figure 16. It reveals nonlinear relation between mass flow rate and pressure ratio, known from turbomachinery theory. The satisfying pressure ratio is achieved for mass flow not higher than 2.15kg/s. Above this value pressure ratio decreases drastically with important increment of deficiency.

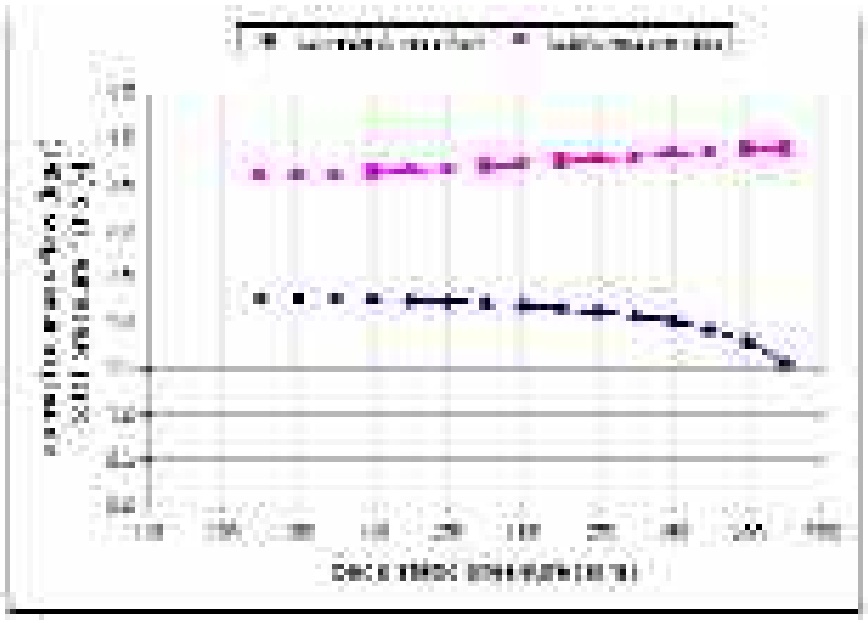

Figure 14. Mass flow and total pressure ratio as a function of backpressure

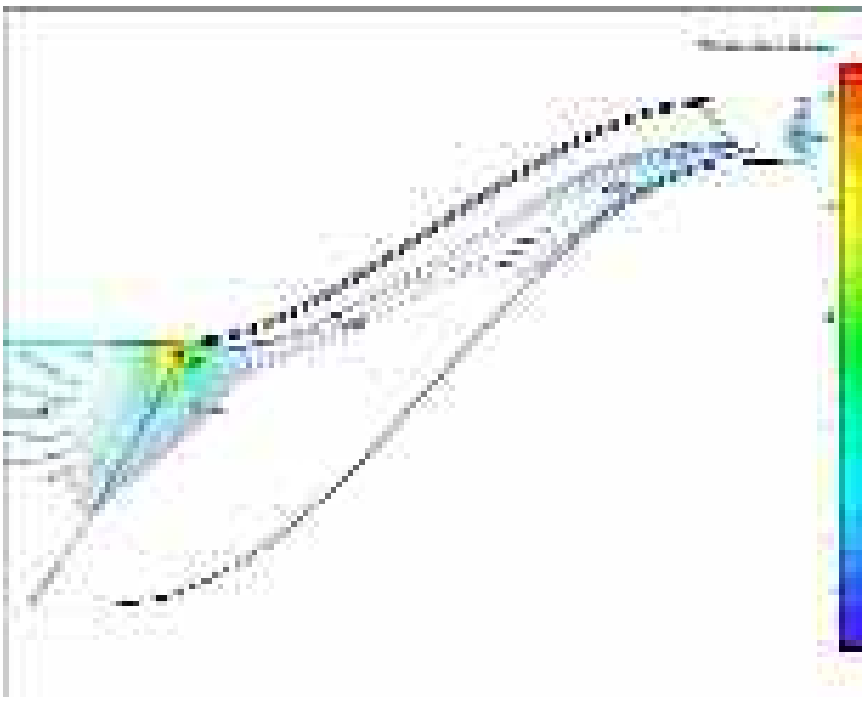

Figure 15. Critical conditions at the impeller outlet

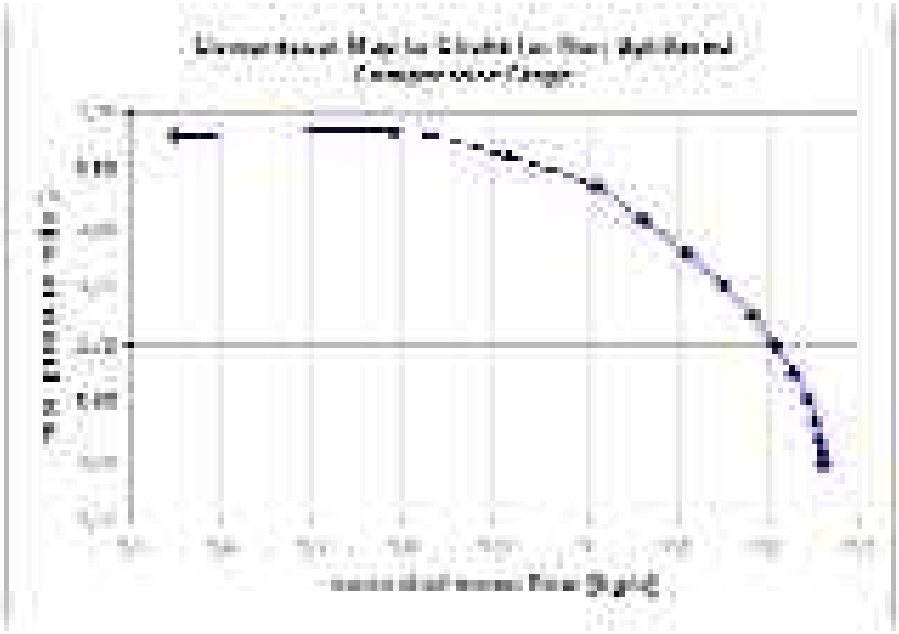

Figure 16. Compressor map to choke for the splittered compressor wheel

8. CONCLUSIONS

During this project several important compressor design issues were addressed. As a result of the initial modification of the centrifugal compressor, splitter blade has been removed. Numerical analysis proved better performance of the non-splittered version. Presence of splitter blade in the flow duct caused disturbed and swirled flow implying significant difference between divided flow passages. This effected lower pressure ratio and mass flow rate. The next improvement regarded to reduction of clearance on the blade tip. The relevant computations showed lower efficiency with increasing tip gap due to increased mixing losses and swirled flow within tip clearance. Linear relation between efficiency loss and tip clearance, obtained in numerical calculations, agreed with turbomachinery theory. The last stage of mixed-flow compressor CFD study provided choke flow predictions. By controlling outlet boundary conditions, a higher mass flow rate through the compressor was produced. As the effect of higher mass flow rate, the relative Mach number reached unity at the geometrical throat of the blade passage and choke flow occurred. Presented relations between mass flow rate and pressure ratio enabled to define upper limitations of stable operating range for the designed compressor.

List of Symbols

C	absolute velocity,
C_m	absolute meridional velocity,
C	absolute tangential velocity,
W	relative velocity,
W_m	relative meridional velocity,
W_θ	relative tangential velocity,
U	blade tip velocity,
h_0	stagnation enthalpy,
L	specific work,
T	static temperature,
T_0	stagnation temperature,
p	static pressure,
p_0	stagnation pressure,
γ	specific heat ratio,

M absolute Mach number,
η efficiency,
π pressure ratio,
τ temperature ratio,
N dimensionless speed,
Θ non-dimensional mass flow,
α absolute flow angle,
β relative flow angle,
β_b blade angle,
$\Delta\beta$ slip angle,
t_c tip clearance.

BIBLIOGRAPHY

[1] Cumpsty N.A., "Compressor Aerodynamics", Longman Scientific and Technical, 1989
[2] Japikse D. and Baines N.C., "Introduction to Turbomachinery", Concept ETI, Inc. and Oxford University Press, 1997
[3] Japikse D., "Centrifugal Compressor Design and Performance", Concept ETI, 1996
[4] Japikse D., "Decisive Factors in Advanced Centrifugal Compressor Design and Development", Concepts ETI, Inc. paper
[5] Krain H., "Flow in Centrifugal Compressors. Experimental Observation of the Flow in Impellers and Diffusers", Von Karman Institute for Fluid Dynamics. Lecture Series 1984-07, May 1984
[6] Fagana J.R. and Fleeter S., "Impeller Flow Filed Measurement and Analysis", The American Society of Mechanical Engineers paper 90-GT-146
[7] Krain H., Hoffmann B. and Pak H., „Aerodynamics of a Centrifugal Compressor Impeller with Transonic Inlet Conditions", the American Society of Mechanical Engineers paper 95-GT-79, 1995
[8] Witfield A. and Baines N.C., "Design of Radial Turbomachines", Longman Scientific and Technical, 1990

B. Bogucki

ANALIZA NUMERYCZNA PRZEPŁYWU W STOPNIU SPRĘŻARKI OSIOWO-PROMIENIOWEJ SAMOLOTU BEZZAŁOGOWEGO

Streszczenie

Sprężarki odśrodkowe, które straciły w ostatnich dekadach swoje zastosowanie w silnikach wojskowych samolotów załogowych, są często stosowane przy napędzie małych samolotów bezzałogowych. Ich relatywnie duży stopień sprężania z jednego stopnia przy jednocześnie małych wymiarach, umocniły ich pozycję w nowoczesnych konstrukcjach małych statków powietrznych. Przy dążeniu do poprawienia ich sprawności, konstruktorzy ciągle napotykają szereg niestacjonarnych i nieliniowych zjawisk, które wymagają ustawicznych badań.

Projekt prezentowany w tej pracy został przeprowadzony na uczelni Ecole Nationale Supérieure d'Ingénieurs of Constructions Aéronautiques (ENSICA) w Tuluzie, w ramach programy rozwoju silnika do samolotu bezzałogowego. Prace były współ prowadzone przez Wydział Mechaniki Płynów z tejże uczelni oraz przez firmę JPX z Francji. Celem pracy było przeprowadzenie analizy numerycznej rozwiązań konstrukcyjnych zaimplementowanych w sprężarce osiowo-promieniowej silnika T100 o ciągu 100kN.

COMPUTER METHODS IN OPTIMALIZATION OF FIBER COMPOSITES STRUCTURE

Katarzyna Haintze
Institute of Aviation

Summary

Composite materials are currently the most dynamic area of the modern engineering industry. Engineers around the world are trying to improve the composites performance to fulfill the requirements of modern constructing. Due to the existing optimization algorithms and computer tools, there is a huge potential in this area. The following article covers a study of the fiber composites optimization using the computer methods both in micro and macro scale. The results of computer analysis have been compared with the well-known analytical models.

1. INTRODUCTION

Due to coupling of FEM (Finite Element Modeling) and optimalization algorithms, it is possible to perform calculations in order to determine the best construction, and not only to analyze. Composites mechanics [11] is one of the most interesting fields, in which such method can be applied. Optimalization designing can refer to the composites in both scales − micro (representative volume element's structure) or macro (the structure of laminate, the shape of constructing element).

The homogenization of a layer's features is a part of the computer assisted designing. The material properties of a layer − considered as homogeneous orthotrophy material − result from the parameters of each components shapes and features. The number of layers, their thickness and the way they are combined influence mechanical properties of the multilayer constructing elements. Design variables, such as parameters determining the composite's structure or material properties, are part of the data used in the optimalization process. The most desirable combination of design variables results in the minimal value of the function of goal. The function of goal represents the features of particular structure. It is defined in the way that its reduction results with an improved quality.

The optimalization analysis has been performed on a laminate shell and multilayer cylindrical shell examples. The results show that the FEM simulation models are useful for designing of composites structures. The results of the optimalization process depend on many factors and require multiple analyses with varying start parameters and convergence criteria. Verifying the obtained solutions is also crucial.

The fiber reinforced metal matrix composites are becoming more and more popular theses days [8, 9]. It is due to their particular physical and strenght properties. The following features: good resistance to axial tension, modulus of rigidity, electrica and thermal conductivity, determine possible functionnality/application of the composities. However, due to relatively high production costs, the composites are only being used in construction elements, when financially viable.

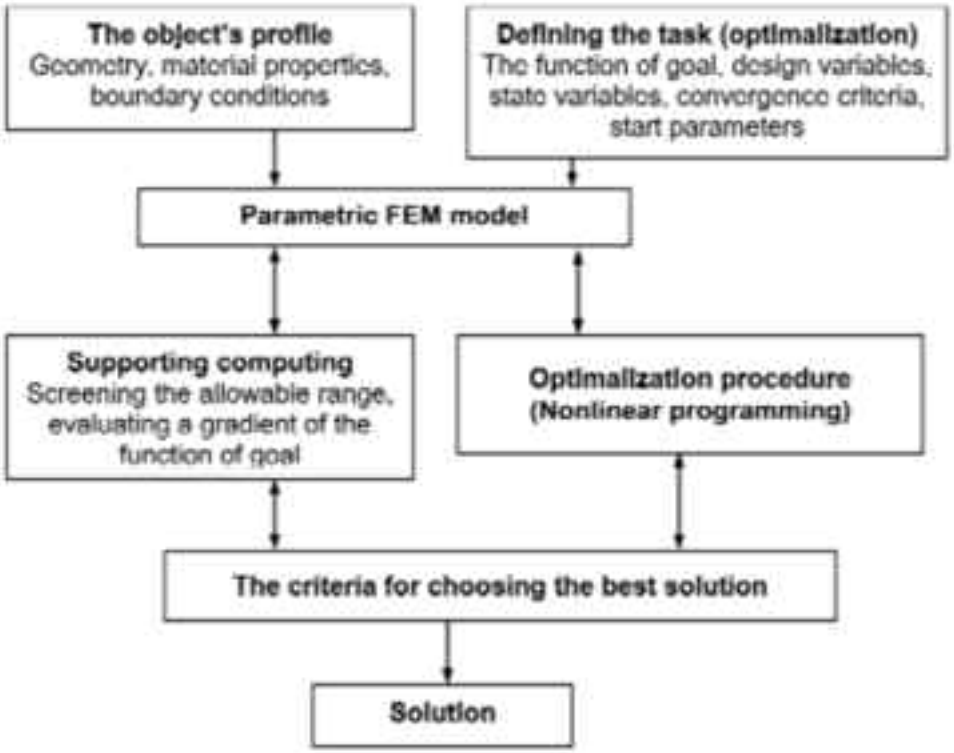

Fig. 1. Final element modeling and optimalization algorithms in the computer assisted designing of composites

Final element modeling method [3] is widely implemented for the analysis of properties and resistance of the composites' structures. Fields of stresses, strains, heat transfers, electric and magnetic field, as well as coupled fields are analyzed [2, 4, 5, 6, 7].

It is highly probable, that computer methods will be commonly used in engineering, not only to analyze particular structures, but also to design them.

2. PARAMETRICAL OPTIMALIZATION ALGORITHMS

The implementation of both FEM and numeric optimalization techniques is possible on the condition of building a parametric FEM model. The parametric process consists of three stages: preprocessing, solution and post processing. Such procedure is an iterating process. The design variables are different for each iteration; however they are being determined according to one optimalization algorithm. All possible parameters defining the shape of the object, material properties, constrain or loads conditions can make for the design variables. Design variables' vector is expressed as: $x=[x_1,x_2,...,x_n]$. Possible criteria of the function of goal $f=f(x)$, could be as follows: minimum of stresses, minimum of volume or minimum of weight etc.

The allowable range X can be defined by determining the minimal and maximal values of design variables or by physical parameters of the modeled object.

$$x_i^* \le x_i \le x_i^{**} \quad (i=1,2,...,k), \quad w_i^* \le w_i(x) \le w_i^{**} \quad (i=1,2,...,m) \tag{1}$$

The allowable range of solutions is a set of points in n-dimensional Euklidean space, corresponding with the above- mentioned conditions.

$$x \in X, \quad X \subset R^n$$

The function of goal is becoming close to the minimum for the subsequent iterations. The process of iteration calculations stops, when the vector of current design variables $x^{(j)}$ is within allowable range and all predefined conditions are met.

$$\left|f^{(j)} - f^{(j-1)}\right| \le \tau, \quad \left|x_i^{(j)} - x_i^{(j-1)}\right| \le \rho_i \quad (i=1,2,3,...,n) \tag{2}$$

In order to find the minimum of the function of goal, gradient and non gradient methods of the nonlinear programming are being applied [10]. The optimalization process of a construction, performed with the use of complex FEM models made of huge number of finite elements, requires significant expenditure of numeric computing/is related with serious numeric costs. Therefore in order to increase effectiveness of the analysis, FEM equations are being used for fast evaluation of the gradient of function of goal (by examining in what way the solution changes, depending of variations of design variables). Parametric FEM models be effective tools for designers (Fig. 1). The supporting computing includes:

- A separate analysis of a specified set of design variables. Such computing can be performed for any allowable *x* vector.
- Evaluation of the gradient. There is a special procedure to calculate the gradient of function of goal for a given *x* vector. The procedure shows to what extend the function is sensitive to the alteration of x_i parameter.
- Screening the allowable range, either randomly or by altering one of the variables. Assuming the rest of variables is predefined.

All of the above techniques are useful for optimalization method and its particular parameters (start point, primal step, criteria of convergence). They are also helpful, when optimalization is particularly difficult. The best solution is being chosen from/within the results of supporting computing. The analysis presented in this thesis was performed, using Ansys FEM program (in Ansys Parametric Design Language).

3. PARAMETRIC MODELS OF REPRESENTATIVE VOLUME ELEMENT OF THE COMPOSITE

Resultant coefficient of rigidity for the complex and non homogeneous structures can be estimated using theortical formulas or numerical computing. The computing can be performed for RVE, loaded with subsequent component of stress. Representative volume is the smallest hording fragment of the composite. The fragment, analysed under the right boundering conditions (load, constrain), allows to evaluate the stress in micro scale, as well as the composite's properties in a macro scale.

Examples of models used for evaluation of composite's resultant ellasticity coefficients are shown on the Fig. 2.

Knowing the components of stress, the element is exposed to and having obtained components of strain, it is possible to evaluate elements of the matrix of elasticity coefficients from constitutive equation:

$$\varepsilon_i = S_{ij}\sigma_j \quad (i, j = 1, 2, \ldots, 6) \tag{3}$$

where: ε_i – stands for components of strain, σ_j – stands for components of stress, S_{ij} – matrix of vulnerability [1].

The following start values of geometrical parameters were assumed (Fig. 2):
$X_1 = r = 0.7$[mm], $X_2 = a = 0.15$[mm], coordinate axe *y*: $X_3 = b = 0.15$[mm], $c = 2a = 0.3$[mm].
The volume contribution of fiber in this case is:

$$V_f = \frac{0.5\pi r^2}{ab} = \frac{0.5\pi \cdot 0.07^2}{0.15 \cdot 0.15} = 0.34208$$

The following properties of material were assumed:

Copper: $E_m = 126\,086$[MPa], $v_m = 0.32$;
Silicon and carbide fiber: $E_f = 413807$[MPa], $v_f = 0.16$.

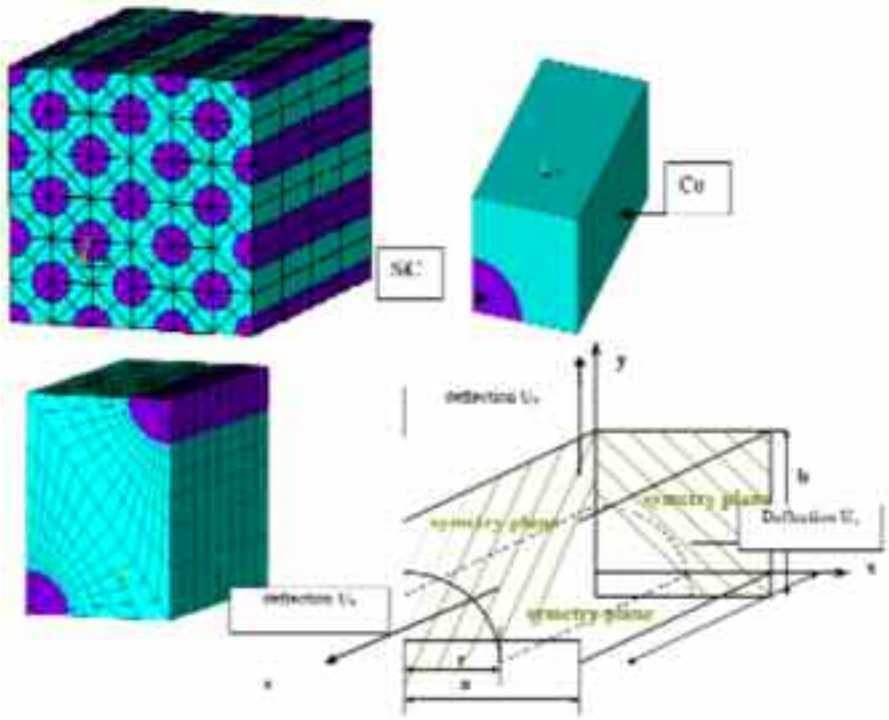

Fig. 2. Hording RVE and the bounding condition in FEM analysis

Subsequent simple loads, corresponding to the stretching σ = 100[MPa] on the three coordinate axes x, y and z, and to the shearing in three perpendicular planes, allow to identify stress and strain fields (Fig. 3, 4).

Table 1 shows the resultant coefficients estimated for the assumed values. The resultant coefficients can be evaluated by using theoretical formulas, however the accuracy of results may not be precise enough.

Building a parametrical model helps to estimate the sample's performance, contingent on particular parameters of the composite's structure. (Fig. 5, 6, 7). The results show (Fig. 6, 7) that increased fiber volume contribution leads to reduction of stress in both, the fibers and the matrix.

Table 1. Calculated resultant elasticity coefficients

	Theoretical model	FEM model
E_z[GPa]	224.5	225.6
E_x[GPa]	165.4	177.7
E_y[GPa]	165.4	177.7
$\nu_{zx}=\nu_{zy}$	0.27	0.26
$\nu_{xz}=\nu_{yz}$	0.19	0.20
$\nu_{xy}=\nu_{yx}$	0.24	0.35
G_{xy}[GPa]	63.7	71.4

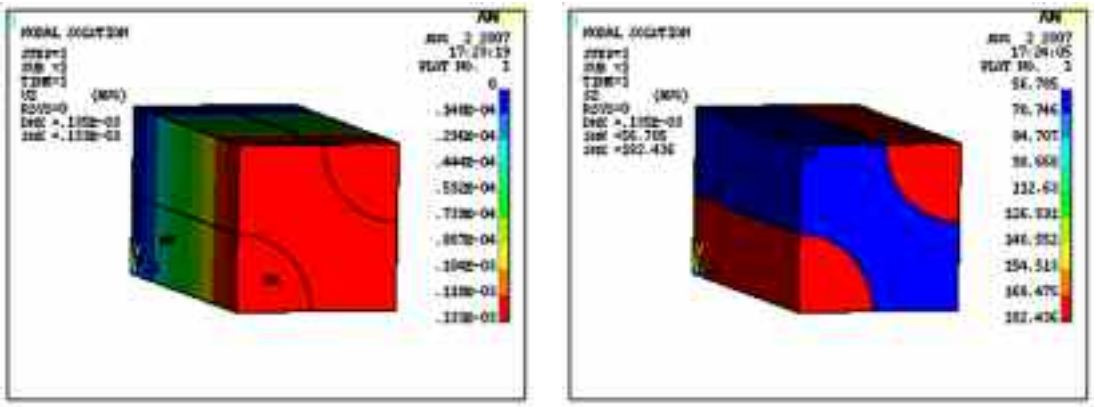

Fig. 3. Axial tension test (fiber direction) σ_z = 100[MPa] – distribution u_z[mm] and σ_z[MPa]

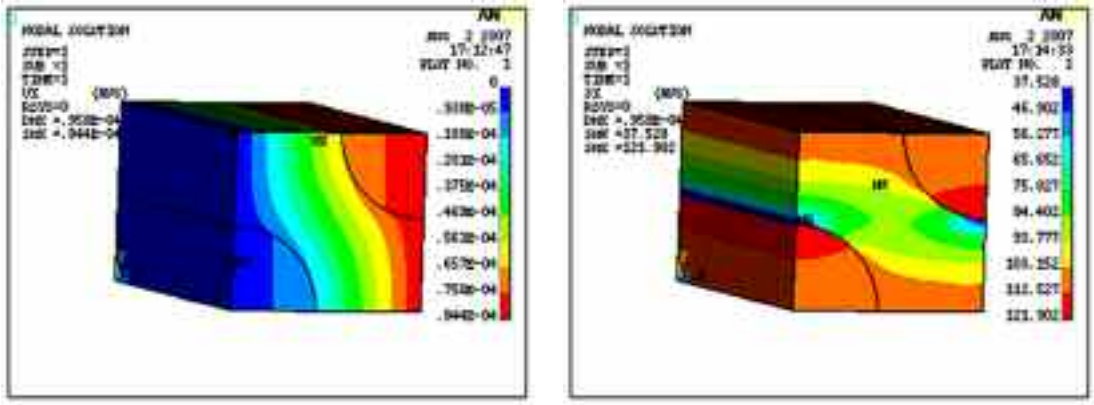

Fig. 4. Axial tension test (fiber direction) σ_x = 100[MPa] – distribution u_x[mm] and σ_x[MPa]

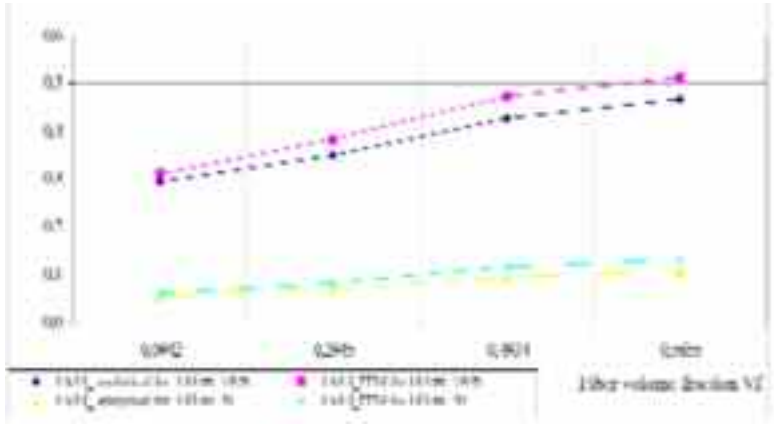

Fig. 5. Function of E_x/E_f to the fiber volume contribution for different proportions E_f/E_m

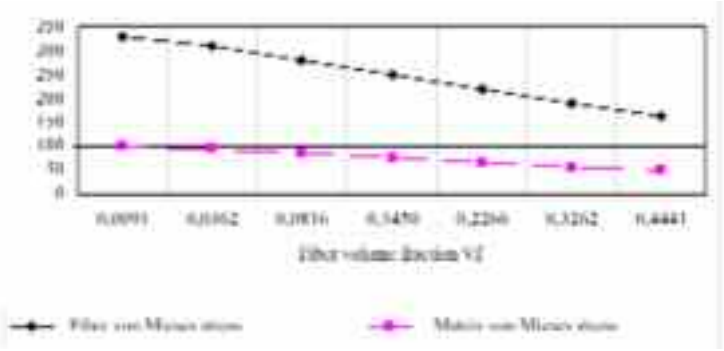

Fig. 6. Function of von Mieses stress in fiber and matrix to fiber volume contribution – Axial tension 100[MPa]

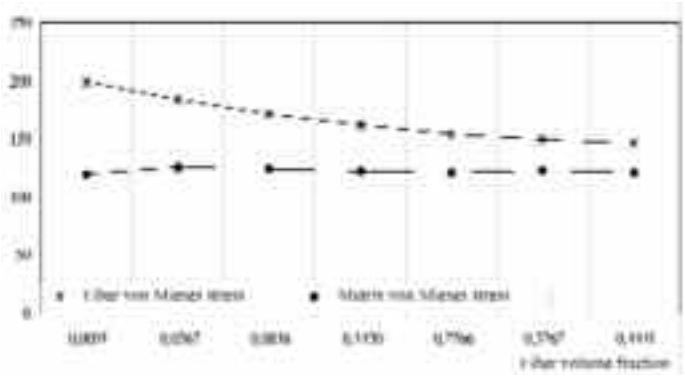

Fig. 7. Function of von Mieses stress in fiber and matrix to fiber volume contribution – diagonal tension 100[MPa]

4. THE EXAMPLES OF APPLIANCE OF NON LINEAR PROGRAMMING FOR DESIGNING OF THE COMPOSITE'S STRUCTURE

4.1. Validation of the numerical model of a laminate

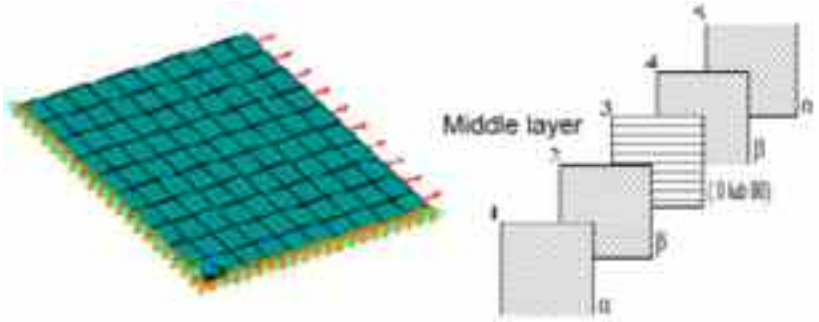

Fig. 8. Model of a 5-layers plate

The following geometrical parameters and material properties of the multilayer plate were assumed for computing (Fig. 8):

width: a = 20[mm],
height: b = 20[mm],
tightness of the laminate: t = 5[mm],
number of layers: n = 5,
longitudinal Young modulus: E_x = 225.6[GPa],
diagonal Young modulus: E_y = 177.7[GPa],
Poisson's coefficient: v_{xy} = 0.26,
coefficient of rigidity: G_{xy} = 71.4[GPa].

The laminate plate was loaded with continuous loads q = 100[kN/m] in direction of x axial. The properties of laminate can be determined, basing on the previously evaluated properties of a single layer.

Table 2. The table shows the summary of results from analytical and FEM analysis – 2D laminate model (layers' sequence 90°, 0°, 90°, 0°, 90°)

	Theoretical stress values		Numerical stress values	
Layer	0°	90°	0°	90°
σ_x[MPa]	23.07	17.95	23.08	17.95
σ_y[MPa]	0.67083	–0.44732	0.6889	–0.4593

4.2. The optimalization of layers' sequence in a multilayer plate

The angles of fibers in a single layer were variables in the parametric model of a laminate plate:

1. $x_1 = \alpha$,
2. $x_2 = \beta$,
3. 0,
4. $x_2 = \beta$,
5. $x_1 = \alpha$.

For this kind of model, each element of the solution can be considered a function of two arguments $f(x_1,x_2)$. A series of optimalization computing was performed, using gradient and non gradient methods. (respectively: Subproblem Approximation Method and First Order Method). The results were being analyzed, with regard to both: design variables and optimalization method. Minimal deflections were the function of goal. The Fig. 9 and 10 show the course and the results of optimalization computing of a simple tension of the plate.

The numeric computing results correspond with the assumption (fiber packing in the direction of tension). The function of goal (the deflection u_x) was reduced by 18% approx.

Table 3. The values of parameters before and after optimalization process of the stretched plate (Fig. 8)

Method	BEFORE OPTIMALIZATION			AFTER OPTIMALIZATION			Improvement [%]
	$X_1=\alpha$	$X_2=\beta$	$f=UX$ [mm]	$X_1=\alpha$	$X_2=\beta$	UX [mm]	
Gradient (Fig. 9)	80°	85°	0.00225	0°	0°	0.00185	17.65
Non gradient (Fig. 10)	80°	85°	0.00225	0°	0°	0.00185	17.61

The computing was repeated for different loads. The results corresponding with the two-directional loads (Fig. 11) are shown in Fig. 12, 13 and the Table 4. In this case both results are convergent; however the accuracy of the minimum of the function of goal is worst.

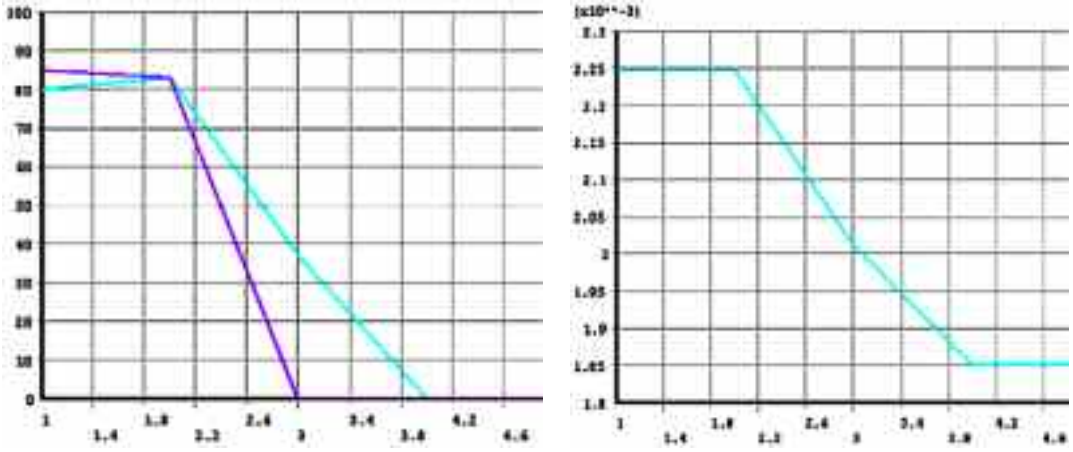

Fig. 9. The course of search for the minimum of deflection in the stretched laminate plate (Fig. 8): changes in angles of fibers in a single layer x_1, x_2 and corresponding alternations of the function of goal $f(x_1,x_2) = \max u_x$. Gradient method

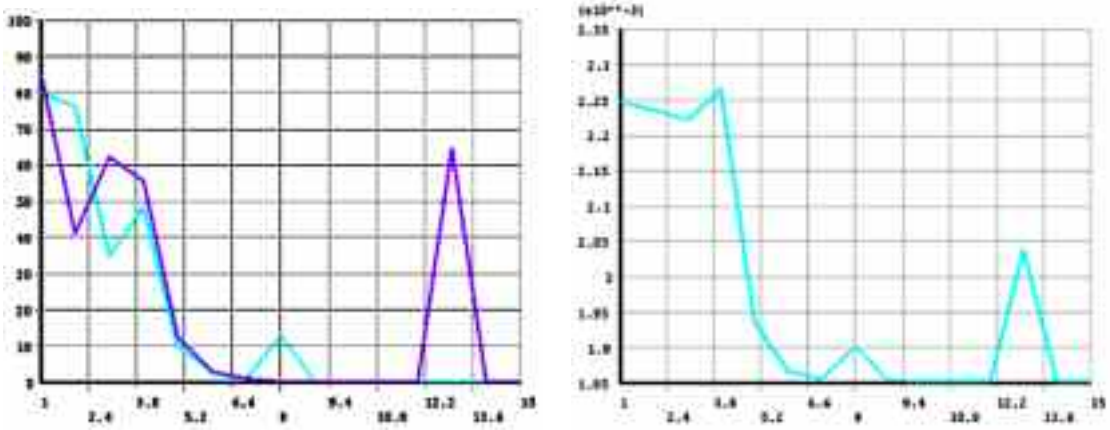

Fig. 10. The course of search for the minimum of deflection in the stretched laminate plate (Fig. 8): changes in angles of fibers in a single layer x_1, x_2 and corresponding alternations of the function of goal $f(x_1,x_2) = \max u_x$. Non gradient method

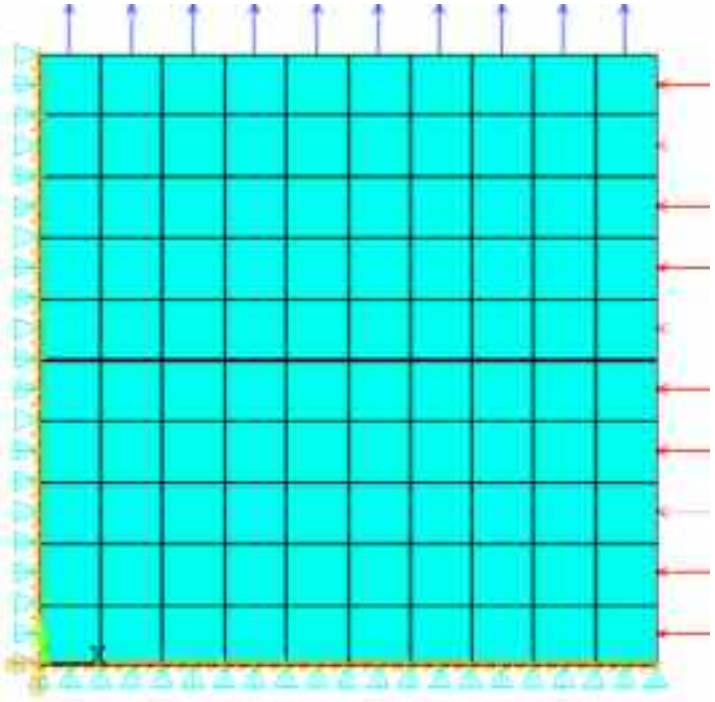

Fig. 11. Two-directionally loaded multilayer plate ($q_x = -100$[kN/m], $q_y = 100$[kN/m])

Table 4. The values of parameters before and after the optimalization process of two-directionally loaded plate (Fig. 11)

Method	BEFORE OPTIMALIZATION			AFTER OPTIMALIZATION			Improvement [%]
	$X_1=\alpha$	$X_2=\beta$	$f=UX$ [mm]	$X_1=\alpha$	$X_2=\beta$	UY [mm]	
Gradient (Fig. 12)	5°	85°	0.005	53°	53°	0.00037	25.18
Non gradient (Fig. 13)	5°	85°	0.005	56°	55°	0.00037	25.01

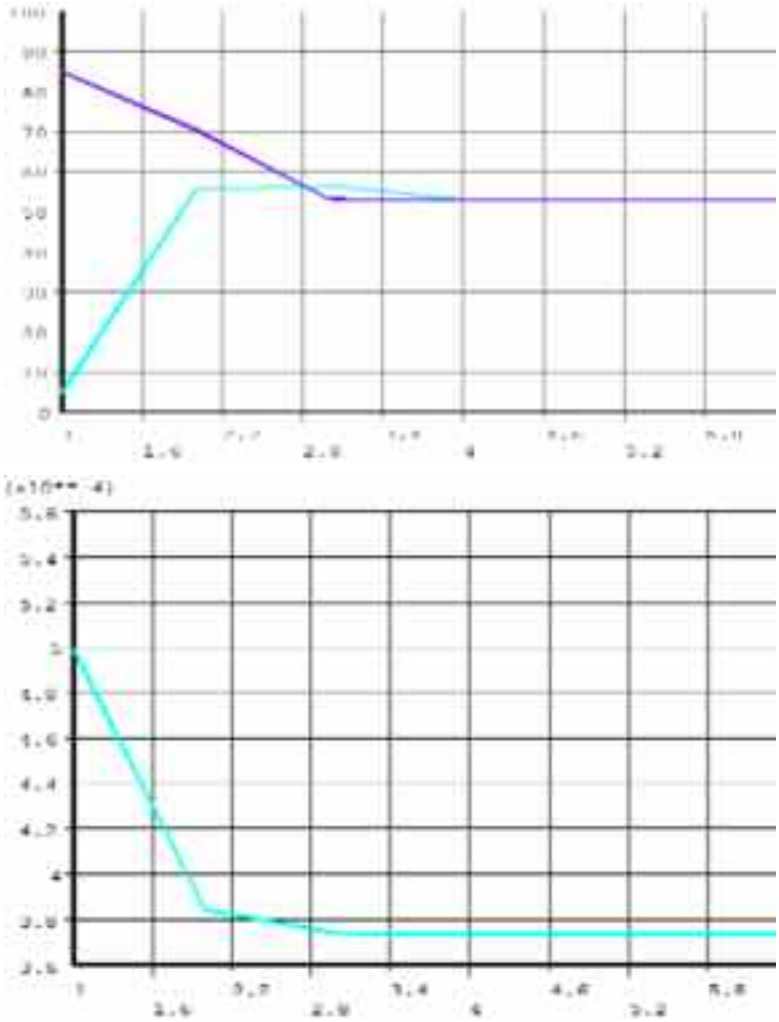

Fig. 12. The course of searching for the minimum of deflection in the stretched laminate plate (Fig. 11): changes in angles of fibers in a single layer x_1, x_2 and corresponding alternations of the function of goal $f(x_1,x_2) = \max u_x$. Gradient method

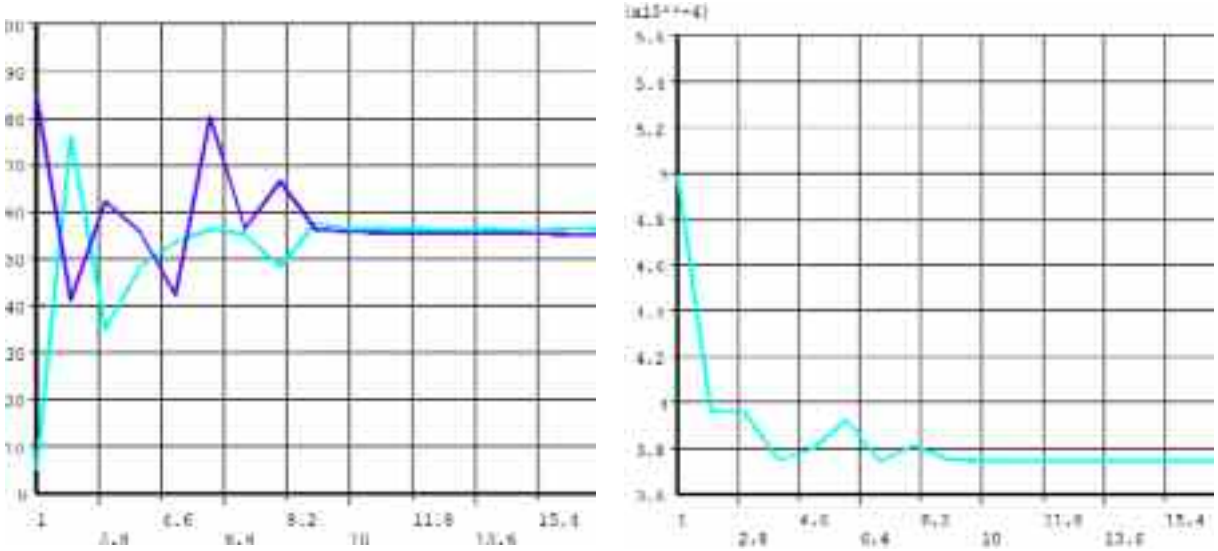

Fig. 13. The course of search for the minimum of deflection in the stretched laminate plate (Fig. 11): changes in angles of fibers in a single layer x_1, x_2 and corresponding alternations of the function of goal $f(x_1,x_2) = \max u_x$. Non gradient method

4.3. The optimalization of the layers sequence in cylindrical shell

The computing was repeated for different loads. In the following section, the authors present results of search for the minimal value of twist angle. The structure and properties of the laminate are the same as in case of other examples.

The results corresponding with the two-directional loads (Fig. 11) are shown in Fig. 12, 13 and the Table 4. In this case both results are convergent; however the accuracy of the minimum of the function of goal is worst.

For the balanced distribution of the twist moment in a form of coupled forces, a "stiff rib" was joint to the model (Fig. 14).

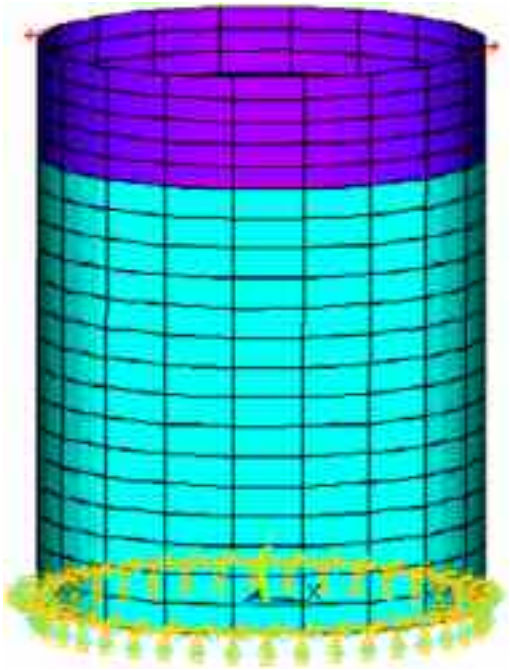

Radius: r = 20[mm]
Height: b = 20[mm]
Fig. 14. FEM model of multilayer model of a twisted cylindrical shell

The results are shown in Table 5 and in the Fig. 15, 16. In this case the vulnerability of function of goal (twist angle) to the variation of design variables was small. The differences in optimal results are due to lack of accuracy in numerical computing (different x_i after optimalization). The values of the function of goal are close to equal in both cases.

Table 5. The values of parameters before and after optimalization process of twisted cylindrical shell (Fig. 14)

Method	BEFORE OPTIMALIZATION			AFTER OPTIMALIZATION			Improvement [%]
	$X_1=\alpha$	$X_2=\beta$	$f=\varphi$ [mm]	$X_1=\alpha$	$X_2=\beta$	$f=\varphi$ [mm]	
Gradient (Fig. 15)	5	85	0.0581	36	0	0.05580	3.98
Non gradient (Fig. 16)	5	85	0.0581	37	18	0.05585	3.89

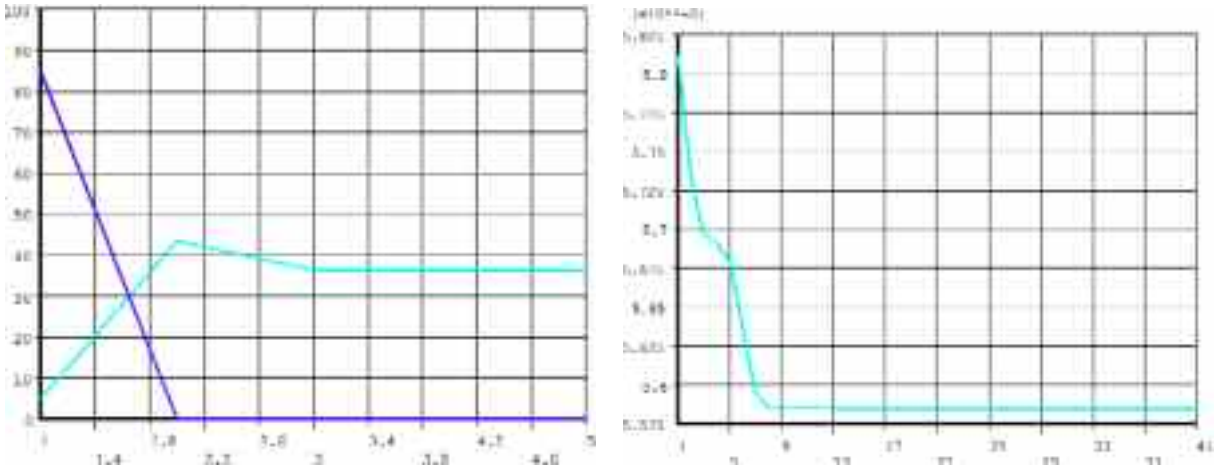

Fig. 15. The course of searching for the minimal angle of twist in cylindrical shell: changes in angles of fibers in a single layer x_1, x_2 and corresponding alternations of the function of goal $f(x_1,x_2) = \varphi = \max u_z/R$. Non gradient method

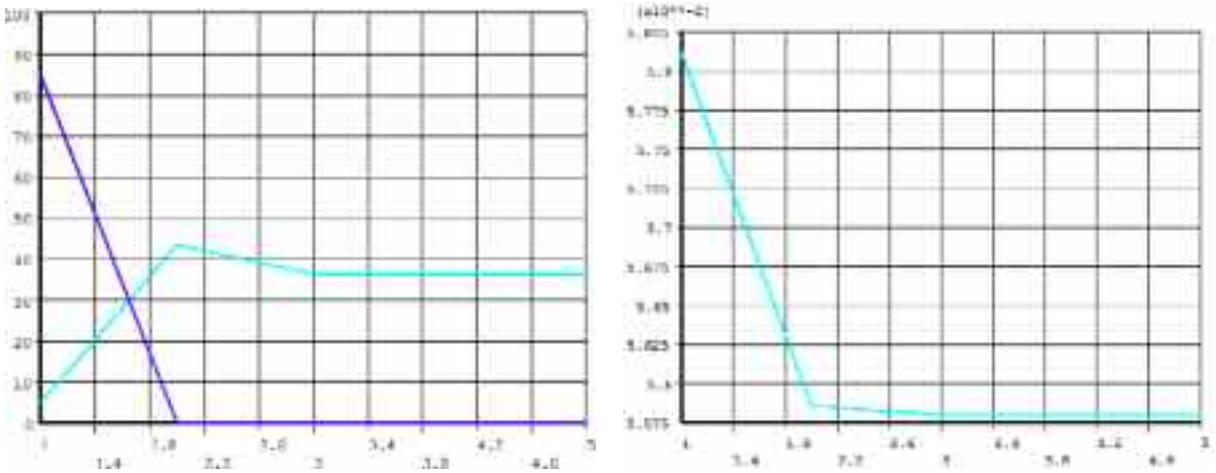

Fig. 16. The course of searching for the minimal angle of twist in cylindrical shell: changes in angles of fibers in a single layer x_1, x_2 and corresponding alternations of the function of goal $f(x_1,x_2) = \varphi = \max u_z/R$. Gradient method

5. CONCLUSIONS

The way of designing the composites is quite simple, in practice. It possible however, to obtain better results, using numeric methods for designing.

The FEM analysis method offers reliable results, in terms of both micro and macro scales. The examples presented in this thesis show significant utility of parametric FEM models.

The potential of analytical methods in terms of composites mechanics is limited to simple models. In such cases FEM results are similar to theoretical formulas. Numeric methods are irreplaceable when solving an engineering issue is necessary. Almost all of these issues are very complex cases.

It was proven, the theoretical formulas allow accurate evaluation of the average elasticity properties (e.g. resultant longitudinal Young modulus for the continuous fiber composite) and only approximate evaluation of other properties (resultant diagonal Young modulus, stress values). Parametric FEM models allow evaluate mechanical parameters with significant precision if refers the composite material's structure, as an element of construction.

The building of parametric FEM models offers more algorithmic approach to designing. An optimal structure of a composite element is defined by common procedures of non linear programming [10]. Designing with the use of numeric methods requires a critical approach to obtained results. The computing is vulnerable to streamlines in a model and to FEM desecrating. Moreover iteration techniques of optimalization lead to finding local minima for the function of

goal, instead of global minima, within the whole allowable range.

Therefore in order to make sure the obtained solution is correct, the optimalization process is repeated several times, for different values of parameters of optimalization process (Fig. 1).

BIBLIOGRAPHY

[1] Bijak-Żochowski M., Jaworski A., Krzesiński G., Zagrajek T.: Mechanika materiałów i konstrukcji, Tom 2, Oficyna Wydawnicza Politechniki Warszawskiej, Warszawa, 2006.

[2] Ciupiński Ł., Krzesiński G., Kurzydłowski K.: FEM modeling of residual thermal stresses in Cmm composites and their inluence on macroscopic properties in a tensile test, Third International Conference on Thermal Stresses, J.J. Skrzypek and R.B. Hetnarski (Eds), Cracow, 1999, pp. 553-557.

[3] Huebner K.H., Dewhirst D.L., Smith D.E., Byrom T.G.: The finite element method for engineers, J. Wiley & Sons, 2001.

[4] Krzesiński G., Dobosz R.: Wyznaczanie własności kompozytów warstwowych z zastosowaniem homogenizacji i MES, X SeminariumTworzywa Sztyczne w Budowie Maszyn, Kraków, 2003, s. 211-214.

[5] Krzesiński G., Ludwikowski T., Marek P., Zagrajek T.: Symulacja numeryczna zachowania się kompozytu metalowego o osnowie metalicznej w warunkach obciążeń cieplnych, Górnictwo odkrywkowe (2006), 5-6, 218-221.

[6] Krzesiński G., Zagrajek T., Marek P., Dobosz R., Czarkowski P., Kurzydłowski K.J.: FEM analysis of coil support connections in the Wendelstain 7-X magnet system, Fusion Engineering and Design, Elsevier, 2007 (in press).

[7] Niezgoda T., Małachowski J., Szymczyk W.: Modelowanie numeryczne mikrostruktury ceramiki, WNT, Warszawa, 2005.

[8] Ochelski S.: Metody doświadczalne mechaniki kompozytów konstrukcyjnych, WNT, Warszawa, 2004.

[9] Sobczak J.: Kompozyty metalowe, Wydawnictwo Instytutu Odlewnictwa i Instytutu Transportu Samochodowego, Kraków-Warszawa, 2001.

[10] Stadnicki J.: Teoria i praktyka rozwiązywania zadań optymalizacji, Wydawnictwo Naukowo-Techniczne, Warszawa, 2006.

[11] Wilczyński A.P.: Zagadnienia optymalizacji struktury kompozytów włóknistych, Komputerowe Wspomaganie Projektowania Kompozytów Do Celów Cywilnych i Wojskowych, Oficyna Wydawnicza Politechniki Warszawskiej, Warszawa, 1999.

[12] You J.H., Bolt H.: Prediction of plastic deformation of fiber-reinforced copper matrix composites, Journal of Nuclear Materials (2002), pp. 74-78.

K. Haintze

METODY KOMPUTEROWE W OPTYMALIZACJI STRUKTUR KOMPOZYTOWYCH

Streszczenie

Materiały kompozytowe to obecnie bardzo dynamicznie rozwijająca sie branża. Inżynierowie na całym świecie pracują nad ich udoskonalaniem pod kątem wymagań stawianych przez współczesne konstrukcje. Rozwój metod i narzędzi do analizy komputerowej daje olbrzymie możliwości działań na tym polu. Prezentowany tu artykuł zawiera przykłady optymalizacji materiałów kompozytowych z włóknem węglowym zarówno w skali mikro jak i makro. . Wyniki komputerowej analizy zostały porównane z dobrze znanymi modelami analitycznymi.

APPLICATION OF FUZZY SETS TO RAIL VEHICLE RELIABILITY ASSESSMENT

Malgorzata Krupa
Institute of Aviation

Abstract

This article presents main theses and results of Ph. D. dissertation "Application of fuzzy sets to rail vehicle reliability assessment". The reliability estimation of rail vehicle elements and whole rail vehicle (e.g. tram 105 Na) using fuzzy set theory has been presented. Definition of fuzzy reliability consisted with fuzzy event notion has been shown. In fuzzy model pseudo-random number generators have been applied. Results of the fuzzy modeling have been compared with reliability from statistical analysis based on operating data (source: MPK Krakow). Doctor's thesis has been ended with summary and conclusions.

1.INTRODUCTION

Because reliability of rail vehicles has main influence on rail transport system safety, identification of reliability indicators in operating time of vehicle has particular meaning. Classical methods of reliability identification of technical objects derive from mathematical statistic and theory of probability. Complete reliability analysis of object is a complex and, in many cases, ambiguous process because of not always possible to detect conditions or its influences. In operating time reliability indicators of object elements and reliability structure of object cannot be precisely identified. Fuzzy sets and fuzzy inference are efficient method for modeling of incomplete knowledge about object and operation environment of it.

After analysis of professional literature from reliability and fuzzy sets theory, the main goal of doctoral thesis has been formulated: analysis and showing of suitability of fuzzy sets theory for reliability assessment of technical objects with incomplete information about it. Utilitarian goal: preparing fuzzy models useful for reliability models of rail vehicles in condition of operating system control in real time.

Construction trial of mathematical model and algorithm to obtain fuzzy reliability has been taken. Fuzzy model has taken into account imperfection of information (fuzziness and randomness). Because of many different interpretations, in doctoral thesis fuzzy event and membership function interpretation has been assumed.

Statistic and simulates reliability methods have been used. All calculation has been done in Matlab 6.5 (mainly Statistic and Fuzzy Toolboxes have been used).

In this work, fuzzy reliability notion and method of reliability assessment of elements (rail vehicle sets) with using fuzzy sets has been presented as a main part of doctoral thesis. All methodology on the example of shoe brake has been introduced.

2. FUZZY RELIABILITY - FORMULA

Reliability model based on probability of fuzzy event contains two parts:
- fuzzy part: membership function of fuzzy event (expert assessment of durability of rail vehicle element),
- crisp part: probability density function of occurrence of failures.

Fuzzy reliability definition can be obtained by changing characteristic function into membership function and event into fuzzy event. It is extension of classical notion. Fuzzy reliability of element in given time t is a probability of fuzzy event occurrence „time to failure T of object is fuzzily greater than t". Fuzzy reliability:

$$\tilde{R}(t) = P(T \tilde{>} t) \tag{1}$$

signifies fuzzy probability of proper work of object with incomplete information about its durability T.
In doctoral thesis, probability of fuzzy event is defined as:[3]

$$P(\tilde{A}) = \int_{-\infty}^{+\infty} \mu_{\tilde{A}}(x) f(x) dx \tag{2}$$

where: X – random variable, $f(x)$ – probability density function, $\mu_{\tilde{A}}(x)$ - membership function of fuzzy event .

If $f(x)$ is cumulative distribution function of T and $\mu_{\tilde{R}(t)}(x,t)$ ($\mu(x)$) is membership function of fuzzy event „time to failure T of object is fuzzily greater than t", $t \geq 0$, from definition of fuzzy probability:

$$\tilde{R}(t) = P(T \tilde{>} t) = \int_{t}^{\infty} \mu(x) dF(x), \tag{3}$$

And if $f(x)$ is known:

$$\tilde{R}(t) = P(T \tilde{>} t) = \int_{t}^{\infty} \mu(x) f(x) dx, \; 0 \leq t \leq x \leq \infty \tag{4}$$

where fuzzy reliability is given, another fuzzy reliability indicators can be obtained, e.g. fuzzy failure rate $\tilde{\lambda}$. If object dose not fail in time t, probability of fuzzy failure occurrence in $(t, t+\Delta t)$ is:

$$\tilde{\lambda}(t) = \lim_{\Delta t \to 0} \frac{P\{t \tilde{<} T \tilde{\leq} t + \Delta t\} | \{T \tilde{>} t\}\}}{\Delta t} = \lim_{\Delta t \to 0} \frac{\tilde{R}(t) - \tilde{R}(t + \Delta t)}{\tilde{R}(t) \Delta t} = -\frac{1}{\tilde{R}(t)} \frac{d\tilde{R}(t)}{dt} = -\frac{d \ln \tilde{R}(t)}{dt} \tag{5}$$

According to definition of failure rate:

$$\tilde{\lambda}(t) = \lim_{\Delta t \to 0} \frac{P\{t \tilde{<} T \tilde{\leq} t + \Delta t\} | \{T \tilde{>} t\}\}}{\Delta t} = \lim_{\Delta t \to 0} \frac{\tilde{R}(t) - \tilde{R}(t + \Delta t)}{\tilde{R}(t) \Delta t} = -\frac{1}{\tilde{R}(t)} \frac{d\tilde{R}(t)}{dt} = -\frac{d \ln \tilde{R}(t)}{dt} \tag{6}$$

3. FUZZY RELIABILITY – INTERPRETATION

In (2) formula two integral parts can be noticed.

Fuzzy part reflects randomness of fuzzy event occurrence. It answers to membership function $\mu(x)$ which represents incomplete information about object – expert assumption of element life (operation time range of rail vehicle subassembly). $\mu(x)$ is a membership grade of event $\{T \tilde{>} t\}$ - below lower range of assumed life, event does not occur for sure ($\mu(x)$=0), above upper range of assumed life, event occurs for sure ($\mu(x)$=1).

Shape of membership function which models transition from full membership to zero membership for proposed function is open right membership function defined as:

$$\mu(x)=\begin{cases}0 & x\le t_1\\ \dfrac{x-t_1}{t_2-t_1} & t_1<x\le t_2, t_1\ge 0\\ 1 & x>t_2\end{cases} \tag{7}$$

where t_1 - lower assumption of element life, t_2 - upper assumption of element life.

Crisp part of fuzzy reliability represents knowledge about object (here: rail vehicle element). $f(x)$ - density function of failure probability – to choose one from much ordinary used density function, information about type of failure modes is necessary. This knowledge is generally easy available. There is only problem with selection of parameters of probability function (e.g. shape and scale parameter, mean and standard deviation). For this purpose pseudo-random number generators can be very useful – it allows obtaining approximate values of selected distribution parameters dependently on operation conditions based on mean time of proper work of object.

When goodness of fit (pseudo-random numbers and simulated process) is kept, number generator can be used in fuzzy reliability model – indirectly it is used for obtaining parameters of distribution of a random variable of occurrence of failure of rail vehicle sets. Factors correlated with operating conditions of technical object work have been introduced (very light operating conditions, light operating conditions, medium-difficult operating conditions, very difficult operating condition). It has made generation of pseudo-random numbers connected with life of selected elements possible (depending on medium value of proper work time of element). Approximation of obtained pseudo-random numbers has allowed determining parameters of probability distribution of random variable T (time to failure) depending on operating conditions.

For checking efficiency and correctness of proposed method, operating research of rail vehicles has been making (object: 105 Na tram, sets: starter, converter, engine, pantograph, door, shoe break, rail brake, gear). Especially time to failure of selected elements has been taken under consideration (as an expert assessment).

After complex statistic analysis of operating data, based functions and values of reliability indexes have been determined.

4. EXAMPLE OF RELIABILITY ASSESSMENT OF TRAM ELEMENTS USING STATISTICAL AND FUZZY METHOD - SHOE BRAKE

Using pseudo-random number generator:

$$XWEI = C + A * \log(1 - rand(n,m)).\hat{}\,1/B \tag{8}$$

where:

A – factor connected with scale parameter,
B – factor connected with shape parameter,
C – displacement parameter (here element life assessed by expert),
rand(*n,m*) – function which gives matrix nxm of pseudo-random numbers (uniform distribution).

Weibull parameters in different operating conditions have been obtained.

For calculation fuzzy reliability values as an intermediate step fuzzy reliability membership function has been determined. -Cuts method has been used. Results in fuzzy form (range of reliability depend on how durable element is and in which operating conditions exists – VL, L, MD, D, N, VD) have been obtained.

To transfer results in real number domain, defuzzification has been used. In that case method of maximum value of membership function has been chosen.

Table 1. Weibull parameters in different operating conditions

Shoe brake (Weibull)					
	C	A	B	Shape parameter	Scale parameter
VL	0.7	0.3	0.3	4.7816	1.8927
	0.7	0.5	0.4	4.3652	1.7582
L	0.7	1	0.5	4.4949	1.563
	0.7	1.5	0.6	4.713	1.7906
MD	0.7	2	0.8	4.723	1.7421
	0.7	2.5	0.9	4.6849	1.8149
N	0.7	3	0.9	4.3599	1.5991
	0.7	3.5	1.1	4.2927	1.427
D	0.7	4	1.2	4.853	1.7081
	0.7	4.5	1.3	4.5456	1.6151
VD	0.7	5	1.5	5.0459	1.7274

(VL –very light, L – light, MD – medium-difficult, N – normal, D – difficult, VD – very difficult)

Table 2. Defuzzificated values of fuzzy reliability for different operating conditions successively very light operating conditions – 1, 2, light operating conditions -3, 4, medium-difficult operating conditions – 5, 6, normal operating conditions – 7, 8, difficult operating condition – 9, 10, very difficult operating condition – 11

	Operating conditions										
Element	1	2	3	4	5	6	7	8	9	10	11
Shoe brake	0.7828	0.7459	0.7235	0.7671	0.7610	0.7690	0.7230	0.6897	0.7614	0.7343	0.7713

For compression of reliability assessment method of 105 Na tram elements based on fuzzy sets and results of statistical analysis (e.g. shoe brake):

- on graph of reliability function (result of observed times of proper work of elements) two position statistics (mean and modal value) have been indicated (Fig. 1)
- reliability function value for modal value has been read, on comparative graph (Fig. 2) reliability values determined using fuzzy method in different operating conditions have been put together with empirical reliability for modal durability (T).

On the graph above comparability results obtain using statistical (classic reliability) and fuzzy methods has been observed.

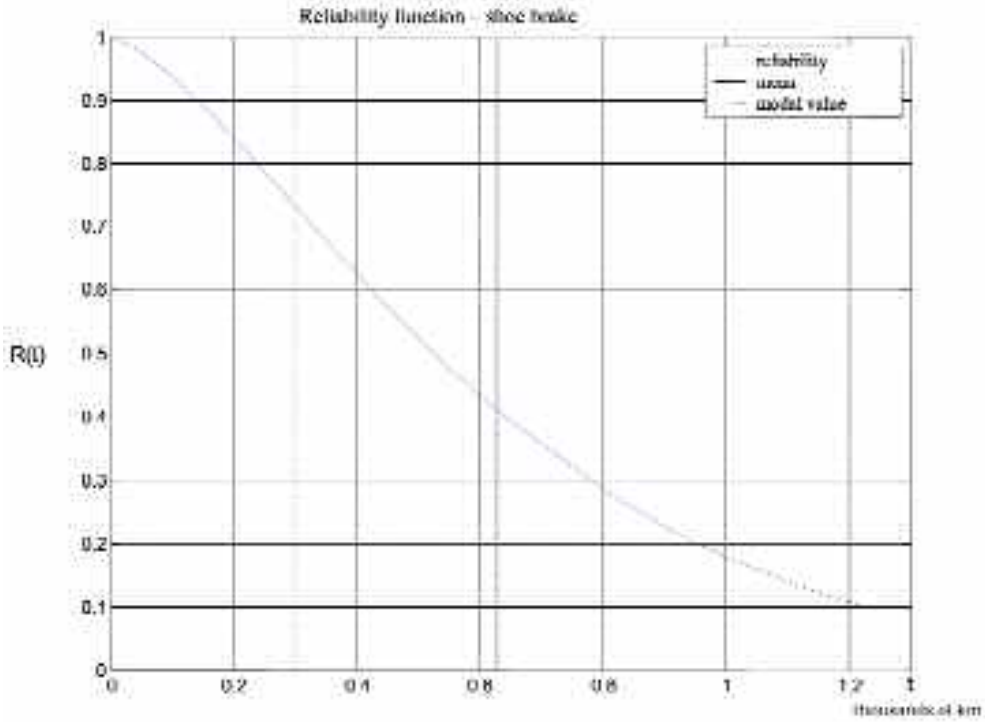

Fig. 1. Reliabilty function fot shoe brake

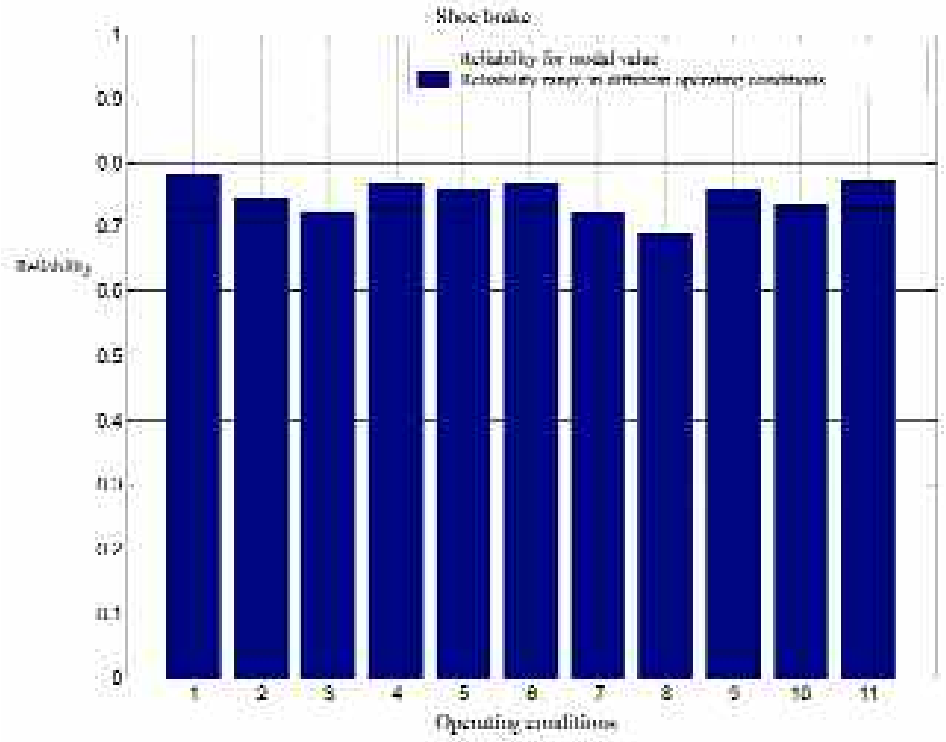

Fig. 2. Reliabilty of shoe brake for different operating conditions (fuzzy metod) in comparrision of empirical reliability for modal value

4. SUMMARY

Useful of fuzzy sets for reliability parameter assessment with incomplete information about technical object has been confirmed by conducted research. Application of fuzzy sets for reliability assessment of rail vehicle elements allows finding solution with precision comparable with statistic method.

Analysis of reliability based on expert assessment of tram 105 Na element life and pseudo-random number generators for different operating conditions have given results closet empirical research results.

Method proposed in PH. D. dissertation takes into consideration operation conditions influence on value of reliability of studied elements (as distinct from classic method). It has particular meaning for reliability assessment of technical objects as rail vehicles which operating proceeds in very diversified conditions.

Differences between reliability for modal value of element life (according to "crisp" method) and reliability values obtained with fuzzy method are caused by taking into consideration influences of many different operating conditions.

The biggest differences (more than 5%) have occurred in case of elements: engine and door. It can results from over or underprediction of element life. For specific situation proper choice of estimating expert is one of main and difficult task connected with proposed method (it was not subject of that work).

Praca doktorska wykonana w ramach projektu badawczego 4 T12C 052 29 pod tytulem: „Analiza zastosowania zbiorów rozmytych do oceny niezawodności elementów pojazdów szynowych"

BIBLIOGRAPHY

[1] **Bobrowski D.:** *Modele i metody matematyczne teorii niezawodności*, WNT, Warszawa 1995
[2] **Cai Kai-Yuan.:** *Introduction to fuzzy reliability*, Kluwer Academic Publishers, Boston-Dordrecht-London, 1996
[3] **Ching-Hsue Ch.:** *Fuzzy repairable reliability based on fuzzy gert*, Microelectron. Reliability, Vol. 36, 1996
[4] **Czogała E., Pedrycz W.:** *Elementy i metody teorii zbiorów rozmytych*, PWN, Warszawa 1985
[5] **Guzowski S., Krupa M.:** *Porównanie klasycznych i rozmytych metod oceny niezawodności pojazdów szynowych*, Mat. konf. X Jubileuszowego Kongresu Eksploatacji Urządzeń Technicznych, Stare Jabłonki, 2005
[6] **Kacprzyk J.:** *Wieloetapowe sterowanie rozmyte*, WNT, Warszawa 2001
[7] **Kosko B.:** *Fuzzy engineering*, Prentice Hall International, 2000
[8] **Łachwa A.:** *Rozmyty świat zbiorów, liczb, relacji, faktów, reguł i decyzji*, EXIT, Warszawa, 2001
[9] **Oprzędkiewicz J.:** *Komputerowa metoda oceny niezawodnoœci systemów technicznych*, Lubelskie Towarzystwo Naukowe, PNNTE, Warszawa-Lublin-Kraków, 1997
[10] **Zadeh L. A.:** *Fuzzy Algorithms*, Information and Control, Vol. 12, 94-102, 1968

M. Krupa

ZASTOSOWANIE ZBIORÓW ROZMYTYCH DO OCENY NIEZAWODNOŚCI POJAZDÓW SZYNOWYCH

Streszczenie

Artykuł prezentuje główne założenia i rezultaty rozprawy doktorskie pod tytułem: „Wykorzystanie zbiorów rozmytych do oceny niezawodności elementów pojazdów szynowych". Przedstawione zostało szacowanie niezawodności pojazdu szynowego i jego elementów (na przykładzie tramwaju typu 105Na) wykorzystujące teorie zbiorów rozmytych. Opisano wprowadzone w pracy doktorskiej pojecie rozmytej niezawodności oparte na zdarzeniu rozmytym. W modelu rozmytym zastosowano generatory liczb pseudolosowych. Otrzymane wyniki rozmytego modelowania niezawodności porównano z wynikami badan empirycznych (MPK Kraków). Prace zakończyło podsumowanie i wnioski.

EXPERIMENTS ON THE UPPER EXPLOSION LIMITS OF GASEOUS ALKANES-OXYGEN MIXTURES AT ELEVATED CONDITIONS OF T AND P IN A SPHERICAL VESSEL

Grzegorz Rarata
Institute of Aviation, Space Technology Department
Jacek Szymczyk
Warsaw University of Technology, Division of Pumps, Drives and Plants
Piotr Wolański
Warsaw University of Technology, Division of Aeroengines

Summary

This experimental work has been completed in the Institute of Heat Engineering Laboratories of Warsaw University of Technology. The article reports on the explosion pressure data and the influence of chosen physical parameters on the value of the Upper Explosive Limit (UEL) of gaseous alkanes-oxygen mixtures. Such explosion behavior data of common gases for different initial conditions are essential for a quantitative risk assessment in many industrial environments. A number of higher alkanes-oxygen mixtures were examined (up to n-butane). Summarized research data is presented in the paper. All the presented data have been obtained from the experiments conducted in a 2.3 dm^3 spherical, steel vessel. Exploding wire was used as the mean of ignition source. It released about 0.1 J energy each time. The pressure histories in the combustion vessel have been recorded by means of piezoelectric pressure transducer. The influence of the increased initial temperatures of the tested mixtures on their value of UEL was investigated in the range of 20°C up to 200°C. Further experiments on the influence of elevated pressure, as well as the position of the ignition source, were carried out too. The experiments allowed the authors to find a distinct dependencies in the values of obtained UEL under elevated conditions of pressure and temperature.

Keywords: *Flammability, Explosive limits, Flammability limits, Elevated conditions, Explosion pressure*

1. INTRODUCTION

The upper explosion limits (UEL) data of common gases such as gaseous alkanes in their mixtures with air and oxygen at elevated conditions are essential for a factual risk assessment. Many industrial processes involve the mixing of these flammable gases with oxygen at standard and elevated conditions [1]. Mixtures of light alkanes and oxygen can be converted into many useful products (such as acetylene) by partial combustion (oxidation) in excess of fuel at moderate conditions of temperature and pressure. The flammability limits for all commonly used gaseous fuels, including those used in experiments here, are rather well documented in the literature.

However, the data available almost always applies to ambient temperature and pressure conditions, Thus, despite the fact of extensive research on explosibility limits have been carried out for nearly 200 years now, there is only limited data on the influence of pressure and temperature on upper explosion limits even common gaseous fuels[2].

The determination of the UEL is more difficult compared to the lower explosion limit (LEL). The UEL value changes significantly over a wide range to higher fuel composition with pressure and temperature [3]. Various research explosion centers have published explosion limits values which often differ quite significantly from each other [4,5,6]

The report presents the explosion pressure data for four gaseous alkanes homologues-oxygen mixtures; i.e. methane, ethane, propane and n-butane (all at the upper flammable limit) at both; standard and elevated conditions of pressure and temperature. All the presented data have been obtained from the experiments conducted in the steel spherical explosion vessel of 2,3 dm^3 volume, equipped with external heating/cooling system. The initial temperatures of the examined mixtures have oscillated from 20°C up to 200°C and the initial pressures varied from 1 been 6 bar for methane and ethane.

The pressure histories in the combustion vessel have been recorded by means of special pressure transducer with additional cooling system. The effects of higher initial temperature or pressure of the mixture on the pressure curves have also been investigated and qualitatively analyzed. The effect of the ignition position on the explosion pressure history has been explored as well. The results are plotted as functions of time, with respect to the ignition configuration, temperature and pressure.

2. THE RESEARCH STAND

The experimental set-up consist of following parts: spherical steel vessel, fusing wire ignition system, data acquisition system with pressure transducer, amplifier, acquisition card and a computer, bottle with mixture and vacuum pomp. To control the initial conditions i.e., pressure and temperature, electronic precise manometer and a type K thermocouple were used. The pressure transducer (together with cooling system) used in this research was manufactured by Kistler.

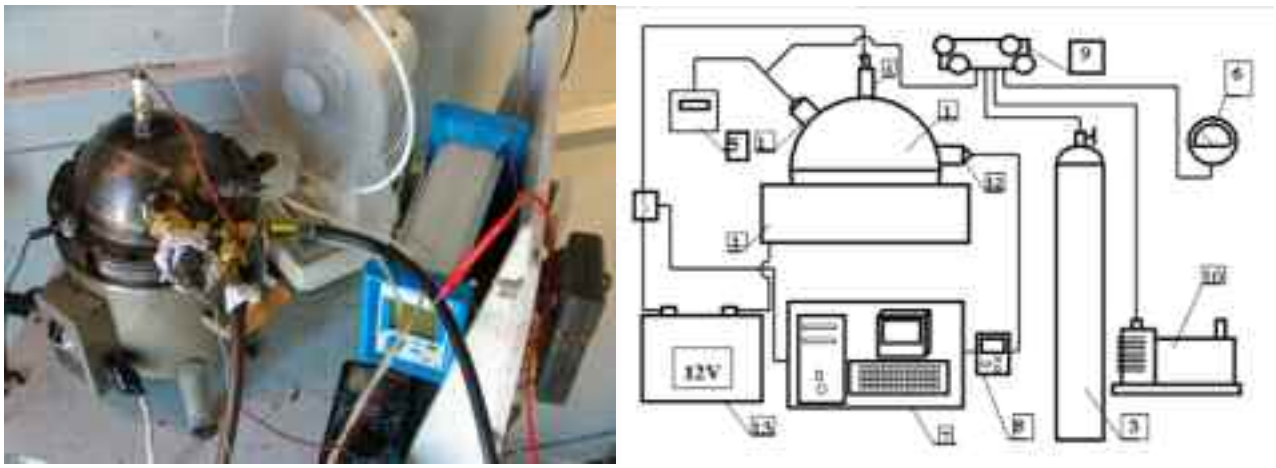

Fig. 1. Photography of the experimental test stand and its schematic diagram

Location of the ignition was changeable, that is was inserted in the center or on the bottom of the vessel in order to evaluate its position on the course of oxidation process.

A general view of the research stand and its schematic diagram is presented in Fig. 1. The explosion vessel (1) was placed on hemispherical electrical heater (2). The ignition system were assembled at the top of the vessel (4), and connected via cable with the battery (13) as well as with the data acquisition system and computer (7). Piezoelectric pressure transducer (12) was mounted in the vessel wall and connected to the amplifier (8), and then to the computer (7). The

thermocouple was also placed in the vessel close to the wall (5). The same valve was used to fill vessel with fresh mixture and evacuate the products.

3. EXPERIMENTAL PROCEDURE

Before each experiment the vessel was evacuated by vacuum pump and then filled with test mixture. The gas mixture was allowed to come to rest by waiting at least 5 min. before executing each test. All the test mixtures were prepared at least one day in advance, by using the partial pressure method. The stand for mixtures preparation was equipped with steel bottles, a vacuum pump and a set of precise manometers of high reading accuracy. The first step of the experimental procedure was evacuating the test chamber and then filling it in with the appropriate mixture, then preheating the test vessel containing the mixture to the required temperature, igniting the quiescent test mixture and recording the explosion overpressure inside the chamber. The test mixture was considered as an explosive one, if the measured explosion overpressure was equal to (or greater) than the overpressure formed by the ignition source itself (signal at the level of the reading resolution of the instruments), and exceeded 7% of the initial mixture pressure.

During tests the composition of all mixtures was continuously increased until no ignition was observed (lack of pressure rise). The mixtures were ignited by an exploding wire (aluchrome resistance wire, 0,2 mm diameter), with average energy ignition estimated ~ 0,1 J. The ignition source must be of sufficient energy to guarantee ignition, otherwise the property under investigation would be that of the limiting ignition energy and not of explosibility. Two positions of ignition were utilized during the research; centre and the bottom of the vessel. The limits were evaluated for initial pressure and temperature varied from 1 to 5 bar, and from 20°C to 200°C respectively. The pressure data were measured by water-cooled Kistler piezoelectric pressure transducer mounted in one of the side walls of the vessel. The data acquisition system was used to record all experimental data. The initial pressure of the mixture in the vessel was measured with high accuracy digital pressure manometer. The initial temperature of mixture was controlled by a K-type thermocouple located almost in the centre of the vessel. The temperature of the vessel was controlled by means of special electric heaters. The top half of the vessel was covered with an insulating material.

4. EXPERIMENTAL RESULTS

The increase of the initial mixture temperature causes a significant increase of the upper explosion limit in the case of all investigated mixtures. The change of that explosion limit versus the initial temperature of the mixture can be approximated by means of a linear function. Similarly, the increase of the initial mixture pressure causes a significant widening of the UEL, especially in the case of ethane-oxygen mixtures.

Table 1. Qualitative results of the flammability of methane-oxygen mixtures in the spherical vessel of 2,3 dm³ volume and central position of ignition source

UFL %[v/v]		55	56	57	58	59	60	61	62	63	64	65	66	67	68
1bar	20°C	↔	↔	↓	↓	↓	↓	↓	↓	↓	↓	↓	↓	↓	↓
1bar	50°C	↑	↑	‹ ›	↓	↓	↓	↓	↓	↓	↓	↓	↓	↓	↓
1bar	100°C	↑	↑	↔	↓	↓	↓	↓	↓	↓	↓	↓	↓	↓	↓
1bar	150°C	↑	↑	↔	↔	↔	↔	↓	↓	↓	↓	↓	↓	↓	↓
1bar	200°C	↑	↑	↑	‹ ›	‹ ›	‹ ›	↓	↓	↓	↓	↓	↓	↓	↓
20°C	2bar	↑	↔	↔	↑	↔	↔	↔	↓	↓	↓	↓	↓	↓	↓
20°C	3bar	↑	↑	↑	↑	↑	‹ ›	‹ ›	‹ ›	‹ ›	↓	↓	↓	↓	↓
20°C	4bar	↑	↑	↑	↑	↑	↑	↔	↔	↔	↔	↓	↓	↓	↓
20°C	5bar	↑	↑	↑	↑	↑	↑	↑	↑	‹ ›	‹ ›	‹ ›	↓	↓	↓
20°C	6bar	↑	↑	↑	↑	↑	↑	↑	↑	↑	↑	↔	↔	↔	↓
↑ flammable, ↓ non-flammable, ‹ › the ignition occurred only once during 3 repetitions															

The table 1 presents bulk results on the upper flammability limit of methane-oxygen mixtures

at elevated conditions of temperature and pressure (separately). The results are plotted as functions of molar percentage methane content, with respect to the pressure and temperature conditions. It can be seen that the upper explosibility limit increases along with the increase of the initial temperature/pressure of the methane-oxygen mixture. It was also found, that the upper explosion limit of methane-oxygen mixture does not depend on the residual time within investigated initial conditions of pressure and temperature.

The UFL values for gaseous alkanes in their mixtures with oxygen at ambient conditions are given in the table 2. In the tables 3 and 4 the values of UFL at elevated conditions are presented, together with their graphical interpretation in the figure 3.

Table 2. The UFL measured in the spherical vessel of 2,3 dm^3, central position of ignition source, 20°C

	methane	ethane	propane	n-butane
GGW [% v/v]	57	55	50	49

Table 3. The influence of mixture initial pressure on the UFL

pressure [bar]	methane	ethane	propane	n-butane
1	57	55	50	49
2	59	61,5	51	52
3	62	64	53	
4	63	65,5	54	
5	65	66		
6	66	66,5		

Table 4. The influence of mixture initial temperature on the UFL

temperature [°C]	methane	ethane	propane	n-butane
20	57	55	50	49
50	57,5	55	50,5	49
100	58,5	55,5	51,5	49,5
150	59	55,5	51,5	49,5
200	60,5	56	52,5	50

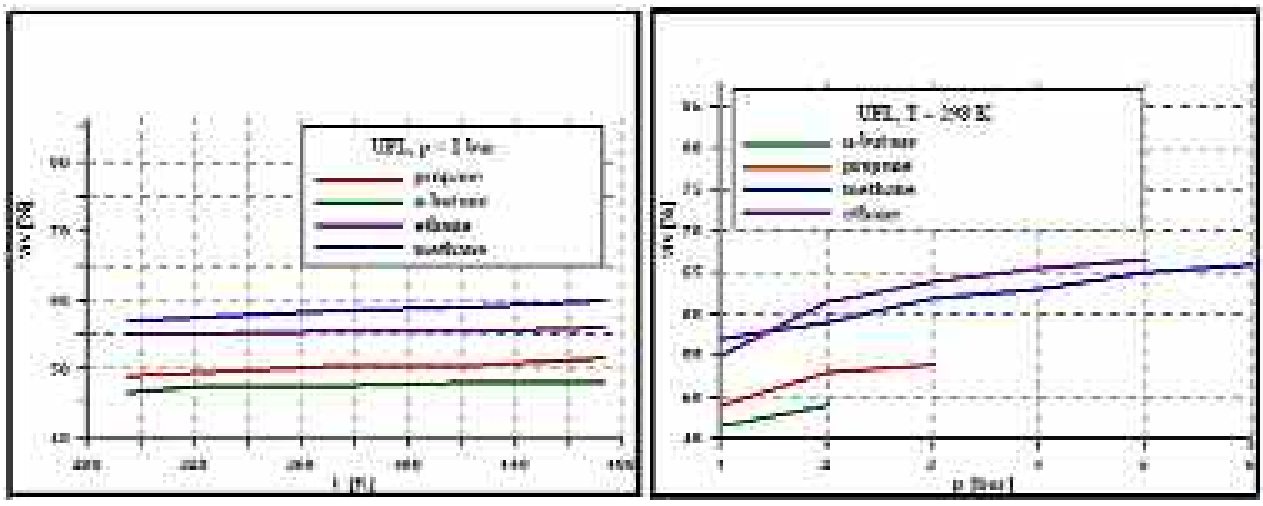

Fig. 2. The influence of elevated temperature and pressure on the UFL value

5. DISCUSSION

The obtained values of the UFL are the consequence of many experimental measurements. The

7% initial pressure rise was used as a criterion of the UEL (Fig. 4). Experiments on the ignition of extremely fuel-rich methane, ethane propane and n-butane −oxygen mixtures in the 2,3 dm^3 spherical vessel at elevated initial pressure (up to 6 bar) and temperature (473 K) reveal significant influence of the ignition position on the maximum explosion pressure. Direct results of pressure course versus time for the examined mixtures in the UFL regime are shown in Fig. 5.

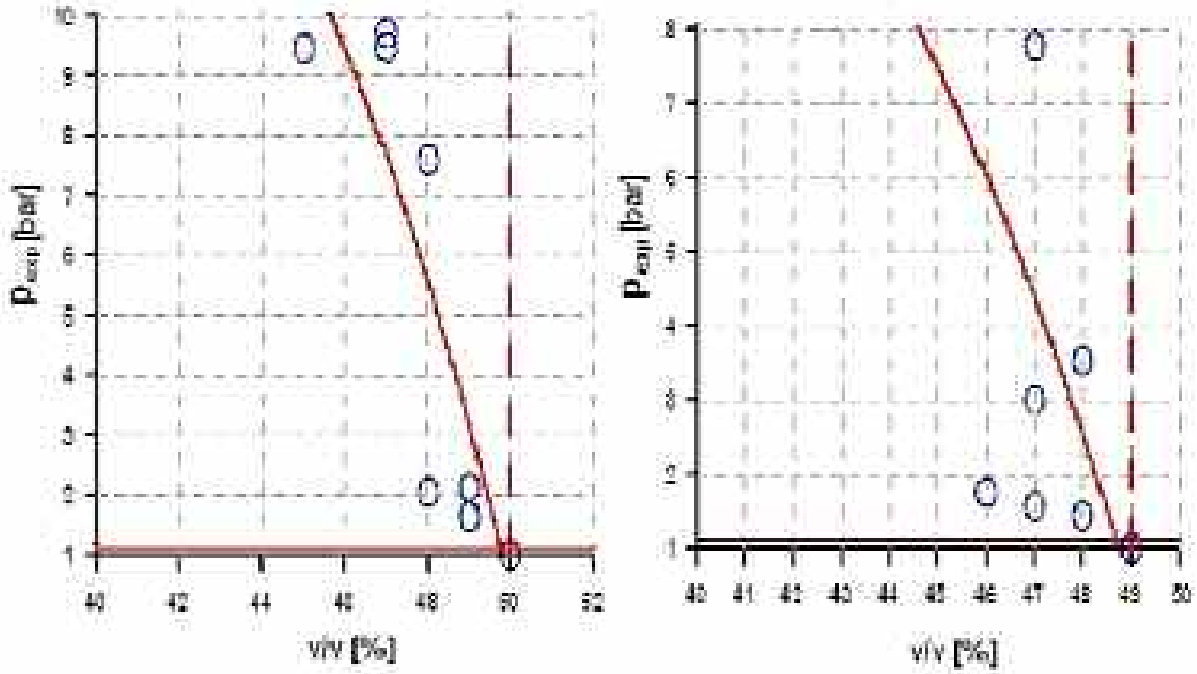

Fig. 3. The UEL approximation of propane-oxygen (left) and n-butane-oxygen (right) mixtures; 2,3 dm^3 vessel, 20°C, 1 bar, central ignition, 7% criterion

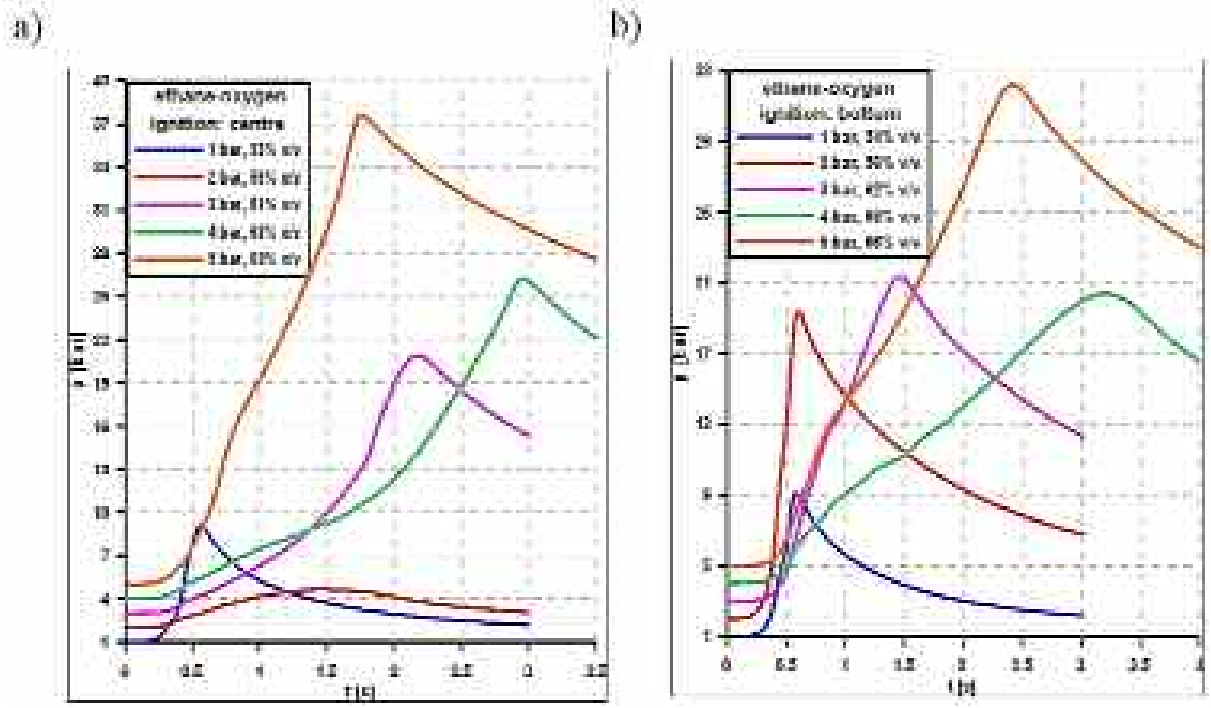

Fig. 4. The comparison of pressure rise for 5 different initial pressures for 2 ignition positions; 2,3 dm^3 vessel, 20°C

Maximum explosion pressure decreased as initial temperature increased in the case of all investigated mixtures. Examples are presented in Fig. 6. This was probably due to the decrease of the mass of mixture inside the chamber (at given initial pressure).

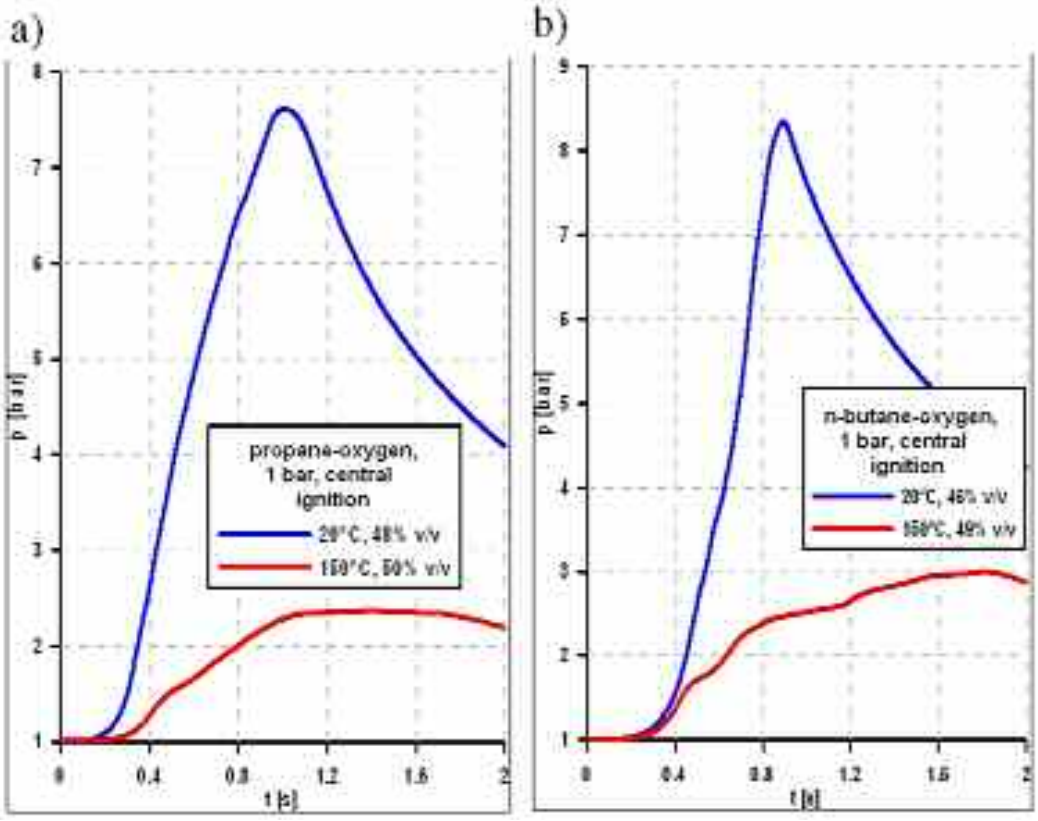

Fig. 5. The comparison of the pressure histories in the combustion vessel 2,3 dm³ for two initial temperatures for central ignition position, 20°C

At higher initial pressure mixture ignition occurred quite easily but the time of the explosion development lengthened. It means that the higher pressure, the slower flame propagation velocity. When increasing the initial pressure in a rich mixture, the expanding flame ball becomes more irregular in shape (Fig. 7).

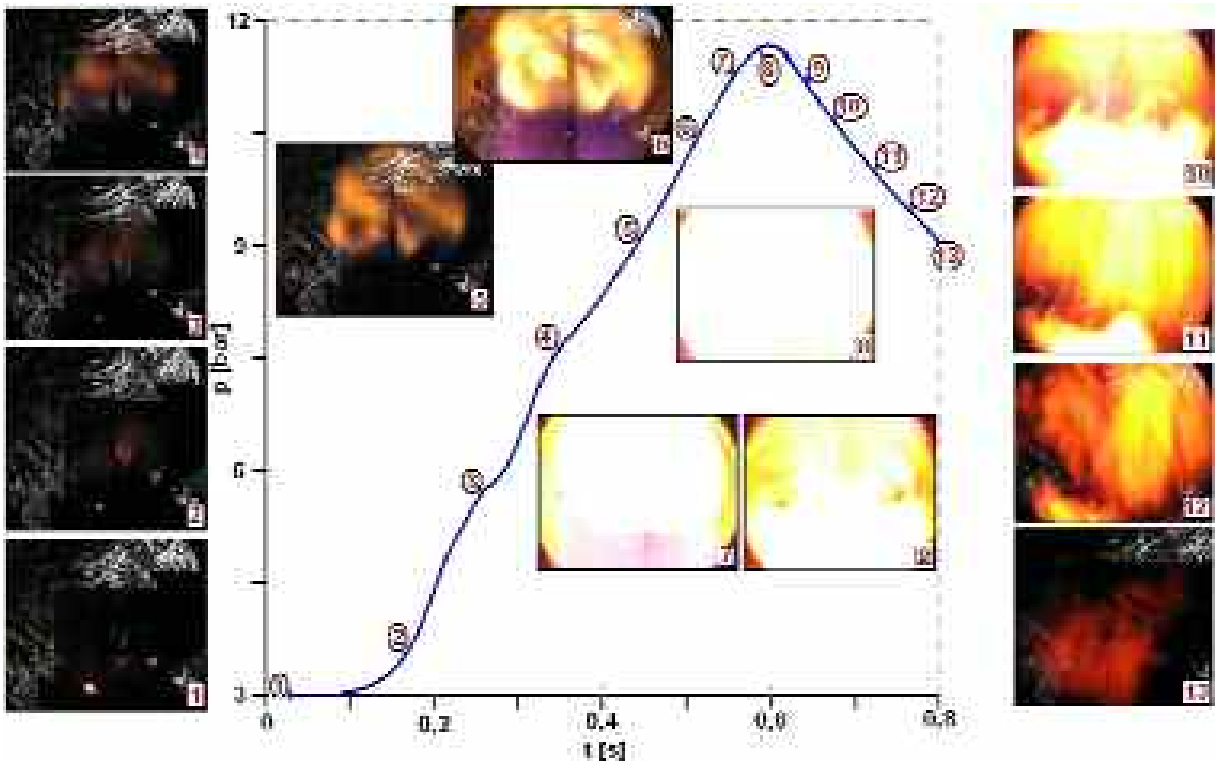

Fig. 6. Flame propagation in 2,3 dm³ vessel; 62 mol.% ethane-oxygen mixture, bottom ignition (~ 0,1 J), 20°C, 3 bar

The experimental results generally show an increase in soot volume fraction with increasing fuel content in the test mixture cases. Besides, it was possible to find the sooting tendency, that can be described as follows;

methane < ethane < propane < n-butane.

In some experimental cases the soot volume fraction was very high, especially at higher pressure and lower temperature (Fig. 8).

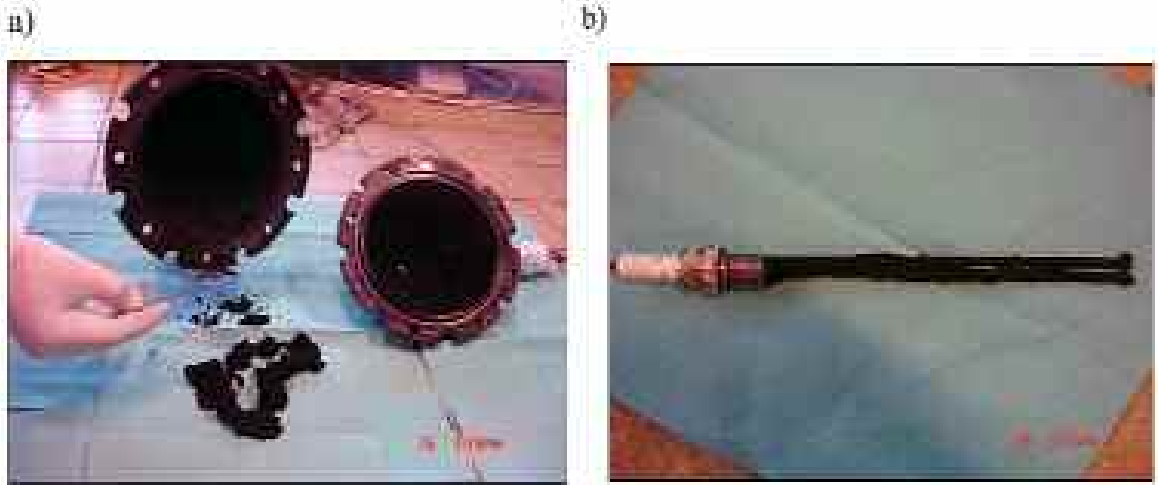

Fig. 8. The effect of soot formation; propane-oxygen mixture in 2,3 dm^3 vessel, 20°C, 3 bar; a) inside the combustion chamber, b) ignition device

6. CONCLUSIONS

Methane, ethane, propane and n-butane in their rich mixtures with oxygen were examined during the experimental work. Key findings of this part of the research are:

- the upper explosion limits, in the examined range of the mixtures, strongly depend on the initial mixture temperature
- it was also observed that initial pressure has a significant influence on rich explosion limits, especially in the case of ethane-oxygen mixtures
- also the duration time of the explosion at rich limit increases significantly in the case of ethane-oxygen rich mixtures for higher initial pressures
- maximum explosion pressure decreases as initial temperature increases in the case of all investigated mixtures - due to the decrease of the mass of mixture inside the chamber (at given initial pressure)
- the change of the maximum explosion pressure versus initial mixture temperature can be approximated by means of a linear function for all oxygen mixtures
- the change of the upper explosion limit versus initial mixture pressure can be approximated by means of a linear function only for methane, ethane and propane -oxygen mixtures, not for ethane-oxygen mixtures
- lowering the ignition source position leads to easier ignition and higher explosion pressures for near upper limit mixtures, especially those with higher initial pressures – probably due to the fact that in this case more mixture is involved in combustion, and the whole process takes more time

Obtained results of the upper explosion limit for lower gaseous alkanes mixtures with oxygen as a function of initial pressure and temperature might be very useful not only for better understanding of explosive properties of this combustible mixtures but also would contribute to improve the safety conditions in many industry applications. The results of the study indicate that apparently inflammable mixtures can nevertheless become hazardous depending on the initial mixture conditions.

7. LITERATURE

[1] A. Pekalski, E. Terli, J. F. Zevenbergen, S. M. Lemkowitz, and H. J. Pasman, *Combustion Institute Proceedings*, **30**, 1133−1139 (2005).

[3] L.G. Britton, Two hundred years of flammable limits, *Process Safety Progress*, **21**, 1-11, (2002).

[4] K. Holtappels, V. Schroeder, A. Kobiera, P. Wolanski, M. Braithwaite, H.J. Pasman, Gas explosion safety characteristics and anomalies at unusual conditions, *Proceedings of the 12th international symposium on loss prevention and safety promotion in the process industries* Edinburgh, UK, (2007).

[5] K.K. Eltschlager, et al. *Technical Measures for the Investigation and Mitigation of Fugitive Methane Hazards in Areas of Coal Mining* U.S. Department of The Interior Office of Surface Mining, Pittsburgh, 2001.

[6] D.J. Halliday *Investigation of Natural Gas Explosions* Forensic Science Service Metropolitan Laboratory, London, 2004.

[7] J. Dwyer, J.G. Hansel, T. Philips *Temperature Influence on the Flammability Limits of Heat Treating Atmospheres* Air Products and Chemicals, Allentown, 2000.

G. Rarata, J. Szymczyk, P. Wolański

BADANIA GÓRNEJ GRANICY WYBUCHOWOŚCI (GGW) MIESZANIN GAZOWYCH ALKANÓW W TLENIE W NACZYNIU KULISTYM W WARUNKACH PODWYŻSZONEJ TEMPERATURY T ORAZ CIŚNIENIA p

Streszczenie

Przedstawiona praca doświadczalna została wykonana w laboratoriach Instytutu Techniki Cieplnej Politechniki Warszawskiej. Artykuł zawiera wyniki serii pomiarów, których celem było ustalenie wpływu wybranych parametrów fizycznych na wartość ciśnienia wybuchu dla mieszanin gazowych alkanów z tlenem. Dane takie, łącznie z wyznaczoną wartością górnej granicy wybuchowości (GGW) dla poszczególnych mieszanin, mają podstawowe znaczenie dla ustalania odpowiednich norm bezpieczeństwa w przemyśle chemicznym. Badaniom poddano gazowe alkany, a więc metan, etan, propan oraz n-butan. Wyniki, prezentowane w postaci sumarycznych danych (tabel) zostały uzyskane w wyniku przeprowadzenia pomiarów w stalowym naczyniu kulistym o objętości 2,3 dm^3. Jako źródło zapłonu użyto tzw. eksplodujący drucik (exploding wire), który uwalniał za każdym razem około 0,1 J energii. Przebieg zmian ciśnienia w czasie rejestrowano przy użyciu szybkiego czujnika piezoelektrycznego. Zbadano wpływ temperatury początkowej mieszanin testowych, w zakresie od 20°C do 200°C. Przeprowadzono również pomiary w zakresie wzrastającego ciśnienia początkowego mieszanin. Na ich podstawie autorzy wyznaczyli wyraźne zależności GGW od początkowej wartości T oraz p badanych mieszanin.

SELECTED SOURCES OF THE BALLSCREW NOISE

Przemyslaw Pieniecki
Institute of Aviation

Summary

Increasing of machines yield has been a permanent challenge for the new generation of machine designers and engineers for years. Recently they also have to consider the noise reduction requirements according to European directives and Global ISO norms. Modern machine, for example CNC Machining Center, consists of many systems and components that emit noise during their work. Ballscrew drive is one the most significant component emitting noise (Fig.1).

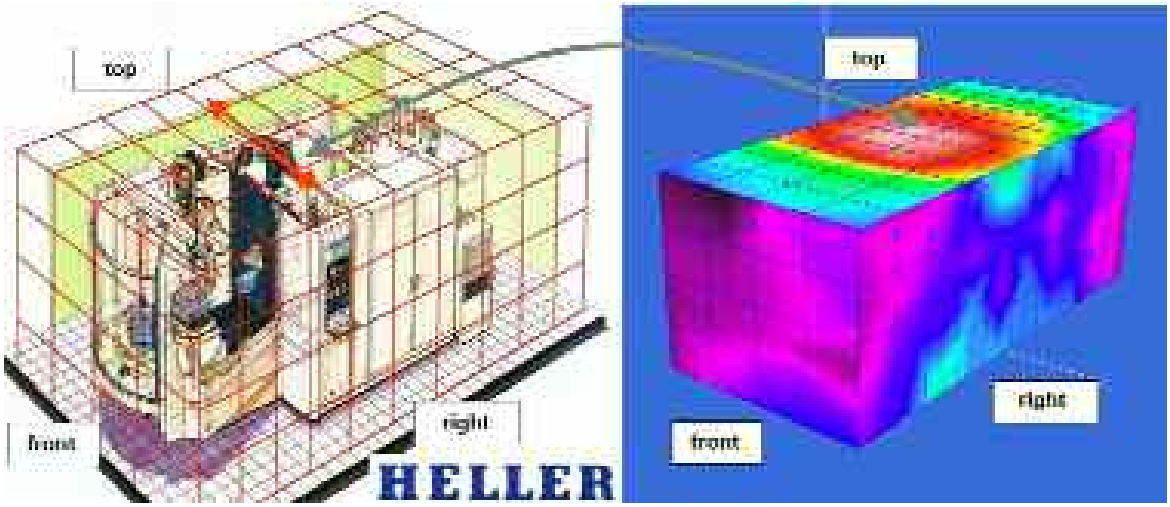

Fig. 1 Determination of sound power levels of noise sources using sound intensity measurement at discrete points of the CNC machining center. The investigation confirms that the ballscrew system is the most significant source of noise - 80dB(A) was measured at the top of machine [1]

Full motion cycle of each ball in the ballscrew has the following phases: working, transient and the return motion phase (Fig.2). Significant source of the noise is the circulation of balls in the closed circulation, especially in the transient zone of the balls' circulation, when a ball enters the working circulation and its load increases, or when it leaves the working circulation and its load decreases to zero. When the speed of the balls reaches certain levels, the repetitive shock (impact forces) generated by the balls in the "transient" phase of the balls' motion and forces acting in the return channel cause damage to the recirculation ball system. The impact forces in the transition zone are direct reason for the ballscrew noise.

A simulation of impact forces for variable length of transient phase in function of the rotational speed was made. A transient phase forces take a major part on the ball screw friction phenomenon. The mathematical model of transition zone is shown in the Fig. 3.

Drill friction on ball track and friction on the inside surface of return elements are also important sources of the noise. Rolling quality coefficient depends on of nut and screw lead angle.

Small ball diameter determinates accurate rolling quality, which decreases the noise emission. Analysis of dynamic and friction phenomena is essential to understand properly the main noise sources on ball screw drive.

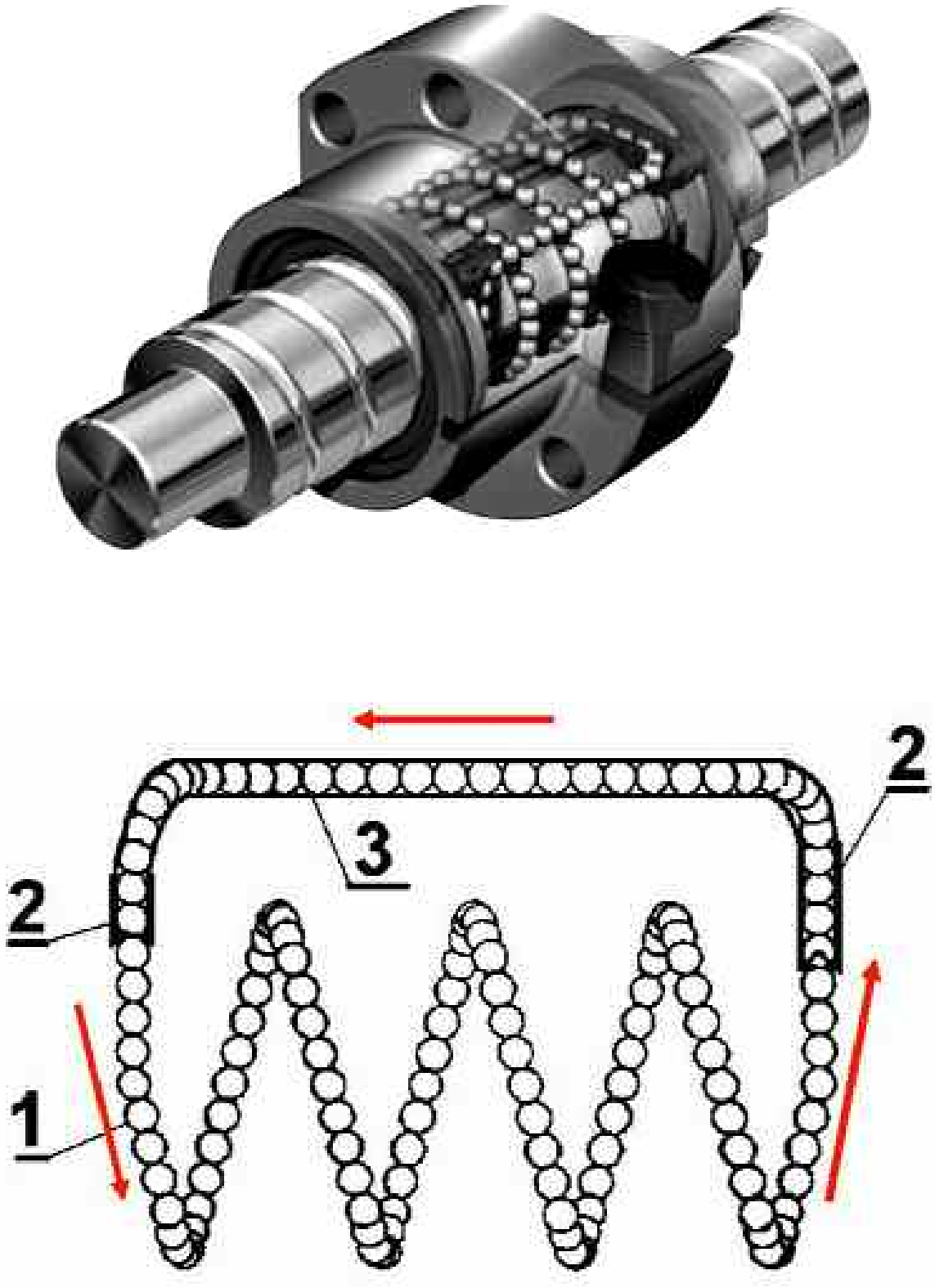

Fig. 2 Example of the ballscrew drives [2] - upper picture, and the full cycle of balls circulation: 1 – working phase, 2 – transient phase, 3 – return phase [3] - lower picture.

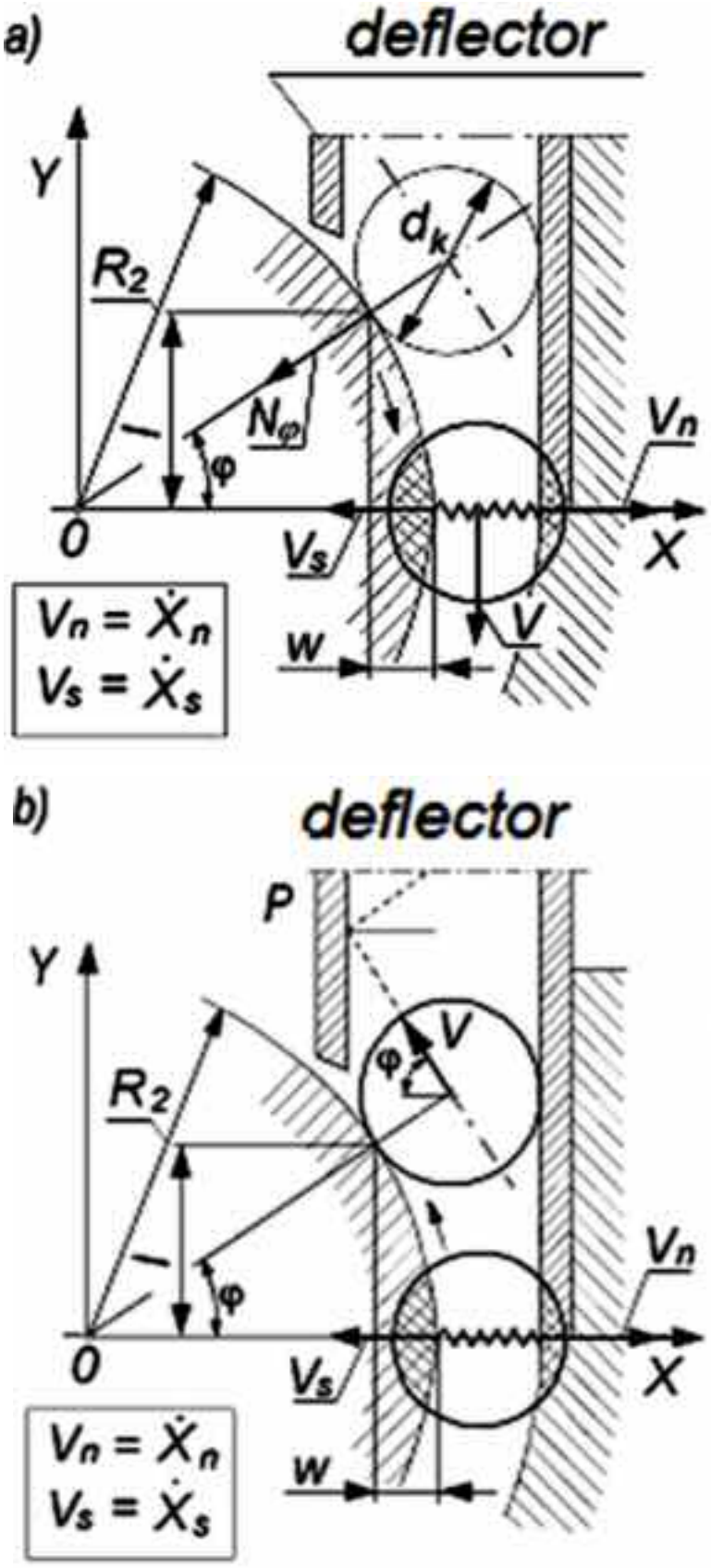

Fig. 3 Mathematical model of transition zone (external circulation circuit): a) ball's entrance to circulation circuit, b) ball's exit from z circulation circuit: d_k − ball diameter, R_2 − one of the main radiuses of curvature (proportional to ball diameter), l − length of transition zone, $V_{s,n}$ − velocity of contact deflection, V − ball velocity, $V_{s,n}$ − velocity of contact deflection properly for screw shaft and nut [4]

Particularly dangerous for the servo drives which included ball screw is the resonance frequency of the transmission at the entry of balls into the load, which may cause an increase of vibration and associated with it noise. It was examined what rotational speeds set off the harmful phenomenon of the agreement of the frequency of the arrangement of the impact forces with the frequency of the servo drive system resonance.

A higher length of the lead of the thread leads to a lower number of revolutions and lower noises as well as prolonged the life time cycle of the ball screws.

Table 1. Comparison of the nut and screw shaft lead angle differences for the 40×40 ball screw (balls diameter in range 3–6 mm, rotation 1000 rpm, number of loaded turns 3, screw shaft length 1000 mm). λ_s – screw shaft lead angle, λ_n – nut lead angle, F_{u1} – impact force, C_a – dynamic load based on ISO Norm [4].

Nominal diameter [mm]	Lead [mm]	Ball diam. [mm]	Angle differ. $\lambda_n - \lambda_s$ [°]	Impact Force F_{u1} [N]	Dynamic Load. Based on ISO C_a [N]
40	40	6	2,9	133,2	23329
40	40	5,953	2,88	132,31	23245
40	40	5,556	2,68	119,34	21207
40	40	5,5	2,63	118,38	21012
40	40	5	2,36	110,33	18465
40	40	4,762	2,23	104,21	17225
40	40	4,5	2,09	95,16	16078
40	40	4,366	2,02	92,95	15386
40	40	4	1,84	86,63	13635
40	40	3,969	1,82	86,05	13526
40	40	3,572	1,62	72,76	11732
40	40	3,5	1,59	71,53	11408
40	40	3,175	1,43	65,85	9961
40	40	3	1,35	62,74	9167

Table 1 describes analysis of lead angle differences depending on steel balls dimension [4]. Selected diameters are the standard ones in current quotation of the steel ball manufactures. As expected, smaller ball diameter causes smaller lead angle difference and makes roll quality become higher value. Additionally, smaller ball diameter (lighter ball) causes less impact force in the transition zone.

Fig. 4 presents correlation between impact force and ball diameter d_k (lead angle difference) for the calculations shown in the Table 1. In practice this relation is the function of the ball diameter. The approximated trend line formula for these analyses is shown in graph on Fig. 4.

$$F_{u1} = 5,65 d_k + 54,12 \tag{1}$$

The formula (1) is valid only for the example described above and presents approximated linear relation between maximum impact force F_{u1} and ball diameter d_k. The Ball screw impact forces and their noise level correlations are described in work [4].

Usage of smaller steel ball diameters can cause in fact increasing of roll quality and decreasing of impact forces in transition zone. This is correlated directly with ball screw noise level reduction. Unfortunately smaller ball diameter affects ball screw loading decreasing. It is very significant limitation of this noise reduction proposal.

The adoption of the modern ball materials (e.g. composites) is recommended to meet the high load and lower noise emission requirements on ball screw.

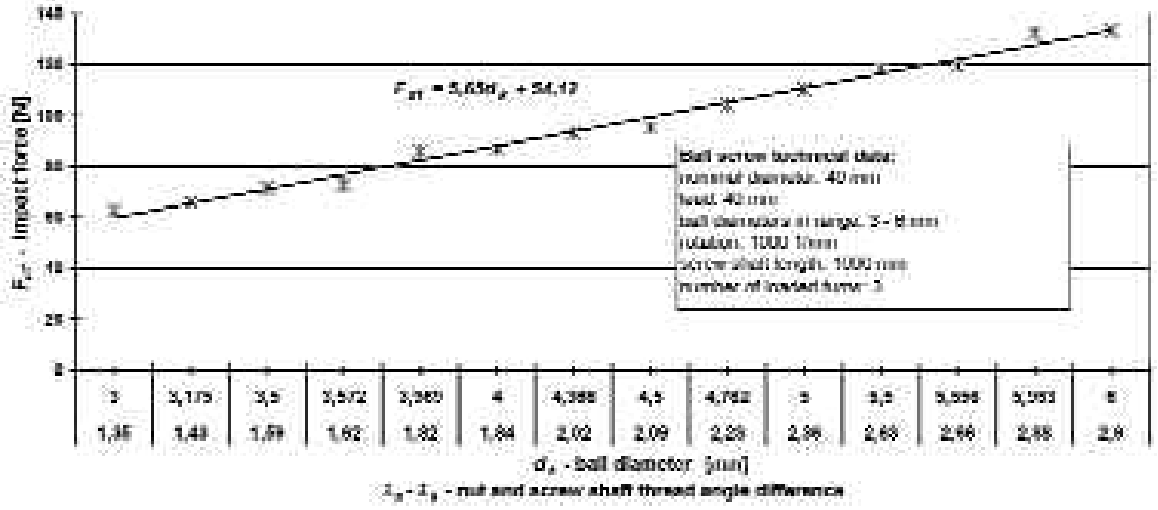

Fig. 4. Impact forces dependence on nut and screw shaft lead angle difference for the 40×40 ball screw [4]

Bibliography

[1] Neithardt W., Pieniecki P.: Analyse von Geräuschursachen an Kugelgewindetrieben und Linear-führungen, Conference - Strategien zur Geräuschminderung METAV München, 2004, Munich

[2] Ballscrew Catalog - based on the Boschrexroth web portal: www.boschrexroth.com

[3] Sobolewski J.Z.: Selected Problems of ball screws noise, Machine Engineering, Vol. 4, No. 1-2, Wroclaw 2004, page 193-200

[4] Pieniecki P., Sobolewski J.Z.: Selected sources of the ball screw noise, Machine Dynamics Problems, Vol. 32, No 2, 2008, page 49-56.

P. Pieniecki

WYBRANE ZAGADNIENIA HAŁASU PRZEKŁADNI ŚRUBOWYCH TOCZNYCH

Streszczenie

Nieustanne zwiększanie wydajności obrabiarek jest od wielu lat wyzwaniem dla kolejnych pokoleń inżynierów i projektantów maszyn. Od niedawna, podczas procesu projektowania, uwzględniane muszą być także wymagania poziomu hałasu zgodne z europejskimi dyrektywami, normami ISO oraz światowymi normami. Nowoczesne maszyny, jakimi mogą być na przykład centra obróbkowe CNC, składają się z wielu podsystemów i komponentów emitujących hałas podczas swojej pracy. Przeprowadzone badania pokazują, że przekładnia śrubowa toczna jest jednym z ważniejszych źródeł hałasu obrabiarki.

THE WIRE ELECTRO DISCHARGE MACHINE SETTING PARAMETERS ANALYSIS INFLUENCING THE MACHINED SURFACE ROUGHNESS AND WAVINESS

Radoslaw Serwiński
General Electric Company Polska
Faculty of Production Engineering, Institute of Machines Technology, Warsaw University of Technology

Summary

Wire Electro Discharge Machining is one of the methods, which allows to machine even the hardest materials. Factors which directly influence the quality of WEDM are dielectric conductivity and machines setting parameters. In this paper the influence of dielectric conductivity, dielectric pressure, wire tension and number of passages on the surface roughness and waviness will be presented. Generator setting parameters of were chosen from the internal memory of Robofil 190 machine on which research were held.

1. Introduction

Asking a question "Who invented a electro discharge machining?" there is no simple answer, but it is commonly claimed that it was an invention of Russian scientists couple Natali and Borys Lazarenko. Very often few scientists make a research of the same problem − it this case it was the same, where invention of EDM was a long term process and not immediate development.

In electro discharge machining the removal of the material from the machined item is due to electric erosion which takes place during electric discharges between two electrodes. These electrodes are isolated by liquid dielectric. One of the electrodes is the machined item and the second one is the thin wire usually made of cooper, brass, tungsten or molybdenum with a diameter between 0,02 − 0,05 [mm]. The wire electrode is a single use, it reaches very high temperatures during machining due to electric discharges, than it gets cooled down because of heat exchange with liquid dielectric and finally put on second spool or destroyed by special wheels.

Materials, which can be machined by EDM, must conform to conductivity condition − their conductivity must be greater than 0,01 [S/cm]. To this group all metals and their alloys, big group of ceramic materials, composites can be assigned. Working electrode (wire) and machined item are connected to the impulse generator of constant current. Current intensity vary between 1 and 1000[A] and voltage between few tens to few hundreds volts. There are two types of polarity of working electrode and machined item depending on impulse course, parameters and material of which electrodes are made. "Simple" polarity is characterized by negative connection of working electrode (cathode) and machined item is an anode. Reverse polarity is a connection when machined item is a cathode.

Basic features of WEDM

- High accuracy of machining (between 0.02 and 0.001 [mm])
- High smoothness (by few finishing passages implementation)
- Possibility of materials machining independently of their hardness
- Big electrode universality
- Wire is constantly moved from the spool so there is no need of including an electrode use in the cutting process
- Ability of machining even very small details
- No danger of fire or explosion (dielectric is based on water)

In WEDM water is mostly used as dielectric due to it's low viscosity what influences the facility of cut material debris removal.

2. Research

Research were made using WEDM machine ROBOFIL 190 made by Charmilles Technologies (Pic. 1.). Biggest item that can be machined using Robofil 190 is cubicoid with dimensions of 400x250x400 [mm] and maximum angle of wire electrode relative to horizontal direction is +/- 30 deg. Productivity of the machine is up to 250 [mm^2/min] and it can be programmed manually by keyboard or by floppy disc. Material roughness and waviness were measured using FORM Talysurf Series 2 machine production of Taylor Hobson GB (Pic. 2).

Pic. 1. ROBOFIL 190 Machine

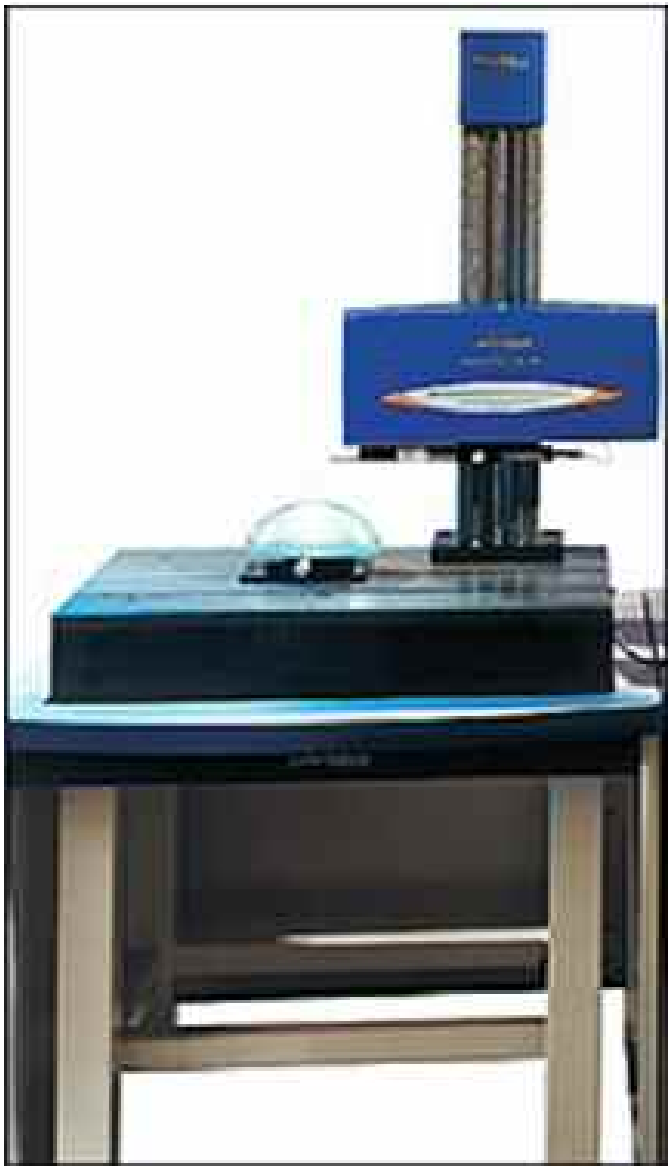

Pic. 2. FORM TALYSURF Series 2

Cubicoid, from which samples were cut, had a dimensions of 300x100x60[mm] and it was made of tooling steel NC 10 which was thermally treated to 62 HRC of hardness (Pic. 4.). This material is characterized by big resistance to grinding and it would be very hard to machine by any conventional method, furthermore for some methods it would be even impossible to machine. Elements which were cut off from the cubicoid had a dimension of 10x100x10 [mm] and they are shown in the picture 3. On shape which has left in the cubicoid further machining was performed. During research 25 samples were performed and for each of them different setting parameters were chosen.

Parameters which were changed:

- liquid dielectric conductivity
- liquid dielectric pressure
- wire tension
- number of wire passages

WEDM machine generator setting parameters were taken from the internal machine memory and they were identical for every machining, depending on the number of passages. Dielectric conductivities were respectively: 15, 40, 70, 100 and 150 [μS/cm], dielectric pressures: 0.6, 0.75, 0.9, 1.05 [MPa], wire tension was changed from 10 to 14 [N] with separation of 1 [N], number of wire passages was 1 for rough machining and 5 for a finishing machining.

Research matrix was based on method invented by Japanese engineer and statistic Genichi Taguchi and was generated using statistics program Minitab 15. In this software experiment matrix was created for four variables (conductivity, pressure, tension, number of passages) and five levels of these variables. Matrix for 25 runs was generated using mentioned method (it is also worth saying that if all possible combinations were run − there would be 625 of them).

After machining of all 25 samples their roughness and waviness was measured using Form Talysurf Series 2 machine in the direction that conformed to wire electrode run. Diagrams of primary profile, roughness and waviness of surface were obtained and measurements were taken on the length of 4 [mm]. To illustrate the results roughness diagram of sample no. 4 was shown in the picture 5 and waviness diagram in the picture 6.

Pic. 3 and 4. Respectively: one of the elements which was cut off from the base material and cubicoid

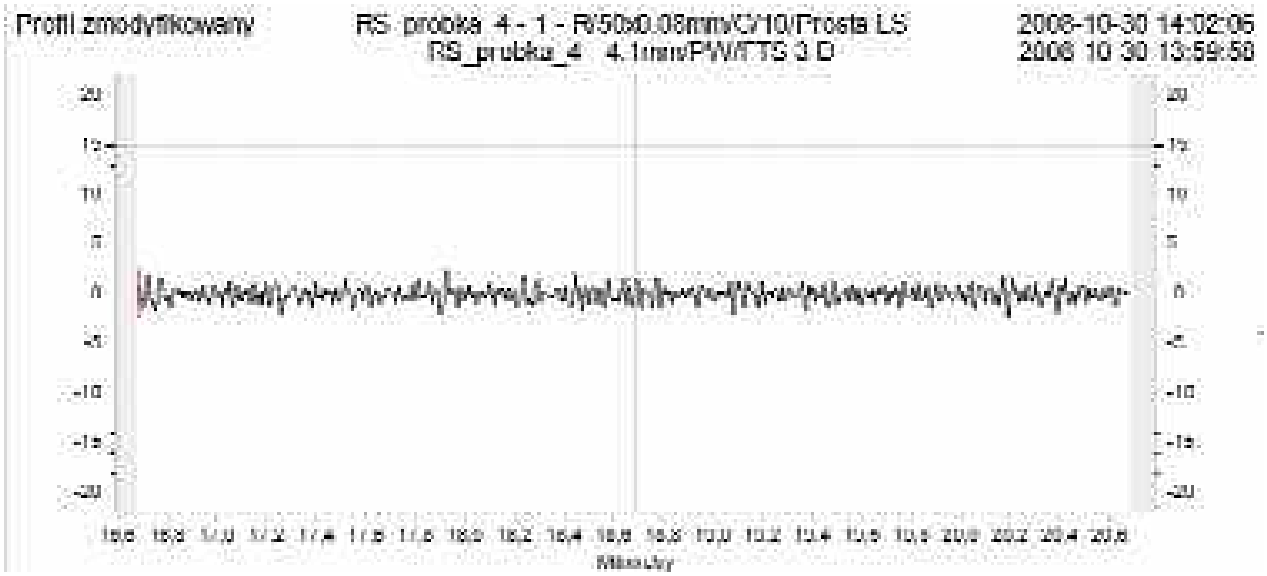

Pic. 5. Roughness profile of the sample no 4

Pic. 6. Waviness profile of the sample no 4

Table 1 shows the experiment matrix generated by Minitab software using Taguchi method with given values of surface roughness parameter *Ra* and waviness parameter *Wa* for every sample.

Table 1

Sample number	Dielectric conductivity	Number of passages	Dielectric pressure	Wire tension	Roughness parameter *Rs*	Waviness parameter Ws
	µS/cm		MPa	N	µm	µm
1	15	1	0,6	10	0,9712	1,171
2	15	2	0,75	11	0,7859	0,5198
3	15	3	0,9	12	0,5601	0,5341
4	15	4	1,05	13	0,547	1,7045
5	15	5	1,2	14	0,3438	1,3047
6	40	1	0,75	12	0,7837	1,05
7	40	2	0,9	13	0,6329	0,5501
8	40	3	1,05	14	0,4198	1,0948
9	40	4	1,2	10	0,4796	1,3427
10	40	5	0,6	11	0,3807	2,2676
11	70	1	0,9	14	0,763	0,6842
12	70	2	1,05	10	0,7954	0,7938
13	70	3	1,2	11	0,4937	0,6841
14	70	4	0,6	12	0,4166	3,4424
15	70	5	0,75	13	0,3089	3,2659
16	100	1	1,05	11	0,7854	0,8407
17	100	2	1,2	12	0,825	1,0803
18	100	3	0,6	13	0,3884	2,5237
19	100	4	0,75	14	0,4252	3,8492
20	100	5	0,9	10	0,3915	3,1242
21	150	1	1,2	13	0,7984	0,8376
22	150	2	0,6	14	0,7026	1,3787
23	150	3	0,75	10	0,4526	0,6192
24	150	4	0,9	11	0,3773	0,5542
25	150	5	1,05	12	0,415	1,2573

These values were put into the Minitab to check the influence of each of the four process variables into the surface roughness and waviness. Roughness diagrams are shown in the picture 7 and waviness parameter diagrams in the picture 8.

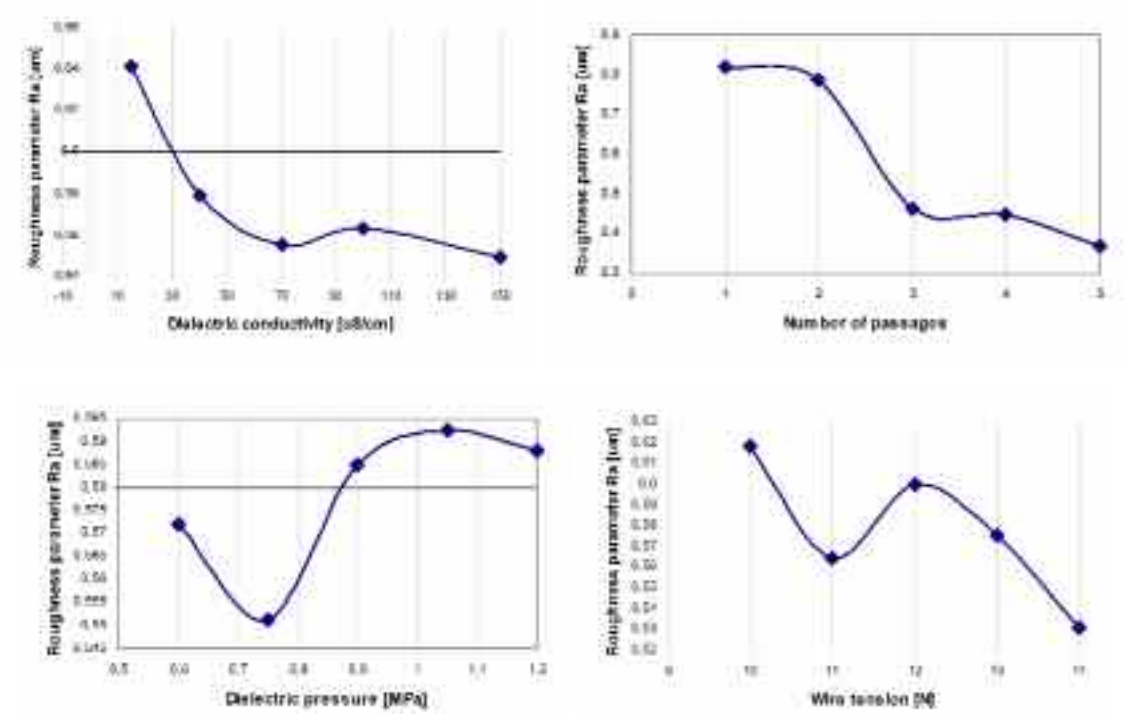

Pic.7. Diagrams showing roughness parameter Ra in the function of every of the 4 variables

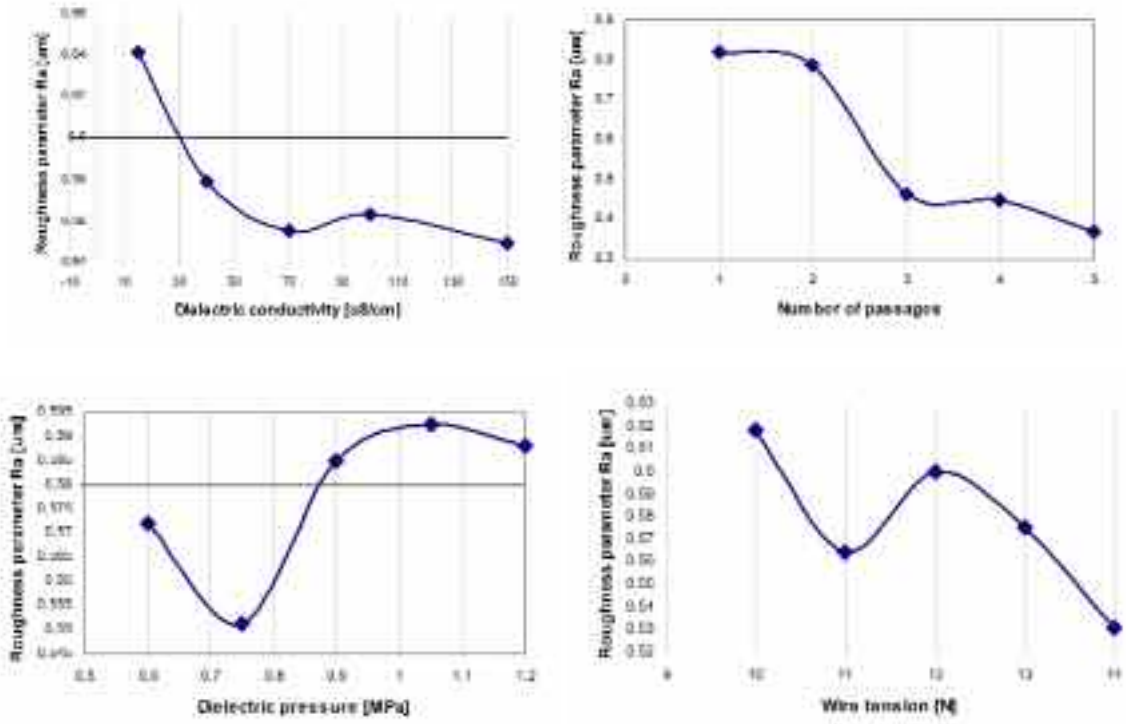

Pic.8. Diagrams showing waviness parameter Wa in the function of every of the 4 variables

The subject of future investigation will be to measure the influence of wire tension of samples barreling in the height direction using CNC measuring machine. Another part of research will be simulation of liquid dielectric flow in the working gap using computational fluid dynamics software in order to determine the optimal pressure and to understand how the base material debris are moved out of the working electrode.

3. Conclusion

The aim of the research was to measure how the machine setting parameters influence the quality of the surface of the cut. By quality it is meant roughness and waviness. The measure of the surface roughness is the roughness parameter *Ra* which can be expressed as medium arithmetic deviation of profile from the middle line:

$$Ra = \sum \frac{y_n}{n}, \tag{1}$$

Sample waviness was measured using the waviness parameter *Wa* in other words medium arithmetic deviation of waviness profile:

$$Wa = \frac{1}{n} \sum_{y=1}^{n} |h_{wi}|, \tag{2}$$

Conductivity − results which are presented by this variable seem to be the most interesting. It can be noticed that surface roughness decreases when dielectric conductivity increases. Very expensive dejonizators have been used on the WEDM machines, which purpose is to keep dielectric conductivity on specified low level, because it's been commonly claimed that this parameter has a key influence on electro erosive machining including roughness and waviness. Presented research show that idea of very low dielectric conductivity should be reconsidered. Picture 8 shows the influence of dielectric conductivity on the surface waviness. During conductivity increase from 20 to 100 [μS/cm] the waviness parameter increases than decreases to initial level. Conclusion is that liquid dielectric conductivity does not strongly influence the surface waviness so keeping conductivity at a very low level does not have a strong meaning even if *Wa* parameter value is crucial to the customer.

Number of passages − opposite to conductivity influence on surface waviness in this case increase of passage numbers has a negative influence to *Wa* parameter, so optimal solution would be to restrict the number of passages to 3. In terms of surface roughness the results seem to be obvious − every next wire electrode passage roughness decreases − that's the main reason of multiple wire passages.

Dielectric pressure − presented research proved that dielectric pressure doesn't have a measurable impact on surface roughness but it has an impact on the waviness − it decreases. It can be explained by the fact that bigger pressure at the machine dielectric nozzle stiffens the wire, so it vibrates with the smaller amplitude. Bigger pressure also causes that machined material debris are much faster removed from the working gap, what significantly influences the surface quality.

Wire tension − similarly to the pressure this variable also doesn't have a measurable impact on the surface roughness. It can be noticed that roughness parameter insignificantly decreases. It can be explained by the fact that more tensed wire vibration amplitude decreases what directly influences the roughness and waviness. In the waviness parameter diagram shown in the picture 8 it can be noticed that firstly *Wa* parameter value decreases and after reaching the value of 11[N] of wire tension is starts to increase. This can be the area of further research.

References

[1] Praca dyplomowa SS „Technologia elektroerozyjnego wycinania złożonych kształtów", promotor Lucjan Dąbrowski Warszawa 2003
[2] http://www.scemama.ch/Pdfs/2090027_EN.pdf
[3] Tadeusz Dobrzański „Rysunek Techniczny Maszynowy", WNT, Warszawa 2002
[4] Lucjan Dąbrowski, Internetowy podręcznik z obróbki elektroerozyjnej (EDM i WEDM), www.meil.pw.edu.pl/~edm/
[5] www.wikipedia.pl
[6] Minitab 15.1.0.0 Tutorials

R. Serwinski

WPŁYW PARAMETRÓW NASTAWCZYCH WYCINARKI ELEKTROEROZYJNEJ NA CHROPOWATOŚĆ I FALISTOŚĆ POWIERZCHNI CIĘCIA

Streszczenie

Obróbka elektroerozyjna pozwala na obróbkę nawet najtwardszych materiałów, przez co z łatwością można ją stosować w przypadkach gdzie zastosowanie konwencjonalnych metod obróbki jak na przykład frezowanie czy szlifowanie byłoby bardzo trudne lub nawet niemożliwe. Czynnikami, które bezpośrednio wpływają na jakość wycinania elektroerozyjnego (WEDM) są przewodność dielektryka oraz parametry nastawcze obrabiarki. W poniższej pracy zostanie przedstawiony wpły czterech zmiennych: przewodności dielektryka, ciśnienia dielektryka, naciągu elektrody roboczej oraz ilości przejść na chropowatość i falistość powierzchni cięcia. Parametry nastawcze generatora zostały dobierane z wewnętrznej pamięci obrabiarki Robofil 190 na której również przeprowadzana była obróbka.

USE OF PIEZOELECTRIC ELEMENTS IN COMPOSITE TORSIONAL SYSTEM WITH DYNAMIC VIBRATION ELIMINATOR

Michal Stepkowski
Institute of Aviation

Abstract

This article describes the outcome of author's Master Thesis written in the Institute of Machine Design Fundamentals of Warsaw University of Technology.

One of development directions of automotive industry is mass reduction. In many cases this is brought to change of material from conventional steel/aluminum to composite structures. This kind of change may have major influence on dynamic response of the system, resulting sometimes with higher vibration amplitude and/or moving system's natural frequencies into machine's operational speed range.

One of most common parts uprated this way is car's drive shaft. Following study concerns the problem of torsional vibration acting on composite shaft system and dynamic elimination of these vibrations. Starting with the physical model and its translation to mathematical model, results, system dynamics improvement, and benefits of chosen method are presented.

1. GENERAL DESCRIPTION

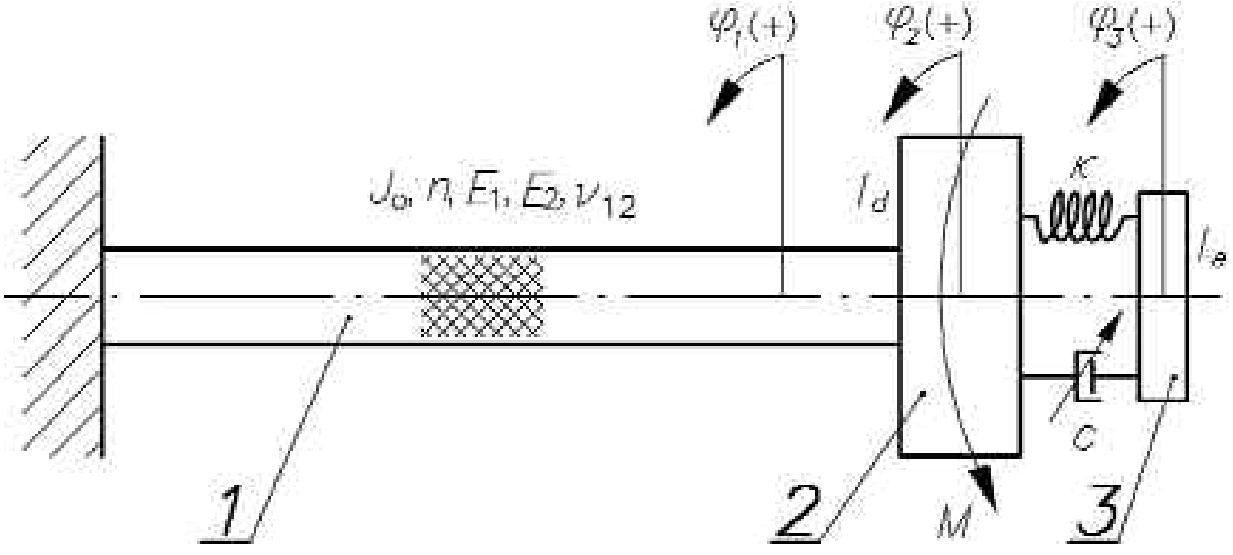

Picture 1. Physical model of considered system

Considered is n-layer laminated shaft treated as continuous system, and described by following physical properties: length l, Young's Modulus E_1 (in fibers direction) and E_2 (in direction

perpendicular to fibers), and Poisson's Ratio v_{12}. Shear Modulus in this case is a function of lamination angle and laminate's physical properties. Shaft's section is described with geometrical moment of inertia J_O. Shaft is fixed on one side and has a plate (discrete system) representing running gear properties attached to the other side. Plate is characterized by mass moment of inertia I_d. Sinusoidal moment *M* attached to the plate describes the reaction to loads that are taken by the engine. Eliminator described by mass moment of inertia I_e is attached to the plate by torsional spring (characterized by stiffness), and torsional damper (characterized by damping coefficient *c*). Connections between plate and eliminator are shown on picture 2.

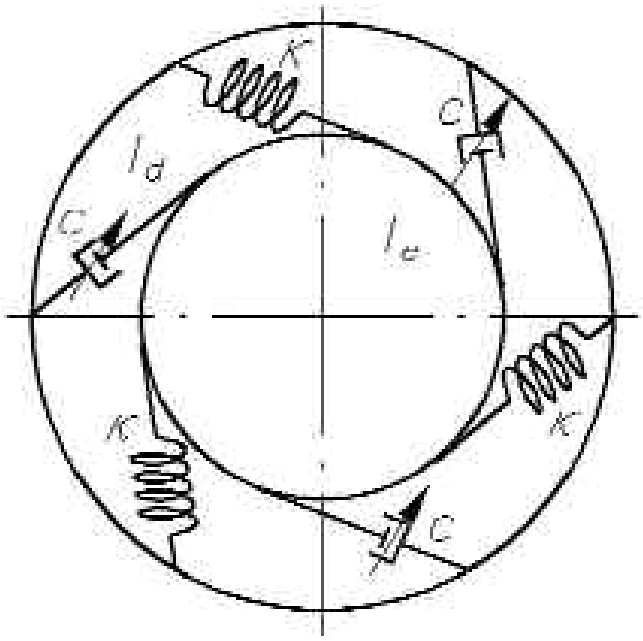

Picture 2. Joints between plate and eliminator

2. FORCED TORSIONAL VIBRATION OF LAMINATED SHAFT TREATED AS CONTINUOUS SYSTEM

Vibratory motion of considered system can be modeled with following equation [1]:

$$\rho J_o \frac{\partial^2 \phi}{\partial t^2} - G_{12} J_o \cdot \frac{\partial^2 \phi}{\partial x^2} - G_{12} T \cdot \frac{\partial^3 \phi}{\partial x^2 \partial t} = M(x,t) \tag{1}$$

where: - shaft's density, - eigenfunction, $M(x,t) = M_O \sin(vt)$, M_O – moment's amplitude, - inner damping.

Given inhomogeneous differential equation describes forced vibratory motion of continuous system with inner damping taken into account. In this case eigenfunction is a function of displacement (shaft's length) and time: (*x,t*).

Solution for equation (1) is amplitude given by formula (2):

$$\left|\vec{A}\right| = \left| \frac{M_o \cdot X_1}{X_2 \cdot (X_{e1} - X_{e2}) + X_1 \cdot (X_{e4} - X_{e2})} \cdot \left(e^{\frac{-\gamma}{a\sqrt{1-\gamma v}} x} - e^{\frac{+\gamma}{a\sqrt{1-\gamma v}} x} \right) \right| \tag{2}$$

where:

$$X_1 = \kappa + icv + I_e \cdot v^2 \tag{3}$$

$$X_2 = \kappa - icv \tag{4}$$

$$X_{s1} = -\kappa \cdot e^{-i\frac{v}{a}\frac{l}{\sqrt{1-i\gamma v}}} - icv \cdot e^{-i\frac{v}{a}\frac{l}{\sqrt{1+i\gamma v}}} \tag{5}$$

$$X_{s2} = -\kappa \cdot e^{+i\frac{v}{a}\frac{l}{\sqrt{1+i\gamma v}}} - icv \cdot e^{+i\frac{v}{a}\frac{l}{\sqrt{1-i\gamma v}}} \tag{6}$$

$$X_{s3} = -\kappa \cdot e^{-i\frac{v}{a}\frac{l}{\sqrt{1+i\gamma v}}} + icv \cdot e^{-i\frac{v}{a}\frac{l}{\sqrt{1+i\gamma v}}} - I_d v^2 \cdot e^{-i\frac{v}{a}\frac{l}{\sqrt{1+i\gamma v}}} - \frac{iG_{12}J_o v \cdot e^{i\frac{v}{a}\frac{l}{\sqrt{1-i\gamma v}}}}{a \cdot \sqrt{1+i\gamma v}} \tag{7}$$

$$X_{s4} = -\kappa \cdot e^{+i\frac{v}{a}\frac{l}{\sqrt{1+i\gamma v}}} + icv \cdot e^{-i\frac{v}{a}\frac{l}{\sqrt{1-i\gamma v}}} - I_d v^2 \cdot e^{+i\frac{v}{a}\frac{l}{\sqrt{1+i\gamma v}}} - \frac{iG_{12}J_o v \cdot e^{i\frac{v}{a}\frac{l}{\sqrt{1-i\gamma v}}}}{a \cdot \sqrt{1+i\gamma v}} \tag{8}$$

3. DATA USED FOR SIMULATION

For simulation of composite structure, epoxy/graphite laminate was chosen. This laminate is very popular in the industry because of its physical and strength properties. Following table briefly describes most important of these properties:

Table 1. Physical properties of epoxy/graphite laminate

Parameter	Value
E_1 [10^{11} Pa]	2.11
E_2 [10^{11} Pa]	0.053
G_{12} [10^{11} Pa]	0.026
ν_{12}	0.25
ρ [kg/m^3]	1560

Plate representing car's drive train, and eliminator's plate were modeled with steel. They are characterized with following properties:

Table 2. Physical properties of steel

Parameter	Value
ρ_s [kg/m^3]	7850
E_s [Pa]	$2.06 \cdot 10^{11}$
G_s [Pa]	$7.92 \cdot 10^{10}$

Considered shaft is treated as laminated structure with symmetrical layers. Number of orthotropic layers in this case is uneven (middle layer creates the plane of symmetry).
Following data was taken for simulation:

- shaft length l = 2 m. Shafts of this length appear in cars [2],
- shaft section described with outer radius r_Z = 0.04 m, thickness g_W = 0.8 mm, and number of layers n = 9;
- lamination angle = 45;
- orthotropic layer delay time describing inner damping: $_{11}$ = 0 (in fibers direction), $_{22}$ = 0 (perpendicular to fibers direction), $_{12}$ = 0.01 s (in shear direction);
- material data for composite and steel in accordance to tables 1 and 2;

- steel plate thickness l_d = 0,5 m (to calculate mass moment of inertia);
- moment's amplitude M_0 = 10 Nm. Because moment is proportional to torsional vibration amplitude, and the result is analyzed in relative scale (amplitude of one case is compared with amplitude of another case), moment's amplitude has no impact on the system, considering performed simulations.

Considered case is a study of vibration reduction, that's why shaft properties will remain unchanged. Variables in this system are: torsional damping coefficient c, torsional spring stiffness and eliminator's mass moment of inertia I_e. Because first natural frequency of the system is close to 750 rad/s, analysis is focused to that work area.

4. NUMERICAL SIMULATIONS RESULTS

Analysis of amplitude vs frequency charts for different values of c, , and I_e, allowed to choose following data for eliminator dimensions simulations: = 0.5S (where S is shaft's torsional stiffness $\frac{G_{12} \cdot J_o}{2 \cdot l}$), c = 50 Ns/rad, $I_e = I_d/5$. Semi-active change of damping is made by change of dimensions of rings made from zircon and titan oxidants (PZT ceramics). Rings are installed in torsional damper. In addition to that feature, spring will be switched on to the system using the same rule.

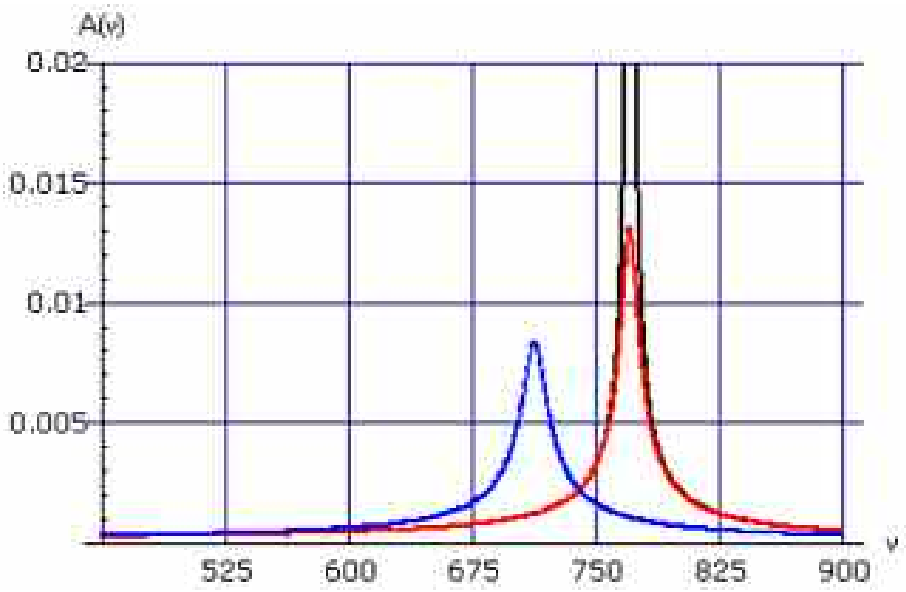

Picture 3. System's resonance characteristic: black curve is showing the system without eliminator, red curve – system with eliminator and with spring switched off ($_1$ = 0, c_1 = 1 Ns/rad, $I_e = I_d/5$), blue curve – system with eliminator and with spring switched on ($_2$ = S/2, c_2 = 50 Ns/rad, $I_e = I_d/5$).

System's parameters change strategy is brought to change of voltage that drives piezoelectric rings radial dimension change. This voltage change is made when red curve crosses the blue curve in the area of first natural frequency (picture 3).

What should be mentioned is the eliminator's moment of inertia effect on system's first natural frequency when spring is not connected. It is negligible. Using small values of damping coefficient (below c = 20 Ns/rad), curves representing system with and without eliminator are overlaid. Increase in damping coefficient result only with decrease in amplitude. Change of natural frequency can be seen only for higher values of c (above c = 20 Ns/rad). Because of that, one may assume that with relatively small damping, and spring not attached to the system, whole model in the area of first natural frequency acts like there is no eliminator at all.

5. CONCEPTUAL DESIGN OF SEMI-ACTIVE VIBRATION ELIMINATOR

Knowing the characteristic on which the amplitude of torsional vibration will be kept, one can try to estimate eliminator's dimensions and driving parameter changes strategy. As was mentioned, to allow the designed eliminator to semi-actively tune to the conditions dictated by system's dynamics, PZT ceramics will be used. Following table briefly describes this material:

Table 3. Physical properties of PZT (lead zirconate titanate) ceramics

Parameter	Symbol	Value
Density	ρ_{PZT} [kg/m^3]	7500
Young's Modulus	E_{PZT} [Pa]	$5 \cdot 10^{10}$
Piezoelectric Charge Constant	d_{31} [m/V]	$-170 \cdot 10^{-12}$
	d_{33} [m/V]	$400 \cdot 10^{-12}$
	d_{15} [m/V]	$500 \cdot 10^{-12}$

Picture 4 shows the concept of the eliminator – torsional dampener with spring attached.

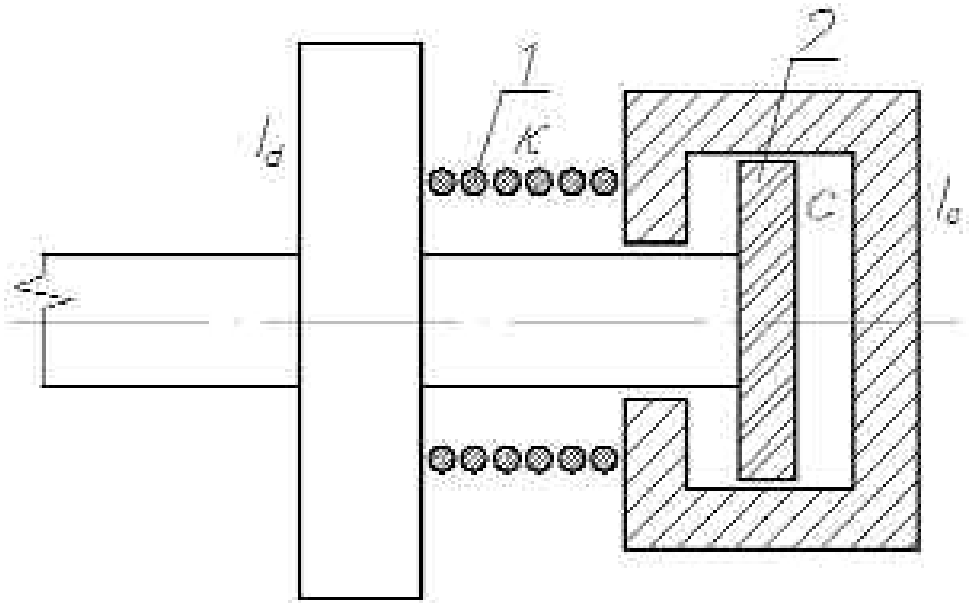

Picture 4. Conceptual design of eliminator

Torsional spring (1) which in the lower range of frequencies (below the limiting frequency for which the change of piezoelectric electrode polarization will be performed) would not be attached to the assembly, will be switched on also by piezoelectric components (frictional joint). Because of low inertia of the spring, one can assume that while being not attached to the system, spring don't have any influence to the overall assembly.

Change of damping will be performed by change of radial dimensions of ceramic rings (2), and in result by decreasing the gap between eliminator casing's inner diameter and PZT rings outer diameter.

6. DATA USED FOR SIMULATION

Following table holds the data used for simulation of designed eliminator's dimensions. Limiting frequency, at which we want to change PZT rings dimensions is a frequency, at which curves for parameters: $_1 = 0$, $c_1 = 1$ Ns/rad, and $_2 = 0$, $c_2 = 1$ Ns/rad are crossing.

Table 4. Data used for eliminator dimensions simulation

Parameter	Symbol	Value
Plate's Mass Moment of Inertia	I_d [kg/m^2]	0.0945
Eliminator's Mass Moment of Inertia	$I_e = I_d/5$ [kg/m^2]	0.0189
Spring Stiffness	$k_S = \frac{G_{gr} \cdot J_o}{2 \cdot l}$ [N/rad]	14400
Damping Coefficient For Bigger Gap	c_1 [Ns/rad]	1
Damping Coefficient For Smaller Gap	c_2 [Ns/rad]	50

Below, one can find the chart showing the result amplitude and the curves crossing point, which is amplitude's maximum point.

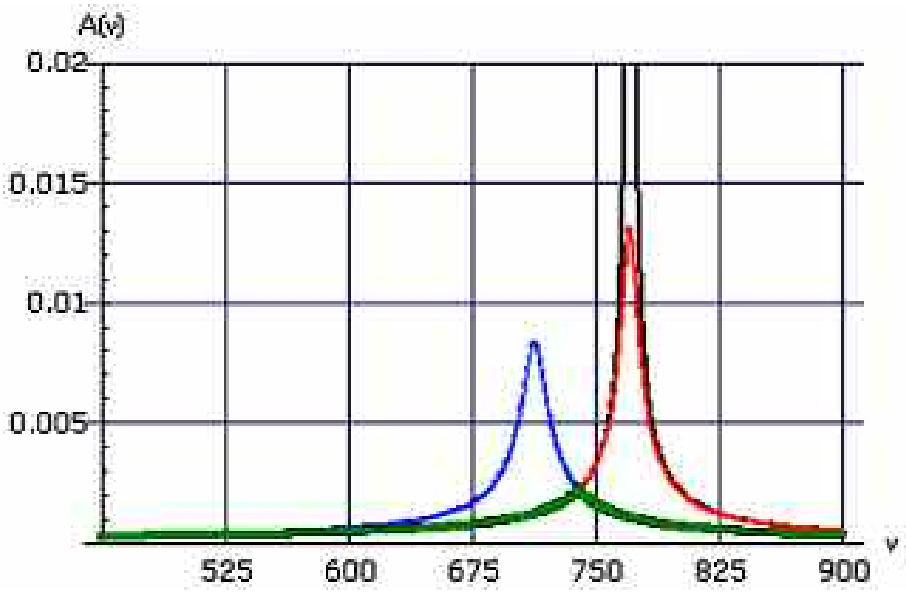

Picture 5. System's parameters change strategy: black curve is showing the system without eliminator, red curve - system with eliminator and with spring switched off, blue curve – system with eliminator and with spring switched on. Green color indicated resulting amplitude.

Searched frequency value is v_{gr} = 740 rad/s. Based on this value, scheme representing PZT Ceramics electrodes polarization change strategy can be shown.

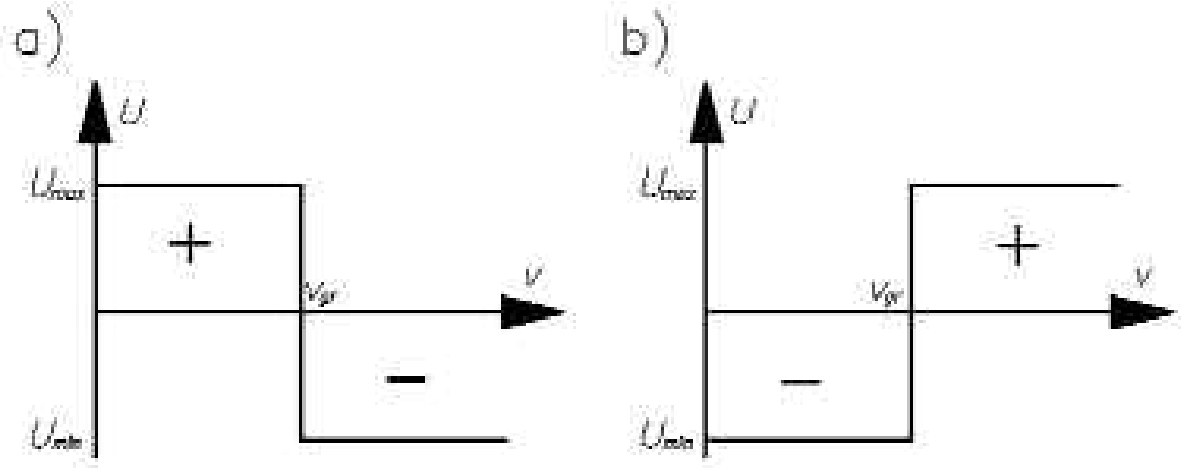

Picture 6. Piezoelectric elements electrodes polarization change strategy: a) for case of rings assembled on the shaft, b) for case of rings assembled on the casing's inner surface.

7. SUMMARY

Use of semi-active dynamic vibration elimination method allowed to obtain very gentle change of amplitude in studied frequency range (very sharp resonance was eliminated). Comparing to conventional dynamic elimination, following results were obtained:

three times smaller amplitude comparing to conventional eliminator characterized by following parameters: c = 50 Ns/rad, = $\frac{G_{12} \cdot J_o}{2 \cdot l}$ = 14400 N/rad,

five times smaller amplitude comparing to conventional eliminator using c = 1 Ns/rad, = 0.

What should be mentioned again is the must to switch the spring off the system when it's working below limiting frequency. If one would like to count only on inertia influence (that can be visualized by moving the curve created with eliminator taken into account, away from the curve created with eliminator not taken into account), obtained results would be unsatisfactory – results are almost the same as for conventional eliminator using the same parameters. Further increase in eliminator's inertia would result in bigger size of the overall assembly, that's why other solution was needed. Satisfactory results were obtained by periodic elimination of the spring from the system.

BIBLIOGRAPHY

[1] **Kurnik W., Tylikowski A.:** *Mechanika elementów laminowanych*, WPW, Warszawa, 1997

[2] **Pollard A.:** *Polymer matrix composites in driveline applications*, 3rd International Conference on Materials for Lean Weight Vehicles, Warwick, 1999

[3] **Przybyłowicz P.M.:** *Application of Piezoelectric Elements to Semi-adaptive Dynamic Eliminator of Torsional Vibration*, Journal of Theoretical and Applied Mechanics, 1999, 37: 319-334

Michal Stepkowski

WYKORZYSTANIE ELEMENTÓW PIEZOELEKTRYCZNYCH W ZŁOŻONYM SYSTEMIE SKRĘTNYM Z DYNAMICZNYM ELIMINATOREM DRGAŃ

Streszczenie

Poniższy artykuł opisuje wynik Pracy Magisterskiej napisanej w Instytucie Podstaw Budowy Maszyn Politechniki Warszawskiej.

Jedną z celów przemysłu samochodowego jest redukcja masy. W wielu przypadkach sprowadza się ona do zmiany materiału z konwencjonalnej stali bądź aluminium na kompozyt. Tego typu zmiana może mieć bardzo duży wpływ na na odpowiedź dynamiczną układu, co w wyniku może się objawić wyższą amplitudą drgań oraz/lub przesunięciem częstości własnych układu do zakresu prędkości pracy maszyny.

Jedną z najczęściej przeprojektowywanych w ten sposób części jest wał napędowy samochodu. Poniższa praca opisuje problem drgań skrętnych działających na układ z wałem kompozytowym oraz dynamicznej eliminacji tych drgań. Począwszy od modelu fizycznego i jego przełożenia na model matemetyczny, przedstawione są wyniki pracy, sposób poprawy dynamiki układu oraz zalety wybranej metody.

CURRENT CHALLENGES IN COMPUTATIONAL FLUID DYNAMICS WITH REGARD TO ROCKET ENGINE THRUST CHAMBER SIMULATION

Karol Swiderski
Institute of Aviation

Abstract

Aerospace industry is the first and most prevalent in the use of numerical techniques. It is worth mentioning that the beginning of CFD is dated for early 1960's and the first successes came to prominence in the 1970's. Creation of the CFD-service industry started in the 1980's and its significant expansion took place in the 1990's. In most phases of the development process the aerospace industry was driving CFD to answer to its needs.

In the past decade Computational Fluid Dynamics (CFD) became a common tool in applied aerospace where many different numerical techniques are currently used. The main areas are in the geometrical definition (CAD) of the model which is to be analysed, the computational solution of the flow field (Mesh generation and CFD) including grid adaptation which may be further combined with other disciplines like shape optimisation, structural analysis and so forth. The scientific area of CFD includes technical advances for accurate numerical methods for resolving flow phenomena and realistic physical modeling of the flow itself. CFD can be defined as the analysis of systems involving fluid flow, heat transfer and associated phenomena such as chemical reactions by means of computer-based simulation. In all cases the key factor is the discrete continuum representation.

With regard to rocket applications modeling and numerical simulation allows qualitative and/or quantitative analysis of processes difficult to analyse experimentally. This paper presents useful hints to handle complex flows and their setup for a successful solution and the mathematical basis behind the industrial application which allow further developments for rocket applications.

INTRODUCTION

The history of CFD started in the period of 1965-1975. Around that time, it became a combination of physics, numerical mathematics, and, to some extent, computer sciences employed to simulate fluid flows. The first application of the CFD methods was the simulation of transonic flows based on the solution of the non-linear potential equation [1; 2; 3]. With the beginning of the 1980's, the solution of first two-dimensional (2-D) and later also three-dimensional (3-D) Euler equations became feasible. Thanks to the rapidly increasing speed of supercomputers and due to the development of a variety of numerical acceleration techniques like multigrid, it was possible to compute inviscid flows. With the mid 1980's, the focus started to shift to the significantly more demanding simulation of viscous flows governed by the Navier-Stokes equations. CFD has now matured to the point at which it is widely accepted as a key tool for complex design such as rocket. The complexity and range of phenomena is well illustrated in [4].

Rocket propulsion CFD has, in general, lagged behind aeronautical applications. Complexity of the flow physics and hardware geometry involved in rocket engines probably delayed the application of CFD to this area. One of the most significant applications of CFD simulation to rocket engines began in the early 1980's, when NASA carried out a series of upgrades to the Space Shuttle main engine (SSME), developed in the 1970's.

Algorithms have been the subject of intensive development for the past two decades. The principles underlying the design and implementation of robust schemes which can accurately resolve shock waves and contact discontinuities in compressible flows are now quite well established. Despite this, CFD is still not being exploited as effectively as one would like in the design process. This is partially due to the long set-up times and high costs, both human and computational, associated with complex flow simulations. The essential requirements for industrial use are:

- assured accuracy
- acceptable computational and human costs
- fast turn around.

Improvements are still needed in all three areas. Several routes are available toward the reduction of computational costs, including the reduction of mesh requirements by use of higher order discretization schemes, improved convergence to a steady state by sophisticated acceleration methods, fast inversion methods for implicit schemes, and the exploitation of massively parallel computers.

DESIGN PROCESS AND CFD

The design process can generally be divided into three phases: conceptual design, preliminary design, and final detailed design. Improvements in CFD which would allow the elimination of a major cycle in preliminary design would significantly shorten the overall design process and therefore reduce costs.

Many critical phenomena of fluid flow, such as shock waves and turbulence, are essentially nonlinear. They also exhibit extreme disparities of scales. Moreover computational costs vary drastically with the choice of mathematical model. The computational simulation of fluid flow presents a number of severe challenges for algorithm design. At the level of inviscid modeling, the inherent nonlinearity of the fluid flow equations leads to the formation of singularities such as shock waves and contact discontinuities. When viscous effects are also included in the simulation, the extreme difference of the scales in the viscous boundary layer and the outer flow, which is essentially inviscid, is another source of difficulty, forcing the use of meshes with extreme variations in mesh interval. For these reasons CFD, has been a driving force for the development of numerical algorithms.

The algorithm designer faces a number of critical decisions. The first choice that must be made is the nature of the mesh used to divide the flow field into discrete subdomains. The Cartesian mesh minimises the complexity of the algorithm at interior points and facilitates the use of high order discretization procedures, at the expense of greater complexity, and possibly a loss of accuracy, in the treatment of boundary conditions at curved surfaces. This difficulty may be alleviated by using mesh refinement procedures near the surface. With their aid, schemes which use Cartesian meshes have recently been developed to treat very complex configurations [5; 6].

Rocket engine thrust chamber design provides many challenges:

- spray combustion process encompasses many physical processes of different types, temporal and spatial scales, tightly coupled to each other (two-phase mixing, combustion, turbulence, kinetics, instabilities) making environment definition and modeling very difficult
- extremely high heat loads require exotic materials and active cooling
- transient phenomena can lead to severe instabilities in the combustor and nozzle
- performance and durability issues require trade-offs and limit the design envelope

- test data are difficult and very expensive to obtain.

Engineering challenges and technology needs include:
- ability to rapidly predict the flow and thermal environment in the combustion chamber (another CFD challenge – dynamic grid adaptation; highly efficient solvers for 3D transient mixed flows; workable turbulence models; mechanistic combustion models and correlations; PC-based parallel computing capability and large database management and postprocessing technologies)
- interfacing CFD predicted flow and thermal environments and loads with stress and structural dynamics codes and material databases to select materials and coatings, yield and failure limits, active cooling requirements, and margins of safety (triple challenge – CFD has to provide what material scientists and stress engineers need, and they have to understand CFD's limitations and areas of uncertainty)
- chamber durability and injector performance
- combustion stability especially with hydrocarbon based fuels
- acquiring safety test data and experiments to validate models and predictions.

Computational fluid dynamics analyses have been successfully applied in areas related to the prediction and simulation of combustion flow behavior and heat transfer to the internal walls of rocket engine injectors, combustion chambers, and nozzles. These analyses have been used to optimize nozzle entrance geometries, evaluate new step nozzle exit configurations that adapt to altitude changes, determine pressure and temperature profiles in rocket engine chambers and nozzles, and to study the effects of coolant flows in liquid rocket engine chambers on internal walls. These analytical procedures have helped to evaluate anomalies discovered in actual engine firings and to design reliable combustion chamber, nozzle, and coolant arrangements that result in high thrust coefficients under various atmospheric and space conditions. Computational fluid dynamics simulations have also been useful in determining pressure, heating, and insulation requirements for launch vehicles during liftoff, ascent, and reentry into the atmosphere.

CHALLENGES AND POSSIBILITIES

CFD capabilities have been advanced along with computational technologies in general. Many fluid engineering problems can now be simulated, however these are mostly at a single-component level. For instance, it is possible to generate solutions to problems like a combustion chamber or turbopump. To realize the full benefits of CFD, more inclusive modeling will be required, such as systems of pumps; in general coupling of subsystems which are dependent on each other. Attempts to solve these types of problems have been made with some qualitative successes. However, the predictive capability is still very limited, and prediction with accurate physics is yet to be accomplished. This will require inclusion of not only fluid dynamics modeling but modeling of other quantities like thermal loading, turbulence and transition prediction, droplet formation, separation and cavitation physics.

Future development of rockets will rely heavily on system level thinking, robust design principles, multidisciplinary analysis and optimisation, and on the use of high fidelity predictive tools even in the conceptual design cycle. Development testing will be significantly reduced in favour of large scale, high fidelity simulations and virtual engineering practices.

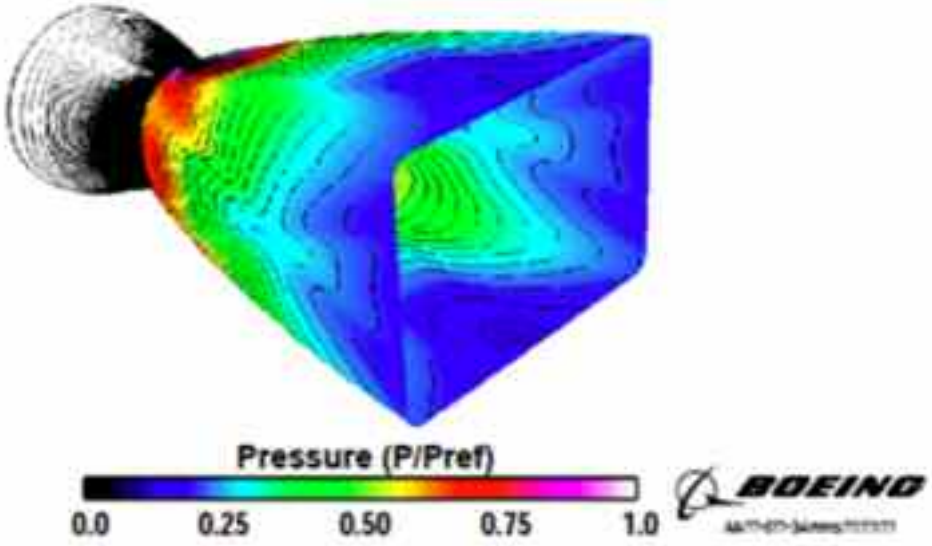

Fig. 3. X-33 thruster analysis [7]

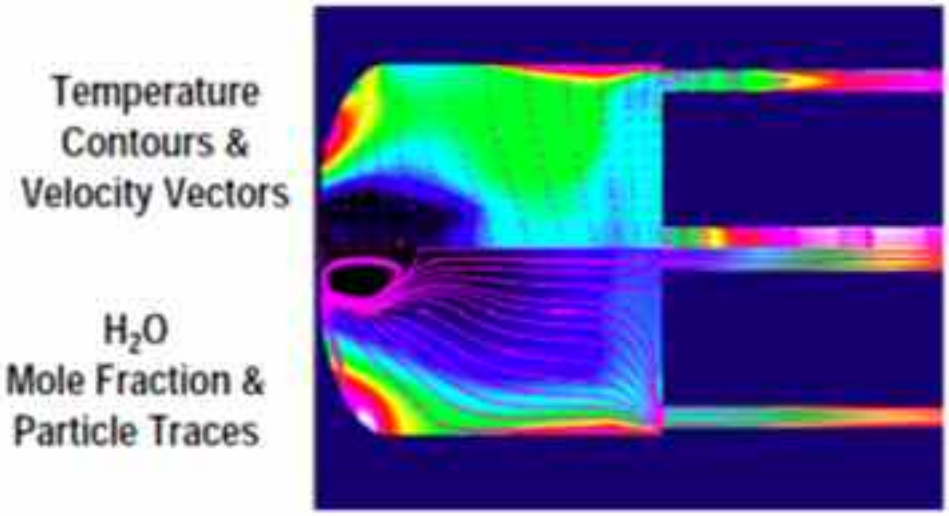

Fig. 4. Hybrid engine combustion chamber [7]

REFERENCES

[1] **E.M. Murman, J.D. Cole.:** *Calculation of plane steady transonic flows*. AIAA Journal. 1971.
[2] **Jameson, A.:** *Iterative solution of transonic flows over airfoils and wings, including flows at Mach 1*. AIAA 2nd CFD Conference. 1975.
[3] **Eberle, A.:** *A finite volume method for calculating transonic potential flow around wings from the minimum pressure integral*. NASA TM 75324. 1978.
[4] **Dyke, M. Van.:** *An album of fluid motion*. The parabolic press, Stanford. 1982.
[5] **J.E. Melton, S.A. Pandya, J.L. Steger.:** *3D Euler flow solutions using unstructured Cartesian and prismatic grids*. AIAA Paper 93-0331. 1993.
[6] **M. Berger, R.J. LeVeque.:** *An adaptive Cartesian mesh algorithm for the Euler equations in arbitrary geometries*. AIAA Paper 89-1930. 1989.
[7] **Boeing.** Overwiew of the state-of-the-practice Liquid Propellant Rocket Engine Design, Analysis, and Test. *AFOSR Conference.* 2004..

Karol Swiderski

AKTUALNE WYZWANIA DLA KOMPUTEROWEJ MECHANIKI PŁYNÓW W ODNIESIENIU DO SYMULACJI KOMORY SPALANIA I DYSZY SILNIKA RAKIETOWEGO

Streszczenie

Przemysł lotniczy przoduje w zastosowaniach i najszerzej wykorzystuje techniki numeryczne. Warto wspomnieć, że początki metody CFD datowane są na początek roku 1960, a jej pierwsze sukcesy zostały wyeksponowane w roku 1970. Tworzenie branży usług CFD rozpoczęło się w roku 1980 a jej znaczne rozszerzenie miało miejsce w roku 1990. W większości etapów rozwoju branży CFD przemysł lotniczy zmuszał ją do udzielania odpowiedzi na swoje pytania.

W ostatnim dziesięcioleciu Computational Fluid Dynamics (CFD) stała się powszechnym narzędziem w obszarze kosmonautyki stosowanej, gdzie obecnie zastosowanie znajdują różne techniki obliczeń numerycznych. Główne obszary zastosowania metody to definicja geometrii analizowanego modelu (CAD), rozwiązania obliczeniowe w polu przepływu (generowanie siatki i CFD), w tym dostosowywanie siatki, które może być połączone dalej z innymi dyscyplinami, takimi jak optymalizacja kształtu, analiza strukturalna, itd. Obszar zastosowań naukowych CFD obejmuje rozwój dokładnych metod numerycznych do rozwiązywania zjawisk przepływu i realistyczne modelowanie fizyczne samego przepływu. Metodę CFD można określić jako analizę systemów przeprowadzaną za pomocą symulacji komputerowych z udziałem przepływu płynów, wymiany ciepła i związanych z nimi zjawisk, takich jak np. reakcje chemiczne. We wszystkich przypadkach, kluczowym czynnikiem jest dyskretna reprezentacja continuum.

W odniesieniu do zastosowań techniki rakietowej, numeryczne modelowanie i symulacja pozwalają na jakościową i/lub ilościową analizę procesów, które trudno jest analizować doświadczalnie. W pracy przedstawiono wskazówki przydatne do modelowania skomplikowanych przepływów oraz ich konfigurowania, które zapewnią pomyślne ich rozwiązywanie oraz matematyczne podstawy dla zastosowań przemysłowych, umożliwiające dalszy rozwój metody dla zastosowań rakietowych.

STRENGTH ANALYSIS OF NITRIDED LAYERS ON AUSTENITIC STAINLESS STEEL BASED ON ACOUSTIC EMISSION (AE) MEASUREMENTS

Jan Wojnar
Institute of Aviation

Summary

The aim of this work was to characterize deformation and failure mechanisms of layers formed during nitriding on austenitic stainless steel. The characterization was based on acoustic emission measurements performed during the static tensile test. The experimental work included the plasma nitriding process of stainless steel grade 304 samples, microhardess measurements, microstructural investigation and XRD phase analysis. The main investigation technique used was the acoustic emission measurement. The acoustic characteristics - RMS voltage, and energy, have turned out to be especially useful, as they enable to determine the real yield limit, the exact stress-strain conditions of fracture initiation at the nitrided surface and the dynamics of the fracture progress.

1. INTRODUCTION

Austenitic stainless steels are broadly used in the industry, as they are well known for their excellent corrosion resistance. However, their applicability is often constraint by their relative low mechanical properties, in particular, low hardness (< 215HB) and wear resistance. These properties can be improved by various surface hardening techniques. The Ion nitriding process has been shown in many publications as an effective solution for improving the surface characteristics of stainless steels.

The chemical and phase composition of nitrided layers formed on austenitic stainless steels differs much from typical nitrided layers that are formed on ferritic tool steels. For this reason detailed studies are required in order to characterize their properties and find optimal processing parameters.

It has been shown that the most beneficial surface properties can be obtained by low temperature plasma nitriding (below 500˚C). Stainless steels processed in this way show a significant increase in hardness while keeping their desirable corrosion resistance. This improvement has been attributed to the formation of the so called, single „m-phase" zone at the surface. The „m-phase" is a metastable iron nitride phase with a tetragonal body centred (TBC) crystallographic structure.

This paper focuses on the phenomena taking place during plastic deformation of the material. The main investigation method used was the acoustic emission measurement. This method allows registering *in situ* signals generated by microstructural phenomena taking place in the material under applied load. In a stressed material internal energy is stored, which under certain circumstances is being released by local phenomena (e.g. micro crack propagation, dislocations

movement), so called AE origins. That energy generates transient acoustic waves propagating through the material and can be registered by acoustic sensors. Detailed analysis of these signals allows describing the phenomena taking place in the stressed material. The goal of this work was therefore:

- to describe plastic deformation and cracking mechanisms of nitrided layers in correlation with the behaviour of the bulk material
- to define load conditions leading to failure of the nitrided layers

2. EXPERIMENTAL

The base material was AISI type 304 austenitic stainless steel. Flat tensile test samples with the geometry shown in Fig.1 have been laser cut from sheet. The samples have been shot-peened with glass beads. Ion sputtering has been applied to clean and activate the surface. A conventional DC ion nitriding process has been used with parameters shown in Tab.1. The cooling has taken place under vacuum.

The thickness of nitrided layers has been measured on metallographic cross sections. Vickers microhardess tests of the surface have been carried out at 0.2 kgf load (HV0.2) and 15 s indentation time. Qualitative XRD phase analysis has been performed on the Philips PW 1140 diffractometer equipped with a cobalt X-ray source with a wave length CoK_1 equal to 0,178897 nm. The static tensile test has been run on Zwick/Roell Z005 universal testing machine at a test speed of 1.5 mm/min.

Table 1. Nitriding process parameters of AISI type 304 stainless steel

Sample designation	Process	Number of samples	Temperature [°C]	Time [h]	Processing atmosphere	
					Gas proportion (vol.)	Pressure [hPa]
SW	raw sample	3	-	-	-	-
-	ion sputtering	-	550	1	$Ar:H_2$ – 1:4	1.5
430_2h	nitriding	3	430	2	$N_2:H_2$ – 1:1	2.5
430_8h	nitriding	3	430	8		

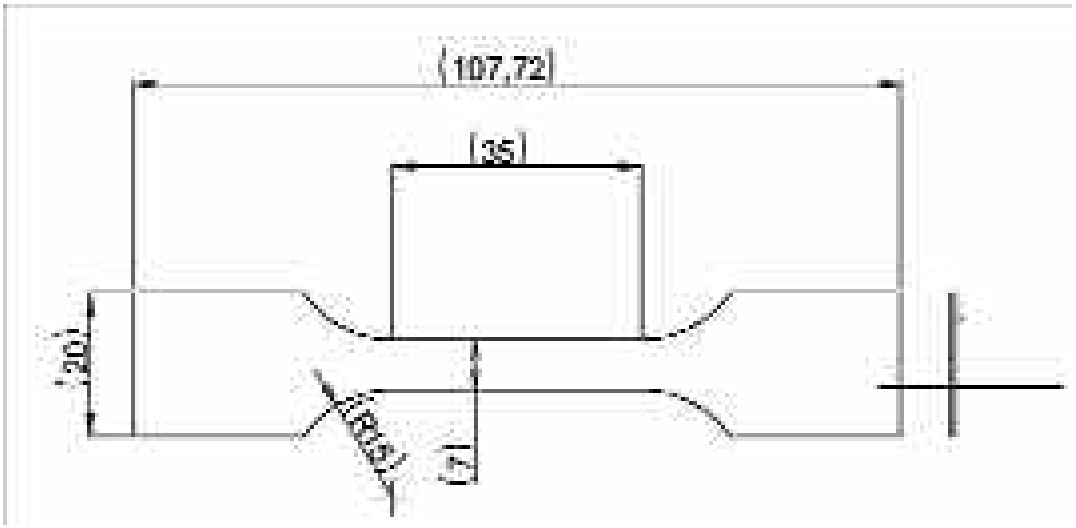

Fig. 1. Geometry of test samples

Acoustic emission measurements have been carried out during the tensile tests, using the AE equipment AMSY-5 Vallen Systeme GmbH with preamplifiers AEP4 (amplification 34dB) and broadband acoustic sensors M31-FUJICERA with a detection range up to 1,5MHz. As frequency filters have been applied, the actual detection range was 95 – 850 kHz. The fractographic examination has been carried out on the HITACHI S-2600N scanning electron microscope.

3. RESULTS AND DISCUSSION

Microstructural characteristics and mechanical properties have been shown on Fig. 2 and Table 2. It could be observed that ion nitriding led to the formation of surface layers with m-phase structure. The layer thickness of samples treated for 8 hours was around 10m and was about 30% thicker than the thickness of layers formed after 2 hours. The influence of the nitriding treatment on tensile properties was negligible, however after nitriding a significant hardness increase to values exceeding 800HV0.2 has been observed.

Table 2. Structure and mechanical properties

	Layer Thickness[μm]	Phase Composition	Microhardness [HV0,2]	Tensile Strength [MPa]	Total Elongation [%]
SW	-	γ, martensite	351 ± 34	709.7	71.3
430 2h	6 – 8	m-phase, γ	864 ± 103	710.0	70.3
430 8h	9 – 12	m-phase, γ	837 + 83	707.3	71.2

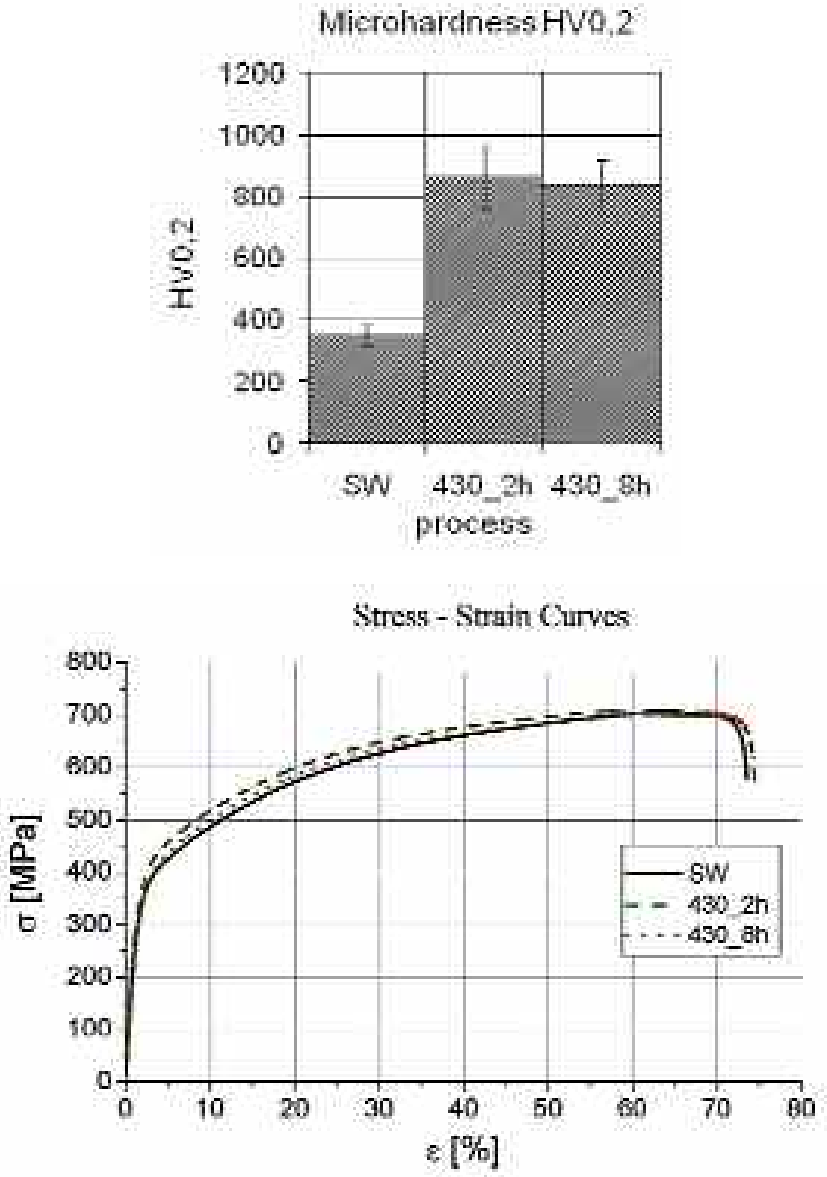

Fig. 2. Mechanical properties of the investigated samples

Fractographic examination of the fracture surface and the free surface of the raw sample has shown a ductile character of the deformation and fracture (Fig. 3.a. and 3.b.). On the other hand, SEM images of nitrided samples have shown a brittle fracture surface of the nitrided layer and a ductile one of the bulk material (Fig. 3.d and Fig. 3.f).

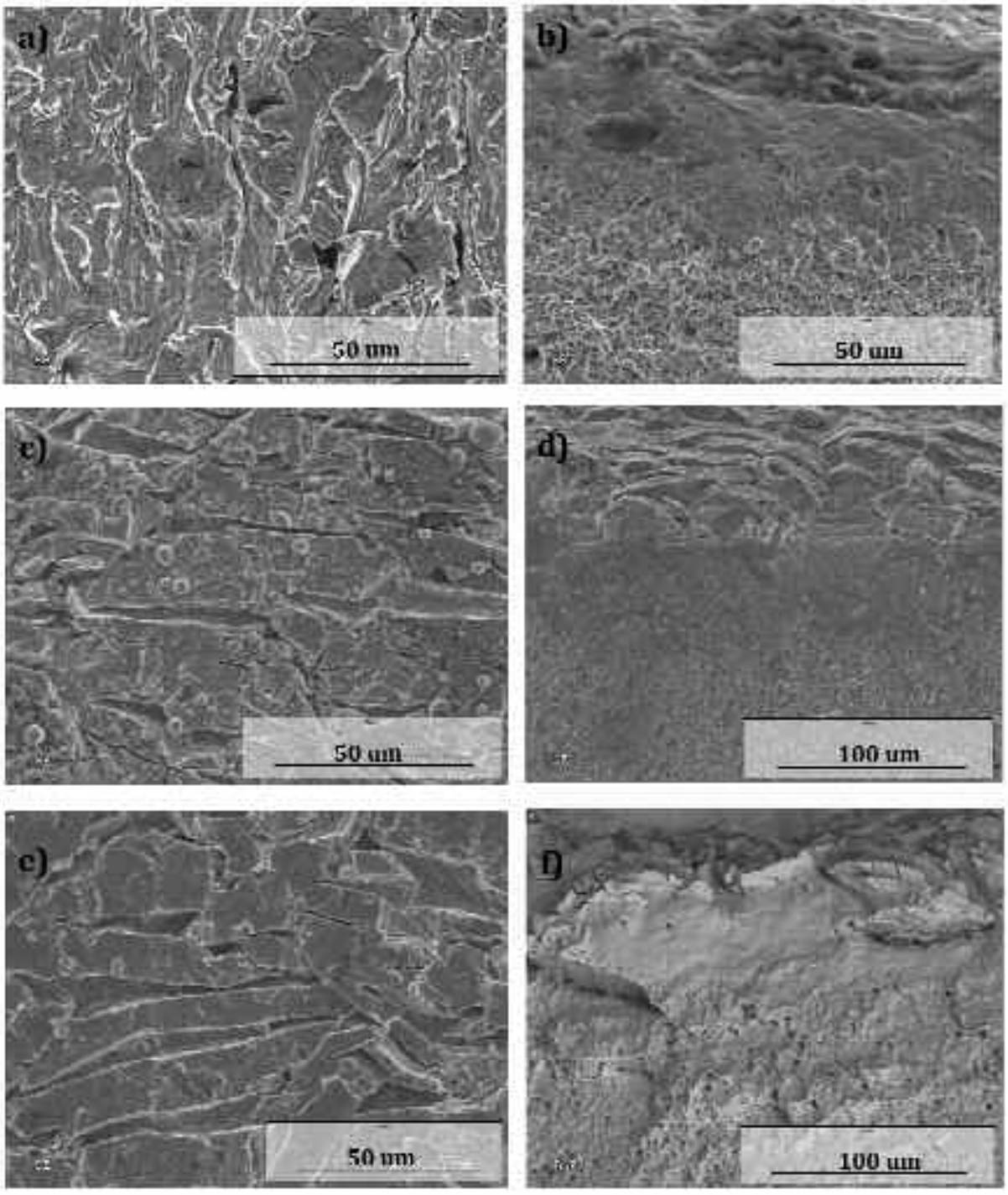

Fig. 3. SEM images after the tensile test: a,b) the topography and fracture surface of the raw sample; c, d) the topography of the layer and the fracture surface of samples nitrided for 2h; e, f) the topography of the layer and the fracture surface of samples nitrided for 8h

The examination of free surfaces of these samples has revealed in the nitrided layer a dense network of microcracks perpendicular to the surface. Worth mentioning is the fact that the SEM images of samples nitrided for 2 hours and for 8 hours looked very similar, which indicated that the deformation processes in both sample series must have been very similar as well.

AE energy and RMS voltage in function of time of the tensile test (Fig. 4) were the most useful acoustic emission characteristics in the analysis of deformation and cracking of the test samples. To allow a confrontation of AE with the load, tensile force vs. time has also been placed on these graphs.

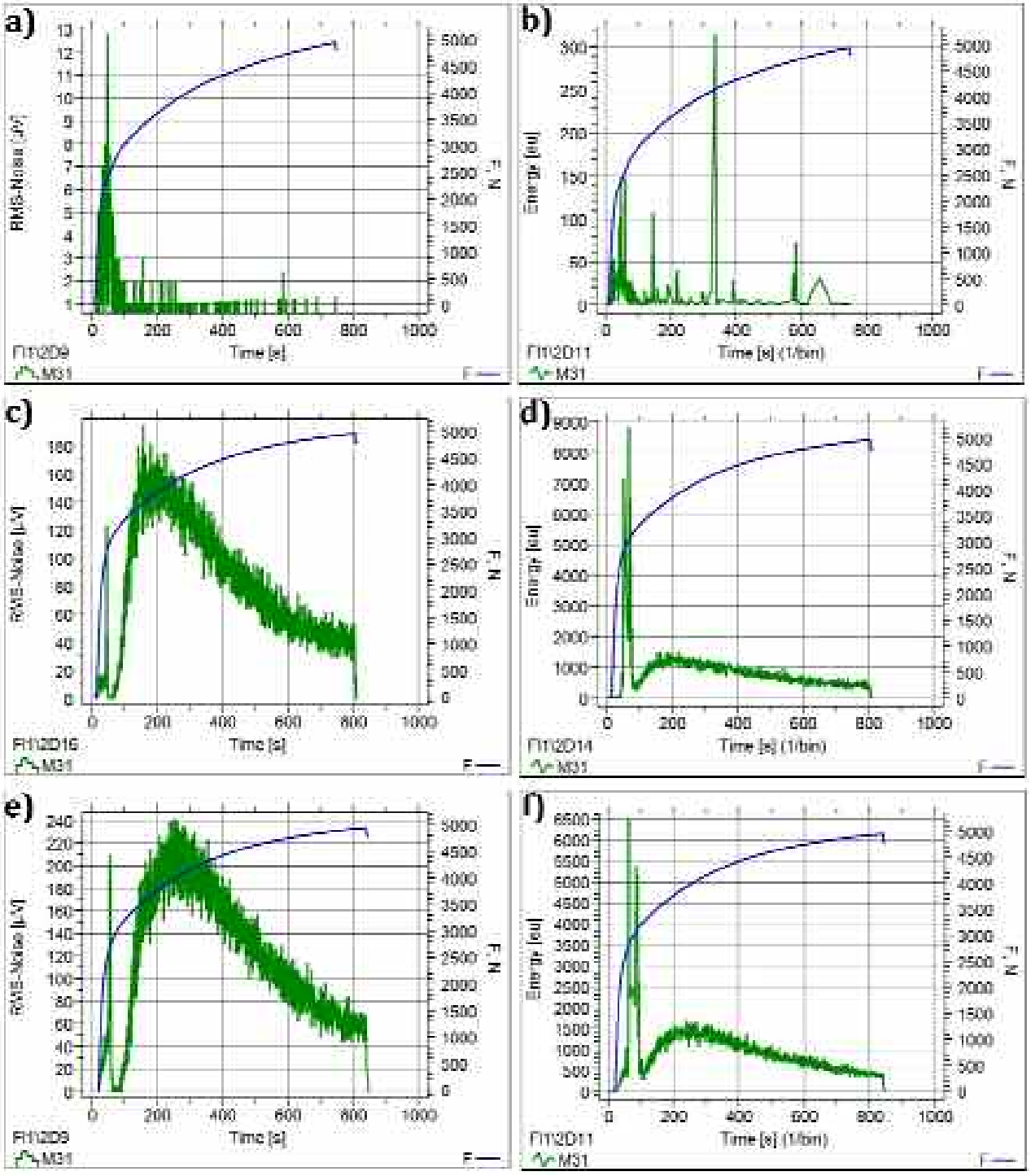

Fig.4 Selected acoustic emission history graphs: a, b) RMS voltage and AE energy in the raw sample; c, d) RMS yoltage and AE energy in the sample after 2 hours nitriding; e, f) RMS voltage and AE energy in the sample after 8 hours nitriding

The RMS voltage of the AE signals, which has been registered for the range of low amplitudes (below the threshold level) has provided valuable information about the general level of acoustic activity, in particular, the level of co called continuous emission, that is usually generated by plastic flow.

On the other hand, the EA energy, that is proportional to the energy released by particular EA origins, has provided useful information about the so called transient emission, which is usually generated by sudden microstructural changes, like crack propagation and delamination.

Test results of the raw sample (Fig. 4.a. and 4.b.) have shown one single maximum of both AE parameters, RMS and energy, close to the yield limit, which has indicated the initiation of plastic flow. During further plastic deformation AE was at a very low level.

The results of the nitrided samples, otherwise than the raw sample, have shown a high level of RMS and energy registered in the plastic region (Fig. 4.c.-4.f.). That has indicated that this emission must have been related with the presence of the nitrided layer and mechanism taking place in that layer. Confronting these results with the fractographic examination has led to the conclusion that the acoustic emission recorded in the plastic region must have been related with the formation of the observed microcrack network, and that the microcracks at the surface formed and propagated in the whole plastic region of the tensile test.

Worth mentioning is also the presence of two maxima of the AE energy at a load close to the yield limit (Fig 4.d. and 4.f.). The first maximum of energy has taken place simultaneously with the maximum of the RMS voltage, which, similar like in the raw sample, has indicated the initiation of plastic flow of the sample material. The second maximum of the energy however has been accompanied by a significant reduction of the RMS voltage. That has indicated the presence of high energy transient signals, thus most probably the initiation of multiple cracking of the nitrided layer. In the sample nitrided for 8 hours this maximum has taken place at a higher strain than in the sample nitrided for 2 hours, which, according to the above interpretation, would indicate a higher strength of the layer formed after 8 hours nitriding.

4. CONCLUSIONS

Based on the results the following could be concluded:

- Low temperature nitriding did not have any adverse effect on the tensile strength of the test samples.
- Cracking of the nitrided surface layer has been initiated beyond the yield limit of the bulk material, and further initiation and propagation of microcracks at the surface has continued till the final break of the sample.
- The most valuable information, that can be obtained via AE measurements for surface hardened materials during the tensile test are:
- The real yield limit of the bulk material and load conditions leading to crack initiation of the hardened layer
- The character of the cracking progress of the hardened layer

5. ACKNOWLEDGEMENTS

This work is based on the MSc thesis [1] performed under the supervision of dr inż. Janusz Bucki (Warsaw University of Technology, Dep. of Materials Science and Engineering), and was part of the project PBZ-4/RM-7/2004.

6 REFERENCES

[1] **J.Wojnar:** *Badania zjawisk emisji akustycznej zachodzących podczas odkształcenia plastycznego i pękania warstw azotowanych na stali austenitycznej*, Praca magisterska, prom. J. Bucki, Wydział Inżynierii Materiałowej Politechniki Warszawskiej, 2007

[2] **L. Dobrzański:** *Metalowe Materiały Inżynierskie*, Wydawnictwo Naukowo Techniczne, Warszawa, 2004, s.321-336

[3] Norma PN-EN 10088-1: 2005(u)

[4] **E. Menthe, A. Bulak, J. Olfe, A. Zimmermann, K.T. Rie:** *Improvement of the mechanical properties of austenitic stainless steel after plasma nitriding*, Surface and Coatings Technology 133-134 (2000), s. 259-263.

[5] **B. Larisch, U. Brusky, H.-J. Spies:** *Plasma nitriding of stainless steels at low temperatures*, Surface and Coatings Technology 116–119 (1999), s. 205–211

[6] **V. Singh, K. Marchev, C.V. Cooper, E.I. Meletis:** I*ntensified plasma-assisted nitriding of AISI 316L stainless steel*, Surface and Coatings Technology 160 (2002), s. 249 – 258.

[7] **Wang Liang:** *Surface modification of AISI 304 austenitic stainless steel by plasma nitriding*, Applied Surface Science 211 (2005), s. 308-314.

[8] Standard Definition of Terms Relating to Acoustic Emission, Philadelphia, PA: *American Society for Testing and Materials* (ASTM) (1982).

[9] **R.K Miller.:** *Nondestructive Testing Handbook*. Acoustic Emission Testing – vol. 5, ASTN, Columbus 1987

[10] **I. Malecki, J. Ranachowski:** *Emisja Akustyczna. Źródła, metody, zastosowania*, Biuro PASCAL, Warszawa 1994.

Jan Wojnar

ANALIZA WYTRZYMAŁOŚCIOWA WARSTW AZOTOWANYCH WYTWORZONYCH NA AUSTENITYCZNEJ STALI NIERDZEWNEJ NA PODSTAWIE POMIARÓW EMISJI AKUSTYCZNEJ (AE)

Streszczenie

Celem niniejszej pracy był opis przebiegu deformacji i niszczenia warstw azotowanych wytworzonych na stali austenitycznej w oparciu o badania zjawisk emisji akustycznej (EA) w czasie statycznej próby rozciągania. Warstwy na stali typu (AISI 304) wytworzono metodą azotowania jarzeniowego. Wykonano badania mikrotwardości, badania mikrostruktury oraz składu fazowego. Główną metodę badawczą w tej pracy stanowił pomiar emisji akustycznej. Wykazano, że na podstawie przebiegu charakterystycznych parametrów EA, energii i napięcia skutecznego RMS, możliwe jest określenie granicy plastyczności, początku propagacji pęknięć w warstwie oraz dynamiki przebiegu pękania warstwy.

NUMERICAL METHODS USED IN ROTATING DETONATION SIMULATIONS

Karol Swiderski
Institute of Aviation

Abstract

The detonation is a phenomenon which has been known for over a hundred years. We generally understand this process of rapid combustion, however the details of the shock structure and chemical mechanism of the detonation is still a subject of intense research due to its practical importance. Recently, the study on the rotating detonation engine (RDE) has given a new impulse for the science of detonation. Because of geometrical complexity of the spinning and rotating detonation, new experimental and numerical tools are necessary. Especially very robust codes for simulating the rotating detonation engines are important. They should allow resolving details of the flow field which are unavailable or even impossible to obtain from analysis of the experimental results. On the other hand, when they are validated, they could be a useful tool for optimization of the rotating detonation engine in the future.

This paper presents recent attempt to use such methods that are supposed to enable three-dimensional modeling of the detonation (in general) and the rotating detonation engine (in particular).

INTRODUCTION

The concept of the rotating detonation engine (RDE) was introduced by Wolanski and Fujiwara and described in their works: [1], [2], [3]. The working principle of RDE is based on propagation of spinning detonation wave in annular chamber, which causes high centrifugal forces that influence on combustion products resulting in suction of fresh mixture. A fresh mixture must have a sufficient time to refill the reaction zone, where the detonation wave has already passed, before the next appearance of detonation front. At the same time the combustion products are being exhausted via the nozzle producing thrust for the engine. Due to continuous propagation of the detonation in circular chamber, the engine utilizes the advantages of detonative combustion and avoids the main problem of a pulsed detonation engine – the pulsations and vibrations.

The schematic diagram of the RDE is shown below in Figure 1. More information about this engine can be found in [1], [2], [4]. The Rotating Detonation Engine was applied for a patent by P. Wolanski, T. Fujiwara and Mitsubishi group [3] and has recently gain significant interest among numerous laboratories.

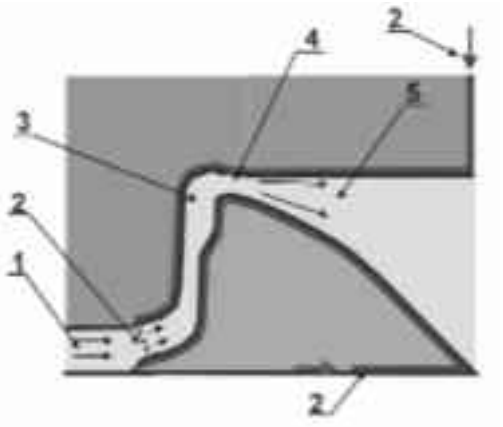

Figure 1. Schematic diagram of RDE. 1-inlet (air), 2-fuel injection, fuel cooling of combustion chamber, 3-„ring-like combustion chamber", 4-throat, 5-expansion nozzle; [2]

2. MATHEMATICAL EXPRESSION OF THE FINITE VOLUME METHOD

Associated with choice of mesh type is the formulation of discretization procedure for the equations of fluid flow. In the finite volume method, the discretization is accomplished by dividing the domain of the flow into a large number of small subdomains, and applying the conservation laws in the integral form:

$$\frac{\partial}{\partial t}\int_{\Omega} u dV + \int_{\partial\Omega} \mathbf{f} d\mathbf{S} = 0 \tag{1}$$

Here u is a component of the matrix of the state (e.g. density, momentum, energy) and $\mathbf{f}$ is corresponding flux. The use of the integral form has the advantage that no assumption of the differentiability of the solutions is implied, with the result that it remains a valid statement for a subdomain containing a shock wave.

3. MATHEMATICAL MODEL AND NUMERICAL METHODS

3.1. Mathematical model of inviscid reacting gas flow

A semi-ideal gas model may be used. The gas is a multi-component mixture with nsp number of components and it fulfils following equation of state:

$$\frac{p}{\rho} = RT \tag{2}$$

where

$$\rho = \sum_{i=1}^{n_{sp}} \rho_i \qquad Y_i = \frac{\rho_i}{\rho} \qquad R = \sum_{i=1}^{n_{sp}} \frac{Y_i}{W_i} R_u$$

Specific heat, enthalpy and entropy of the gas components can be described as functions of temperature:

$$c_{pk}(T) = R\sum_{i=1}^{5} a_{ik} T^{i-1} \tag{3}$$

$$h_k(T) = RT\left(\sum_{i=1}^{5} a_{ik} T^{i-1} + \frac{a_{6k}}{T}\right) \tag{4}$$

$$s_k(T) = R\left(a_{1k}\ln(T) + \sum_{i=2}^{5} \frac{a_{ik}}{i-1} T^{i-1} + a_{7k}\right) \tag{5}$$

Gas dynamics is expressed by Euler equations:

$$\frac{\partial Q}{\partial t} = -\frac{\partial E}{\partial \xi} - \frac{\partial F}{\partial \eta} - \frac{\partial G}{\partial \zeta} - H - S \tag{6}$$

In Cartesian coordinates :

$$\xi = x, \quad \eta = y, \quad \zeta = z \qquad u = \mathbf{v}_x, \quad v = \mathbf{v}_y, \quad w = \mathbf{v}_z \tag{7}$$

The following vectors are used in equation (6):

$$Q = \begin{pmatrix} \rho \\ \rho u \\ \rho v \\ \rho w \\ e \\ \rho_i \end{pmatrix} E = \begin{pmatrix} \rho u \\ \rho u^2 + p \\ \rho v u \\ \rho w u \\ (e+p)u \\ \rho_i u \end{pmatrix} F = \begin{pmatrix} \rho v \\ \rho u v \\ \rho v^2 + p \\ \rho w v \\ (e+p)v \\ \rho_i v \end{pmatrix} G = \begin{pmatrix} \rho w \\ \rho u w \\ \rho v w \\ \rho w^2 + p \\ (e+p)w \\ \rho_i w \end{pmatrix} S = \begin{pmatrix} 0 \\ 0 \\ 0 \\ 0 \\ 0 \\ \omega_i \end{pmatrix} \tag{8}$$

In case of cylindrical coordinates:

$$\xi = x, \quad \eta = r, \quad \zeta = \phi \qquad u = \mathbf{v}_x, \quad v = \mathbf{v}_r, \quad w = \mathbf{v}_\phi \tag{9}$$

the vectors are the same but H is not equal zero:

$$H = \frac{1}{r} \begin{pmatrix} \rho v \\ \rho u v \\ \rho v^2 \\ \rho w v \\ (e+p)v \\ \rho_i v \end{pmatrix} \tag{10}$$

The source term S describes chemical composition change rate resulting from the chemical reactions. The production rate of chemical compounds ω_i is an overall sum of the production and destruction rates for a given chemical compound in all reactions taken into account in the chemistry model:

$$\omega_i = \frac{d\rho_i}{dt} = W_i \left[\sum_{k=1}^{\alpha} \pm \nu_{i,k} \alpha \left(k_{k,for} \prod_j C_j^{\nu'_{j,k}} - k_{k,back} \prod_j C_j^{\nu''_{j,k}} \right) \right] \tag{11}$$

The rate of the reactions is described by the Arrhenius equation:

$$k_{k,for} = A_k T^{n_k} \exp\left(-E_{a,k} / RT\right) \tag{12}$$

The rate of backward-reactions is counted from the assumption of temporary, local thermodynamic equilibrium:

$$K_k = \frac{k_{k,for}}{k_{k,back}} (RT)^{\Delta \nu_k} \tag{13}$$

where

$$\ln K_k = \frac{\pm \nu_{i,k} s_i^\circ}{R} - \frac{\pm \nu_{i,k} \Delta h_{f,i}^\circ}{RT} \tag{14}$$

The model described above is a typical one and mostly used in numerous works concerning simulations of the gaseous detonations [5], [6], [7], [8], [9], [10], [11].

3.2. General numerical approach

A class of wave propagation algorithms for three-dimensional conservation laws and other hyperbolic systems may be used. These Finite Volume Methods are based on solving one-dimensional time-dependent Riemann problems at the cell interfaces and applying flux-limiter functions to suppress oscillations arising from second-derivative terms in second order upwind schemes. One-dimensional solvers are discussed here, although the algorithms may be also extended to three dimensions by applying two-step splitting method [12] or by applying unsplit method.

The performance and accuracy of some of these schemes is illustrated by numerical examples for one- and three-dimensional gas-dynamics problems. Much of mathematical theory is omitted. However, when appropriate, sufficient references will be provided. Moreover, only some numerical methods are discussed here– upwind methods which achieve the best performance and accuracy for wave propagation problems.

These methods base on the Finite Volume Method (FVM), which is often used in the Computational Fluid Dynamics (CFD). FVM methods are the most intuitive because they are based on the local mass or energy conservation over volumes (control volumes, finite volumes or co-volumes). These methods is situated somewhere between the Finite Element (FEM) and Finite Difference Methods (FDM) [13]. They pose grid flexibility analogous to that of FEM, and they can be implemented in a way comparable to the FDM. The FVM methods may be mathematically treated as Petrov-Galerkin methods with trial function spaces associated with certain finite element spaces and test spaces related to finite volumes.

The upwind methods for the computational fluid dynamics form a respectable class of numerical techniques available to the CFD practitioner today. This is the result of an intensive research activity spanned over many years. The distinguished works of Godunov [14]; van Leer [15], [16]; Roe [17]; Osher and Solomon [18]; Harten [19]; and many others, have provided a solid theoretical framework for further advancement.

3.3. Riemann solvers for convective terms

A Riemann solver is a numerical method used to solve the Riemann problem in general. Extensive discussion of the class of Riemann solver is provided by Toro [9]. The basic algorithm of this solver may be described as follows (figure 2):

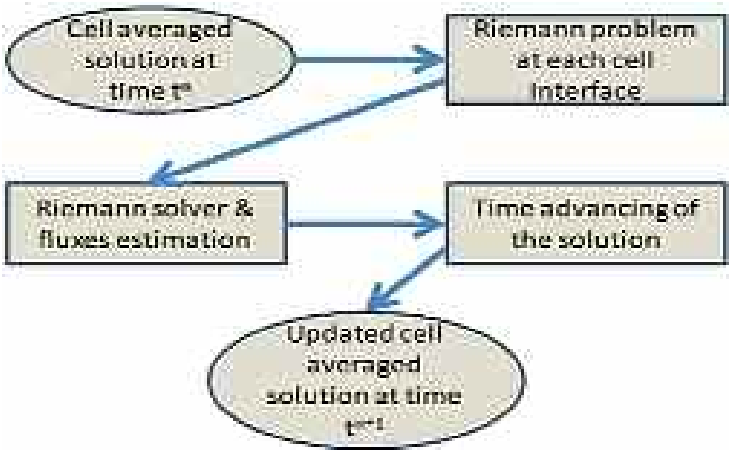

Figure 2. Flowchart of Riemann solver.

There are two ways of evaluating the numerical flux employed in a numerical method: one approach is to find an approximation to the state at the interface and then evaluate the physical flux function at this location; the second approach is to find an approximation to the numerical flux, directly from the cell averaged states. The second approach is recommended because of its accuracy, which has been proven by numerous application of this method.

3.3.1. The HLLC Riemann solver

The HLLC Solver is more accurate than the Roe solver is [20]. It includes four possible states near the discontinuities. While it demands pressure-velocity estimation in the „star region", it may be obtained by applying iterative Newton-Raphson method [21] or other (non-iterative, heuristic etc.). The numerical flux in the HLLC solver is calculated as:

$$F_{i+\frac{1}{2}} = \begin{cases} F_L & 0 \le S_L \\ F_{*L} = F_L + S_L(U_{*L} - U_L) & S_L \le 0 \le S_* \\ F_{*R} = F_R + S_R(U_{*R} - U_R) & S_* \le 0 \le S_R \\ F_R & 0 \ge S_R \end{cases} \tag{15}$$

where

$$U_{*K} = \rho_K \left(\frac{S_K - u_K}{S_K - S_*} \right) \begin{bmatrix} 1 \\ S_* \\ v_K \\ w_K \\ \frac{E_K}{\rho_K} + (S_* - u_K)\left[S_* + \frac{p_K}{\rho_K (S_K - u_K)} \right] \end{bmatrix} K = L, R \tag{16}$$

This solver restores the missing rarefaction wave by some estimates, like linearization. The linearization methods is simple but also more advanced ones exist, such as using Roe average velocity for the middle wave speed.

The significant advantage of the HLLC Riemann solver is its universality in terms of the model of the gas. The mathematical structure of the solver is based only on very limited assumptions about the gas features. Indeed, the solver's equations are valid for any gas model which comply the equation of state of the ideal gas. Therefore, extension of the solver to more complicated models of the gas is relatively simple. Due to this feature, the presented solver can be easily adopted to semi-ideal gas where the specific heat and specific heat ratio are functions of temperature. Moreover, for the semi-ideal gas only the values of γ_i are to be updated comparing to the ideal gas solver. For comparison, the Roe solver demands replacing the relationships describing the eigenvalues and eigenvectors for every specific model of the gas.

The advective mass fluxes of each chemical compound may be calculated as proportional to the total mass flux:

$$F_{\rho_i} = y_i F_\rho \tag{17}$$

however, some special treatment is necessary in order to avoid negative partial densities after time integration.

The well known problem of all solvers used in simulation of shock waves is preserving the monotonicity or avoiding spurious oscillations in the vicinity of flow discontinuity. ENO or WENO schemes are one of the answers to this problems. The HLLC Riemann solver is excellent background for high-ordered monotonic numerical schemes.

3.3.2. Lax-Wendroff numerical flux

The Lax-Wendroff scheme is one method which can reduce numerical diffusion arising from numerical diffusivity of first order schemes. Here an additional (corrective) term is presented. This corrective flux should be restricted by TVD method (Total Variation Diminishing) and limiting functions (limiters): Superbee, van Leer, Minmod, Monotonic-Centered etc. The limiter allows the numerical dispersion of high-order scheme to be reduced. Mathematical description of mentioned limiters can be found in [9].

The corrective flux is expressed by the formula [22]:

$$\hat{F}_{i-\frac{1}{2}} = \frac{1}{2}\sum_{p=1}^{m}\left|\tilde{\lambda}^p\right|\left(1-\frac{\Delta t}{\Delta x}\left|\tilde{\lambda}^p\right|\right)\tilde{\alpha}_p\tilde{K}^{(p)}\Phi\left(\theta^p\right) \tag{18}$$

where

$$\theta^p = \frac{\tilde{\alpha}_p^I}{\tilde{\alpha}_p^{I-1}} \qquad I = \begin{cases} i-\frac{1}{2}, \tilde{\lambda}^p > 0 \\ i+\frac{3}{2}, \tilde{\lambda}^p \le 0 \end{cases} \tag{19}$$

Φ is the limiting function (limiter).

The main flux - resulting from first order scheme - has to be computed for every grid cell in the computational space. Then the corrective flux (18) should be added to the main flux.

3.3.3. The WAF-TVD numerical flux

Another option of improving the stability and accuracy of calculation is use of a WAF-TVD schemes. The WAF-TVD (Weighted Average Flux TVD version) flux may be written as [23], [24]:

$$F_{i-\frac{1}{2}} = \frac{1}{2}(F_i + F_{i-1}) - \frac{1}{2}\sum_{k=1}^{m} sign(c_k)\Phi^k_{i-\frac{1}{2}}\Delta F^k_{i-\frac{1}{2}} \tag{20}$$

The limiting functions for WAF scheme differ from previous limiters what is shown below:

$$\Phi_{WAF} = 1-(1-|c|)\Phi \tag{21}$$

The WAF-TVD scheme in conjunction with the HLLC Riemann solver is second order accurate in time and space. It allows obtaining very accurate results generally, but has larger numerical cost.

The WAF approach has been shown to be successful in applications to a variety of practical problems (reactive flows, shallow water equations, time-dependent Euler equations). Its key feature is, that the second order accuracy can be achieved by solving the conventional piecewise constant Riemann problem like in the first order Godunov method – no reconstruction/evolution steps are necessary, although these processes may also be admitted. The accuracy results from utilizing this solution averaged over space and time. This averaging takes the form of an integral of the flux, or chosen variables, over some volume. The standard way to extend this scheme to two and three space dimensions is via space operator splitting, as discussed by Strang [25], in which the one-dimensional difference operators are used in each dimension in turn. This approach has been shown to be successful.

3.3.4. Dimensional splitting

Here the possibility of using dimensional splitting is discussed with an assumption that structural grids are implemented for discretization of the computational domain. This approach enables using techniques which simplify some programming issues and allow significant reduction of necessary memory. For example use of dimensional splitting reduces the size of storage for fluxes by immediate updating the conservative variables instead of storing the fluxes for each cell boundary. The dimensional splitting can be mathematically described as follows:

$$\begin{aligned} U^{t2} &= U^{t1+\Delta t} = L_x L_x L_z L_z L_y L_y U^{t1} \\ U^{t3} &= U^{t2+\Delta t2} = L_z L_z L_y L_y L_x L_x U^{t2} \\ U^{t4} &= U^{t3+\Delta t3} = L_y L_y L_x L_x L_z L_z U^{t3} \end{aligned} \tag{21}$$

The technique of alternating the order of the sweeps is called Strang splitting and it increases the order of accuracy of the 3D update from first to second order assuming the one-dimensional methods are at least second order accurate.

The other advantage of operator splitting technique is that it allows writing one-dimensional algorithms which are relatively simpler than multi-dimensional and easy to optimize. For example, when sweeping in z-direction, one can break up the data into one-dimensional columns and operate on the independent columns in parallel.

3.4. Time advancing methods

3.4.1. Timestep splitting

Each term: the advective one, the chemical one and the geometrical one (for cylindrical coordinates system) may be integrated separately with appropriate numerical method. For instance: the advective terms may be integrated using explicit Euler method or fourth-order Runge-Kutta method (RK4); the chemical source term can be integrated using Chemeq2 or DVODE subroutines.

3.4.2. Integration of the advective terms

For advancing in time typical explicit formula may be used:

$$U_i^{n+1} = U_i^n + \frac{\Delta t}{\Delta x}\left(F_{i-\frac{1}{2}} - F_{i-\frac{1}{2}}\right) \tag{22}$$

Formula (22) is called an Euler explicit method. It advances a solution from state n to n+1 with interval Δt. The formula is unsymmetrical – uses derivative information only at the beginning of the interval. Moreover, that means that the step's error is only one order of Δt smaller than the correction.

However, there are several reasons that Euler's method is not recommended for practical use, among them, the method is not very accurate when compared to other. On the other hand, it is very fast and simple.

For more accurate simulations the conventional fourth Runge-Kutta method may be implemented. This method uses approximations of the time derivatives at fractional timestep:

$$\begin{aligned} y(t+\Delta t) &= y(t) - \frac{1}{6}(A+2B+2C+D) \\ A &= \frac{dy}{dt}(y(t)) \cdot \frac{dt}{2} \\ B &= \frac{dy}{dt}(y(t)+A) \cdot \frac{dt}{2} \\ C &= \frac{dy}{dt}(y(t)+B) \cdot dt \\ D &= \frac{dy}{dt}(y(t)+C) \end{aligned} \tag{23}$$

3.4.3. Integration of the chemical source terms

The integration of chemical sources, which describe the production and destruction of chemical compounds, is difficult from numerical point of view because the set of chemical ODEs is stiff. It means that each equation describes the processes occurring in different time scales. From this fact, it can be pointed out that the special integration procedures must be used. It precludes the use of explicit integration schemes. Indeed, theoretical considerations and numerical practice

show that when explicit integrator is applied to stiff ODEs, the code will choose prohibitively small integration steps in order to preserve stability. However, implicit integrators have infinite stability regions, so the step size selection is done by monitoring local truncation errors to meet the accuracy requirements set by the user. For integration of the chemistry rate equations, implicit integrators work with relatively large step sizes when the accuracy requirements are not too stringent. This is done at the cost of solving a nonlinear system of equations at each integration step.

The author recommends using DVODE or Chemeq2 procedure in order to integrate the chemical source terms.

DVODE (Variable-Coefficient Ordinary Differential Equation solver, with fixed-leading-coefficient implementation) solves the initial value problem for stiff or non-stiff systems of first order ODEs of the form:

$$\frac{dy}{dt} = f(t, y) \tag{24}$$

or, in component form:

$$\frac{dy(i)}{dt} = f(i) = f(i, t, y(1), y(2), \ldots, y(n_{eq})), i = 1, \ldots, n_{eq} \tag{25}$$

DVODE is a package based on the EPISODE and EPISODEB packages, and on the ODEPACK user interface standard, with minor modifications.

DVODE internally uses functions which calculate the reactions rate at the place where chemical reaction rates are needed to determine the instantaneous rates of change of the species and temperature. A solver takes initial concentrations, initial temperature and timestep and returns final concentrations and temperature.

Chemeq2 is a solver for the Stiff Ordinary Differential Equations (SODEs) of chemical kinetics [26]. It integrates sets of coupled, nonlinear ordinary differential equations (ODEs) of the form:

$$\frac{dy_i}{dt} = g_i = q_i - p_i y_i \qquad 1 \le i \le n \tag{26}$$

where

y_i - density of the i-th species ,

g_i - rate of production of i-th specie,

$p_i y_i$ - rate of destruction of i-th specie,

g_i, g_j - rate of production/destruction of i-th specie

Chemeq2 uses the α -QSS (quasi-steady-state) predictor-corrector method [27]. This approach is fast and moderately accurate as well as easy to couple to reacting flow simulation models.

4. SUMMARY

The paper presents a comprehensive description of numerical methods for simulation of inviscid reactive flows. Recent years are period of important change in computer technology applied in common desktops and workstations. One can obtain a powerful multi-core computer with a large amount of shared memory at very low cost. This methods may utilize this opportunity. Although, the presented theory should be treated rather as a starting point where the further development begins.

During the development of an in-house code several problems have been encountered and solved. The tests proved that the selected methods work correctly for many classes of the problems including fully multidimensional reacting flows (Figure 3).

The numerical simulations of the RDE may uncover the complicated flow structure, what is very hard or even impossible to achieve only from experimental data. They may also confirm some experimental results where the interpretation of measurement was unclear.
The paper is intended to be a source of information for scientist developing own CFD software and potential users as well. Thus, anybody who is interested in more detailed information about it is encouraged to contact the corresponding author for further communications.

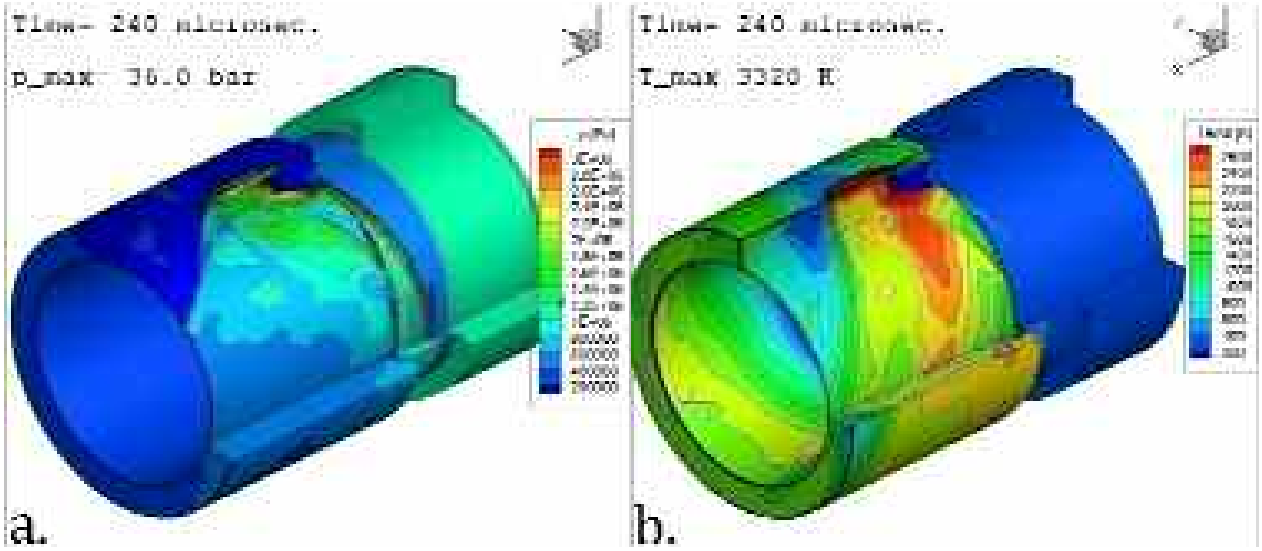

Figure 3. Propagation of the detonation in RDE chamber: a)pressure field ; b)temperature field [28]

REFERENCES

1. **Wolanski, P.:** *Cooperation of the Institute of Heat Engineering with Japanese Universities and Reasearch Institutes*. Warsaw : WUT, 2007.
2. *An experimental study of Rotating Detonation Engine*. **Wolanski, P., Kindracki, J., Fujiwara, T. et.al.** Montreal : MC Gill University, 2005.
3. Patent application for RDE by Mitsubishi Heavy Industries. 29 June 2004.
4. **Wolanski, P., Kindracki, J., Fujiwara, T.:** *An experimental study of small Rotating Detonation Engine*. Moscow : Torus Press, 2006.
5. *Theory of Detonation*. **Zeldovich, I.B., Kompaneets, A.S.** NY & London : Academic Press, 1960.
6. **Tsuboi, N., S. Katoh, A.K. Hayashi.** *Three-dimensional numerical simulation for hydrogen/air detonation: Rectangular and diagonal structures*. Proceedings of the Combustion Institute. 2002, Vol. 29.
7. **Lefebvre, M.H., Fujiwara, T.:** *Robust Euler Codes for Hypersonic Reactive Flows*. Memoirs of the School of Engineering. 1994, Vol. 46, 1.
8. **Leblanc, J.E., Lefebvre, M.H., Fujiwara, T.:** *Detailed Flowfields of a RAMAC Device in H2-O2 Full Chemistry*. Shock Waves. 1996, Vol. 6, 2.
9. **Toro, E.F.:** *Riemann Solvers and Numerical Methods for Fluid Dynamics*. Berlin : Springer, 1999.
10. **Hu, X.Y., et al.** *The structure and evolution of a two-dimensional H2/O2/Ar cellular detonation*. Shock Waves. 2005, Vol. 14, 1.
11. *Numerical Simulation of Rotating Detonation in Cylindrical Channel*. **Milanowski, K., et al.** Poitiers, France: 21st ICDERS, 2007.
12. **Billet, S.J, Toro, E. F.:** *On the accuracy and Stability of Explicit Schemes for Multidimensional Linear Homogeneous Advection Equations*. J.Comp.Phys. 1997, Vol. 131.
13. **Chen, Z.:** *On the control volume finite element methods and their applications to multiphase flow*. American Institute of Mathematical Sciences. 2006, Vol. 1, 6.

14. **Godunov, S.K.:** *A Finite Difference Method for the Computation Discontinuous Solutions of the Equations of Fluid Dynamics*. Mat. Sb. 1959, Vol. 47.
15. **van Leer, B.:** *Towards the ultimate conservative differnece scheme IV. A new approach to* numerical convection. J. Comput. Phys. 1977, Vol. 23.
16. **van Leer, B.:** *Towards the ultimate conservative differnece scheme V. A second order sequel to Godunov's method*. J. Comput. Phys. 1979, Vol. 32.
17. **Roe, P.L.:** *Approximate Riemann Solvers, Parameter Vectors, and Difference Schemes*. J.Comput. Phys. 1981, Vol. 43.
18. **Osher, S., Solomon, F.:** *Upwind difference schemes for hyperbolic systems of conservation laws*. Math. Comput. 1982, Vol. 38.
19. **Harten, A.:** *On a class of high resolution total-variaton-stable finite dif ference schemes*. SIAM J. Numer. Anal. 1984, Vol. 21, 1.
20. **Toro, E.F., M.Spruce, W.Speares.** *Restoration of the Contact Surface in the HLL-Riemann Solver*. Shock Waves. 1994, Vol. 4.
21. **Maron, M.J., R.J.Lopez.:** Numerical Analysis: A Practical Approach. Belmont, CA : Wadsworth, 1991.
22. **LeVeque, R.J.:** *Wave Propagation Algorithms for Multidimensional Hyperbolic Systems*. J.Comput.Phys. 1997, Vol. 131.
23. **Toro, E. F.:** *A weighted average flux method for hyperbolic conservation laws*. Proc Roy Soc Lond A. 1989, Vol. 423.
24. **Toro, E. F.:** *The weighted average flux method applied to the Euler equations*. Philos Trans Roy Soc Lond A. 1992, Vol. 341.
25. **Strang, G.:** *On the construction and comparision of difference schemes*. SIAM J. Numer. Anal. 1968, Vol. 5.
26. **Mott, D., E.S.:** Oran. *Chemeq2: A solver for the stiff ordinary differential equations of chemical kinetics.* Washington : Naval Research Lab., 2001.
27. **Liu, F., Schaller, E., Mott, D.:** *Application of -QSS to the numerical integration of kinetic equations in tropospheric chemistry.* Atmos.Chem.Phys.Discuss. 2005, Vol. 5.
28. **A. Kobiera, K. Swiderski, M. Folusiak, P. Wolanski.:** *"REFLOPS" - a New Parallel CFD Code for Reactive Euler Flow Simulation.* Archivum Combustionis. 2009.

Karol Swiderski

METODY NUMERYCZNE WYKORZYSTYWANE W SYMULACJI WIRUJĄCEJ DETONACJI

Streszczenie

Detonacja jest zjawiskiem, które znane jest nauce od ponad stu lat. Na ogół rozumiemy ten proces szybkiego spalania, jednak szczegóły struktury detonacji i jej mechanizm chemiczny są nadal przedmiotem intensywnych badań ze względu na ich znaczenie praktyczne. W ostatnim okresie prace badawcze nad silnikiem z wirującą detonacją (RDE) dały nowy impuls dla badań nad zjawiskiem detonacji. Z powodu geometrycznej złożoności zjawiska wirującej i obracającej się detonacji, konieczne są nowe narzędzia do badań, eksperymentalne i numeryczne. Szczególnie ważne są bardzo silne programy do symulacji silników z wirującą detonacją. Powinny one umożliwić rozwiązanie szczegółów w polu przepływu, które są niedostępne lub nawet niemożliwe do uzyskania z analizy wyników eksperymentalnych. Z drugiej strony, jeżeli zostaną one potwierdzone, mogą być one użytecznym narzędziem w przyszłości do optymalizacji silnika z wirującą detonacją.

W artykule przedstawiono najnowsze próby wykorzystania takich metod, które mają umożliwić trójwymiarowe modelowanie detonacji – w ogólności, a w szczególności – modelowanie silnika z wirującą detonacją.